DESARROLLO DE MATERIALES FUNCIONALES A PARTIR DE BIOMASA RESIDUAL DE PALMA DE ACEITE PARA EL MEJORAMIENTO DE EFLUENTES DE LA INDUSTRIA PALMERA

ANDREA PAOLA MARTÍNEZ RAMÍREZ

B.S CHEMISTRY

UNIVERSIDAD INDUSTRIAL DE SANTANDER

FACULTAD DE CIENCIAS

ESCUELA DE QUÍMICA

DOCTORADO EN QUIMICA

BUCARAMANGA

2024

DESARROLLO DE MATERIALES FUNCIONALES A PARTIR DE BIOMASA RESIDUAL DE PALMA DE ACEITE PARA EL MEJORAMIENTO DE EFLUENTES DE LA INDUSTRIA PALMERA

ANDREA PAOLA MARTÍNEZ RAMÍREZ

A doctoral dissertation submitted in partial fulfillment of the requirements for the Doctor degree in Chemistry

Advisors
PhD. Marianny Yajaira Combariza Montañez
PhD. Cristian Blanco Tirado

UNIVERSIDAD INDUSTRIAL DE SANTANDER
FACULTAD DE CIENCIAS
ESCUELA DE QUÍMICA
DOCTORADO EN QUIMICA
BUCARAMANGA
2024

Table of contents

List of Figures

List of Tables

List of Appendices

Resumen

Desarrollo de materiales funcionales a partir de biomasa residual de palma de aceite para el mejoramiento de efluentes de la industria palmera[*]

Autor: Andrea Paola Martínez Ramírez[**]

Palabras clave: Raquis de palma de aceite, celulosa, biomateriales, magnetita, POME

El procesamiento del fruto de palma aceitera genera una variedad de residuos sólidos y líquidos, incluyendo fibras de raquis, mesocarpio, almendra, cascarilla, y un efluente conocido como POME (Palm Oil Mill Effluent). El raquis o tusa vacía (EFB por sus siglas en inglés Empty Fruit Bunch) es la biomasa residual más abundante del cultivo de palma y se compone principalmente de celulosa, lignina y hemicelulosa. En Colombia se producen alrededor de setenta y nueve mil de toneladas por año. Este estudio se centró en investigar el potencial de las fibras de EFB para la síntesis de materiales funcionales que incorporen biopolímeros derivados de esta biomasa para el tratamiento de aguas residuales de la industria de aceite de palma. En Colombia se cultivan principalmente dos tipos de variedades de palma *Elaeis guineensis* (E.G) y el híbrido interespecífico *Elaeis guineensis* × *Elaeis oleifera* (O×G). La primera parte del estudio se centró en determinar las características composicionales de esta biomasa en términos de partes del racimo (tallo y espiguillas), proceso de esterilización y cultivar. Posteriormente se exploró el aislamiento de nanocelulosa a través de procesos químico-mecánicos. Se investigó el impacto de diferentes parámetros de reacción en la funcionalidad del material. Considerando que las fibras de raquis son abundantes y contienen biopolímeros como la celulosa, estas pueden servir como matrices para depositar óxidos metálicos con actividad catalítica en la oxidación de contaminantes orgánicos. Por lo tanto, se investigó la síntesis de un material biocompuesto (fibras de raquis-óxido metálico) con potenciales aplicaciones en procesos de oxidación avanzada para la eliminación del color del POME. Además, se investigó el uso de recubrimientos de nanocelulosa para incrementar la estabilidad del material biocompuesto y mejorar su desempeño en términos de ciclo de reúso del material. Finalmente, se determinaron los parámetros cinéticos y termodinámicos de la remoción del color en el POME mediante la oxidación Fenton heterogénea con catalizadores de raquis/magnetita.

---

[*] Tesis Doctoral

[**] Facultad de Ciencias. Escuela de Química. Doctorado en Química. Directora: Marianny Yajaira Combariza M, Ph.D. Co-director: Cristan Blanco Tirado PhD.

Abstract

Development of functional materials from residual palm oil biomass for the improvement of palm oil industry effluents[*]

Autor: Andrea Paola Martínez Ramírez[**]

Keywords: Empty fruit bunch, cellulose, biomaterials, magnetite, POME.

The processing of oil palm fruit generates a variety of solid and liquid wastes, including rachis fibers or Empty Fruit Bunch (EFB), mesocarp, kernel, shell, and an effluent known as POME (Palm Oil Mill Effluent). EFB is the most abundant residual biomass of palm cultivation and is primarily composed of cellulose, lignin, and hemicellulose. In Colombia, approximately seventy nine thousand tons are produced annually. This study focused on investigating the potential of EFB fibers for synthesizing functional materials incorporating biopolymers derived from this biomass for the treatment of wastewater from the palm oil industry. In Colombia, mainly two types of palm cultivars are cultivated: *Elaeis guineensis* (E.G) and the interspecific hybrid *Elaeis guineensis* × *Elaeis oleifera* (O×G). The first part of the study aimed to determine the compositional characteristics of this biomass in terms of fruit bunch components (stalk and spikelets), sterilization process, and cultivar. Subsequently, the isolation of nanocellulose through chemical-mechanical processes was explored, investigating the impact of different reaction parameters on the material's functionality. Considering that EFB fibers are abundant and contain biopolymers like cellulose, they can serve as matrices for depositing metallic oxides with catalytic activity in the oxidation of organic contaminants. Therefore, the synthesis of a biocomposite material (EFB fiber-metal oxide) with potential applications in advanced oxidation processes for POME color removal was investigated. Additionally, the use of nanocellulose coatings to increase the stability of the biocomposite material and improve its performance in terms of material reuse cycles was investigated. Finally, kinetic and thermodynamic parameters of color removal in POME through heterogeneous Fenton oxidation with EFB/magnetite catalysts were determined.

---

[*] Doctoral Thesis

[**] Faculty of Science. School of Chemistry. Doctorate in Chemistry. Director: Marianny Yajaira Combariza Montañez, Ph.D. Codirector: Cristian Blanco Tirado, Ph.D.

Introduction

Colombia is an agricultural country, holds the position of the world's fourth-largest producer of palm oil. As of 2022, the country reported a palm oil production of $18.0x10^5$ tons (IPAD International Production Assessment Division, 2022). From 1000 kg of fresh fruit bunches, approximately 225 kg of oil, 234 kg of Empty Fruit Bunch (EFB), and 5000 kg of aqueous effluent, known as Palm Oil Mill Effluent (POME), are generated (Lam & Lee, 2011). EFB is the primary lignocellulosic waste generated by the palm oil industry during the mechanical separation of fruit from its natural carrier (Amran, Zakaria, Chia, Fang, & Masli, 2017). Commonly used as fuel for boilers and in plantation fertilizer production to enhance soil physico-chemical properties, proper storage is essential to prevent leachate generation and environmental issues (Ramírez-Contreras et al., 2011). EFB's primary components, including cellulose, lignin, and hemicellulose, make it a promising matrix for cellulose isolation (Mohammad Padzil, Lee, Ainun, Lee, & Abdullah, 2020; Rui et al., 2019; Shi, Wang, Davaritouchaee, Yao, & Kang, 2020), EFB has porous and rough structure with hydroxyl groups (Asadpour et al., 2021).

The focus of this project was to evaluate and explore EFB, a lignocellulosic waste, for the synthesis of functional materials for wastewater treatment in the palm oil industry (Scheme 1). In Colombia, two main cultivars of palm are primarily cultivated, *Elaeis Guineesis* (E.G) and the interspecific hybrid *Elaeis oleifera*×*Elaeis guineensis* (O×G). Therefore, the first chapter focused on the physicochemical characterization of EFB, analyzing the components of the bunch (stalk and spikelets), the bunch conditions (sterilized or fresh), and the cultivar (E.G or O×G). Typically, EFB fibers in processing plants are a blend of sterilized fibers from bunchs comprises approximately 75% stalks and 25% spikelets of various cultivars (Rama Rao & Ramakrishna, 2022).

Secondly, given the high cellulose content in EFB, the chemical/mechanical isolation and characterization of nanocellulose derived from the EFB were explored. The functionality of this material relies on the extraction conditions, which were thoroughly explored in the second chapter. The process involves oxidation with TEMPO (2,2,6,6-Tetramethylpiperidin-1-oxyl) radicals, followed by mechanical treatment to obtain TEMPO-oxidized cellulose nanofibers (TOCN). An experimental design was employed to analyze the influence of variables such as reaction time, oxidant amount, and matrix pretreatment on the degree of TOCN oxidation, particle size, Z-potential, and carboxylate group content. Delignification processes are essential for EFB fibers to remove lignin, making cellulose accessible, given the high lignin content. Notably, when TEMPO oxidation is conducted without prior delignification, the reaction yield diminishes by 50% due to the competitive nature between delignification and oxidation processes.

Considering that EFB comprises biopolymers such as cellulose can served like a support matrix for synthesizing biomaterials with catalytic activity for treatments on POME using advanced oxidation process. The third chapter details the synthesis of three biocomposites based on EFB/magnetite for color removal from POME. Furthermore, recognizing the potential leaching of active substances in these biocomposites, leading to decreased oxidation efficiency. The study investigated the use of nanocellulose coatings (discussed in the second chapter) to enhance the stability of the EFB/magnetite biocomposite and improve its performance in the color removal of POME during material reuse cycles.

Finally, in the last chapter a comprehensive kinetic and thermodynamic study was conducted to examine the removal of color from POME with EFB/magnetite biocomposites, at three distinct temperatures. The primary focus of the study was to determine the reaction order, constant values, and thermodynamic parameters associated with the color removal process. In addition, due to the complex nature of POME, standard solutions were not applicable due to the differences in conditions between standard solutions and POME.

Scheme 1. Project development

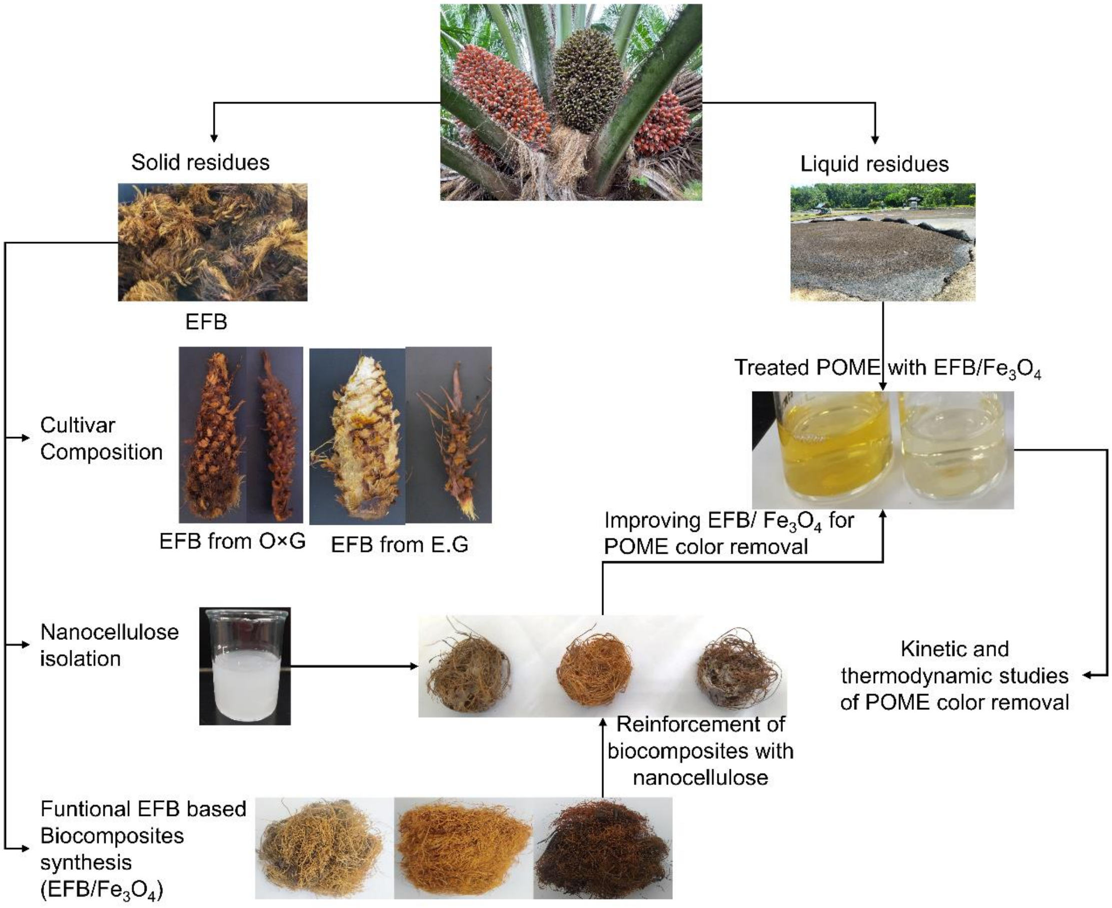

This dissertation is divided into four sections as follows:

CHAPTER 1: Comparative Physicochemical Analysis of Empty Fruit Bunches from *E. guineensis* and *E. oleifera* x *E. guineensis* Hybrid Palm Oil Cultivars in Colombia

CHAPTER 2: Influence of Reaction Variables on the Surface Chemistry of Cellulose Nanofibers Derived from Palm Oil Empty Fruit Bunches

CHAPTER 3: Empty Fruit Bunch Fiber-based Composite Materials for the Heterogeneous Advanced Oxidation of Palm Oil Mill Effluent (POME)

CHAPTER 4: Kinetics and thermodynamics of empty fruit bunches/magenite quaternary biocomposites for POME color removal

1. Comparative Physicochemical Analysis of Empty Fruit Bunches From *E. guineensis* and *E. oleifera x E. guineensis* Hybrid Palm Oil Cultivars in Colombia

1.1. Abstract

Colombia's fresh fruit bunches processing generates 1.7 million tons of empty fruit bunches (EFB) annually, offering a renewable energy and material source rich in cellulose, lignin, and hemicellulose. This study focuses on the compositional and physicochemical variations within stalks and spikelets of fresh and sterilized EFB from *Elaeis guineensis* (E.G) and the interspecific hybrid *Elaeis guineensis* × *Elaeis oleifera* (O×G), the primary cultivars in Colombia. Elemental content and calorific values exhibit notable variations within each cultivar, with sterilization processes affecting mainly the elemental content. EFB cellulose crystallinity and thermal stability remain unaffected by cultivar differences, sterilization, or specific bunch parts. These findings offer valuable insights for sustainable palm oil practices, contributing to environmentally friendly and economically viable circular processes towards EFB uses in bioenergy and value-added materials development.

1.2. Introduction

Oil palm produces the highest oil yield among major vegetable oil crops worldwide, delivering 3.3 metric tons per hectare (statista, 2020). Indonesia, Malaysia and Thailand are the top producers of palm oil, with 46 and 19 million metric tons, respectively, followed by Colombia, which ranks fourth globally and first in America, with 1.8 million tons produced in 2022 (U.S. Department of Agriculture, 2023). Palm oil is a highly versatile commodity used in a variety of industries, including food, pharmaceuticals, and energy. The oil palm belongs to the *Elaeis* genus, which has two main species, *Elaeis guineensis* (African palm) and *Elaeis oleifera* (American palm) (Arunachalam, 2012).

Oil from *Elaeis guineensis* (E.G), the primary commercial palm cultivar, contains an equal proportion of saturated and unsaturated fatty acids, carotenoids (500 – 700 ppm), and vitamin E (600 -1000 ppm) (Daud et al., 2012). This cultivar also produces fresh fruit bunches continuously from the second year after planting. Additionally, after extracting the oil from the mesocarp, palm kernel oil can be obtained from the fruit seed, which is used in the food and cosmetics industries (Choo et al., 1998; K. T. Tan et al., 2009). However, E.G is susceptible to bud rot, a disease that affects the growth of leaves and stalks, minimizing the production of fresh fruit bunches. Bud rot causes tissue breakdown, leading to the death of the plant (Moreno-Chacón et al., 2013; Navia et al., 2014). In the last 25 years, bud rot has affected 150,000 hectares of Colombian crops, resulting in a 50% loss (Bastidas, 2013). Although *Elaeis oleifera* (E.O) is a non-commercial cultivar, due to low oil yields, its oil has superior composition and quality compared to E.G oil in terms of unsaturated fatty acids (Arunachalam, 2012). E.O is primarily used to collect germplasm for producing the E.O×E.G (O×G) interspecific hybrid (Lieb et al., 2017). The O×G interspecific hybrid is an alternative cultivar for palm oil production because of its resistance to diseases such as bud rot (Mozzon et al., 2013). These hybrids are favored by the palm industry in Colombia due to their high-quality oil, which results from a higher content of unsaturated fatty acids compared to E.G oil (Moreno-Chacón et al., 2013).

In addition to high oil yields, the palm oil industry generates a significant amount of lignocellulosic biomass. For instance, processing 1 tonne of fresh fruit bunches yields 220-243 kg of empty fruit bunches (EFBs), 135-180 kg of palm pressed fibers, 50-73 kg of palm kernel shells, 25-122 kg of palm kernel cake, and 180 kg of decanter cake (Boonsawang & Youravong, 2017). Currently, these biomasses are primarily used as fertilizer to improve crops and fuel for steam generation in mills (Gan et al., 2023; Ramirez-Contreras et al., 2020). EFB, the most abundant palm oil residue, comprises stalks from the central axis of the fruit cluster and spikelets, originally containing the fruits (Asadpour et al., 2021; Rama Rao & Ramakrishna, 2022). Due to its unique compositional and structural characteristics, EFB is considered a high-value residue with potential applications as an energy and biomaterial source. Cellulose (23 to 65 wt%), hemicellulose (19 to 35 wt %), lignin (19 to 29 wt %), and ash (2 to 7 wt %) are the main components of EFB (Moreno-Chacón et al., 2013; Navia et al., 2014). The wide range of compositional variation is associated with palm variety, climate, location, and ripeness among other factors(Chang, 2014). Structurally, Khalil et al. (2008) reported that EFB consists of porous, multicellular fibers with an average lumen perimeter and cell wall thickness of 12.5 µm and 7.9 µm, respectively, and a cellulose crystal size of 2.53 nm (Khalil et al., 2008). Also, the thermal behavior of EFB is similar to other natural fibers (Ahmadzadeh & Zakaria, 2009).

The sterilization process is a crucial initial step in extracting palm oil at the mill. Its main purpose is to soften the fruits and prevent the growth of lipase-producing lipolytic organisms that can adversely affect the quality of the oils (Mohd Omar et al., 2018). However, sterilization can also affect EFB structure and composition. For instance, Hassan et al. reported that hemicellulose in the fruit's mesocarp fibers is hydrolyzed during sterilization, facilitating the release of oil from the globules that contain it (Mat Hassan et al., 2021). Other researchers have suggested that cellulose, hemicellulose, and lignin depolymerize during sterilization changing contents due to the process. Transformations in material morphology are attributed to lignins and wax removal, while cellulose and hemicellulose increase after sterilization (Shamsudin et al., 2012; Simarani et al., 2009). Changes during sterilization could -for instance- enhance the efficacy of biomass breakdown, leading to a more efficient bioconversion process. However, this effect has only been reported for the whole EFB. The influence of different cultivars and the anatomy of EFB fibers have not been thoroughly investigated to date.

The EFB fibers are characterized by their high moisture content, low calorific value, low combustion efficiency, and susceptibility to microbial degradation. EFB is predominantly employed as organic fertilizer in agricultural plantations, contributing to eutrophication, elevated soil toxicity, and the proliferation of stable flies (*Stomoxys calcitrans*). EFB is also utilized for composting. During the composting process, EFB can generate waste such as odors, and bioaerosols, which may have adverse effects on human health (Gallego et al., 2020; Kahar et al., 2022; Yoshizaki et al., 2013). EFB has the potential to be used in renewable energy bioconversion through thermochemical processes. These processes may generate contaminants and harmful gases. Moreover, the high moisture content in EFB hinders the application of thermochemical processes, necessitating prior drying (Kahar et al., 2022). EFB can also undergo chemical transformation to yield bio-sugar and serve as a matrix for nanocellulose production. These processes require acid, alkali, and hydrothermal treatments, potentially resulting in waste generation and environmental repercussions (Norrrahim et al., 2022). The generation of waste and effluents poses environmental and management challenges, necessitating efforts to enhance understanding and develop innovative techniques for utilizing EFB fibers sustainably.

Designing efficient biorefining processes aimed at materials or energy production that increase circularity and decrease the environmental impacts of palm oil is vital. Compositional knowledge plays a crucial role in achieving these goals by enabling the design of more effective processes that strengthen the crop's value chain. We aim to investigate the compositional and physicochemical variations in stalks and spikelets, as well as the influence of the sterilization process composing the residual EFB from the E.G and O×G hybrid, the two primary cultivars in Colombia.

1.3. Experimental

1.3.1. EFB sampling

Fresh fruit bunches (FFB) from E.G and the O×G hybrid cultivars were harvested at Cenipalma's *Palmar de las Corocoras* Experimental Farm (Cundinamarca, Colombia); O×G hybrid was planted in 2012 and E.G. in 2015. Since FFB undergo sterilization in the palm oil mills before crude oil extraction samples of both fresh and sterilized bunches were included in this work. Sterilization was conducted in an oil extraction unit at 40 psi for 1 hour. Four bunches were used to compose "fresh bunches" and "sterilized bunches" samples. Fresh and sterilized stalks were separated from spikelets-containing fruit and subsequently the spikelets from the fruits. Each sample was knife-reduced to sizes of 1 to 3 cm^3. Moisture content analysis followed the NREL-TP-51042621 protocol. All collected samples underwent drying, grinding, and sieving as per the NREL-TP-510-42620 method, ensuring uniform particle size and sample homogeneity. Figure 1 guides sample identification and provides optical images of EFB, stalks, and spikelets.

Figure 1. Sample identification and optical images of EFB, stalks, and spikelets

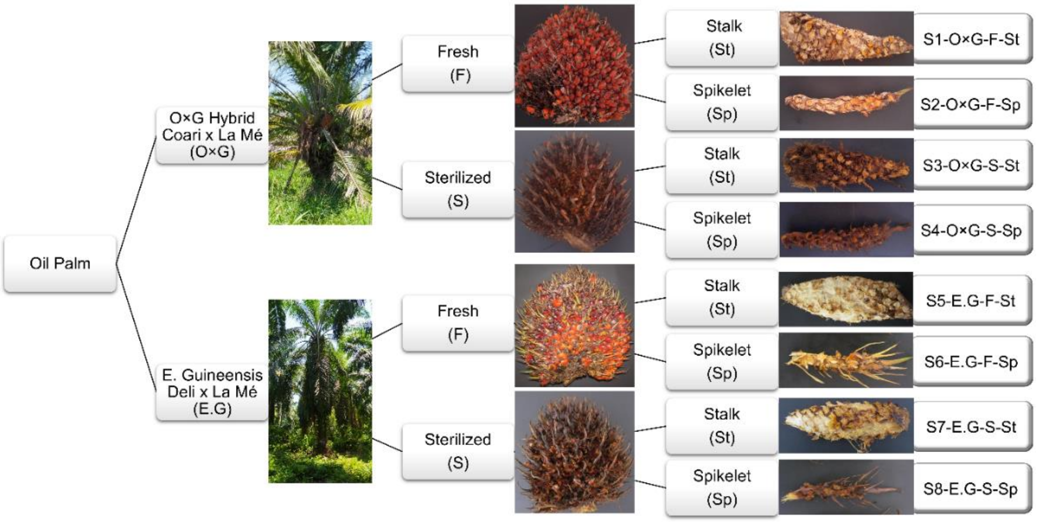

1.3.2. Compositional analysis

The EFB compositional analysis in this work comprises two sections, one corresponding to structural carbohydrates and lignin content and the other to lignocellulosic composition. Moisture and ash determination are essential for both characterizations. In the case of structural carbohydrates, the biomass was exhaustively extracted in water and ethanol (total extractives). Additionally, the extractives in water, ethanol, and hexane were determined separately. For lignocellulosic material, the initial step involves ethanol-toluene extraction. The standards, and methods for each determination are outlined in Table 1. Standard deviation was calculated for duplicate and triplicate measurements for compositional and physicochemical data. The t-student test, with 95% confidence, was employed to assess whether there was a statistically significant difference between the results, considering the type of variety, fresh/sterilized EFB, and specific EFB part (Daniel C.Harris, 2003).

Table 1. EFB characterization methods

Structural carbohydrates methods	**Lignocellulosic composition methods**

Total extractives, water extractives and ethanol extractives, NREL-TP-510-42619	Ethanol-toluene soluble matter, ASTM-D1107
	Moisture, NREL-TP-510 42621
	Ash, NREL-TP-510 42622
Ash, NREL-TP-510 42622	Lignin, TAPPI 222
Moisture, NREL-TP-510 42621	Cellulose, Kurschner and Hoffer method (Hessler & Merola, 1949)
Structural carbohydrates and lignin, NREL/TP-510-42618	Holocellulose Jayme-Wise method (Yao, 2012)
	Hemicellulose*

**Calculated as the difference between holocellulose and cellulose*

1.3.3. EFB Physicochemical analysis.

The morphology of EFB fibers was examined through field emission scanning electron micrographs (FESEM). FESEM data was generated at 30 kV using a QUANTA FEG 650 scanning electron microscope, which was equipped with a secondary electron detector (SED), an Everhart Thornley (ETD) detector, and a backscattered electron detector (BSE). Fibrils, randomly selected from each sample type, were secured with conductive carbon tape, and coated with gold. Cellulose crystallinity was assessed using X-ray diffraction and a dwell time of 0.65 per step. The cellulose crystallinity index (CI) was derived from the intensity of the crystalline and amorphous signals following the Segal equation (1).

$$CI = \frac{I_{200} - I_{am}}{I_{200}} x\ 100 \quad (1)$$

Where I_{200} is the maximum intensity of the lattice diffraction (200) at about 2ɵ 22.5° and I_{am} is the diffraction intensity of the amorphous band at 2ɵ 18.5°(Poletto et al., 2014).

Elemental analysis for C, H, N, and S contents was performed on an Elcube Elemental instrument, using high-temperature oxidation. Oxygen content was determined by difference. Using C, H, and O data, a Van Krevelen diagram was constructed to compare EFB fibers with other carbon-based fuels (Rocha et al., 2020). Additionally, inorganic elemental analysis was carried out using x-ray fluorescence (XRF) on an S8 TIGER BRAND BRUKER instrument, covering elements from Na to U in a helium atmosphere, following the quant express method. The superior Calorific Value (SCV) was determined by the Calorimetric Bomb method according to the ASTM D5865 Standard. Finally, the materials thermal stability was assessed through thermogravimetric analysis (TGA) using a NETZSCH STA 449 F5 Jupiter instrument. A heating ramp of 10°C/min, ranging from 32°C to 600°C, and a N2 flow of 50 mL/min were employed. Three system purges were conducted before initiating the measurement.

1.4. Results and Discussion

1.4.1. EFB Composition

The EFB sample composition is categorized by cultivar type (O×G hybrid *vs.* E.G), bunch condition (fresh *vs.* sterilized), and bunch part (stalks *vs.* spikelets). Additionally, experimental data indicates that EFB from O×G hybrids consists of 23.8% stalk and 76.2% spikelet content, while EFB from E.G contains 18.2% stalks and 81.8% spikelets in dry basis; these ratios were utilized to determine the composition average of whole bunch (EFB). Figure 2 illustrates the initial moisture and total solids contents for all samples involved in this work. Stalks consistently exhibit higher moisture than spikelets in both cultivars, with average differences of 13.6% in O×G hybrid and 15.5% in E.G. Sterilization slightly reduces moisture content, although the change is not statistically significant. Specifically, the *t-student* analysis confirms no significant moisture differences between cultivars and fresh *vs.* sterilized samples but a significant difference in bunch parts (stalks *vs.* spikelets).

The average moisture content of the whole bunch calculated from Figure 2 indicates 65.0% for the O×G hybrid and 60.7% for E.G (sterilized samples). Literature commonly reports EFB, a mixture of stalks and spikelets referred to as EFB fibers, with moisture content ranging from 60 to 70% (J. Han & Kim, 2018; Yahya & Talari, 2010). While less information is available for individual EFB components, a 2011 report notes higher moisture content in stalks (82.6%) than in spikelets (57.5%) (Omar et al., 2011). Our findings are consistent with these reported values. The high moisture content in EFB fibers, attributed to their hydrophilic nature, influences their functionality in wet environments (Tan et al., 2017). Cross-sectional images (Appendix A) reveal fibrous and porous voids in EFB fibers, facilitating water absorption and molecular-level hydration. Interestingly, Tan et al. reported that despite affecting mechanical properties, the hydration process induces EFB fibers' microstructure alteration, providing functionalization opportunities (Tan et al., 2017).

Figure 2. Changes in moisture and total solids contents in EFB as a function of variety (OxG vs. E.G), bunch part (stalks vs. spikelets), and bunch condition (fresh vs. sterilized)

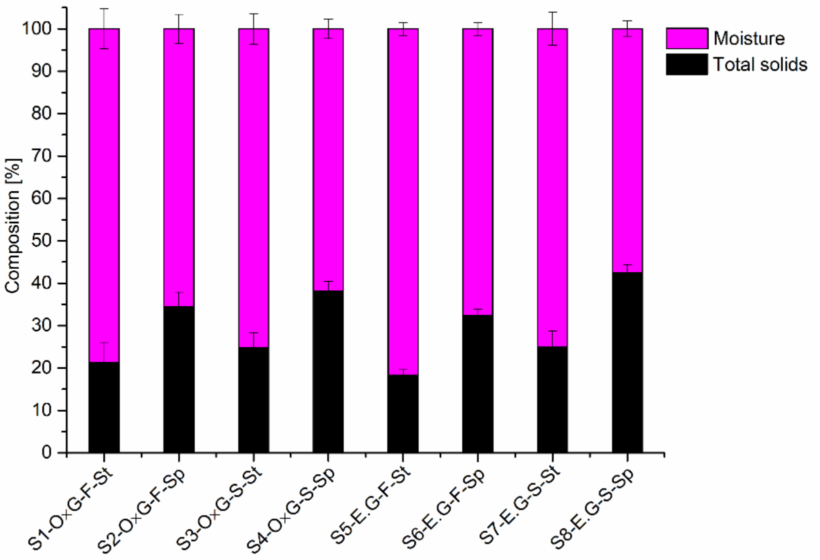

Conversely, stalks consistently exhibit less total solids (TS) than spikelets in both cultivars. Sterilization slightly increases total solid content, although the differences are not statistically significant. Total solids in EFB comprise mostly structural polysaccharides such as cellulose and hemicellulose, as well as lignin, plus minor components such as proteins, ash, wax, and other non-structural substances (Veluchamy & Kalamdhad, 2020). These TS play a crucial role in the efficiency of biomass bioconversion, particularly in anaerobic fermentation processes. It has been determined that a TS range between 15% and 20% is optimal for these processes. Within this interval, an appropriate balance between substrate concentration and water availability is achieved, promoting high microbial activity and efficient conversion of biomass into desired products (Ghimire et al., 2018). In thermochemical processes such as combustion, pyrolysis, and gasification, a low total solids content (<50%) can lead to reduced energy efficiency and decreased carbon and hydrogen conversion rates. To address this challenge, drying techniques are employed, typically conducted at temperatures ranging from 70-200 °C, as an initial step to remove moisture before thermochemical conversion (Hu et al., 2021; X. Zhao et al., 2017). While stalks are suited for biochemical conversion (high moisture content), spikelets are more suitable for thermochemical conversion (high TS content). However, to enhance the efficiency of thermochemical conversion for spikelets, a drying process like torrefaction is needed to remove moisture and increase TS content. Determining biomass composition, specifically lignin and structural carbohydrate contents, is crucial for devising effective processing strategies and final applications. For instance, carbohydrates from biomass hydrolysis can be utilized as feedstocks for producing biofuels through microbial fermentation. However, the type and amount of carbohydrates present significantly impact the product type (*i.e.*, ethanol) and the yield. This, in turn, directly affects the economic feasibility of the entire process (Sluiter et al., 2010).

1.4.2. EFB extractives and structural carbohydrates

Following NREL biomass characterization protocols for quantifying structural polysaccharides and lignin requires an initial step to remove solvent extractives (Sluiter et al., 2008). Figure 3 displays the water, ethanol, hexane, and total extractives content and the structural carbohydrate and lignin composition for all samples involved in this work. Extractives are the fraction of non-structural components outside the cellulose-hemicellulose-lignin matrix, whose composition varies based on biomass origin. For example, those from oil crops contain mostly fats and waxes, while those from agro-industrial residues of sugarcane production are sugar-rich (Lama-Muñoz et al., 2020; Tajmirriahi et al., 2021).

Figure 3. Changes in EFB (a) extractives and (b) composition as a function of variety (OxG vs. E.G), bunch part (stalks vs. spikelets), and bunch condition (fresh vs. sterilized)

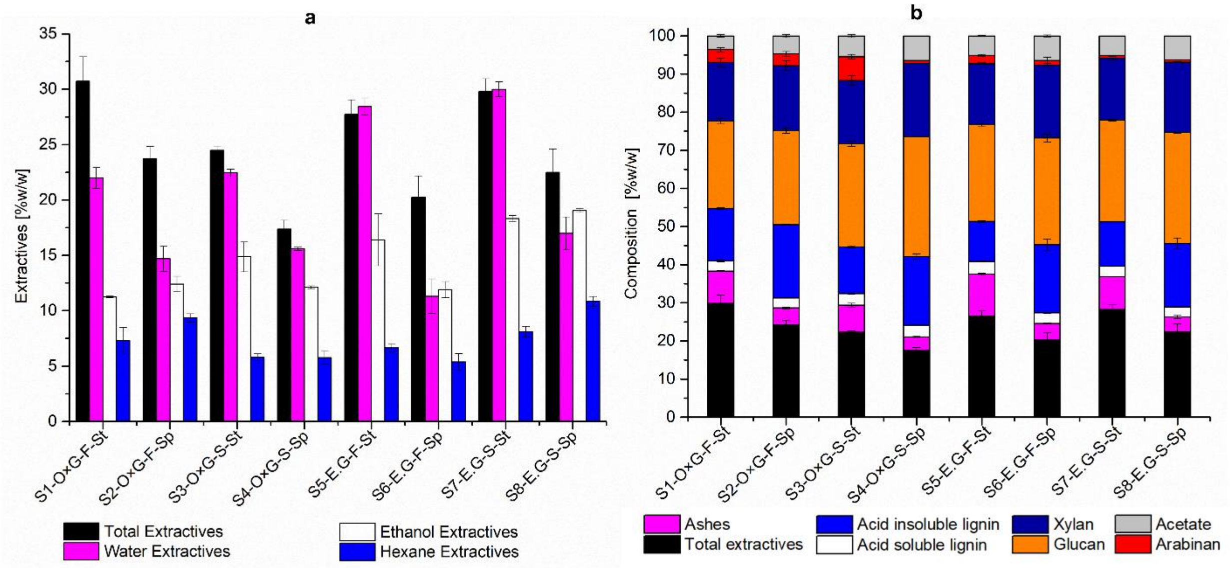

Stalks showed 7.2 % higher total extractives content compared to spikelets. This could be attributed to the transport of nutrients through the central part of the rachis towards the spikelets. Regarding the sterilization process, it was observed that there was a decrease in the total extractives content in the E.G cultivar; while for the O×G hybrid cultivar, there was an increase. At cultivar level, sterilized EFB of E.G contains more total extractives (4.7%) than O×G hybrid; while the opposite is true for fresh EFB, E.G contains less total extractives (3.8%) than cultivar O×G hybrid. A statistically significant difference was found in the total extracts when comparing the stalks and spikelets of each variety, as well as in bunches condition only in the E.G. The extractives in water and ethanol showed a significant difference between the stalks and spikelets of each cultivar. The sterilization process did not affect the extractives in water, but it did affect the extractives in ethanol and hexane. At the cultivar level, there was a statistical difference in extractives in water, ethanol, and hexane. No behavior or trend was observed in the extractives present in each solution.

Extractives, both organic and inorganic, play a crucial role in biomass conversion processes, either facilitating or inhibiting them. Organic solvent extractives contain lipophilic compounds like fatty acids, triglycerides, or waxes, while ethanol extractives may include chlorophyll and wax (Hafid et al., 2021; Naik et al., 2022). Biomass water extracts are mainly composed of sugars such as glucose and fructose, organic acids, and inorganic compounds. Ethanol extractives are composed of phenyl and tannin compounds, mainly gallic acid. These compounds are the secondary metabolites of plants (Tajmirriahi et al., 2021). Depending on the type of biomass and its components, the content of extractives in water and ethanol varies. For example, water extractives reported for different biomass are 27% corn stover,(Chen et al., 2007) 25% arbequina, 27 % royal and 29 % picual (different olive cultivars) (Lama-Muñoz et al., 2020), and 5% *Indigofera tinctoria* (Pattanaik et al., 2019). Ethanolic extractives reported for the cultivars of olive trees are 15% arbequina, 14 % royal and 16 % picual (X. Wang et al., 2012), for *indigofera tinctoria* is 14% (Pattanaik et al., 2019). Hexane extractives include aliphatic, aromatics, lipids, waxes (Pattanaik et al., 2019; Pattiya, 2017; S. I. Yang et al., 2014). For *Indigofera tinctoria*, 4% hexane extracts have been reported (Pattanaik et al., 2019). For EFB fibers 11% extractives in hot water,(X. Wang et al., 2012) 7% for water extractives and 1% for ethanolic extractives are reported

(García-Núñez et al., 2008). According to our results, the extractives reported on literature for EFB are quite low (< 11 %) compared to those obtained in this study. This could be explained by two reasons. The first one is the methodology for evaluating the samples, since in this study, the extractions were exhaustive in time (24 h) while the ASTM D1105 report has 4 hours. The second reason is the difference in the sample analyzed due to reducing the effect of heterogeneity for this study, the stalks and spikelets were separated. In addition, bunches of the same age, two cultivars, same region, and climate were carefully selected. On the other hand, the calorific value of biomass is significantly influenced by the type of extractives present. Extracts containing terpenoid hydrocarbons and lipids generally display lower oxidation levels, which can contribute to a higher calorific value. Conversely, those containing phenolic compounds tend to have higher oxidation levels, resulting in a lower calorific value (Esteves et al., 2023). Extractives are key in biogas conversion. A 21% higher biogas yield was observed in biomass with higher water extractive content compared to those with lower content (a 7% difference) (Naik et al., 2022). However, in ethanol production via fermentation, water extracts (sugars) act as fermentation inhibitors and must be removed (Pesce et al., 2023). Based on the extractives content, the spikelets may be a more favorable substrate for ethanol production compared to the stalks, due to their lower water-extractive content; while the stalks are more suitable for biogas production due to their higher water-extractive content.

Knowing amount of structural carbohydrates and lignin in EFB is crucial for optimizing process efficiency in biorefining settings. Also, detailed compositional information will aid in end-use viability and decision-making for biofuel production, material properties, process economics, and environmental impacts. Figure 3b shows compositional changes in monosaccharides (pentoses and hexoses from cellulose and hemicellulose acid hydrolysis), acid-soluble and insoluble lignin, ash, and total extractives as a function of variety (OxG *vs.* E.G), bunch part (stalks *vs.* spikelets), and bunch condition (fresh *vs.* sterilized). After conducting extractive-free biomass hydrolysis, acid-soluble lignin (ASL) dissolves, leaving acid-insoluble lignin (AIL) and ash in the biomass acid-insoluble residue. ASL contains amorphous low-molecular-weight materials, while AIL is considered a complex high-molecular-weight polymeric network (Bolker et al., 1965; Sander et al., 2023). The average ASL and AIL contents in EFB reached 2.8% and 16.7%, respectively (Figure 3b). Notably, lignocellulosic biomass typically exhibits lower ASL content compared to AIL. Literature reports ASL content between 1.1 - 7.8 % and acid-insoluble lignin ranging from 23.0 to 32.2 % for extractive-free EFB (Chiesa & Gnansounou, 2014; Coral Medina et al., 2015; Isroi et al., 2012; Nieves et al., 2011; Zawawi et al., 2018). The ASL content falls within the reported ranges, but the AIL content is comparatively lower. The variability of lignin content arises from climate, location, fertilization schemes, EFB handling, and cross-contamination with other biomass (Zawawi et al., 2018). Shaiful et al. (2019) reported that the content of lignin and carbohydrates in EFB varies depending on location and season (Shaiful-Sajab et al., 2019). We observe statistically significant variations in ASL content between fresh and sterilized samples and among different cultivars. However, the ASL content in the EFB samples is below 3.1%. Despite the statistically significant difference between cultivar types and bunch conditions, the overall concentration remains low. AIL exhibits a clear trend regarding biomass components, with spikelets containing, on average, 5.9 % more acid-insoluble lignin than stalks. The spikelets' elevated lignin content is primarily linked to their role in providing mechanical support to the fruit. Additionally, the sterilization process results in an average reduction of 1.2% in AIL content. Lignin represents a significant challenge in biomass bioconversion processes, acting as a physical barrier by interacting with cellulose, thereby limiting enzyme and pretreatment access and reducing enzymatic hydrolysis efficiency and conversion to biofuels and chemicals (Yoo et al., 2020). In this context, stalks, with lower lignin content, emerge as better precursors for biomass bioconversion. However, a comprehensive understanding of the composition of lignin aromatic subunits is necessary, as positive effects of lignin on biomass biorefining have been reported (Rodríguez-Zúñiga et al., 2015; Westereng et al., 2015).

In addition to acid-soluble lignin, extractive-free EFB sulfuric acid hydrolysis solubilizes monosaccharides and acetic acid, products of hemicellulose and cellulose depolymerization.(A. Sluiter, Hames, Ruiz, et al., 2008) Hemicelluloses in palm oil EFB, whose function is to contribute to the structural integrity of the plant's secondary cell walls and xylem, are predominantly composed of xylan (21.5 to 24%), a branched polymer of D-xylose often substituted with glucuronosyl or 4-O-methyl glucuronosyl residues. Glucuronoarabinoxylans can be also found on the primary cell walls of oil palms (Lassfolk et al., 2022; Rahman et al., 2006; Rathamat et al., 2021). Most naturally occurring xylans exhibit xylose acetylation, with a degree of substitution ranging from 30 to 60% (Lassfolk et al., 2022). Cellulose, conversely, is a linear homopolymer of glucose units primarily responsible for providing shape and mechanical strength to the plant's primary cell wall (Hsieh & Harris, 2009; Ishii, 1991; Teleman et al., 2000). Figure 3b illustrates compositional changes in xylan, arabinan, and acetic acid (resulting from hemicellulose hydrolysis) along with glucose (from cellulose hydrolysis). Glucose is the most abundant monosaccharide in all samples, averaging 36.0%, followed by xylan (23.3%) and arabinan (2.4%). Acetic acid, originating from acetylated xylan, corresponds to an average content of 7.4%. Literature reports glucose ranging from 30.2 to 39.1 % and xylose from 8.7 to 26.6 % in whole extractive-free EFB (Chiesa & Gnansounou, 2014; Coral Medina et al., 2015; Isroi et al., 2012; Nieves et al., 2011; Zawawi et al., 2018).

The glucan content differs significantly between spikelets and stalks, with the former exhibiting an average 2.8% higher sugar content than the latter. Additionally, fresh E.G. stalks and spikelets contain more glucan than their O×G hybrid counterparts. Notably, the sterilization process positively influenced glucan contents in both cultivars, with an increase of 5.4% for O×G and 1.2% for E.G. This observation suggests that the sterilization conditions enhance autohydrolysis facilitating the release of monosaccharides during the process in the E.G. cultivar. The xylan and acetic acid contents were higher in spikelets, while no significant difference in arabinan content was observed between stalks and spikelets. The sterilization process led to an increase in xylan and acetic acid and a decrease in arabinan. Notably, the sterilized O×G hybrid exhibited higher levels of arabinan (2.8%), and acetic acid (0.2%) compared to the sterilized E.G. The significant difference in xylan content is attributed to the parts of the bunch, while arabinose content correlates with the sterilization process and the cultivar type, and acetate content varies between the parts of the bunch and the cultivar type. The slightly higher content of glucan, xylan, and acetate in spikelets compared to stalks is attributed to spikelets serving as the primary site for oil palm fruit development. Spikelets require more energy and resilience for fruit development and growth. Glucan assumes a pivotal role in plant growth and development by orchestrating developmental transitions, fostering the synthesis of photosynthetic pigments, shielding against abiotic stress, modulating plant metabolism and growth (Saksena et al., 2020; Siddiqui et al., 2020). Xylose and arabinose serve as the main monosaccharide components of hemicelluloses (Levantovsky et al., 2017). Xylan is a polymer composed of xylose monomer units with galactose, manose, acetyl groups, and glucuronic acid as side-chains. Xylose and arabionse plays a crucial role in vital processes such as regulating cell growth, responding to adverse environmental conditions, and providing structural resistance (Dutta & Chakraborty, 2019; Luo et al., 2017; Mccann et al., 2013).

The composition of glucan, xylan, arabinose, and extractives in EFB varies with geographical location and climate, as previously reported, despite employing the same testing method (NREL) (Shaiful Sajab et al., 2019). For example, EFB from Brazil contains 33.5% glucan, 26.8% xylan, 2.0% arabinan, and 12.9% extractives,(Raman & Gnansounou, 2014) while EFB from the Republic of Benin has 29.6% glucan, 18.8% xylan, 1.2% arabinan, and 15.7% extractives. Compared to these, our results align more closely with EFB from the Republic of Benin for glucan and xylan content, but our extractive levels are higher (Chiesa & Gnansounou, 2014). The EFB emerges as a promising material for ethanol and byproduct biorefinery, due to its high glucan and xylan content. However, unlocking its full potential relies heavily on effective pretreatment methods that remove inhibitory components in EFB, associated with extractives and lignin content (Chiesa & Gnansounou, 2014; Choi et al., 2013; Raman & Gnansounou, 2014). Various pretreatment methods for EFB have been explored, including acid hydrolysis, enzymatic hydrolysis, steam pretreatment, alkaline treatments, and combinations thereof. These pretreatments have demonstrated increased efficiency in bioethanol production (Cui et al., 2014). Notably, treatments such as Formiline have shown success in biomasses like bagasse and EFB (Cui et al., 2014; X. Zhao et al., 2013). Formiline treatment for EFB effectively removes lignin and hemicellulose, resulting in the production of 166 g of ethanol, 140 g of lignin, and hemicellulosic syrup with a xylose concentration of 2.8%. This is achieved starting with EFB containing 37.01% glucan, 15.0% xylan, 17.4% lignin, 1.83% acid-soluble lignin, 3.56% acetyl group, and 3.34% ash (Cui et al., 2014). Similarly, studies report the bioconversion of chestnut shells (with alkaline treatment) and artichoke waste (with water-extractives removed) with glucan contents of 45.1 and 34.3%, yielding 150 and 283 g bioethanol/kg biomass, respectively (Lee et al., 2022; Pesce et al., 2023). The difference in process efficiency is due to the biomass pretreatment and fermentation process used. The foregoing suggests that the ethanol yield from biomass is closely linked to the pretreatment method employed, as higher ethanol quantities can be achieved with lower glucan content. Additionally, EFB holds an advantage over other biomasses due to its sterilization process conducted at the refinery. The sterilization process significantly influenced the sugar and lignin content in the biomass. This process partially hydrolyzed the hemicelluloses and decreased the lignin levels, leading to an augmentation in the glucan content. Consequently, this facilitated the conversion of EFB into ethanol, as documented previously (Shamsudin et al., 2012; Simarani et al., 2009).

Xylose derived from biomass serves as a precursor for valuable chemicals such as lactic acid, xylitol, and furfural, through recombinant microorganisms and metabolic enhancement (Rashid et al., 2021). Xylitol, an artificial sweetener, is used in the food, pharmaceutical, and dietary industries due to its low-calorie content and anticariogenic properties (Bajpai, 2013; Meng et al., 2022; Venkateswar Rao et al., 2016). The direct production of xylitol from lignocellulosic biomass is an attractive alternative to the chemical synthesis of xylose through lignocellulose hydrolysis. It has been reported that the amount of xylose in biomass has a positive impact on xylitol production using *Aspergillus niger*. Biomasses with high xylose contents (20-22%) showed greater efficiency in xylitol production, while the content of other sugars such as glucose and arabinose did not significantly affect production (Meng et al., 2022). On the other hand, furfural is essential in the manufacture of resins, pharmaceuticals, and agricultural chemicals, as well as in the refining of lubricating oils (Bajpai, 2013; Y. Luo et al., 2019). One of the reported methods for biomass conversion into furfural involves the use of aluminum chloride ($AlCl_3$) catalyst in ionic liquids. This process has demonstrated that biomass samples with an average of 19% xylose achieved superior efficiency in furfural production (L. Zhang et al., 2013). Additionally, the content of arabinan and acetate did not significantly affect the production of xylitol and furfural. According to above, EFB spikelets are regarded as the most suitable matrix to produce value-added materials due to their xylan content, which approximates 19-20%, compared to stalks with lower xylan content.

Data in Figure 3b exhibits statistically significant differences in terms of ash content between stalks and spikelets, and EFB pretreatment (sterilization). Stalks contained more ash than spikelets, with 3.7% for O×G hybrid and 5.7% for E.G. The sterilization process reduced ash content by 1.1% for O×G hybrid and 1.4% for E.G. The average ash content of the fibers was 6.4%. The stalks typically exhibit higher ash content compared to the spikelets, as previously reported (Reneta Nafu et al., 2015). This is attributed to their tendency to accumulate more nutrients owing to their cellular structure and lesser exposure to environmental factors. Biomass ashes are the solid residues resulting from burning plant biomass to generate heat and electricity (Insam & Knapp, 2011). The ash content, which must be kept below 10% to avoid issues during thermochemical processes. Overall, EFB has an ash content below 10%. However, spikelets, with their lower ash content, emerge as a more favorable option for initiating thermochemical conversion processes, as they reduce the risk of equipment corrosion, product contamination, and environmental damage (Anand et al., 2023). Another use of ash is as a fertilizer, in which case nutrient-rich biomass with low concentrations of heavy metals or organic contaminants is sought (Insam & Knapp, 2011); for this application, stalks would work better.

Lignocellulose content of the fibers of both cultivars is shown in Figure 4. Compared to the bunch’s parts, spikelets contain more cellulose, lignin and less hemicellulose and ash than the stalks of both cultivars. On average, the fresh bunch of the O×G hybrid EFB fiber contains 47.2% cellulose, 19.8% lignin, 20.4% hemicellulose, 6.8% ash, and 5.5% ethanol-toluene extracts; while EFB fiber from E.G contains 47.9 % cellulose, 19.7 % lignin, 20.9 % hemicellulose, 7.3 % ash, and ethanol-toluene extract 4.2 %. The lignocellulosic content of sterilized EFB fibers (stalks and spikelets) from O×G hybrid cultivar was 49.1 % cellulose, 19.6 % lignin, 20.6 % hemicellulose, 6.4 % ash, and 4.1 % ethanol-toluene extracts; and EFB fiber from E.G it was 45.1 % of cellulose, 19.4 % of lignin, 19.9 % of hemicellulose, 8.8 % ash, and 6.7 % ethanol-toluene extracts. The t-student test showed that there was no statistically significant difference between the parts of the bunch, the bunch condition and the type of cultivar in terms of cellulose, lignin, and hemicellulose content. The only statistically significant differences are in ash content (described above) and ethanol-toluene extracts content. The ethanol-toluene extracts varied according to the bunch condition and cultivar type, showing a statistically significant difference based on the three variables studied, bunch part, bunch condition, and cultivar type.

EFB fibers are heterogeneous materials and vary in their lignocellulosic composition depending on age, growth stage, geographical location, weather, and characterization methods (Chang, 2014); consequently, it is typical to find ranges of lignocellulosic content. EFBs contain between 36.7 - 65.0% cellulose, 15.0 - 36.6% lignin, 12.5 - 35.8 % hemicellulose, 2.3 – 9.2% ash, and 4.2 – 12.5 % ethanol-toluene extracts (Chee Ching & Sean Ng, 2014; Y. W. Chen et al., 2017; García-Núñez et al., 2008; Garcia-Nunez et al., 2016; Karunakaran et al., 2020; Ramlee et al., 2021). Our samples' lignocellulosic composition is within the reported range. Xiang et al. (2016) reported that stalks contained 40 % cellulose, 35 % hemicellulose, and 10 % lignin, while spikelets contained 20 % cellulose, 19 % hemicellulose, and 40 % lignin (Xiang et al., 2016). In comparison with our values, we observed a difference of more than 20 % between the cellulose and the lignin content in the stalks and spikelets. This is because, the lignocellulose content was determined using detergent fibers, and not the methods of our work.

The cellulose is defined as a polysaccharide formed by a linear chain of D-anhydroglucose (AGU) units linked by β-(1-4)-glycosidic linkages. Cellulose supports plant tissues (Jawaid et al., 2017). Lignin is an aromatic polymer found in plant cell walls. It provides strength, rigidity, and hydrophobicity, allowing the plant to grow and transport water and solutes (Vanholme et al., 2008). Lignin is covalently bonded to cellulose and hemicellulose to form highly resistant networks (Chang, 2014). Hemicellulose consists of a group of structurally diverse xylans, mannans, β-glucans and xyloglucans. The hemicellulose acts as a cement, giving the plant fiber strength and hardness (Ebringerová et al., 2005). It makes sense that the spikelets contain more lignin and cellulose than the stalks, as both compounds provide resistance to support and maintain the fruit. In addition, ashes are a complex mixture of organic and inorganic materials that include crystalline, semicrystalline and no-crystalline minerals (Munawar et al., 2021). The main compounds in the ash are metal oxides such as silicon, magnesium and calcium oxides; we will see below (Chang, 2014). Finally, ethanol-toluene extractives correspond to waxes, fats, resins and oils, tannins and other ether-insoluble constituents and therefore their value is less than 10 %. EFB fibers have been used as a matrix material for the isolation of cellulose nanofibers by TEMPO oxidation TOCN (TEMPO-oxidized cellulose nanofiber), with reaction yields of 60 %, as we have reported (Martínez-Ramírez et al., 2023). The properties and characteristics of TOCN allow it to be used in biomedical, food and other applications (Seddiqi et al., 2021; Zainal et al., 2021). On the other hand, EFB can also be used as a matrix for lignin isolation. As research has progressed, various methods of obtaining lignin with yields of up to 80 % have been reported (Liao et al., 2020; Z. Wang & Deuss, 2023). Lignin can be used as a dispersant, adhesive and surfactant, bioplastic, concrete additive and for biomedical applications (Bajwa et al., 2019).

Figure 4. Lignocellulosic composition

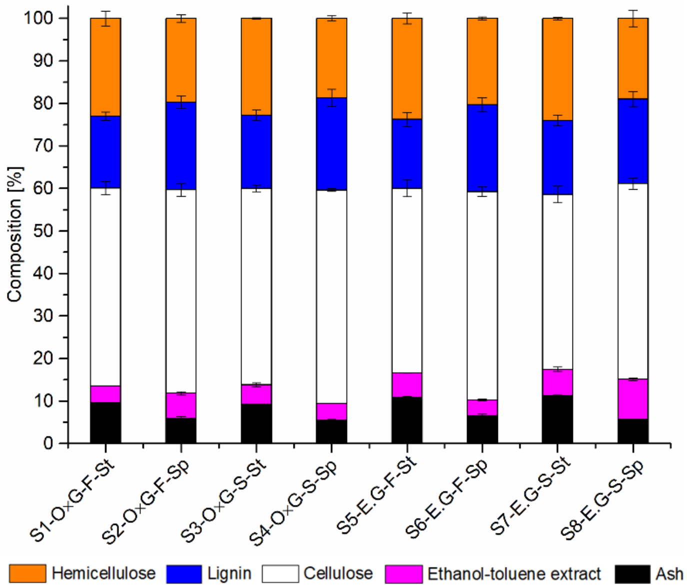

Finally, when comparing the structural carbohydrates (NREL) with the lignocellulosic composition obtained by gravimetry using the TAPPI 222, Kurscher-Hoffer and Jayme-Wise methods, we observed, the extractives and hemicellulose were higher, while the cellulose and lignin content were lower using the NREL method (Appendix B). Note that the main difference between is the extractive content. At NREL, exhaustive extraction was used and the fiber free of extracts was then subjected to acid hydrolysis for the quantification of sugars. In the case of the gravimetric method, only ethanol-toluene extraction was carried out, followed by lignocellulose quantification. As mentioned above, exhaustive extractions eliminate certain sugars and components that can interfere with gravimetric methods and for this reason the cellulose and lignin contents were higher in the gravimetric methods (Pattiya, 2017).

1.4.3. Material Morphology

The surface of the biomass appears heterogeneous and porous (Melati et al., 2019). The EFB fibers from both stalks and spikelets of both cultivars exhibit a porous and rough surface, containing impurities such as waxes and lignin (Figure 5). These waxy substances serve as a barrier to retain moisture within the fibers (Rama Rao & Ramakrishna, 2022). Notably, silicon residues are present on the surface of both stalks and spikelets, even after sterilization processes. Consequently, there are no significant morphological differences observed between cultivars, sterilization methods, and parts of the bunch. Silicon naturally occurs in most plants, with soil typically containing silicon oxide (50-70%) (Ma & Yamaji, 2008; Omar et al., 2014). This element is transported to the stalk through the xylem sap and tends to concentrate in the plant's vascular bundles, found within the cell wall or between the cell wall and the plasma membrane. The presence of well-designed silica bodies indicates a structured biological process, primarily serving to shield the plant from both biotic and abiotic stressors. Silicon serves as a protective physical barrier against pests and fungi, enhancing the oil palm's immune resilience (Feng Ma, 2003; Ma & Yamaji, 2008). However, the presence of silica reduces the hydrolysis and sugaring processes because it covers or blocks the cellulose active sites. The removal of silica is therefore necessary for bioconversion and biomass utilization (Omar et al., 2014). These surface morphological features and the presence of silica in EFB have been reported in previous studies (Xiang et al., 2016).

The presence of surface waxes and lignin affects the bioconversion processes of EFB fibers. EFB fibers require chemical treatments that remove these surface compounds to allow access to the structural carbons. Alkaline treatments have been applied to EFB fibers to remove the waxy layer, as they showed in the SEM micrographs (Abdullah et al., 2019; Iskandar et al., 2022). However, silica is not completely removed by alkaline treatments. The effectiveness of the alkaline treatment depends on factors such as the concentration of the base (NaOH) and the reaction time. Higher concentrations of base (e.g., 10% w/v) and longer reaction times (e.g., 48 hours) often lead to surface degradation, resulting in increased roughness and reactivity. However, this can adversely affect the mechanical properties of the fibers (Abdullah et al., 2019). Therefore, it is essential to select the optimal reaction conditions based on the intended use of the biomass.

Figure 5. SEM images of samples S1-S8

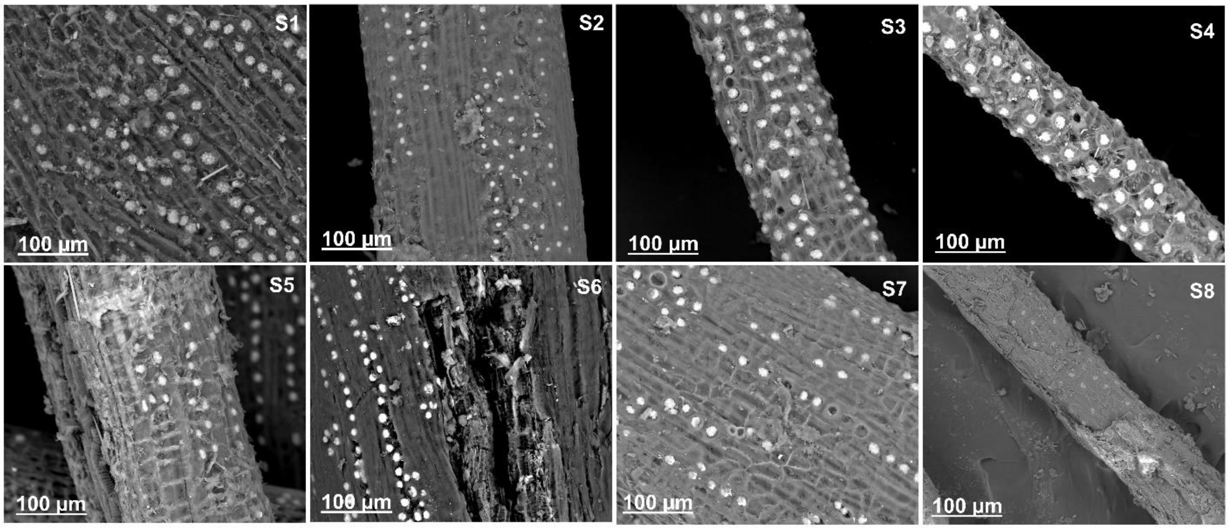

1.4.4. Sample Crystallinity

EFB fibers contain a higher proportion of cellulose, which gives them crystallinity. Crystallinity is related to the physico-chemical, as chemical reactions initially take place in the amorphous regions of the cellulose (Ahmad Kuthi et al., 2015; O. Rojas, 2016). Two types of diffractogram, those obtained for S1 and for S2, are shown in Figure 6. The diffractograms differ in the presence of some peaks in the odd samples which are absent in the even samples (2 ɵ= 5.6, 6.7, 12.6, 13.4, 15.0, 18.2, 20.8, 22.9, 28.6, 31.8 and 33.4) (Appendix C). These peaks probably correspond to unidentified crystalline compounds. This is because it is necessary to carry out different types of treatment and to try to identify them. Generally, the diffractograms show diffraction peaks at 2ɵ=16.5°, 22.8° and 34.6° corresponding to crystallographic planes (1 1 0), (2 0 0) and (0 0 4) respectively, of type I cellulose, space group P21(French, 2014; S. A. Ovalle-Serrano et al., 2018). There were certain shifts in the values of 2 ɵ associated with the heterogeneity of the sample (type of cultivar, part of and the condition of the bunch). The diffractograms reported for the EFB fibers contain the crystallographic planes of the cellulose type I and the diffraction pattern is similar to that obtained for the even samples (D. S. Lai et al., 2021; Latip et al., 2018). So far, the crystalline peaks of the odd samples (stalks) have not been reported. This is because the reported diffractograms correspond to mixtures between stalks and spikelets, which reduces the possibility of detecting them.

Figure 6. Diffractograms of samples S1 and S2

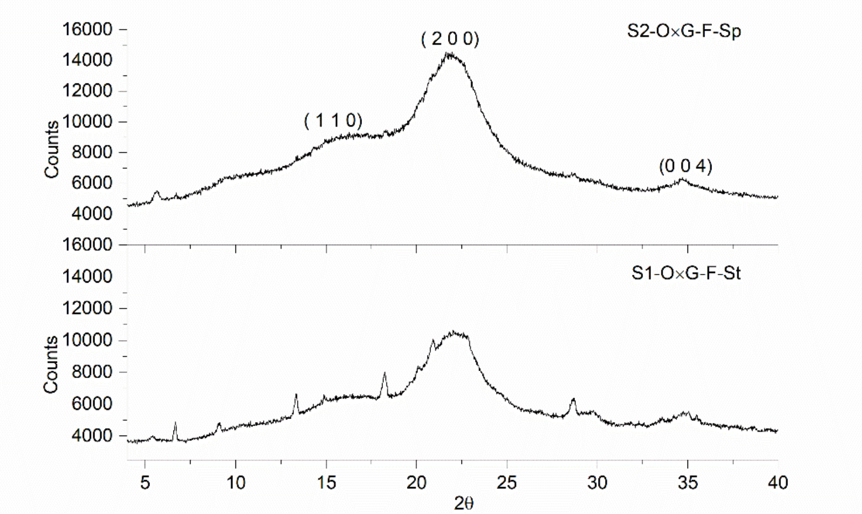

In addition, the crystallinity indices (CI) calculated for each sample using the Segal equation are also shown in Table 2. The CIs ranged from 36.43 to 42.23%. The CIs have no defined trends based on fiber part, cultivar and sterilization method. The CIs indicate that EFB fibers are typically highly amorphous due to the presence of lignin and hemicelluloses. Finally, the reported CIs of the EFB fibers are 37.8% (D. S. Lai et al., 2021), 41.3% (Latip et al., 2018), 43.0% (Hassan & Badri, 2016), and 58.1% (Fatah et al., 2014). Due to XRD measurement conditions and material heterogeneity, CI values vary (Chang, 2014). The CIs of the EFB fibers were less than 43%, indicating that the EFB fibers contain a higher proportion of amorphous domain, allowing easy access for treatment and functionalization. Amorphous cellulose is more reactive and requires less activation energy due to its less ordered and compact structure, allowing its accessibility, easy bioconversion and interaction with solvents and reagents (Abdullah et al., 2019; O. Rojas, 2016).

Table 2. Crystallinity index

Samples	CI [%]
S1-O×G-F-St	39.93
S2-O×G-F-Sp	38.16
S3-O×G-S-St	38.82
S4-O×G-S-Sp	41.95
S5-E.G-F-St	42.23
S6-E.G-F-Sp	41.70
S7-E.G-S-St	41.33
S8-E.G-S-Sp	36.43

1.4.5. Elemental Analysis and Calorific Value

Elemental analysis allows identifying the amount of carbon and minerals present in the biomass. The content of inorganic compounds is related to the ash content, which determines the amount of incombustible solid after the combustion process (Jamari & Howse, 2012). In turn the calorific value is associated with the amount of carbon present in the biomass and allows evaluating its capacity as a biofuel (Motghare et al., 2016). Table 3 shows nitrogen, carbon, hydrogen, sulphur, and oxygen contents determined by the elemental analyzer. The sulphur content obtained (0.05 <) is below the instrument's lower detection limit and, therefore not included in results of this study. The amount of carbon, oxygen, and hydrogen showed significant differences depending on the variables analyzed, while nitrogen only differed between parts of the bunch and cultivar. Spikelets have more carbon (2.5%), hydrogen (0.4%) and less nitrogen (0.1%), oxygen (2.8%) than stalks. The sterilization process changed the elemental content by less than 1 %, increasing C, N, and H contents and decreasing O content. On average sterilized bunch E.G has 0.3% N, 42.6% C, 10.5% H and 46.6% O and sterilized bunch O×G hybrid has 0.3% N, 42.0% C, 10.2% H and 47.4% O. Reported elemental analyses of EFB fibers range from 39 – 44% C, 5-7% H, 0.4 – 2% N, 44 – 54% O, and less than 0.1% sulphur (Kittivech & Fukuda, 2019; Novianti et al., 2015; Umor et al., 2021). Since mixtures of stalks and spikelets are usually analyzed, the variation is a function of the type of cultivar and the heterogeneity of the sample.

EFB fibers are mainly composed of cellulose, its chemical formula is $C_6H_{10}O_5$ with a molecular weight of 162.14 g/mol (Motta et al., 2018). In percentage and theoretical terms, cellulose is composed of 44.4% C, 6.2% H and 49.4% O. Comparing this with our data shows that the carbon and oxygen contents are similar, while the elemental hydrogen is about 4.0 % higher than theoretical. These variations are related to the presence of hemicelluloses, lignin, and other components in the fibers. On the other hand, it is also possible to construct the Krevelen diagram from the elementary composition C, H and O (Figure 7). This diagram shows the O/C and H/C ranges of anthracite, coal, lignite, peat and biomass according to a report by Basu (2018) and Rocha et al. (2020) C and H are oxidized during the combustion process, producing CO_2 and water. The high oxygen and hydrogen content in biomass makes its bioconversion difficult. This is why a low

H/C and O/C ratio results in a high calorific value, as seen with anthracite (Basu, 2018; Rocha et al., 2020). According to this diagram, EFB fibers exhibit a relatively low potential for bioconversion, necessitating pre-treatments like torrefaction for their optimal thermochemical conversion (Anand et al., 2023).

Table 3. Elemental analysis of samples

Sample	**N [%]**	**C [%]**	**H [%]**	**O [%]***
S1-O×G-F-St	0.310 ± 0.008	40.180 ± 0.205	9.803 ± 0.105	49.660 ± 0.084
S2-O×G-F-Sp	0.260 ± 0.022	42.947 ± 0.144	10.584 ± 0.025	46.170 ± 0.049
S3-O×G-S-St	0.377 ± 0.019	40.503 ± 0.198	10.005 ± 0.041	49.087 ± 0.065
S4-O×G-S-Sp	0.267 ± 0.005	42.517 ± 0.189	10.288 ± 0.042	46.902 ± 0.060
S5-E.G-F-St	0.443 ± 0.061	39.450 ± 0.349	10.050 ± 0.069	50.000 ± 0.123
S6-E.G-F-Sp	0.250 ± 0.014	42.347 ± 0.172	10.429 ± 0.033	46.942 ± 0.055
S7-E.G-S-St	0.450 ± 0.008	40.563 ± 0.263	10.168 ± 0.138	48.768 ± 0.104
S8-E.G-S-Sp	0.233 ± 0.005	43.097 ± 0.179	10.563 ± 0.067	46.074 ± 0.063

* Calculated by difference

Figure 7. Van Krevelen diagram of the EFB fibers

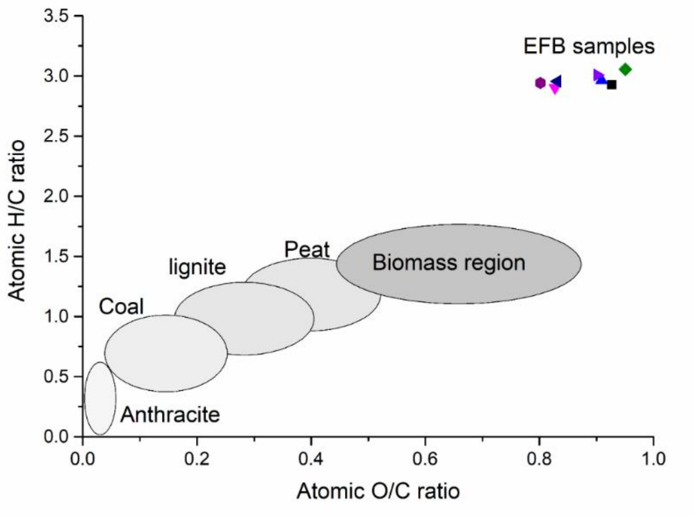

The inorganic elemental content is presented in Table 4, with the most abundant elements being potassium, silicon, chlorine, calcium, and magnesium. Additionally, elements such as phosphorus, sulfur, iron, aluminum, manganese, and copper are present in the fibers, each constituting less than 0.1% by weight. The potassium and chlorine content are higher in the stalks compared to the spikelets, whereas magnesium levels are higher in the spikelets than in the stalks for both cultivars. However, regarding silicon and calcium, the trend varies depending on the cultivar; in the O×G hybrid, the stalks contain more silicon and calcium than the spikelets, while in E.G, the spikelets have higher silicon and calcium content than the stalks. Overall, sterilization processes led to a decrease in the inorganic contents across most of the samples. In terms of cultivar, O×G exhibits higher content of potassium, silicon, and magnesium, and lower content of chlorine and calcium compared to E.G.

The sterilization process involves applying heat to the fresh fruit bunch and subsequently removing the fruit from the bunch (Sukaribin & Khalid, 2009). The sterilization process contributes to the elimination of elements, primarily potassium. The reported elemental (inorganic) content for EFB includes 0.18 - 0.27% phosphorus, 2.0 - 3.9% potassium, 0.25 - 0.40%

magnesium, and 0.15 - 0.48% calcium. Trace elements such as boron, copper, zinc, iron, and manganese are all present at levels below 0.1% (N. Hayawin et al., 2012; Z. N. Hayawin et al., 2014). Compared to that reported in the literature, EFB fibers contain more potassium, silicon and chlorine and less phosphorus. The difference confirms the heterogeneity of the EFB fiber samples (Chang, 2014). On the other hand, Potassium is a macronutrient and is essential for regulating, transporting, adapting and growing plants. Potassium also helps to reduce the negative effects of stress, such as salinity, temperature and metal toxicity (Johnson et al., 2022; Pandey Swatiimahiwal, 2020). Silicon provides resistance to pests and micro-organisms (Feng Ma, 2003; Ma & Yamaji, 2008); while chlorine is mainly present as an anion and is involved in processes of osmoregulation and cation transport (Hänsch & Mendel, 2009; Rom & Marschner, 1991). Calcium is essential for structural functions in the cell wall (White & Broadley, 2003), it is also an element of signaling that allows the plant to detect stimuli such as light, drought and so on (B. Li et al., 2022). Magnesium is a regulator of plant physiological processes and maintains plant health (Huber & Jones, 2013); It is also involved in the processes of photosynthesis, protein synthesis and nucleic acids (Chen et al., 2018). Good functioning and growth of the plant and fruit is indicated by the presence of these elements in the stalks and spikelets. Furthermore, the variation in silicon content implies that the O×G hybrid may possess greater disease resistance compared to E.G. Lastly, the presence of inorganic compounds such as potassium (K), silicon (Si), and magnesium (Mg) in biomass can influence the efficiency of biological conversion, biogas production, or pyrolysis processes. Additionally, metal oxides like silicon, iron, and aluminum can serve as catalysts and impact these processes (Negrão et al., 2021). However, EFB fibers contain less than 7% inorganic compounds, rendering them suitable for biomass utilization.

Table 4. Elemental composition of S1-S8 by XRF

Element [wt. %]	**K**	**Si**	**Cl**	**Ca**	**Mg**
S1-O×G-F-St	5.19	0.64	0.31	0.29	0.18
S2-O×G-F-Sp	2.60	0.49	0.17	0.25	0.22
S3-O×G-S-St	4.40	0.58	0.28	0.23	0.12
S4-O×G-S-Sp	2.58	0.48	0.22	0.23	0.22
S5-E.G-F-St	5.49	0.28	0.51	0.21	0.22
S6-E.G-F-Sp	2.88	0.51	0.33	0.28	0.27
S7-E.G-S-St	4.42	0.42	0.43	0.18	0.16
S8-E.G-S-Sp	2.15	0.51	0.29	0.25	0.18

The higher calorific value is shown in Figure 8. the spikelets exhibit a calorific value 1.14 times greater than that of the stalks. This suggests that spikelets yield more energy compared to stalks. The sterilization process had differing effects on the calorific value of the fibers from each variety. In O×G hybrid fibers, sterilization caused a decrease in calorific value by 457 KJ/Kg, whereas in E.G fibers, it resulted in an increase by 1345 KJ/Kg. Overall, E.G exhibited a higher calorific value compared to the O×G hybrid, with a difference of 900 KJ/Kg. This emphasizes the relationship between calorific value and lignocellulosic content, as it represents the energy released per unit mass after combustion (Llorente & García, 2008). Figure 8 shows the lignocellulosic content and calorific value of each sample, indicating that spikelets contain a higher amount of lignocellulosic compounds compared to stalks. This contributes to a higher carbon content, as observed in the elemental analysis (Table 3) and calorific value. The reported calorific value of EFB fibers ranges between 16,000 and 17,000 KJ/Kg (Azri Sukiran et al., 2009; Llorente & García, 2008; Pua et al., 2020). This range is comparable to the calorific value of other agricultural residues such as wheat straw (17,100 KJ/kg), sugar cane bagasse (18,170 KJ/kg), flax straw (17,000 KJ/kg), and other biomass sources (G. K. Gupta & Mondal, 2019). Additionally, the Krevelen diagram may not be the most suitable tool for analyzing EFB fibers, as they contain additional compounds like lignin and hemicellulose. These complex biomasses exhibit diverse structures and compositions that can challenge the simplicity of the Krevelen diagram. Therefore, it is crucial to complement compositional analysis with more direct measurements of calorific value.

To determine the potential suitability of EFB fibers as a fuel material, we compare certain parameters with those outlined in in ISO 17225-6:2021 Solid biofuels, Fuel specifications and classes, Part 6: Graded non-woody pellets. According to this standard, biomass undergoes no chemical treatment. The EFB fibers from both cultivars exhibit promising characteristics for biofuel application based on the parameters outlined in Table 5. These samples demonstrate high calorific values and low ash and mineral contents, all of which are favorable attributes for efficient combustion and energy generation. However, the high moisture content in the bunches underscores the need for drying processes to reduce the moisture content to below 10%, as indicated in the table. Lowering the moisture content is crucial to enhancing the energy yield and combustion efficiency of the biomass. Elevated moisture levels can impede combustion by necessitating additional energy to evaporate the water, thereby reducing the overall energy output (Komilis et al., 2014).

Figure 8. Comparison between calorific value and lignocellulosic composition of samples

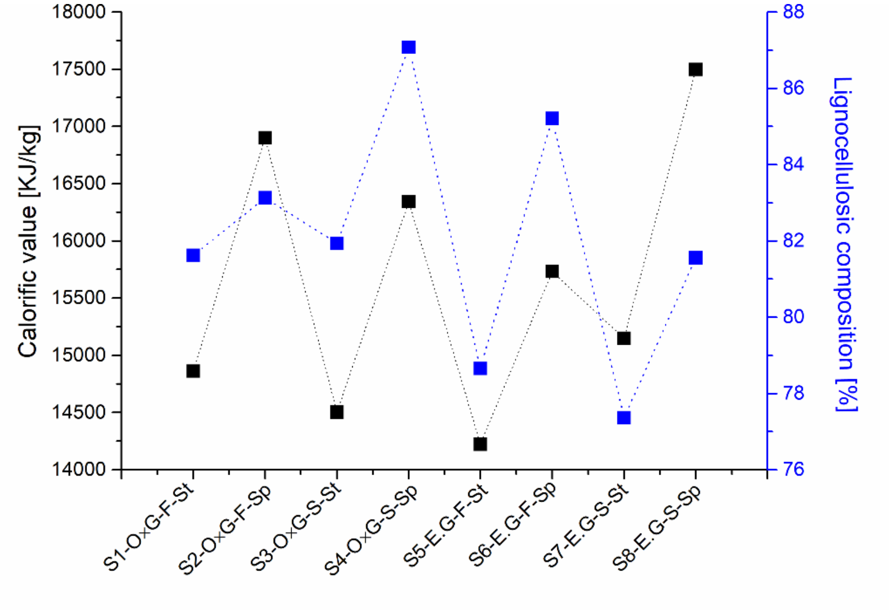

Table 5. Fuel specification comparison

Parameter	ISO 17225-6:2021	O×G hybrid*	E. guineensis*
Ash (% in mas dry)	10	5.35	6.24
Moisture (% in mas as received)	15	64.99	60.70
Calorific value (KJ/Kg)	14500	15423.00	16322.40
Nitrogen (% in mas dry)	2.0	0.32	0.34
Sulfur (% in mas dry)	2.0	0.05<	0.05<
Chlorine (% in mas dry)	0.4	0.25	0.21

* Weighted average sterilized stalks and spikelets

1.4.6. Thermogravimetric Analysis

Thermogravimetric analysis (TGA) identifies the mass loss of components present in biomass across temperature ranges, providing insights into the thermal stability and composition of EFB fibers (Park et al., 2022). Figure 9 illustrates the behavior of a representative sample, its first derivative, and the decomposition steps (similar behavior was observed across all materials) (Appendix D). Table 6 presents the temperature ranges and percentage of mass lost at each stage for each material. Spikelets exhibit broader temperature ranges than stalks at every stage of pyrolysis. In the O×G hybrid, spikelets (S2) experienced greater water loss compared to stalks (S1), while the reverse was observed in E.G. Furthermore, sterilization processes increased the moisture content of E.G fibers (S7 and S8). During the second stage, spikelets displayed higher mass loss than stalks due to their higher lignin and cellulose content. The temperature corresponding to the maximum peak was also higher in spikelets than in stalks of each variety, consistent with their composition. Stalk residues surpassed spikelet residues in both cultivars, aligning with the ash results showing a similar trend. EFB fibers exhibit thermal stability up to 140°C, irrespective of cultivar type, bunch part, or sterilization process. The first stage of EFB fiber pyrolysis, occurring between 30 and 140°C, involves dehydration or water loss. The second stage, active pyrolysis or combustion (200 - 380°C), breaks down glucosidic bonds of cellulose and causes depolymerization of hemicellulose and some lignin. Lignin degradation (200 - 900 °C) in the final stage, passive pyrolysis, results in ash and fixed carbon (Asim et al., 2020; Punia & Kumar, 2014; Yahaya et al., 2017; Yiin et al., 2018). TGA confirms the presence of lignocellulosic compounds in EFB fibers, consistent with prior studies (Al-Maari et al., 2021; García-Núñez et al., 2008).

The effect of sample heterogeneity is evident in the variations observed in compositional analysis. Palm oil extractors typically obtain mixtures of stalks and spikelets from bunches of varying cultivars, ages, locations, and climates. Consequently, batches of samples must be quantified as the composition of EFB fiber falls within a range of values. However, despite this variability, the morphology, crystallography, and thermal resistance of the fibers remain consistent, making EFB fibers generally suitable for a wide range of applications. EFB is an attractive matrix for biofuels (such as biobutanol and ethanol) and high-value-added products due to its high lignocellulosic content (Medina et al., 2016). Additionally, EFB fibers have been utilized for color removal via adsorption processes (Sajab et al., 2013), briquette production, composting, pulp and paper production (Chiew & Shimada, 2013), and as reinforcing material (Zakaria & Poh, 2007).The results also suggest that EFB can serve as a matrix for the isolation of elements such as silicon and potassium due to its high content. Finally, the presence of silica enhances the versatility of the fiber, enabling its use in cements and/or concrete (Katte et al., 2023; Naji Givi et al., 2011).

Figure 9. Stages of thermal decomposition of EFB fibers, TGA and DTG

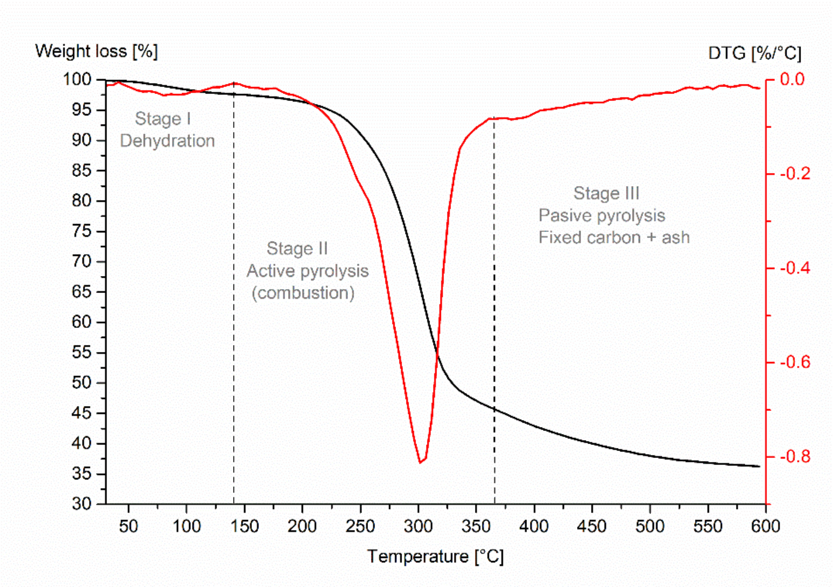

Table 6. Decomposition temperatures and mass loss for each stage

Sample	Stage I		Stage II		Stage III		Residue [%]
	T range [°C]	Mass loss [%]	T range [°C]	Mass loss [%]	T range [°C]	Mass loss [%]	

S1-O×G-F-St	30 - 140	2.30	141 - 365	47.57	366 - 600	10.04	40.09
S2-O×G-F-Sp	30 - 145	3.07	146 - 380	55.63	381 - 600	8.57	32.73
S3-O×G-S-St	30 - 140	2.38	141 - 365	51.93	366 - 600	9.46	36.23
S4-O×G-S-Sp	30 - 145	2.55	146 - 380	54.71	381 - 600	9.05	33.69
S5-E.G-F-St	30 - 140	2.53	141 - 365	48.03	366 - 600	11.49	37.95
S6-E.G-F-Sp	30 - 145	2.10	146 - 380	53.42	381 - 600	8.55	35.93
S7-E.G-S-St	30 - 140	2.65	141 -365	50.82	366 - 600	9.97	36.56
S8-E.G-S-Sp	30 - 145	2.86	146 - 380	56.06	381 - 600	9.92	31.16

1.5. Conclusions

The compositional differences are notable across different parts of the bunch. Stalks demonstrate higher levels of moisture, total extractives, water extractives, ash content, nitrogen, oxygen, potassium, and chlorine compared to spikelets in both cultivars. Conversely, spikelets exhibit higher levels of glucan, xylan, acetate, magnesium, carbon, hydrogen, and calorific value in both cultivars. Moreover, the behavior of silicon and calcium content varies depending on the cultivar type. In the O×G hybrid, stalks contain higher silicon and calcium content than spikelets, whereas in E.G., the opposite trend is observed.

The most pronounced impact of the sterilization process is seen in the sugar content. Sterilization enhances hydrolysis efficiency, resulting in increased sugar contents and biomass bioconversion. Given that palm oil bunches undergo this process during oil extraction, these findings emphasize the significance of sterilization in biomass processing.

When comparing cultivars while considering the contribution of stalks and spikelets, similar values are observed, indicating that both biomasses can be blended. However, for a more efficient utilization of the biomass, separate utilization is recommended. Stalks are better suited for bioconversion processes, whereas spikelets are more suitable for thermochemical processes.

2. Influence of Reaction Variables on the Surface Chemistry of Cellulose Nanofibers Derived from Palm Oil Empty Fruit Bunches

2.1. Abstract

Nanocellulose, a versatile nanomaterial with a wide range of applications, is gaining significant attention for its sustainable and eco-friendly properties. In this study, we investigate the influence of reaction variables on the surface chemistry of TEMPO-oxidized cellulose nanofibers (TOCN) from palm oil empty fruit bunch (EFB) fibers, a high cellulose content

biomass. Reaction time, primary oxidizing agent, and a pretreatment process affect, to various extents, the surface chemistry of EFB-TOCN. Conductometric titrations (CT), X-ray photoelectron spectroscopy (XPS), and statistical analysis indicate a positive and significant influence of reaction time and primary oxidizing agent on EBF-TOCN degree of oxidation and surface charge density. Partial EFB delignification increased EFB-TOCN oxidation and reaction yield compared to EFB without pretreatment. Interestingly, only reaction time has a significant effect on the EFB-TOCN hydrodynamic radii, with a reaction time of over 120 minutes required to obtain nanocellulose less than 100 nm in size. Utilizing palm oil residual biomass for nanocellulose extraction not only valorizes agricultural waste but also enhances the palm oil industry's economic prospects by reducing waste disposal costs and improving material circularity. This research contributes to the growing body of knowledge on nanocellulose production from renewable sources and highlights the potential of palm oil EFB fibers as a valuable raw material for sustainable nanomaterials development.

2.2. Introduction

The need for renewable, functional, and cost-effective materials has increased due to the depletion of fossil fuel reserves, the rise of synthetic plastics pollution, and the increase of greenhouse gas emissions. One solution is to use agricultural byproducts to produce lignocellulosic materials that can be transformed into biopolymers and platform chemicals via chemical transformations (Saez Zobiole et al., 2012). Oil palm (OP) is a high-yield agro-industrial crop in the tropics.(Fedepalma, 2021) Palm oil millers results in aqueous and solid byproducts, with the empty fruit bunch (EFB) being the most abundant solid residue, accounting for about 21 wt% of the fresh fruit bunch (FFB). EFB is typically utilized as composting material in plantations or as a low-grade fuel in boilers (Boonsawang & Youravong, 2017). With a yearly production of over sixty-eight million tons, empty fruit bunches (EFB) from PO extraction have the potential to be a valuable source of biopolymers due to their high cellulose (50.9%), lignin (17.84%), and hemicellulose (29.6%) contents (R. Lou et al., 2019; Mohammad Padzil et al., 2020).

Cellulose, the most abundant biopolymer on earth, is the primary structural component of all plant cell walls.(Farooq et al., 2020) Cellulose is an unbranched homopolysaccharide constructed of D-anhydroglucose units linked by β-(1-4)-glycosidic bonds. Each monomer in cellulose has three free hydroxyl groups, one primary (C6) and two secondaries (C2, C3), able to establish intra- and intermolecular hydrogen bonds. These interactions are responsible for cellulose's highly ordered and mechanically robust macrostructure (Jawaid et al., 2017). Cellulose biosynthesis occurs at the cell wall level by arrangements of spinnerets incorporating an extraordinary molecular machine called cellulose synthase. During cellulose synthesis, individual strands interact to form fibrils through hydrogen bonds. However, fibril assembly does not always produce perfectly aligned individual cellulose strands, resulting in cellulose fibrils containing amorphous and crystalline regions (McFarlane et al., 2014; Turner & Kumar, 2018).

Cellulose extraction from biomass requires chemical, mechanical, or biological deconstruction of the natural biocomposite formed by cellulose, hemicellulose, and lignin. Nanocellulose (NC) is usually derived from pure or partially delignified bulk cellulose, although recent research focuses on nanocelluloses containing lignin (W. Huang, 2018). NC extracted from agricultural biomass is biodegradable and biocompatible, which are crucial properties for applications in the biomedical field for drug delivery, tissue engineering, and wound dressing. Biomass-based NC exhibits excellent mechanical and barrier properties that make it suitable for composites, lightweight structures, and packaging for food preservation. Also, as a modifier and additive, NC has many potential applications, such as a reinforcing agent, rheological modifier, and oil recovery processes due to its exceptional adsorption properties. NC chemical isolation processes are normally faster and more cost-effective and are usually combined with mechanical pre- or post-treatment. Typically, cellulose nanofibers (CNF) are obtained from the oxidation and complete defibrillation of the cellulose bulk macrostructure, while nanocrystals (CNC) arise from defibrillation and the elimination of the fibril's amorphous regions via hydrolysis reactions (Saito et al., 2007). The physicochemical properties of CNF and CNC largely depend on the lignocellulosic source and extraction methods (W. Huang, 2018; O. J. Rojas, 2016).

The TEMPO (2,2,6,6-tetramethylpiperidine-1-oxyl) oxidation reaction is a pivotal chemical method in CNF production from biomass sources, delivering controlled disintegration, colloidal stability, surface chemistry flexibility, and sustainability (S. Liu et al., 2021; Pierre et al., 2017). Requiring sodium hypochlorite (NaClO) as the primary oxidant and the TEMPO radical as a catalyst, the reaction is remarkably selective, targeting only the primary hydroxyl groups of cellulose and sparing the cellulose backbone from significant degradation (Scheme 2) (Jaušovec et al., 2015; Mishra et al., 2012). TEMPO oxidation imparts a substantial surface charge to CNFs, due to the presence of carboxylate units in the form of sodium salts, leading to a significant electrostatic repulsion between individual nanofibers that prevents agglomeration and facilitates the formulation of stable aqueous suspensions (Saito et al., 2007). The number of carboxylate groups reported as cellulose's degree of oxidation (DO) or charge density (s) depends on the isolation conditions and biomass source (Benhamou et al., 2014). DO and s are typically calculated from conductimetric titration (CT) measurements. CNFs from TEMPO have a versatile surface chemistry that can be precisely tailored through functionalization, enabling integration into various nanocomposites and hybrid materials. This adaptability expands their utility in nanocomposite development, drug delivery, and biomaterials. The TEMPO reaction also aligns with green chemistry principles, featuring mild reaction conditions and eco-friendly reagents, minimizing waste and environmental impact (Isogai & Bergström, 2018; S. Liu et al., 2021). In this work, CNF from EFB was isolated using ultrasound-assisted TEMPO oxidation, followed by mechanical disintegration, using a process previously reported for residual biomass (Hastuti et al., 2019; S. A. Ovalle-Serrano et al., 2018).

The conditions of the TEMPO reaction and the biomass source significantly influence the physicochemical properties of TOCN. For example, under the same TEMPO oxidation experimental conditions, Norway spruce (a hardwood) and Eucalyptus (a softwood) pulps resulted in TOCN with 1.4 mmol COO^-/g and 1.2 mmol COO^-/g, respectively. This observation highlights the effect of the biomass source on TOCN properties (Rodionova et al., 2013). Huang et al. (2019) reported that increasing the length of the TEMPO oxidation reaction impacts DO and s in TOCN extracted from wood pulp. Changing reaction time from 1 to 24 h resulted in increased DO (s) from 16.4% (1.00 mmolCOO^-/g) to 25.0% (1.58 mmolCOO^-/g), respectively (C. F. Huang et al., 2019). The reaction length also impacted the crystal size, which decreased from 4.3 nm after 1 hour of reaction to 3.8 nm after 24 hours. Additionally, they observed that the kinetics of the TEMPO oxidation reaction is faster in the first hour of the reaction and decreases with time (C. F. Huang et al., 2019). The biomass pretreatment process also affects the yield and physicochemical properties of TOCN. For instance, Kaffashsaie et al. (2021) tested the influence of a sodium hydroxide/sodium sulfite pretreatment on TOCN extracted from paulownia wood. They observed that carboxylate contents increased from 1.45 mmolCOO^-/g for untreated biomass to 1.68 mmolCOO^-/g for the treated material. Performing TEMPO oxidation on untreated matrices results in decreased oxidation yields, likely due to the occurrence of two simultaneous and competing processes, bleaching and oxidation (Kaffashsaie et al., 2021). Simultaneously, DO and s grow as the oxidizing agent (NaClO) increases, as reported by Isogai et al. (2011) and Milanovic et al. (2012), they studied the combined effects of reaction time and amount of NaClO on the TEMPO oxidation of hemp fibers (Isogai et al., 2011; Milanovic et al., 2012).

Scheme 2. TEMPO-mediated oxidation of cellulose (Adapted fromMishra et al., (2012))

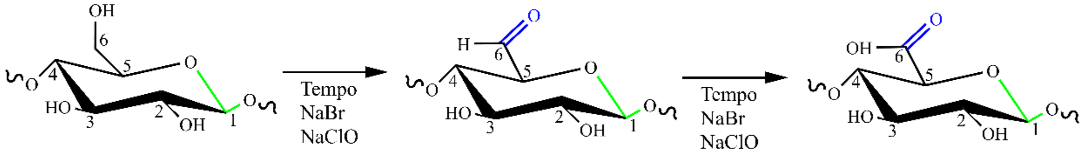

The authors observed increases in DO and σ as reaction time increases from 1 to 4 hours only at higher oxidant concentrations (9.67 mmol NaClO/g of fibers). For lower oxidant concentrations, there was no significant combined effect (Mishra et al., 2012). Finally, Hastuti et al. (2019) reported the TEMPO oxidation of EFB at different concentrations of NaClO. Hastuti observed a linear behavior between the increase of NaClO and the degree of oxidation (1.08, 1.34 and 1.50 mmol COO^-/g using 10, 20 and 30 mmol NaClO /g cellulose). However, in this work, the reaction time was not varied, and the sample was pre-treated with acid (Hastuti et al., 2019).

X-ray photoelectron spectroscopy (XPS) is a highly valuable analytical technique that provides crucial insights into the surface chemistry of nanocellulose. While conductimetric and potentiometric data are commonly used in studies related to cellulose surface oxidation, XPS can also offer valuable information on cellulose surface composition, including carbon and oxygen contents and their oxidation states (H. Huang et al., 2023). In fact, numerous reports have illustrated the effective use of XPS for quantitative and qualitative analysis of nanocelluloses (Dassanayake et al., 2023; Jasmani & Adnan, 2017; Jordan et al., 2019; G. Liu et al., 2022; Y. Zhao et al., 2023). The XPS C 1s band, which contains contributions from bonded carbons exposed to various local environments, can be resolved into four signals attributed to C-H/C-C, C-O, O-C-O/C=O, and O-C=O (Dassanayake et al., 2023). Specifically, the intensity of the O-C=O signal can be correlated with the acids on the cellulose surface and compared with data from potentiometric and conductimetric measurements (Benkaddour et al., 2014; F. Cheng et al., 2017; Fras et al., 2005). This study reports the effects of key variables such as reaction time, temperature, and pH on the surface chemistry of cellulose nanofibers isolated by TEMPO oxidation from Palm Oil Empty Fruit Bunches (EFB). Conductimetric and XPS analysis allowed monitoring the oxidation process and precise characterization of reaction kinetics and surface chemistry. In addition, we performed a rigorous comparative evaluation of data from conductimetric and XPS data. This research holds profound significance, given Colombia's status as the world's fourth-largest Palm Oil producer. Yet, the abundant and versatile lignocellulose matrix, EFB, remains underutilized Palm Oil producer. Yet, the abundant and versatile lignocellulose matrix, EFB, remains underutilized.

2.3. Experimental

2.3.1. Materials and Reagents

Hydrogen peroxide (H_2O_2), sodium hydroxide (NaOH), hydrochloric acid (HCl 37%), and ethanol (analytical grade) were purchased from Merck (Darmstadt, Germany). TEMPO (2,2,6,6 tetramethylpiperidine-1-oxyl) radical was purchased from Sigma-Aldrich (Saint Louis, MO, USA). A commercial sodium hypochlorite solution (NaClO 15%) was purchased from Máster Químicos (Piedecuesta, Colombia) and standardized according to ASTM D2022. All solutions and suspensions were prepared with distilled water. The mixtures of raw EFBs belonging Elaeis guineensis and the interspecific hybrid OxG were kindly supplied by Extractora Central Palm Oil Mill, Puerto Wilches, Santander, Colombia.

2.3.2. EFB fiber pretreatment

The EFB fibers, as received from the palm oil mill were washed with plenty of distilled water, dried at 60°C in an oven, and stored for further use. This sample was labeled clean EFB. Clean EFB fibers were delignified using a previously described hydrogen peroxide alkaline (AHP) method (S. Ovalle-Serrano et al., 2018). Briefly, 2 g of clean EFB fibers were suspended in a 10% (w/v) H_2O_2 solution brought to pH 11.5 by adding NaOH (4 N); the EFB fibers load was 5% w/v of alkaline solution. The mixture was allowed to react for 2 hours at 70 °C. The treated EFB (AHP-EFB) fibers were washed and dried at room temperature. AHP-EFB fibers were cut into 0.5 cm pieces before TEMPO oxidation. The cellulose, lignin, hemicellulose, moisture, ashes, ethanol-toluene soluble matter contents in EFB and AHP-EFB fibers were determined by the Kurscher and Hoffer, TAPPI 222, Jayme-Wise methods, NREL-TP-510 42621, NREL-TP-510 42622, and ASTM-D1107 standards (ASTM International, 2013; Yao, 2012; Sluiter et al., 2008; Hessler & Merola, 1949).

2.3.3. TEMPO-mediated oxidation of EFB and mechanical treatment

The TEMPO-mediated oxidation of EFB fibers followed the process described by Ovalle et al.(2018) Scheme 2 shows the reaction mechanism (S. A. Ovalle-Serrano et al., 2018). In summary, 0.016 g of the TEMPO radical and 0.1 g of NaBr (dissolved in 40 mL of water) were added to a 100 mL aqueous suspension of 1.0 g of AHP-EFB fibers cut into small pieces (2 mm). Gradually, NaClO was added to the suspension; the amount of NaClO added was dependent on the cellulose:NaClO molar ratios 1:1, 1:5, 1;8 and 1:10 (equivalent to 6.17, 30.84, 49.34 and 61.68 mmol NaClO/g dry cellulose respectively). The mixture was stirred, placed, and kept for variable time intervals in an ultrasonic bath (40kHz, 130 W), where the pH was maintained at 10.5 by adding HCl or NaOH 6 N solutions. Once the pH stabilized (10.5), the reaction mixture was taken from the ultrasonic bath and quenched with ethanol (half the volume of NaClO). The mixture was centrifuged (5000 rpm, 10 minutes), the supernatant was discarded together with the unreacted cellulose, leaving behind the oxidized cellulose pellet. Distilled water was added to the pellet, and the mixture was shaken and centrifuged multiple times until neutral pH. The pellet was then dispersed in 100 mL of water and subjected to sonication with an Ultrasonic Processor (Sonics vibra-cell -VC750, 20 kHz, 750 W, A 40%, 1:1 sec cycle for 10 minutes). A direct TEMPO oxidation control experiment was also carried out using raw EFB fibers (without AHP treatment) reacted with TEMPO for 120 minutes using a cellulose:NaClO ratio of 1:8 (49.34 mmol NaClO/g dry cellulose).

A multilevel factorial design (2^4) was conducted to test the influence of variables on the TEMPO-oxidation process and reaction yield of AHP-EFB fibers. The design included two independent variables, namely reaction time and cellulose:NaClO molar ratio, each with four levels (refer to Table 7 and Appendix E). The reaction time ranged from 30, 60, 90, to 120 minutes, while the cellulose:NaClO molar ratios ranged from 1:1, 1:5, 1:8, and 1:10. The statistical analysis of the design was performed using STATGRAPHICS 18 software, with charge density, reaction yield, size distribution, and ζ potential as response variables. The labeled samples indicated their reaction time and the cellulose:NaClO ratio. For example, a sample with a reaction time of 120 minutes and a cellulose:NaClO molar ratio of 1:8 was labeled as TOCN 120-1:8 or 120-1:8. Direct TEMPO-oxidized samples were labeled as EFB-TOCN.

Table 7. Experimental parameters and levels

Parameters	**Levels**			
	1	2	3	4
Reaction time (min)	30	60	90	120
Cellulose:NaClO molar ratio	1:1	1:5	1:8	1:10

The suspension concentration was determined using equation 2, based on the mass of both the wet and dry TOCN suspensions.

$$[TOCN\ suspension]\% = \frac{M_{dry}\ [g]}{M_{TOCN\ suspension}\ [g]} * 100 \quad (2)$$

Where $M_{\text{TOCN suspension}}$ is the mass of a given TOCN suspension volume, and M_{dry} is the mass of this TOCN dried at 60 °C, until constant weight.

The reaction yield was determined using equation 3, which considers the suspension concentration, suspension volume, and the fiber mass used for the TEMPO oxidation.

$$Reaction\ yield\ \% = \frac{M_{total}\ [g]}{M_{fiber}\ [g]} * TOCN\ suspension\ [\%] \quad (3)$$

Where M_{total} is the mass of the TOCN suspension after sonication with the ultrasonic processor, Mf_{iber} is the mass of AHP-EFB or EFB sample used for the TEMPO oxidation and the TOCN suspension % is the value obtained from equation 2.

2.3.4. Materials characterization

Conductimetry was used to determine the TOCN degree of oxidation (DO). First, 0.05 g of each TOCN sample was suspended in 0.01 M HCl solution until pH 2 (excess acid) and stirred for 10 minutes. The suspension was titrated with a previously standardized 0.01 M NaOH solution. The TOCN conductometric titration proceeds through three specific steps. Initially, the mixture's conductivity decreases rapidly due to the excess HCl and NaOH reaction. Secondly, the weak organic acids in the oxidated anhydroglucose units of cellulose react with NaOH, driving a slight and prolonged decrease in conductivity. Finally, conductivity increases sharply due to the excess NaOH. The nanocellulose degree of oxidation (DO) was determined by equation 4 and the charge density (σ) by equation 5, as proposed by Habibi et al (2006) (Habibi et al., 2006). Conductimetric titration was performed in triplicate for each TOCN suspension, and error bars indicate standard deviation.

$$\mathrm{DO} = \frac{162 \, * \, \mathrm{C} * (\mathrm{V}_2 - \mathrm{V}_1)}{\mathrm{m} - 36 \, * \mathrm{C} * (\mathrm{V}_2 - \mathrm{V}_1)} \quad (4)$$

$$(\mathrm{mmol\,COO^-/g}\,)\ \sigma = \frac{\mathrm{C} * (\mathrm{V}_2 - \mathrm{V}_1)}{\mathrm{m}} \quad (5)$$

Where C is the NaOH molar concentration, V_1 and V_2 are the NaOH volumes (mL) used in the second titration step, m is the sample weight (g), 36 corresponds to the difference between the molecular weight of one anhydroglucose (162 g/mol) unit and a glucuronic acid sodium salt residue (198 g/mol).

FESEM images of the raw and delignified fibers (EFB and AHP-EFB) were taken at 30 kV on a FEI QUANTA FEG 650 (Oregon, USA) instrument equipped with a secondary electron detector (SED), an Everhart Thornley detector (ETD) and a backscattered electron detector (BSE). Samples were coated with a thin layer of carbon before imaging. For the TOCN 120-1:8 sample, a suspension was prepared at a concentration of 0.8% w/w and dried at 60°C to form a film. Size distribution and ζ potential (colloidal stability) of EFB-TOCN and TOCN suspensions (0.01% w/v) were estimated by Dynamic Light Scattering Analysis (DLS) using a MALVERN Zetasizer ZS90 instrument (Worcestershire, UK)(Ravindran et al., 2019) DTS-0012 polystyrene and DTS-1070 cells were used for size distribution and ζ potential measurements, respectively. Each measurement of ζ potential was performed in triplicate and error bars indicate standard deviation. TOCN and EFB-TOCN films were produced by drying 0.8% w/v TOCN suspensions at 60°C for 24 hours for FTIR-ATR and XPS analysis. FTIR-ATR enables functional group identification and observing changes caused by the experimental variables tested. FTIR-ATR analysis was performed in a Nicolet iS50 FTIR spectrometer equipped with an integrated diamond ATR module. FTIR-ATR spectra were acquired at a 4 cm^{-1} resolution and wavenumber range of 4000 to 400 cm^{-1} using 64 scans.

XPS experiments were recorded using the A-Centeno-XPS/ISS/UPS surface characterization platform produced by SPECS (Germany). The platform is equipped with a PHOIBOS 150 2D-DLD energy analyzer. During XPS analysis, the pressure in the analysis chamber was approximately $1x10^{-9}$ Pa. The spot size was 2 mm x 2 mm unfocused; the analyzer lens mode was used in Medium Area, the aperture was 4C, and the calibration resolution was $Ag_{3/2}$ FWHM 0.05. A monochromatized Al K_α X-ray source (FOCUS 500) operated at 100 W was used for the measurements. The pass energy of the hemispherical analyzer was set at 100 eV for general spectra and 15 eV for high-resolution spectra. Surface charge compensation was controlled using a Flood Gun (FG 15/40-PS FG 500). After each analysis, the C 1s region was re-recorded to verify the sample's surface charge change during the analysis. The CasaXPS software (Casa Software Ltd.) was used to process the data using a Shirley-type baseline.(Hernández-Maya et al., 2022) All spectra were calibrated with the C 1 s at 284.8 eV. The signals correspond to C1 284.8 eV (C-H), C2 286.7 eV (O-C-C-C), C3 288.0 eV (O-C-O/C=O) and C4 289 eV (O=C-O-) (Le Gars et al., 2020; Rouxhet & Genet, 2011). Atomic oxygen (%) was determined after eliminating the contributions of silicon and calcium oxides.

2.4. Results and Discussion

2.4.1. EFB Fiber composition

Figure 10 displays the EFB and AHP-EFB fibers composition in terms of weight percentage. The EFB fibers were washed only with water and were not degreased prior to TEMPO oxidation. However, less than 4.1% of waxes, fats, resins, and oils that are soluble in ethanol-toluene were present in the raw samples. After AHP treatment, there was a 76% reduction in the ethanol-toluene soluble content, indicating the removal of surface fats and waxes. The AHP treatment increased the moisture content in the fiber because it makes the fiber surface more hydrophilic and water-accessible by removing lignin and hemicellulose (Asim et al., 2020). Ash decreased by 46% in AHP-EFB, which suggests the removal of surface minerals. Cellulose, on the other hand, increased by 16%, while lignin decreased by 48% in AHP-EFB. The AHP process aims to remove lignin, leaving cellulose available, allowing a more efficient surface TEMPO oxidation compared to the non-delignified EFB (Ho et al., 2019; S. Ovalle-Serrano et al., 2018). Hemicellulose showed no notable change (less than 5% variation). The ATR spectra of EFB and EFB-AHP in Appendix F show the bands at 1317, 1164, 1109, 1030, and 900 cm^{-1}, corresponding to functional groups of cellulose common to all samples (Appendix G) (Kaffashsaie et al., 2021). EFB fibers showed signals characteristics of hemicellulose and lignin in 1733 and 1230 cm^{-1}, respectively. These bands were not observed in the delignified fibers (AHP-EFB) or the TOCN samples, indicating their removal by the AHP pre-treatment (S. A. Ovalle-Serrano et al., 2018). Finally, the TOCN film spectra showed a band at 1602 cm^{-1}, corresponding to sodium carboxylate, from TEMPO oxidation (Fujisawa et al., 2011).

Figure 10. EFB and AHP-EFB fiber composition

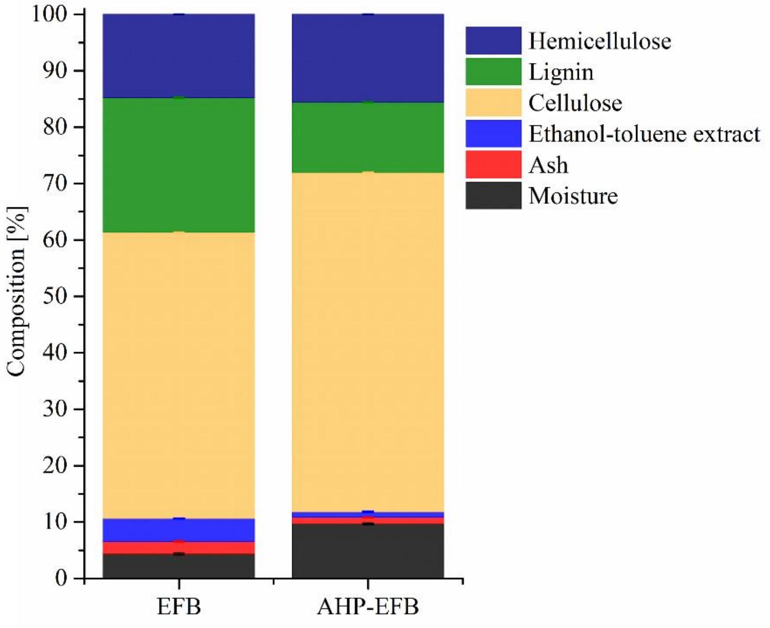

2.4.2. EFB-TOCN degree of oxidation (DO), charge density (σ), and oxidation yield.

Surface charges govern cellulose nanofibers fibrillation and dispersion in water due to electrostatic repulsions. The TEMPO oxidation reaction oxidizes the primary hydroxyl to carboxylate at C6 in the AGU, and the extent of the reaction is determined by both the degree of oxidation (DO) and the surface charge density (σ). These two parameters, determined from conductimetric titrations, exhibit similar trends according to our observations and other authors (Geng et al., 2018). Figure 11 shows the trends in the degree of oxidation (DO) and charge density (σ, mmoles of COO^-/g cellulose) and its standard deviation for TOCN derived from AHP-EFB and EFB fibers. Appendix H of the supplementary information contains all the conductimetric titration plots. Reaction time and cellulose:NaClO ratios have a directly effect on TOCN surface chemistry. The DO increased by 35% when the reaction time changed from 30 to 120 minutes using a 1:1 cellulose:NaClO ratio. According to the stoichiometry of the TEMPO oxidation reaction (Scheme 2), 2 moles of NaClO oxidize one mole of primary hydroxyl groups (Rattaz et al., 2011). Thus, increasing the cellulose:NaClO ratio from 1:1 to 1:10 raised the DO by 52% for 120 minutes of reaction. The maximum DO was 0.27 for the 1:5 cellulose:NaClO at 90 minutes. Interestingly, further increase of the cellulose:NaClO ratio (to 1:8 and 1:10) only slightly raise the DO for 90 and 120 minutes of reaction. Thus, cellulose:NaClO ratios above 1:5 seem to work better for TOCN isolation from AHP-EFB with reaction times above 90 minutes.

The DO of TOCN from untreated EFB was 0.24, using a 1:8 cellulose:NaClO ratio and 120 minutes of reaction. Under the same experimental conditions, the DO for the TOCN from AHP-treated EFB was 0.29, representing an increase in oxidation of 21% upon lignin removal from the fibers, as mentioned above. Lignin removal affects the TEMPO oxidation reaction, making the cellulose surface more susceptible to oxidation, as previously reported in the literature (S. A. Ovalle-Serrano et al., 2018). Considering the complex structure of lignocellulosic biomass, it is important to note that the efficiency of cellulose oxidation via TEMPO is heavily influenced by the exposure of fibrils to the reaction media. Several pretreatment processes, including alkaline treatment, have been investigated to enhance this exposure. This process is effective in promoting fibril swelling and disrupting intermolecular interactions in lignocellulosic materials, as well as removing waxes, polysaccharides, and lignin (Alvarez-Vasco & Zhang, 2017; Balea et al., 2017; Pönni et al., 2014). However, for raw materials with low lignin content (< 5 %), such as hemp, it may be more advantageous to utilize direct TEMPO oxidation without pretreatment, as it is faster and reduces overall costs (Puangsin et al., 2017). Performing TEMPO oxidation on raw EFB fibers (without deslignification) affects the reaction yield and degree oxidation because two simultaneous and competing processes consume the primary oxidant, lignin bleaching and carboxylate formation at the cellulose surface. This effect has been previously observed and reported (Kaffashsaie et al., 2021). Interestingly, the electron micrographs in Figure 11d indicate that EFB fibers are abundant in silica and have a porous surface, as reported earlier (Rama Rao & Ramakrishna, 2022). By partially removing the lignin, the AHP treatment uncovered the cellulosic surface without eliminating the silica microparticles. Even after TEMPO oxidation, the silica particles are still visible within the TOCN, as evidenced by the micrograph. The DO and σ have a positive correlation with reaction time. However, there are two kinetic regimes during the reaction. There is an initial fast oxidation kinetics from cero to thirty minutes. As seen in Figure 11a, during the first 30 minutes of the reaction, increasing cellulose:NaClO ratios from 1:1, to 1:5, 1:8. and 1:10 raises the AHP-EFB oxidation rate from 0.026 to 0.040, 0.047, and 0.051 mmol COO^-/g cell/min, respectively. After 30 minutes of reaction, the process slows down, and the reaction enters a second regime where the oxidation rate is two orders of magnitude lower than during the first 30 minutes.

For instance, Figure 11a shows, for the 1:1 molar ratio, an oxidation rate of 0.004 mmol COO^-/g cell/min from 30 to 120 minutes, in contrast with 0.026 COO^-/g cell/min for the first 30 minutes. Interestingly, at higher molar ratios, reaction time influences the oxidation process less, after the initial 30 minutes, as signaled by decreased oxidation rates of 0.003, 0.002, and 0.002 mmol COO^- g cell/min for 1:5, 1:8, and 1:10, respectively. From 30 to 120 minutes, the oxidation reaction can be considered of pseudo zero order for high cellulose:NaClO ratios (1:5, 1:8, 1:10) because the rate constants do not change significantly. Mao *et al.*[51] and Xu *et al.*[52] reported a zero-order reaction order for NaClO concentration during the TEMPO oxidation reaction of cellulose from softwood and eucalyptus wood (Mao et al., 2010; H. Xu et al., 2022). These differences in oxidation rates are explained by assuming that during the first 30 minutes of the reaction, the chemical attack -by the TEMPO catalytic system- is concentrated at the fiber's surface. Increased ratio cellulose:NaClO (1:5, 1:8, 1:10) promotes high oxidation rates, quickly transforming primary hydroxyl groups into carboxylates. Increased carboxylate contents for the fibers reacted at high cellulose:NaClO molar ratios mean more electrostatic repulsion and increased fiber reactivity. Between 30 and 120 minutes, these systems experience a reduced oxidation rate (21 and 15% for the 1:8 and 1:10 molar ratios) due to a decrease in available C-6 hydroxyl groups (H. Xu et al., 2022). In contrast, AHP-EFB-TOCN isolated at 1:1 cellulose:NaClO molar ratio presents less surface oxidation during the initial 30 minutes; thus, the second kinetic regime (from 30 to 120 minutes) shows faster oxidation rates (50% for the 1:1). Figure 11b also illustrates the percentage of bulk cellulose transformed into nanocellulose (reaction yield %) as a function of reaction time for various cellulose:NaClO molar ratios. Increasing reaction time, from 30 to 120 minutes, resulted in a 28% yield increase for the 1:1 ratio and a 35% increase for the 1:5, 1:8, and 1:10 cellulose:NaClO molar ratios. Once the TEMPO reaction stopped (Figure 11c, image 120-1:8 bottom right), the oxidized material underwent mechanical treatment using an ultrasonic probe (20 kHz, 175 W) to promote defibrillation and uniform dispersion.

Figure 11. Effect of experimental conditions (reaction time and cellulose:NaClO ratio) on AHP-EFB a) DO and σ, b) cellulose oxidation yield. c) Optical images of the TOCN isolation process (after the ultrasound bath). d) Electron micrographs of raw fibers (EFB), delignified fibers (AHP-EFB) and TOCN 120-1:8 film (0.8% w/w)

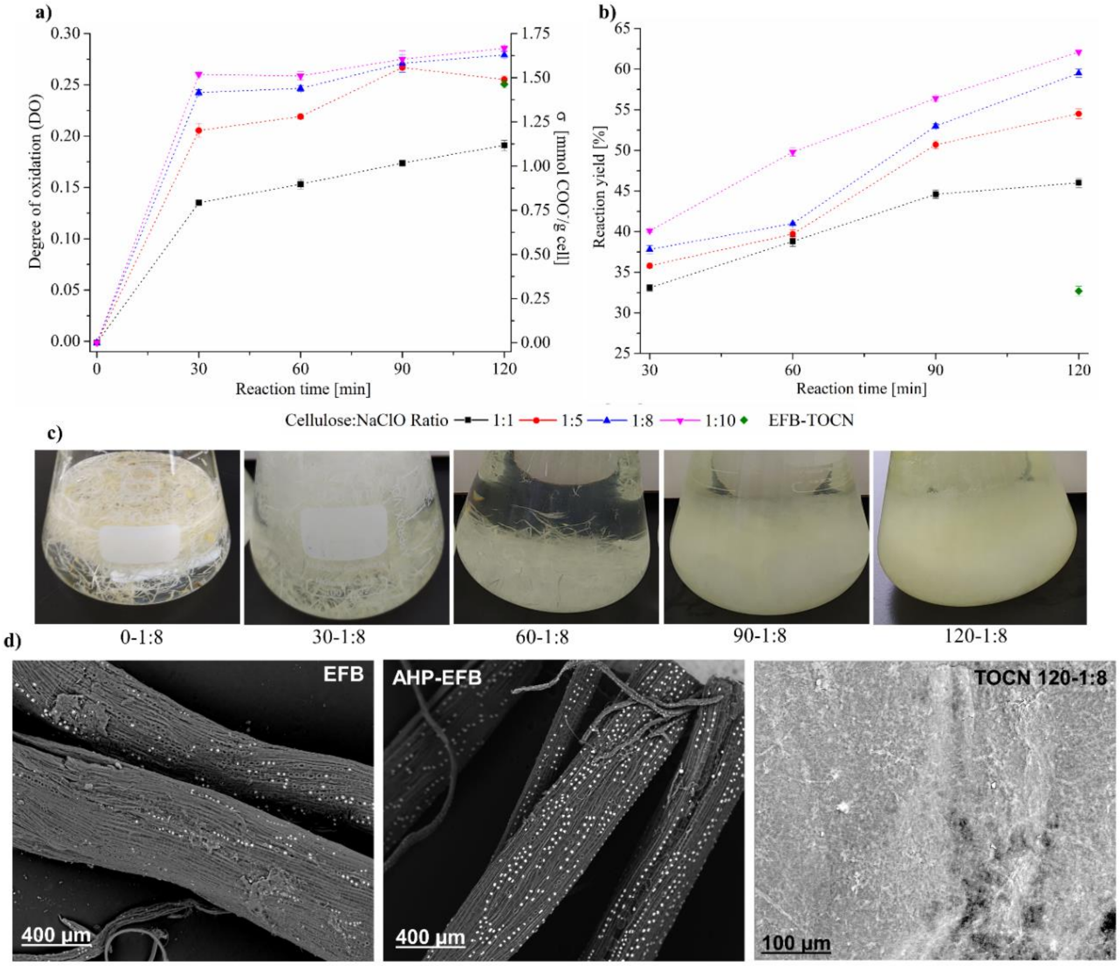

The maximum reaction yield obtained was 61% under the conditions studied using pretreated AHP-EFB. On the other hand, the low yield (32%) of EFB-TOCN, isolated from raw/untreated EFB, deserves attention. Previous studies indicate that performing direct TEMPO oxidation on raw biomass results in higher reaction yields than pretreated biomass but only for low-lignin content materials (Kaffashsaie et al., 2021). The differences in reaction yield are caused by the pretreatment process (AHP) -as discussed above- and the mechanical treatment applied to the oxidized material after the TEMPO reaction, as previously reported (Chew et al., 2017; Kaffashsaie et al., 2021; Levanič et al., 2022). The ultrasonic probes work within a confined region of the suspension -around the probe tip- where mechanical stress (cavitation) overcomes the cohesive forces between cellulose fibrils to promote dispersion (Redlinger-Pohn et al., 2022). As a result, there is some size heterogeneity in the isolated NFCs -represented in the presence of large fibers- which were removed during the washing processes. This fact adversely affects the EFB reaction yields.

The Pareto diagram (Appendix I-1) indicates that reaction time and cellulose:NaClO ratios are statistically significant as independent variables and have no significance when combined for AHP-EFB-TOCN charge density and DO. The significance of the two aspects is individually high, and their increment raises the response (DO, σ) according to the main effects plot (Jiju, 2014). For the reaction yield, variables time, NaClO, and their combination are individually significant (Appendix I-2).

2.4.3. EFB-TOCN size distribution and ζ potential

Figure 12 shows the effect of different experimental conditions on AHP-EFB-TOCN dispersion size, expressed as the maxima of the intensity percent distribution. The reaction time and cellulose:NaOCl ratio affect TOCN size. However, the effect of time is more dramatic. The size distribution range decreases as the time increases. As the cellulose:NaClO ratio increases, the size distribution decreases. When analyzing the maximum intensity values as a function of the size distribution, the AHP-EFB-TOCN size decreased between 76 and 82% when the reaction time increased from 30 to 120 minutes for all cellulose:NaClO molar ratios. In contrast, for any given reaction time, the particle size only decreased by around 40% for increasing cellulose:NaClO ratios. For instance, at 30 minutes, a ten-fold increase in the amount of NaClO -from 1:1 to 1:10- reduced the particle size from 842.9 to 576.3 nm. The Pareto diagram (Appendix I-3) indicates that reaction time is the only statistically significant independent variable affecting AHP-EFB-

TOCN size; the longer the reaction time, the smaller the AHP-EFB-TOCN size, an effect also measured by other authors using atomic force microscopy and scanning electron microscopy (C. F. Huang et al., 2019; Van Hai et al., 2018). Although statistically, there is no significant relationship between TOCN size and NaClO amount, several authors have reported this dependence. Considering that the TEMPO catalytic cycle uses NaClO as a primary oxidant, more NaClO results in more carboxylates (COO^-) which in turn create electrostatic repulsions between the oxidized cellulose fibers allowing their individualization and thus facilitating size reduction (Isogai, 2016; Kaffashsaie et al., 2021).

Figure 12. Effect of experimental conditions on AHP-EFB TOCN a) maximum size distribution and b) ζ potential.

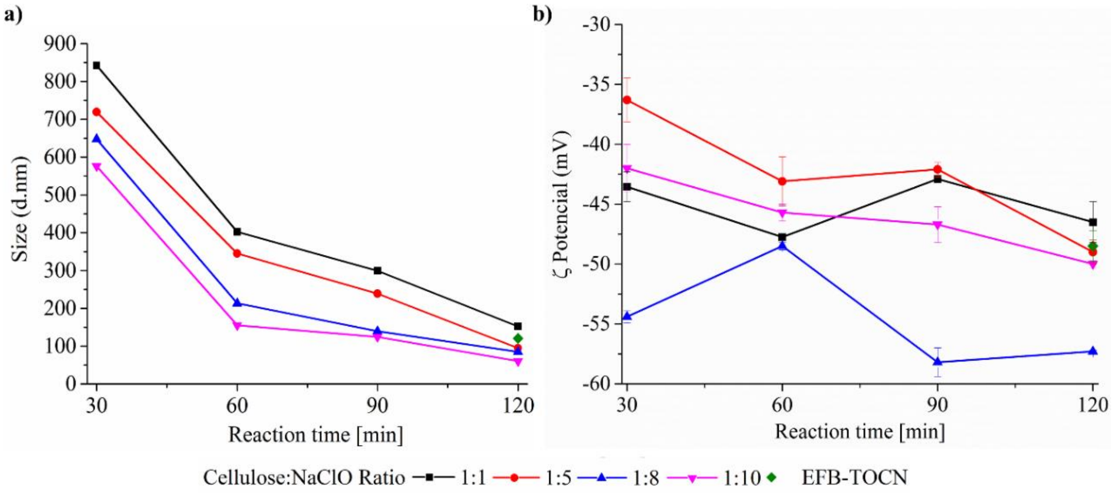

Finally, EFB-TOCN (isolated from EFB without AHP treatment) exhibited a size distribution maximum of 120.4 nm. Under the same conditions, the delignified fibers afforded TOCN with radii of 100 nm, equivalent to a decrease of 29% in particle size. Thus, it is easier to defibrillate the delignified fibers than the raw fibers, as observed by other researchers (Benhamou et al., 2014). Literature reports have demonstrated that the size of TOCNs depends on various factors, such as biomass origin, pre- and post-treatments, and reaction conditions. For instance, TOCNs obtained from eucalyptus sawdust pretreated with a homogenizer had an average diameter of 41.0 nm (Vallejos et al., 2016). Similarly, TOCNs extracted from bleached and unbleached pineapple stubbles had diameters of 15.5 and 47.9 nm, respectively, as determined by atomic force microscopy; a microfluidizer was used after TEMPO (Araya-Chavarría et al., 2022). Additionally, mild shearing was used as a pretreatment for bleached and unbleached paulownia wood to obtain TOCNs with diameters of 5.0 and 6.0 nm, respectively, as observed by FESEM (Kaffashsaie et al., 2021). It is evident that TOCNs extracted from different biomass and subjected to various pre- and post-treatments exhibit distinct sizes. The bleaching process impacted the size of TOCNs isolated from pineapple stubble, but it did not affect TOCNs obtained from paulownia wood. However, all discussed TOCNs had sizes below 50 nm. In the present work, cellulose:NaClO molar ratios above 1:5 and 120 minutes of reaction with an ultrasonic horn as mechanical treatment afforded TOCNs with sizes below 100 nm. Nonetheless, it is worth noting that the actual size of EFB-TOCNs could be smaller than the values measured by DLS due to nanocellulose aggregation, which could affect the size in this technique (Ravindran et al., 2019).

Based on the data presented in Figure 12b, all TOCN suspensions have ζ potential values above ±30 mV, indicating a high level of colloidal stability, likely due to Coulombic repulsions between carboxylate groups (H. D. Silva et al., 2012). Interestingly, there does not appear to be any correlation between the experimental parameters (reaction time and amount of NaClO) and the ζ potential values. Isogai et al. (2011) reported similar results, as there was no relationship between the carboxylate content and ζ potential of TOCNs isolated from various cellulose sources. However, they did observe ζ potential values around -75 mV for TOCNs with COO^- contents ranging from 0.5 to 1.6 mmol/g cellulose (Isogai et al., 2011). Recent theoretical studies have shown that COO^- groups in TOCN dispersions can cause a triple screw conformational change, increasing the repulsion between the cellulose particles and their hydrophilicity (Asgarpour Khansary et al., 2020). In our case, TOCN could potentially undergo conformational changes affecting the surface COO^- density and the ζ potential value. Another factor to consider is the presence of silica (SiO_2) in the TOCN suspensions from the EFB matrix (Figure 11d). SiO_2 has a negative ζ potential, and its presence increases the magnitude of the ζ potential, as previously reported (Carlson & Kawatra, 2013). Considering that the concentration of SiO_2 in the suspensions is variable, a proportional relationship between the number of carboxylate groups and the ζ potential was therefore not observed. Finally, the Pareto diagrams in Appendix I-4 show no influence of the experimental variables on the TOCNs ζ potential value.

2.4.4. X-ray Photoelectron Spectroscopy (XPS)

Table 8 presents the elemental surface composition obtained by XPS for AHP-EFB-TOCN, Appendix J of the Supporting Information shows each sample's the positions and values of FWHM. All samples contain carbon (284.8 eV), oxygen (532 eV), and calcium (343 eV), characteristic of lignocellulosic compounds.(Gong et al., 2019) Calcium can be in the form of CaCO (Genet et al., 2008), CaO, or $Ca(OH)_2$ (Ghods et al., 2011). The EFB fibers contain silicon as carbon-bonded oxide C-(Si-O) associated with biogenic silica. In plants, silicon is deposited as silica within and between cell walls and fibers in the form of amorphous phytoliths or silica bodies (Law et al., 2007). However, silicon only appears in some samples because the AHP-EFB-TOCNs surfaces are heterogeneous. Sodium (1070 eV) and chlorine (198 eV) are in the form of NaCl salts,(Ghods et al., 2011) and are attributed to residual compounds of the TEMPO oxidation reaction. For this reason, chlorine and sodium only appear in the oxidized samples (AHP-EFB-TOCN) and not in the raw EFB or the AHP-pretreated fibers. The major component of EFB fibers is carbon, followed by oxygen, silicon, and calcium. After the AHP treatment, the surface silicon was removed, and the amount of oxygen increased.

During the AHP-EFB-TOCN isolation using different experimental conditions, an increase in the amount of oxygen was expected with increasing reaction time and amount of NaClO, which occurred up to TOCN 90-1:8. However, at TOCN 120-1:8, the percentage of oxygen decreased, and that of calcium increased compared to TOCN 90-1:8. This change can be attributed to a possible diffusion of calcium to the surface of the sample, as a consequence of structural changes (rearrangements) during the chemical treatments (delignification and TEMPO oxidation). Similarly, when the amount of NaClO increased, the percentage of oxygen did not increase after TOCN 120-1:5.

Due to chemical inhomogeneity and roughness on the film surfaces. Depending on the sector in which the interaction with the radiation occurs, the composition will have fluctuations in the compositional percentages (Gray et al., 2010). Also, the depth of the technique is less than 10 nm,(Pintori & Cattaruzza, 2022) limiting the results if diffusion or surface rearrangement processes occur. In a study conducted by Lai et al.(2013) bacterial cellulose (BC) was oxidized using TEMPO and varying NaClO concentrations and reaction times. XPS analysis revealed an increase in oxygen content with prolonged reaction time, whereas the opposite was observed with a fourfold increase in NaClO concentration. However, these findings conflicted with those obtained through ^{13}C NMR analysis, suggesting that XPS only detects surface changes (C. Lai et al., 2013). In our research, XPS analysis demonstrated that the oxidized samples (TOCN) had a greater oxygen content than the raw and delignified fibers (EFB and AHP-EFB), indicating that the oxidation reaction had occurred, as previously reported by other researchers (Cheng et al., 2017; C. Lai et al., 2013).

Table 8. The surface atomic composition of EFB fibers and TONCs by XPS

ID	**% C**	**% O**	**% Ca**	**% N**	**% Si**	**% Na**	**% Cl**
EFB fibers	84.6	11.9	1.3	-	2.1	-	-
AHP-EFB	82.3	15.6	2.1	-	-	-	-
EFB-TOCN	63.7	28.3	4.3	1.2	-	1.2	1.3
TOCN30-1:8	74.8	22.3	1.5	0.2	1.0	0.2	-
TOCN 60-1:8	71.7	24.5	2.5	-	1.1	0.2	-
TOCN 90-1:8	70.8	25.4	1.9	0.3	-	0.7	0.9
TOCN 120-1:8	71.1	21.7	5.6	0.4	0.4	0.8	-
TOCN 120-1:1	74.2	23.2	0.5	0.7	-	0.6	0.8
TOCN 120-1:5	72.3	24.5	1.1	0.1	-	0.9	1.1
TOCN 120-1:10	74.8	22.9	0.9	0.2	-	0.6	0.6

Figures 13 and 14 display the decomposition spectra of the C 1s signals obtained by XPS for the different samples. The EFB, AHP-EFB, and TOCN spectra show 2 (**C**-H and O-**C**-O/**C**=O), 3 (**C**-H, O-**C**-C, and O-**C**-O/**C**=O), and 4 (**C**-H, O-**C**-C, O-**C**-O/**C**=O, and C-**C**OO$^-$) signals respectively. The TOCN C-COO$^-$ signal in XPS increased with increasing reaction time and the amount of NaClO, following the DO trend observed by conductimetric titration. The C-H, O-C-C-C, and O-C-O/C=O signals correspond to alkane carbons, lignin, and hemicellulose, (Espino-Pérez et al., 2014) and the C-COO$^-$ signal corresponds to the primary hydroxyl oxidation in the anhydroglucose units (AGU) of cellulose by TEMPO. Therefore, the C-COO$^-$ signal only occurs in oxidized samples (TOCN), indicating cellulose oxidation. The decomposed C 1s spectra allowed us to examine the cellulose behavior during the delignification and TEMPO oxidation process. The AGUs in cellulose have a molecular formula $C_6O_5H_{10}$, with an O/C ratio of 0.83 (Kolářová et al., 2013); out of six carbons, five are linked to carbon, hydrogen, and oxygen (C-C-O), while the sixth carbon is bonded to two oxygens. Thus, in XPS 5/6 of the carbon contributes to the C-C-O signal, and 1/6 contributes to the O-C-O/C=O signal (Sbiai et al., 2012). Benkaddour and Le Gars reported that the C 1s spectrum of TEMPO oxidized cellulose contains 4 components corresponding to C1 (C-C/C-H), C2 (C-O), C3 (O-C-O/C=O) and C4 (O-C=O), with the C4 signal being associated with oxidation (Benkaddour et al., 2014; Le Gars et al., 2020). The C4 signal is absent in the non-oxidized matrix. In addition, the C2 signal is more intense, followed by C3 and C4, according to the amount of each type of carbon present in the oxidized cellulose (Sbiai et al., 2012). Lai et al.(2013) reported an increase in signal intensity (C-COO$^-$) with increase in reaction time and NaClO concentration in TEMPO oxidation of BC (C. Lai et al., 2013).

Figure 13. C 1 s XPS spectra of a) EFB, b) AHP-EFB fibers, c) direct TEMPO oxidation (EFB-TOCN) and AHP-EFB TOCN isolated using d) 1:1, e) 1:5 and f) 1:10 cellulose:NaClO ratios at 120 minutes of reaction

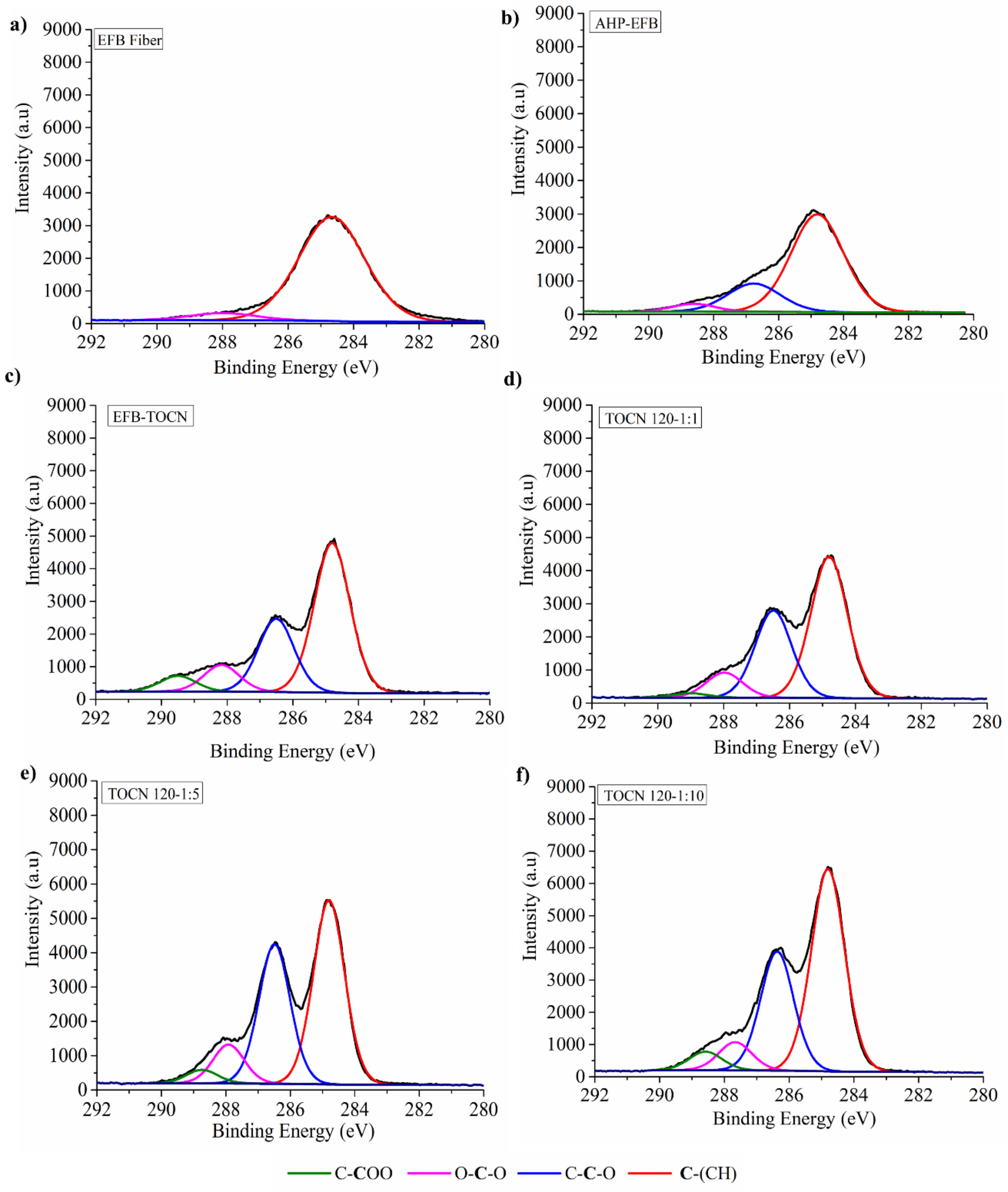

Figure 14. C 1s XPS spectra of AHP-EFB TOCN isolated using 1:8 cellulose:NaClO ratios at a) 30, b) 60, c) 90, and d) 120 minutes of reaction

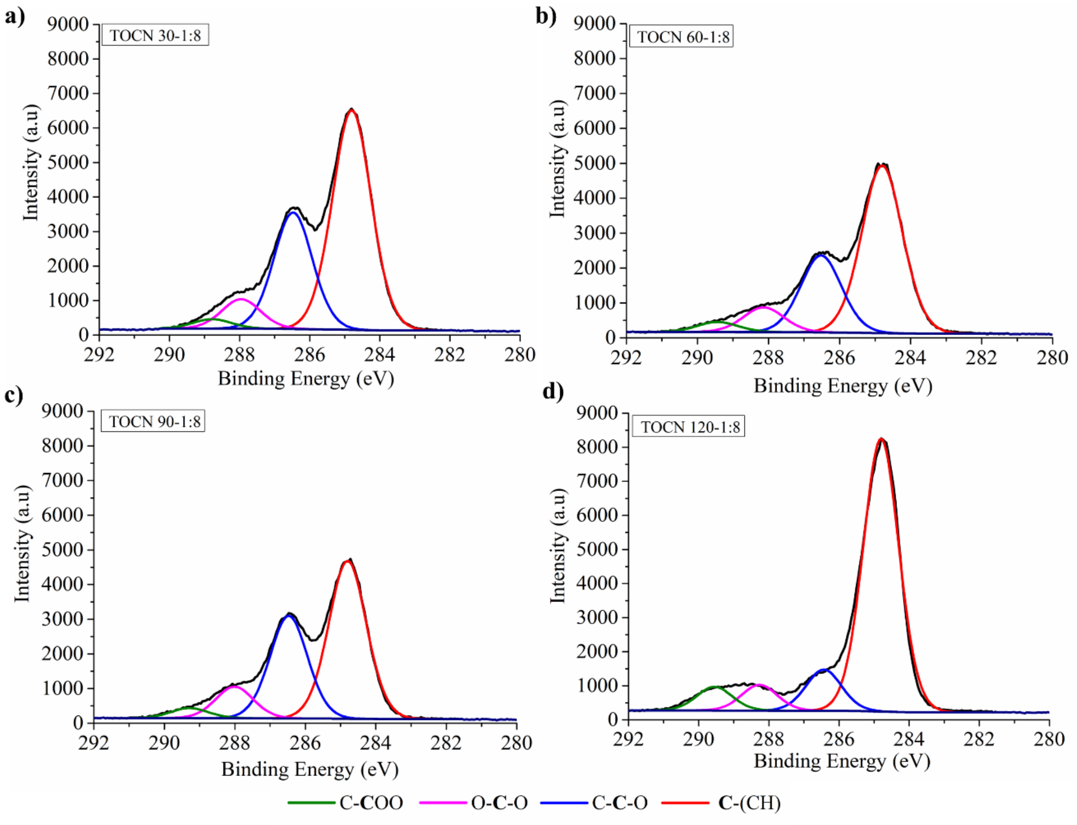

When an AGU in cellulose is oxidized, its chemical formula changes to $C_6O_6H_8$ (Scheme 2) with an O/C molar ratio of 1. The number of carbons in the structure does not change, but their chemical environment does. Thus, for an oxidized AGU, 4/6 of the carbons contribute to the C-C-O signal, 1/6 of the carbons to the O-C-O/C=O signal, and 1/6 of the carbons to the C-COO$^-$ signal. Considering the relationships mentioned above, Figure 15 presents the parity diagrams of the experimental and theoretical values of each type of carbon signal from C 1s by XPS. The theoretical signals were obtained from the sum of the intensities of the carbon signals with oxygen (C-**C**-O, O-**C**-O/**C**= O, and C-**C**OO$^-$), using the ratios 5/6 and 1/6 for AHP-EFB, and 4/6, 1/6 and 1/6 for TOCN. An overall coincidence between the experimental and the theoretical values for the C-C-O signal was observed in most samples (Figure 15a). However, for the O-**C**-O/**C**=O signal, the experimental value tends to be higher than the theoretical one. This result is because aldehydes were not oxidized to carboxylate during the TEMPO oxidation reaction (Figure 15b) (Mishra et al., 2012). Finally, the experimental C-COO$^-$ values were lower than expected, probably due to a heterogeneous carboxylate group distribution on the TOCNs surface (Figure 15c) (Fras et al., 2005).

Figure 15. Experimental and theoretical values for each bond type from the C 1s XPS spectra. a) C-C-O, b) O-C-O, c) C-COO$^-$

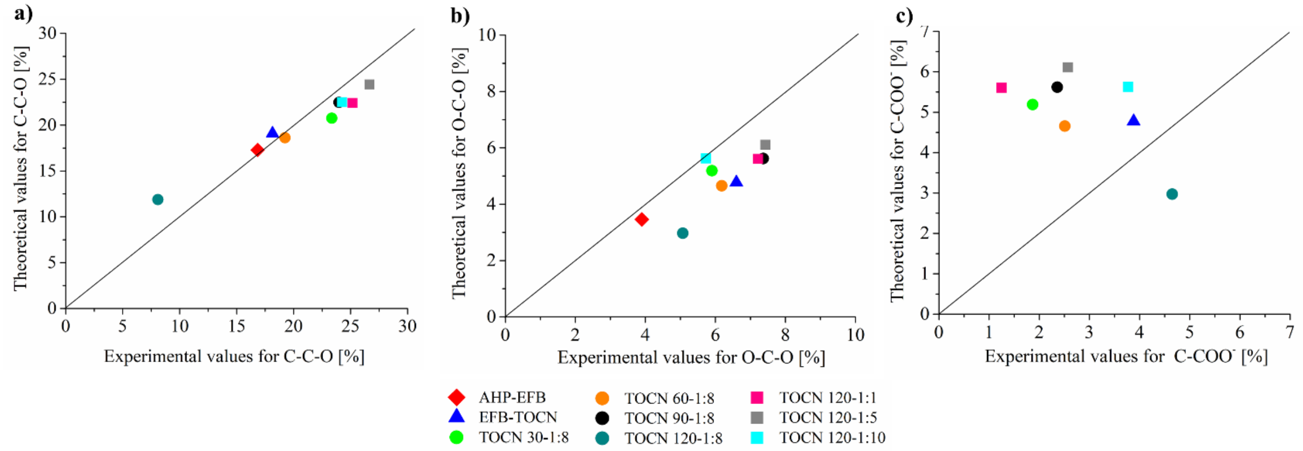

The O/C ratios in Table 9 were calculated using data from the C 1 s and O 1 s spectra. To improve the analysis accuracy, only the C signals with oxygen were considered (C-C-O, O-C-O, and C-COO$^-$) and substracted the contributions of the metals to the oxygen. The EFB fibers have an O/C ratio of 0.88, 0.05 units higher than the theoretical cellulose value. For the AHP-EFB-TOCN 120:1:8 sample, the O/C ratio was 0.92, the closest to the theoretical value. There was a consistent increase in the O/C ratio as the reaction time increased. However, the trend does not hold for increased cellulose:NaClO ratios. This behavior was associated with a heterogeneous surface morphology and composition in TOCNs.(Barazzouk & Daneault, 2012; C. Lai et al., 2013)

Table 9. O/C ratios obtained by XPS

ID	**O/C**

AHP-EFB	0.88
EFB-TOCN	0.83
TOCN 30-1:8	0.64
TOCN 60-1:8	0.76
TOCN 90-1:8	0.74
TOCN 120-1:8	0.92
TOCN 120-1:1	0.72
TOCN 120-1:5	0.69
TOCN 120-1:10	0.68

Figure 16 shows the correlation between the TOCN charge density (g of COO^-/100 g cellulose) data derived from conductimetric titration and the percentage of C 1s carboxylate obtained by XPS. In both techniques, the number of carboxylates increased as the reaction time and the amount of NaClO increased. Figure 16 shows that the XPS technique supports the results of conductimetric measurements (Fras et al., 2005). However, the number of carboxylates obtained by conductimetric titration was higher than that of XPS. The difference could be that XPS quantifies the surface concentration of carboxylates and not the overall concentration as conductimetry does. Therefore, the carboxylates obtained by XPS will normally be lower than those obtained by conductimetric titration. As XPS is a surface technique, it gives the amount of COO^- available on the surface. In addition, XPS and conductimetric titration show that the amount of carboxylate groups increased with both time and cellulose:NaClO molar ratio.

Figure 16. Correlation between charge density (% w/w) from conductimetric titration and C-COO^- bonds from C 1 s XPS spectra

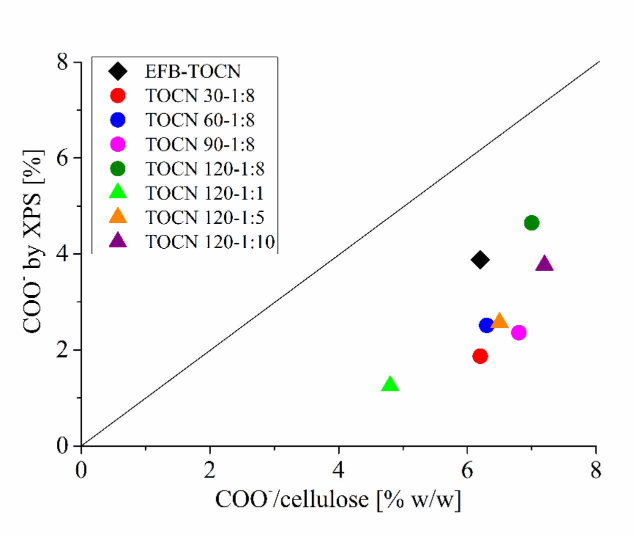

2.5. Conclusions

Changes in reaction time, amount of primary oxidizing agent (NaClO), and matrix pretreatment affected the surface chemistry, particle size, and reaction yield of TOCN isolated from AHP-EFB to various extents. However, the amount of primary oxidizing agent (NaClO) had the most significant impact on the final material's oxidation degree.

The size of TOCNs was affected by the reaction time, with a minimum reaction time of 120 minutes required to obtain sizes below 100 nm with a cellulose:NaClO ratio of 1:5.

Matrix pretreatment affected DO and EFB oxidation yield. A maximum oxidation yield of 61% was achieved using pretreated AHP-EFB, while a low yield of 32% was observed for TOCN isolated from raw/untreated EFB.

All TOCNs formed stable aqueous suspensions with a ζ potential between -36 and -58 mV due to electrostatic repulsions of the carboxylate groups.

The FTIR-ATR spectrum of EFB presented bands corresponding to cellulose, lignin, and hemicellulose functional groups. Sample pretreatment (AHP) and oxidation reaction eliminated lignin and hemicellulose, as evidenced by the absence of bands at 1732 and 1230 cm^{-1}. Also, the increased intensity of the 1602 cm^{-1} band indicated oxidation of cellulose.

XPS data showed the atomic composition of the EFB surface and how the experimental conditions change the surface composition of TOCNs. XPS and conductimetric titration were complementary techniques, with XPS determining the surface chemistry of TOCNs and conductimetric titration quantifying the carboxylate groups on the surface of the TOCNs.

3. Empty Fruit Bunch Fiber-based Composite Materials for the Heterogeneous Advanced Oxidation of Palm Oil Mill Effluent (POME)

3.1. Abstract

Industrial wastewater discharges, such as Palm Oil Mill Effluent (POME), pose a significant threat to water ecosystems due to their complex composition and high organic load. Current treatment methods, including Advanced Oxidation Processes (AOPs) like the heterogeneous Fenton process, face challenges such as catalyst recovery, recycling, and leaching. The structural and morphological characteristics of residual lignocellulosic biomass from Palm Oil production, particularly Empty Fruit Bunches (EFBs) fibers, offer opportunities for effective nanoparticle deposition and stabilization, suggesting its potential as a support matrix in heterogeneous catalytic processes. In addition, EFB-derived nanocellulose, with its remarkable mechanical, chemical, and thermal properties, could serve as a reinforcing agent in catalytic matrices, potentially improving catalytic activity and minimizing catalyst leaching in composite materials. In this study, we explored the use of EFB fibers as a supporting matrix for magnetite in biocomposites, while also isolating cellulose from EFB to reinforce these composites. The materials were employed for color and phenol removal from treated POME using AOPs. Characterization via XRF, TGA, and SEM revealed the presence of magnetite and nanocellulose in the biocomposites. The delignified fiber biocomposites exhibited exceptional efficiency, achieving over 60% color removal across 9 consecutive reuse cycles. In particular, the frozen-reinforced variant of this biocomposite demonstrated superior performance, exceeding 71% color removal efficiency over ten reuse cycles. Additionally, the introduced reinforcements led to a significant 44%

reduction in iron leaching, enhancing catalytic activity and maintaining removal efficiency. To our knowledge, the feasibility of utilizing nanocellulose to enhance catalytic activity in biomaterials has not been explored, presenting a novel avenue for addressing industrial wastewater treatment challenges effectively and sustainably.

3.2. Introduction

In recent years, growing concerns over industrial wastewater discharge into watercourses are prompting the urgent exploration of strategies to mitigate water pollution (United Nations, 2017). Colombia, a major palm oil producer, faces substantial environmental challenges due to its palm oil extraction process, which generates Palm Oil Mill Effluent (POME) alongside solid lignocellulosic residues (Mesa Dishington & Azuero Garcia, 2021). Approximately 2.5 kilograms of POME are produced per kilogram of palm oil extracted (Lam & Lee, 2011). POME is a complex colloidal suspension containing cellulosic residues, oil, suspended solids, phenols, and natural dyes, characterized by its acidic pH (Althausen, 2016). This effluent poses a significant threat to aquatic ecosystems due to its high organic load and color, which can cause anoxic conditions and inhibit photosynthesis in aquatic organisms (Farhan Hanafi & Sapawe, 2020; Kim, 2021). The complex nature of POME, with high chemical oxygen demand (COD) ranging from 15,000 to 100,000 mg/L, biochemical oxygen demand (BOD) around 42,000 mg/L, pH between 3.5 to 4.2, and elevated temperatures of 80-90°C, presents challenges for its effective treatment (Yashni et al., 2020).

Various treatment methods for POME exist, with the traditional ponding system being the most widely used. POME is circulated amongst a series of ponds where a series of anaerobic and aerobic biological processes decompose organic matter into methane (CH_4)

and carbon dioxide (CO_2). In most cases, this process often results in water exceeding regulatory limits for BOD and color, in addition to generating sludge requiring subsequent treatment (Enström et al., 2019; Cheng et al., 2021,Sani et al., 2020). Thus, in many palm oil-producing countries legal mandates require additional pollutant treatments, such as greenhouse gas capture and residual organic matter and color removal before discharge (Khamparia & Jaspal, 2018).

Advanced Oxidation Processes (AOPs) for pollutant degradation, which *in-situ* generate potent oxidizing agents like hydroxyl radicals, are gaining traction in effluent treatment (Miklos et al., 2018). One notable AOP for POME treatment is the homogeneous Fenton process, where hydroxyl radicals are generated through the reaction of ferrous ions with hydrogen peroxide (H_2O_2) under acidic conditions (Sani et al., 2020; Yashni et al., 2020). Gamaralalage (2019) reported a significant reduction in total organic carbon and degradation of complex high-molecular weight carboxylic acids and phenols to biodegradable acids (formyl, acetic, and phthalic acids) using the homogeneous Fenton process (Gamaralalage et al., 2019). However, challenges arise from the generation of sludge composed of difficult-to-recover iron (III) complexes, hindering catalyst recovery and recyclability (Sani et al., 2020). The heterogeneous Fenton process, using solid catalysts supported on matrices, facilitating catalyst recovery and reuse, is an alternative to enhance treatment efficiency and address these challenges. Numerous studies have investigated the application of heterogeneous Fenton for POME treatment. For instance, Arutani et al. (2020) demonstrated lignin photodegradation from the palm industry using a heterogeneous photofenton/TiO_2 system incorporating iron salts, hydrogen peroxide, and TiO_2 as catalysts. The addition of TiO_2 increased lignin degradation efficiency by 88% (Arutanti et al., 2020).

Additionally, aerated nano zero-valent iron (nZVI) has shown promise for POME treatment, achieving a 75% reduction in COD (Taha & Ibrahim, 2014). However, this method requires a high aeration rate for optimal efficiency (Taha & Ibrahim, 2014). Despite the effectiveness of the heterogeneous Fenton process, a significant drawback is the potential leaching of the catalyst from its support, leading to a gradual reduction in removal efficiency with each recycling cycle (Alle et al., 2021). Alle et al. (2021) synthesized a cellulose foam oxidized with TEMPO and gold nanoparticles (NPs), exhibiting exceptional efficiency in color removal for methylene blue and methyl orange solutions. However, a gradual increase in reaction time and significant leaching of gold were observed, impacting catalytic activity (Alle et al., 2021).

Additionally, a key factor in heterogeneous Fenton processes is the selection of the support matrix. A matrix is required to provide long-term stability, high catalytic activity, usability over a wide pH range, reusability, and ease of separation from the reaction medium (Sani et al., 2020). Some materials utilized in heterogeneous Fenton processes to support iron include zeolites, clay, polymers, silica, fibers, carbon, as well as biodegradable polymers like alginate and chitosan and natural fibers from lignocellulosic biomass (Ribeiro & Nunes, 2021; Sani et al., 2020). These latter materials have received special attention due to their characteristics, biodegradability, and sustainability (Akhtar et al., 2020). The structural and morphological characteristics of lignocellulosic biomass, particularly crevices and irregularities on natural fiber surfaces, provide active sites for nanoparticle deposition. Coupled with substantial surface area and good thermal stability, these materials emerge as ideal candidates for matrices in heterogeneous catalytic processes (Nasrollahzadeh et al., 2021). Previous research has highlighted natural fibers as robust, environmentally friendly matrices conducive to the deposition of metal oxides for water treatment processes. For example, Chacón-Patiño et al. (2013) reported the synthesis of biocomposites using fique fibers and manganese oxides, achieving a 98% oxidation/decomposition of the indigo carmine dye in an aqueous solution. A chemical pre-treatment involving HCl-NaOH was employed to generate superficial $CH_2O\text{-}Na^+$ groups on the fibers surface, facilitating the effective attachment of the manganese oxide precursors to the cellulose (Chacón-Patiño et al., 2013). Similarly, Ravelo-Nieto et al. (2013) investigated the deposition of magnetite on cationized fibers through HCl-NaOH treatments for textile wastewater treatment. The resulting biocomposite removed of 24% COD, 100% of surfactants, 99% color, and 99% turbidity in a real sample wastewater sample from a denim mill (Ravelo-Nieto et al., 2023).

Empty Fruit Bunches (EFB) derived from palm fruit processing are primarily composed of cellulose, lignin, and hemicellulose (Palamae et al., 2017). EFB has found diverse applications as a raw material for ethanol production, reinforcing fiber in cement, raw material for activated carbon production, and paper production (Piarpuzán et al., 2011; Hidayu et al., 2013; Yiin et al., 2019; Haqiqi et al., 2021; Rama Rao & Ramakrishna, 2022). However, with approximately 431,000 tons of EFB produced annually in Colombia the material is traditionally used as compost or fertilizer in plantations (Chang, 2014), Nonetheless, EFB has recently been reported as a support matrix for metal nanoparticles (Akhtar et al., 2020). The porous surface morphology of EFB fibers makes it an effective nanoreactor for metal oxide synthesis and stabilization (Rama Rao & Ramakrishna, 2022). Additionally, with a high cellulose content, EFB can serve as a source of functional nanomaterials such as nanocellulose (Jawaid et al., 2017; Gupta et al., 2013). Nanocellulose exhibits outstanding mechanical, chemical, and thermal properties, including a Young's modulus of 114 GPa, crystallinity ranging between 40% and 89% and thermal decomposition upwards 350 C, that make it a reinforcing agent for strengthening composite materials (Ummartyotin & Manuspiya, 2015). Interestingly, to the extent of our knowledge, the feasibility of utilizing nanocellulose as a reinforcing material to improve the catalytic activity of biomaterials by minimizing catalyst leaching has not been investigated.

Given the significant environmental concerns regarding industrial wastewater discharge, particularly from palm oil extraction processes leading to Palm Oil Mill Effluent (POME) generation and considering that conventional treatment only partially removes the color and organic matter in POME, it necessitates tertiary treatments to effectively reduce and mitigate the impact of these effluents. Therefore, this research is focused on utilizing and leveraging EFB fibers as a magnetite support matrix to provide tertiary treatment for palm industry effluents. Additionally, with the goal of enhancing the catalytic activity of the material, cellulose was isolated from the EFB fibers through oxidation with TEMPO (TEMPO-oxidized cellulose nanofiber, TOCN), and various reinforcement techniques were implemented. We hypothesize that the integration of EFB fibers -iron nanoparticles biocomposites reinforced with nanocellulose also derived from EFB into heterogeneous catalytic processes will enhance treatment efficiency and reduce environmental impact of Palm Oil production. The efficiency and durability of the materials were assessed based on color removal in each reuse cycle.

3.3. Experimental

3.3.1. Materials and Reagents

Hydrogen peroxide (H_2O_2 30 %), sodium hydroxide (NaOH), hydrochloric acid (HCl 37 %), sulfuric acid H_2SO_4 (95 - 97%), iron (II) sulfate heptahydrate ($FeSO_4$*$7H_2O$), toluene, ethanol absolute for analysis, acetic acid glacial 100 %, Nitric acid 65 % were purchased from Merck (Darmstadt, Germany). Iron (III) chloride 6-hydrate ($FeCl_3$*$6H_2O$) and ammonia (30 %) were purchased from PanReac (Darmstadt, Germany). TEMPO (2,2,6,6 tetramethylpiperidine-1-oxyl) radical was purchased from Sigma-Aldrich (Saint Louis, MO, USA). Sodium chlorite 25 % was purchased from sigma-Aldrich (Darmstadt, Germany). Sulfuric acid 95-97 % and calcium chloride dihydrate ($CaCl_2$*$2H_2O$) were purchased from Supelco (Darmstadt, Germany). Aluminum sulphate 18-hydrate PRS $Al_2(SO_4)_3$.18 H_2O was purchased from Panreac (E.U.), and sodium hypochlorite (NaClO 15 %) was purchased from Máster Químicos (Piedecuesta, Colombia) and standardized according to ASTM D2022. Solutions and suspensions were prepared with distilled water. Crude POME samples were collected from the aerobic pool of a Palm Oil Mill water treatment system at Extractora Agroince, Aguachica, Cesar, Colombia (Final discharge from the water treatment system). The POME was flocculated, centrifuged, and acidified prior to utilization. EFB was provided by Extractora Central, Puerto Wilches, Santander, Colombia.

3.3.2. EFB fibers pretreatment.

The EFB fibers were washed with distilled water to remove residues and non-lignocellulosic materials. Subsequently, the clean fibers were dried at room temperature before being utilized as starting materials for the processes described below. Alkaline hydrogen peroxide (AHP) treatment: This treatment facilitates the removal of lignin and a portion of the hemicellulose from the biomass (S. Ovalle-Serrano et al., 2018). 15 g of EFB fibers were immersed in 250 mL of a 10% w/w H_2O_2 solution, and the pH was adjusted to 11.5 using 50 mL of a 4 N NaOH solution. The mixture was left to react for 2 hours at 70°C.

Following the reaction period, the EFB fibers underwent thorough washing and subsequent drying at room temperature. The resulting delignified EFB sample was labeled as EFB-AHP.

NaOH and HCl treatment: In this treatment an alkaline initial step removes lignin, hemicellulose, oils, and waxes, followed by neutralization using HCl (Ouarhim et al., 2018). 10 g of EFB fibers were immersed in a 200 ml 10% w/w NaOH solution for one hour at room temperature. Subsequently, the EFB sample was transferred to a 200 ml 10% w/w HCl solution and allowed to react for one hour at room temperature. Following this treatment, the fibers were washed and dried at room temperature. The samples subjected to the NaOH/HCl treatment were labeled as EFB-NaOH-HCl.

3.3.3. EFB- AHP or NaOH-HCl/ Fe_3O_4 Biocomposite synthesis

In-situ deposition of magnetite (Fe_3O_4) nanoparticles was conducted using the co-precipitation method. An individual sample of any of the three different starting materials (EFB, EFB-AHP, and EFB-NaOH-HCl samples) weighing 10 g was mixed with a 200 mL Fe^{2+}:Fe^{3+} aqueous solution (1:1.2 ratio) and stirred for 10 minutes. Subsequently, approximately 10 mL of 30% ammonia was added dropwise, to promote co-precipitation of Fe^{2+} and Fe^{3+} ions in the form of Fe_3O_4 (Faiyas et al., 2010). The mixture was allowed to stand for 1 hour, followed by washing and drying the fibers at room temperature. The three distinct biocomposites were labeled as EFB-Fe, AHP-EFB-Fe, and NaOH-HCl-EFB-Fe.

3.3.4. Biocomposite reinforcement with EFB-derived nanocellulose

3.3.4.1. Isolation of cellulose nanofibers from EFB. TEMPO oxidation and mechanical disintegration were employed to isolate the nanocellulose from delignified EFBs as previously reported (Martínez-Ramírez et al., 2023). A dispersion of 3mm pieces of AHP-EFB fibers (1 g) in 100 mL wate was mixed with 40 mL of a solution containing 0.016 g

TEMPO and 0.1 g NaBr. Sodium hypochlorite (NaClO) was added dropwise to the mixture, maintaining a cellulose:NaClO molar ratio of 1:8. The mixture was stirred and subjected to ultrasonic treatment (40KHz, 130 W) for 2 hours, maintaining a pH of 10.5 by addition of HCl or NaOH 6 N solutions. After stabilizing the pH at 10.5, the reaction was quenched with ethanol, followed by centrifugation (5000 rpm, 10 minutes). The resulting nanocellulose pellet was rinsed repeatedly with water until neutral pH. The pellet was dispersed in water and subjected to sonication using an Ultrasonic Processor (Sonics vibra-cell -VC750, 20 kHz, 750-Watt) for 10 minutes using ON/OFF cycles 1:1 sec cycle. The resulting cellulose nanofibers were labeled as TOCN (TEMPO-oxidized cellulose nanofiber) and stored refrigerated until use. The EFB-Fe, AHP-EFB-Fe, and NaOH-HCl-EFB-Fe biocomposites were reinforced using TOCN by soaking, coagulation, and directional and non-directional freezing techniques.

3.3.4.2. Reinforcement by soaking. Soaking represents the simplest form of creating a TOCN layer on the biocomposite surface. The biocomposites (0.5 g) were immersed in 10 mL of 0.2% TOCN for 1 hour and dried at 100 °C. Biocomposite materials subjected to this method were labeled as S-EFB-Fe, S-AHP-EFB-Fe, and S-NaOH-HCl- EFB-Fe. Literature reports suggest using low concentrations of TOCN to prevent the blockage of surface-active sites on the biocomposite surface (Ghasemi et al., 2018; Jabbar et al., 2020).

3.3.4.3 Reinforcement by coagulation. The biocomposite materials (0.5 g) were immersed in 10 mL of 0.2% TOCN for 1 hour, followed by the addition of 10 mL of 5% $CaCl_2$, leading to gel formation. After 1 hour, the material was washed, dried at 100 °C, and labeled as C-EFB-Fe, C-AHP-EFB-Fe, and C-NaOH-HCl- EFB-Fe. Calcium cations act as cross-linkers between nanocellulose chains, enhancing their stability (H. Xu et al., 2020).

3.3.4.4 Reinforcement by non-directional freezing. Freeze-induced crosslinking aims to increase the adhesion between alcohols, aldehydes, and carboxylate groups at the TOCN surface (Erlandsson et al., 2018). The biocomposite materials (0.5 g) were immersed in 10 mL of 0.2% TOCN for 1 hour, then frozen for 5 hours, thawed with 10 mL acetone (every 20 minutes for a total of one hour), and dried at 100 °C. The samples subjected to this type of reinforcement were labeled as F-EFB-Fe, F-AHP-EFB-Fe, and F-NaOH-HCl-EFB-Fe.

3.3.4.5. Reinforcement by directional freezing. Directional freezing is a controlled freezing process in which ice crystals grow in an ordered, aligned, and uniform manner (L. Liang et al., 2019). The biocomposite samples (0.5 g) were immersed in 10 mL of 0.2% TOCN for 1 hour. Directional freezing was achieved by placing the biocomposite samples (contained in a ziploc bag) within a cooler filled with water (Shafique et al., 2016). After 19 hours in the freezer at -17 °C, the samples were gradually thawed, over a 3-hour period, adding 10 mL of ethanol every 30 minutes. The reinforced biocomposites were dried slowly at 50 °C for 5 days. The resulting materials were labeled as DF-EFB-Fe, DF-AHP-EFB-Fe, and DF-NaOH-HCl-EFB-Fe. Directional freezing was confirmed by comparing ice crystal patterns between directional and non-directional freezing processes. To confirm the directional freezing effect, water and TOCN were frozen through both directional and non-directional processes. Non-directional freezing cause random crystal formation observed as opaque solid ice and TOCN samples, whereas directional freezing produced aligned crystals resulting in transparent solid ice and patterned crystals in TOCN.

3.3.5. POME color removal tests

The as-received POME sample was flocculated at 25°C with aluminum sulfate using a jar test set-up. The flocculated POME was centrifuged, acidified with HCl, and labeled pretreated POME. A 2^3 factorial design was employed to test the biocomposite materials performance towards color elimination from pretreated POME. Biocomposite and H_2O_2 aqueous solution (30%) amounts, and pretreated POME pH were considered as the experimental variables (Appendix K). Color removal from pretreated POME was selected as the response variable and the measurements were taken at three wavelengths according to the ISO 7887:2011 method B (International Organization for Standardization ISO, 2011), as stipulated in Resolution 631 of 2015 by the Ministry of Environment and Sustainable Development. The color removal tests involved placing 20 mL of pretreated POME at acidic pH in contact with the biocomposite sample, followed by addition of H_2O_2. The reaction ran for 2 hours at 50°C. Statistical analysis utilized STATGRAPHICS 18 software. Color removal percentage was calculated using the equation 6.

$$Color\ removal\ [\%] = \frac{C_i - C_f}{C_i} * 100\ (6)$$

Where C_i and C_f are the color values (436 nm) before and after POME treatment with the EFB-Fe_3O_4 biocomposites.

3.3.5.1. Reuse cycles. The biocomposites' performance was evaluated by repeatedly using the same composite sample to treat multiple fresh, pretreated POME samples for color removal. After each removal cycle, the biocomposite sample was taken from the POME solution, washed with water, and air-dried at room temperature for 24 hours. The dried material was then used for subsequent POME treatment cycles, maintaining consistent initial reaction conditions throughout. This approach enabled the assessment of the impact of fiber pretreatments and biocomposite reinforcements on color removal from pretreated POME. Color removal processes and reuse cycles were conducted in triplicate, and the standard deviation was determined for all reported measurements.

3.3.6. EFB and biocomposite materials characterization

Moisture, ash, ethanol-toluene soluble matter, lignin, cellulose, and hemicellulose contents were determined for both raw and treated fibers (AHP and NaOH/HCl) using standardized methods: NREL-TP-510 42621, NREL-TP-510 42622, ASTM-D1107, TAPPI 222 Kurscher and Hoffer Method, and Method of Jayme-Wise, respectively (ASTM International, 2013; Yao, 2012; Sluiter et al., 2008; Hessler & Merola, 1949).

The morphology, composition, and thermal properties of EFB, EFB-AHP, EFB-NaOH-HCl, EFB-Fe, EFB-AHP-EFB-Fe, and NaOH-HCl-EFB-Fe samples were characterized using SEM, SEM-EDS, XRF, and TGA. Field Emission Scanning Electron Microscopy (FESEM) images were obtained using a QUANTA FEG 650 at 30 kV accelerating voltage, equipped with secondary electron (SED), Everhart Thornley (ETD), and backscattered electron (BSE) detectors. Energy dispersive spectroscopy (EDX) was performed with an APOLO X detector with 126.1 eV (in. Mn Kα) resolution and Genesis software, providing semi-quantitative information on chemical elements. XRF analysis was conducted using an S8 TIGER BRUKER instrument to identify elements from Na to U under a helium atmosphere, employing the Quant Xpress method. Thermogravimetric analysis (TGA) was conducted with a NETZSCH STA 449 F5 Jupiter equipment, utilizing a heating ramp of 10 (°C/min) from 32 °C to 600 °C, and a 50 mL/min flow of N_2. Prior to measurements, three system purges were performed. The reinforced biocomposites were characterized using a JEOL-JSM 6490LV Electron Microscope equipped with secondary electron (SEI) and backscattered electron (BES) detectors. The color of POME before and after treatment was determined at three wavelengths following ISO 7887:2011 method B using a UV-vis Thermo Scientific Evolution 300 spectrophotometer. COD was measured according to SM 5200 ed 22/2012. Triplicate measurements of color and COD were performed. Total solids (TS) and total suspended solids (TSS) of POME were determined according to SM 2540 B and 2540 D, respectively. Phenol content was determined in accordance with SM 5530 D. The elemental iron content of POME was determined by inductively coupled plasma optical emission spectroscopy (ICP-OES) using a PerkinElmer ICP-OES Avio 220 max instrument. The colorimetric method with phenanthroline (SM 3500-Fe B) was employed to determine the total iron content in POME treated with unreinforced and reinforced biocomposites.

3.4. Results and Discussion

3.4.1. Raw and treated EFB fibers characterization

Figure 17 presents the changes in lignocellulosic composition from raw to treated fibers after AHP and NaOH-HCl treatments. In natural fibers these chemical processes allow cellulose exposure and surface activation facilitating surface modification. Pre-treatments of natural fibers can involve cleaning the surface, modifying it chemically, preventing moisture absorption, and increasing surface roughness, thereby increasing the availability of active hydroxyl groups. These processes contribute to enhancing the interfacial adhesion between the fiber and other compounds (Kalia et al., 2009; Verma et al., 2020). Both processes effectively increase moisture in the EFB fibers, while decreasing its ash and ethanol-toluene soluble matter contents. The AHP and NaOH-HCl processes utilize alkaline conditions, which are known for solubilizing lignin and hemicelluloses (Ouarhim et al., 2018; Yoshida & Prudencio, 2020). These processes also disrupt hydrogen bond networks in natural fibers, exposing hydroxyl groups to moisture absorption, thereby increasing the fiber's hydrophilicity (Asim et al., 2020). In our case, the treated fibers displayed a 110% increase in moisture content. A noticeable decrease in ash and ethanol-toluene soluble compounds by approximately 43.7% and 71.5%, after the AHP and NaOH/HCl treatments respectively, suggest the removal of inorganic and organic compounds, and residual oil traces. Regarding structural carbohydrate content, the AHP treatment removed a higher percentage of lignin (47.9%) compared to the NaOH-HCl treatment (23.0%), resulting in bleaching of the EFB fibers as seen in Figure 10. Compared to the raw EFB fibers, the cellulose content increased 18.6% in EFB-AHP and 3.5% in EFB-NaOH-HCl, while hemicellulose increased 5.0% and 13.2%, respectively. Overall, the AHP and NaOH/HCl treatments caused significant compositional alterations within the fibers. Literature reports a wide range of ash, moisture, and structural carbohydrate contents in EFB (Chang, 2014; Chong et al., 2017). This compositional variability can be attributed to diverse factors including climate, soil conditions, geographical location, growth phase, and crop age(Chang, 2014). Furthermore, the variations are intensified by the quantification methods selected for analysis (TAPPI or NREL). In a comprehensive compositional review Chang et al. reported a range of 2.4 - 14.2% moisture, 1.3 - 16.6% ash, 3.2 - 3.7% extractives, 23.7 - 65.0% cellulose, 14.1 - 30.4% lignin, and 20.5 – 33.5% hemicellulose in EFB fibers (Chang, 2014). The results shown in Figure 10 fall within these ranges.

Biomass pretreatment processes are typically applied to lignocellulosic feedstocks to isolate specific biopolymers or biomass fractions before hydrolysis (for secondary biofuel production), pulping (paper/cardboard production), nanomaterials isolation (nanocelluloses, nanolignins), or surface activation (biocomposite synthesis). The effects of various preprocessing strategies on EFB composition are well-documented in the literature (Alvarez-Vasco & Zhang, 2017; Ho et al., 2019; Latip et al., 2018). For instance, Palamae et al. (2014) observed the removal of lignin (53.0 %) and hemicellulose (35.1 %) from EFB fibers after AHP treatment, while cellulose increased by 62.2% (Palamae et al., 2014). Additionally, in 2017, the same group reported high lignin removal (92.0 %) and hemicellulose (69.4 %), accompanied by a 189.3% increase in cellulose content via AHP treatment. The authors used an incubator to react EFB for 12 hours with a hydrogen peroxide and 4% NaOH solution at 20 °C or 40 °C (Palamae et al., 2017). Alkaline treatments similarly disrupt the hydrogen bonds in lignocellulosic compounds, resulting in the removal of lignin, waxes, and oils from natural fibers. This process enhances surface roughness, increases the availability of OH-groups, and aids in defribrilation of the fiber's macrostructure increasing surface area (X. Li et al., 2007; Ouarhim et al., 2018). Sudiyani et al. (2010) treated EFB with 1N NaOH at 30 °C for 90 minutes and observed removal of lignin (32.9 %) and hemicellulose (25.5 %) and increase in cellulose by 46.7% (Sudiyani et al., 2010). We observe that the AHP treatment removes more lignin than the NaOH-HCl treatment.

The AHP and NaOH/HCl treatments induced morphological and chemical alterations on the EFB's surfaces, as depicted in the micrographs (Figure 17). Carbon and oxygen were found to be the predominant components in EFB, consistent with the lignocellulosic nature of the material. Untreated EFB fibers exhibited well-defined micrometric-sized pores, some filled with SiO_2 particles. These SiO_2 particles persisted post-AHP treatment. However, NaOH/HCl treatment effectively eliminated SiO_2 from the fiber surface, corroborating previous findings (Khalili et al., 2018). SiO_2 in EFB fibers originates from soil minerals and is located within the pores and internal cavities of the cell wall (Khalil et al., 2008; Wong et al., 2020), serving primarily as a defense mechanism against microbiological and biological attacks (Yunus et al., 2010). Both treatments lead to smoother and more porous surfaces compared to untreated EFB fibers (X. Li et al., 2007). As discussed before, fiber chemical pretreatments increase surface area and functional group availability, facilitating surface modification for biocomposite production (X. Zhang et al., 2018; Nasrollahzadeh et al., 2021). Importantly, neither treatment compromised the mechanical integrity of the fiber.

Figure 17. Composition, images and micrographs of EFB, AHP-EFB, and NaOH-HCl-EFB

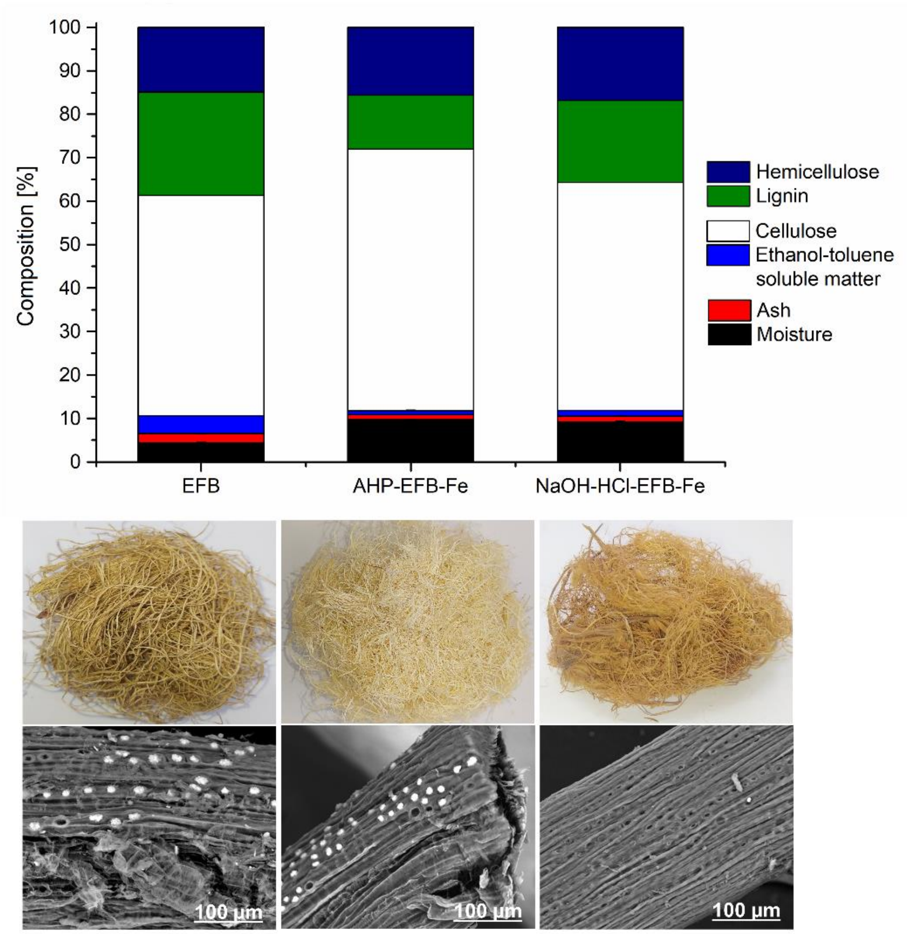

The elemental compositional analysis conducted via X-ray fluorescence (XRF) directly on the EFB fibers, detailed in Table 10, reveals silicon as the most abundant inorganic component in both untreated and treated fibers. The treatments significantly alter the content of various compounds and elements, including potassium, calcium, magnesium, sulfur, phosphorus, aluminum, iron, chlorine, and silicon. Notably, the NaOH-HCl treatment demonstrates higher efficiency in removing elemental compounds compared to the AHP treatment. SEM observations corroborate the absence of surface SiO_2 in EFB NaOH-HCl fibers, contrasting with XRF results, indicating the presence of SiO_2 particles in internal cavities (Yunus et al., 2010). This observation suggests that NaOH/HCl treatment primarily targets surface SiO_2. On the other hand, the increase in sodium in treated fibers is likely related to residual sodium from the alkaline treatments. Furthermore, in literature, a common research practice involves XRF analysis on EFB ashes not fibers. In EFB ashes, reports indicate high potassium content, followed by silicon and calcium, along with low concentrations of chlorine, iron, aluminum, sodium, magnesium, and phosphorus, akin to our results on whole fibers (Konsomboon et al., 2011; Mohammed et al., 2012).

The thermal behavior of raw and treated EFB, plotted in Figure 18, reveals distinctive pyrolysis patterns characteristic of natural fibers. The weight loss in the temperature range of 60-150 °C corresponds to moisture release, with treated fibers exhibiting higher water content, a characteristic also observed in compositional analysis (Asim et al., 2020). Subsequent stages involve hemicellulose (220-315 °C), cellulose (315-400 °C), and lignin (160-900 °C) decomposition (H. Yang et al., 2007). EFB and EFB-NaOH-HCl exhibit two decomposition peaks at 291 °C and 330 °C indicating some residual lignin in the material after the NaOH-HCl process. In contrast, AHP-EFB shows a single peak at 321 °C suggesting less lignin in the material (Figure 18b). This finding aligns with Álvarez et al. (2006), who observed a single peak below 365 °C for alkali-treated jute fibers, attributed to lignin and hemicelluloses removal (Álvarez et al., 2006). Similarly, Ovalle-Serrano et al. (2018) noted two decomposition peaks for fique and a single, lower-temperature peak for delignified fique, emphasizing the elimination of amorphous structures (lignin) through delignification processes (S. Ovalle-Serrano et al., 2018). The presence of a single peak between 300 and 400 °C in delignified fibers (AHP) underscores the effectiveness of the delignification process.

Table 10. Elemental composition by FRX of EFB, AHP and EFB-NaOH-HCl

Compound	**Content of compound by weight [%]**		
	EFB	**EFB-AHP**	**EFB-NaOH-HCl**
K_2O	1.30	0.03	0.01
SiO_2	1.95	1.61	1.03
Cl	0.27	0.03	0.23
CaO	0.30	0.28	0.05
MgO	0.29	0.13	0
SO_3	0.27	0	0.11
P_2O_5	0.24	0.04	0
Al_2O_3	0.03	0	0.02
Fe_2O_3	0.02	0	0
Na_2O	0	0.97	0.15
Lignocellulosic compounds	95.32	96.91	98.40

*Cellulose is used as the quantification matrix.

Figure 18. Thermal analysis of EFB, EFB-AHP, and EFB-NaOH-HCl, a) TGA, b) DTG curves

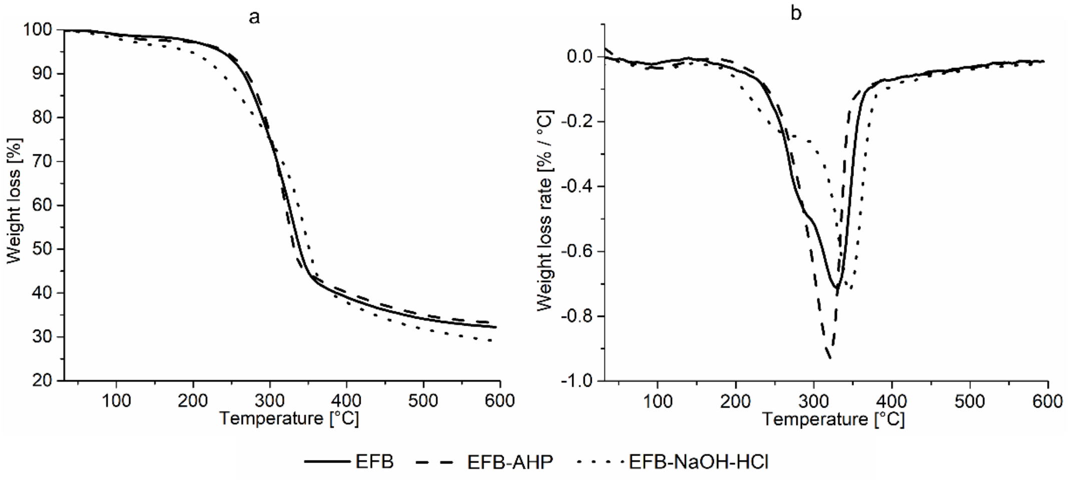

3.4.2. EFB-Fe3O4 biocomposites Characterization

The synthetic approach used for Fe_3O_4 involves the simultaneous co-precipitation of ferrous and ferric ions from iron hydroxides mediated by a strong base as illustrated in Figure 19 (Gupta, 2005; Ravelo-Nieto et al., 2023). The biocomposites containing Fe_3O_4 nanoparticles have a darker coloration compared to the original EFB fibers shown in Figure 17. Iron oxides exhibit highly pigmented properties, manifesting in colors ranging from red, yellow, and orange to brown, even in small amounts (Bigham & Schulze, 2002). Iron oxide biocomposites from AHP-EFB fibers are orange, while EFB-NaOH-HCl composites are dark brown. This color variation is attributed to the surface of treated fibers having accessible OH-groups for potential electrostatic and H-bonding interactions and stabilization of both precursors and magnetite particles (A. K. Gupta & Gupta, 2005; Liu et al., 2008; Ravelo-Nieto. Additionally, studies have reported that the interaction between natural fibers and Fe_3O_4 occurs through ion-dipole interactions between the iron atoms and the electron-rich oxygen atoms (Z. Lou et al., 2021).

Figure 19. In situ Fe_3O_4 coprecipitation on EFB fibers, a) EFB-Fe, b) AHP-EFB-Fe, c) NaOH-HCl-EFB-Fe, and d) diffraction pattern of the synthesized magnetite.

$$2FeCl_3 \cdot 6H_2O + FeSO4 \cdot 7H_2O + 8NH_3 \rightarrow Fe_3O_4 + 6NH_4Cl + (NH_4)_2SO_4 + 15H_2O$$

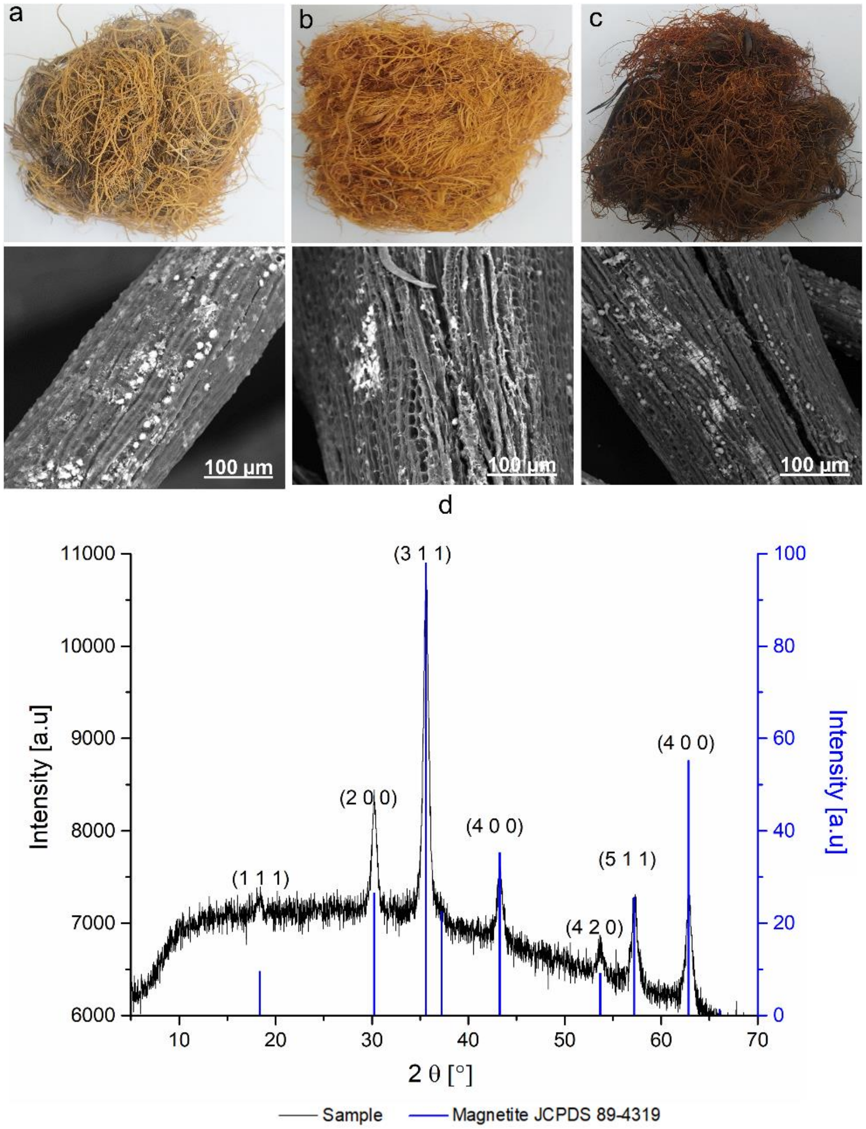

The observed difference in coloration also suggests varying magnetite concentrations in the biocomposites, with NaOH-HCl-EFB-Fe exhibiting the darkest color, potentially indicating the highest magnetite content, followed by EFB-AHP-EFB-Fe with an intermediate color, and finally EFB-Fe with the lightest color. Additionally, the diffractograms of the biocomposites, unfortunately, did not enable the identification of magnetite due to the significant amount of noise present. Consequently, the synthesis of iron oxides was conducted without the addition of fibers. The X-ray diffraction analysis confirmed the successful synthesis of magnetite, as evidenced by characteristic signals at 2θ values of 18.3° 30.1°, 35.4°, 43.0°, 53.4°, 56.9°, and 62.5°. These peaks correspond to the cubic single phase of magnetite, denoted as (111), (220), (311), (400), (422), (511), and (440), respectively card JCPDS # 89-4319 (Mo et al., 2011; Ravelo-Nieto et al., 2023).

The presence of magnetite in the biocomposites was examined via SEM analysis (Figure 19). Iron and silicon oxides appear as high-contrast areas in micrographs taken with a BSED detector. EDS results demonstrate increased oxygen and iron content in the biocomposites relative to their matrices, attributed to magnetite presence. Magnetite nanoparticles tend to aggregate or agglomerate during in situ synthesis. However, the inclusion of SiO_2 enhances stability, thus reducing this agglomeration, while the magnetite covers these SiO_2 particles (Wu et al., 2011; Fuentes-García et al., 2018). Also, SEM images from Khandanlou et al., show cellulose-magnetite biocomposites synthesized by co-precipitation exhibiting magnetite agglomerations on the surface (Khandanlou et al., 2013; Kaco et al., 2017; Qin et al., 2022). XRF elemental compositions in Table 11, show EFB-Fe with high SiO_2, Al (88%) and Na contents and significant reductions in K (97%), Mg (79%), Cl (55%), and P (66%). AHP-EFB-Fe and EFB-NaOH-HCl are characterized by iron as the predominant inorganic element. AHP-EFB-Fe shows a 70% increase in Cl and decreased Ca (64%), Mg (76%), and Na (82%) compared to its matrix, EFB-AHP. In NaOH-HCl-EFB-Fe, Na and Cl contents decrease by 47% and 65%, while Ca and S contents increase by 69% and 71%, respectively, in contrast to the matrix EFB-NaOH-HCl. These changes in inorganic content are linked to the use of iron chlorides and sulfates, as well as ammonia, during magnetite co-precipitation, influencing surface chemistry based on each matrix's characteristics. The bionanocomposites' iron content was determined to be 1.8%, 2.54%, and 3.0% for EFB-Fe, AHP-EFB-Fe, and NaOH-HCl-EFB-Fe, respectively. Thus, higher levels of iron in darker biocomposites were confirmed by XRF measurements. These findings suggest that the NaOH/HCl treatment more efficiently exposes the EFB fiber’s surface to interactions with iron salt precursors, resulting in an increased amount of Fe_3O_4 deposition (Ouarhim et al., 2018).

Table 11. Elemental composition by XRF of EFB-Fe, AHP-EFB-Fe and NaOH-HCl-EFB-Fe

Compound	**Content of compound by weight [%]**		
	EFB-Fe	**AHP-EFB-Fe**	**NaOH-HCl-EFB-Fe**
K_2O	0.04	0.03	0.03
SiO_2	2.25	1.68	1.57
Cl	0.12	0.10	0.08
CaO	0.22	0.17	0.16
MgO	0.06	0.03	0.03
SO_3	0.31	0.14	0.38
P_2O_5	0.08	0	0.03
Al_2O_3	0.25	0.08	0.07
Fe_2O_3	1.80	2.54	3.00
Na_2O	0.07	0.17	0.08
ZnO	0.03	0.05	0.06

*Cellulose is used as the quantification matrix.

The presence of magnetite does not alter the thermal behavior of the biocomposites, as depicted in Figure 20. Thermograms display distinct pyrolysis patterns typical of natural fibers, including water loss and the decomposition of cellulose, hemicellulose, and lignin, as mentioned earlier. Minor variations were observed in the DTG curves, with a 5 °C shift in maximum temperature for the NaOH-HCl-EFB-Fe biocomposite, 15 °C for EFB-Fe, and 24

°C for AHP-EFB-Fe compared to each fiber without magnetite. Furthermore, the impact of magnetite on thermograms is noticeable only at temperatures exceeding 700 °C as has been previously reported (Azizi, 2020; W. Yang et al., 2020).

Figure 20. Thermal analysis of EFB-Fe, AHP-EFB-Fe, and NaOH-HCl-EFB-Fe , a) TGA, b) DTG curves

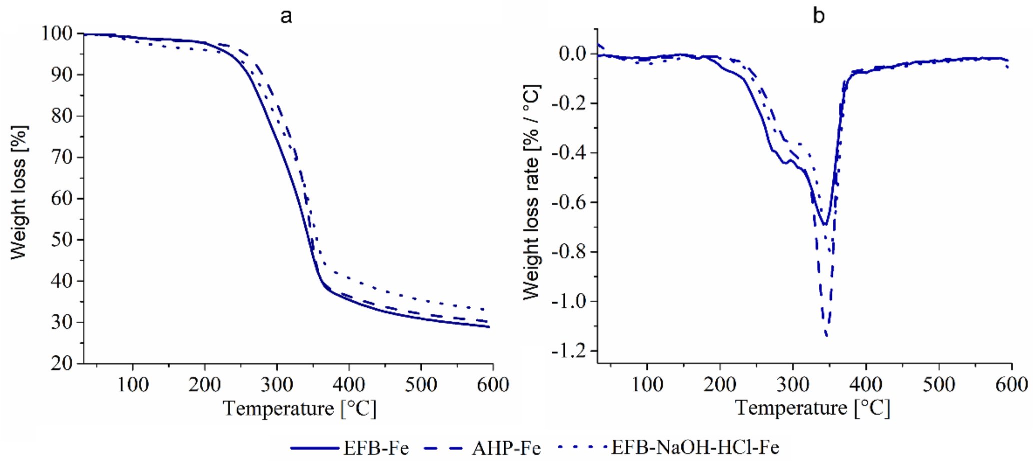

Literature reports and our published data indicate that biocomposites utilized in heterogeneous oxidation processes often experience leaching of the active material from the matrix surface due to the aggressive conditions of these processes. We hypothesize that surface reinforcement with cellulose nanofibers could control Fe_3O_4 leaching and enhance the reusability of the biocomposite. To this end, we isolated cellulose nanofibers from EFB via TEMPO oxidation and deposited the nanomaterial on the biocomposite surfaces using various techniques (soaking, coagulation, non-directional freezing and directional freezing). The TOCNs used in the reinforcement processes have DO of 0.280 ± 0.004 and zeta potential of -57.3 ± 0.1. TOCN was employed at neutral pH, with surface hydroxyl, aldehyde, carboxylate, sodium and silicon groups previously identified by X-ray photoelectron spectroscopy (XPS) (Appendix L). Figure 21 shows EFB-Fe_3O_4 composites reinforced with TOCN via soaking, coagulation, non-directional freezing, and directional freezing. The reinforced materials have both macroscopic and microscopic differences in appearance compared to the "naked" biocomposites seen in Figure 19. The materials in Figure 21 have a smoother surface, which is a result of TOCN acting as a filler or outer layer. Cellulose has been successfully used as a surface reinforcement and filler material, increasing the mechanical properties of the reinforcement matrix (Bhatnagar & Sain, 2005; Jabbar et al., 2020; Jawaid et al., 2017; Peng et al., 2020). Applying TOCN on the surface of EFB leads to efficient coverage of iron and silicon oxides. This is evident from the SEM images in Figure 21, captured using the BSED detector, showing the absence of the high-contrast regions expected for heavy elements (Batista et al., 2018). Instead, the covered nanostructures appear as protruding areas, particularly in the biocomposites treated via directional freezing. Additionally, the reinforcements were carried out at neutral pH. It is important to note that the point of zero charge of magnetite is between 6 and 6.8, meaning that the surface of magnetite carries a negative surface charge due to the presence of hydroxyl groups (Petrova et al., 2011). Therefore, the interaction between each biocomposite's surface and TOCN is specific, attributed to the varied presence of hydroxyl, aldehyde, carboxylate, and Fe_3O_4 groups on each biocomposite surface. The interactions between the carboxylate and hydroxyl groups of cellulose with Fe_3O_4 occur through monodentate and bidentate interactions (Anushree & Philip, 2019; Fan et al., 2019).

In soaking reinforcement TOCN is observed as a thin layer; at the microscopic level, the surface of S-EFB-Fe appears rougher, while S-AHP-EFB-Fe has a smoother surface than the others. In S-NaOH-HCl-EFB-Fe, TOCN fibers are visible on the fiber surface. Soaking represents a straightforward and cost-effective method for reinforcing and/or covering matrices. For instance, Dai et al. reported the reinforcement of hemp fibers with nanocellulose derived from hemp fibers, resulting in a 36% increase in modulus, 73% in tensile stress, and 68% in tensile strain (Dai et al., 2013). Tarrés et al. demonstrated the enhancement of mechanical properties through enzymatic nanocellulose coating with TEMPO oxidized cellulose nanofibers, fostering improved inter-fiber hydrogen bonding and TOCN retention on the cellulose surface (Tarrés et al., 2016). In a different approach, Jabbar et al. reported the spray coating of a 2% w/w nanocellulose solution on alkali-treated jute, followed by drying at 80 °C for 2 hours. The resulting SEM images displayed nanocellulose adhesion to the jute fiber, leading to a 22% increase in tensile strength, 39% in tensile modulus, 24% in flexural strength, and 48% in flexural modulus compared to unreinforced and untreated jute (Jabbar et al., 2020).

In coagulation reinforcement denser pieces of TOCN can be observed; the micrographs show that all three biocomposites have a rough surface and contain TOCN fibers. The process of cellulose regeneration through coagulation bath using aqueous electrolytes induces gelation through ion exchange. The concentration and type of electrolyte play a crucial role in influencing the surface charge, interaction energy, and dissociation of the fibrils, ultimately impacting the interfibrillar aggregation of cellulose (Singh et al., 2015; L. Wang et al., 2019; H. Xu et al., 2020). Medronho and Lindman proposed that cellulose regeneration initiates when the environment becomes energetically unfavorable due to the addition of electrolytes. This leads to hydrophobic interaction of the glucopyran rings, facilitating their subsequent alignment by hydrogen bonds to form monomolecular sheets (Medronho & Lindman, 2015). Generally, cellulose regeneration results in an increase in its mechanical properties, contingent upon the drying process, type of coagulant, temperature, and time (S. Wang et al., 2016). Q. Xu et al. reported the synthesis of transparent and resistant cellulose films using $ZnCl_2$ and $CaCl_2$. Zn^{2+} ions solubilize cellulose by breaking intramolecular hydrogen bonds, while Ca^{2+} cross-links the Zn-cellulose bonds, leading to improved mechanical properties. Tensile strength increased by 250% when $CaCl_2$ was used, suggesting that coagulation enhancement produces ordered sheets of TOCN linked by intra- and intermolecular hydrogen bonds (Q. Xu et al., 2016). Additionally, Sailah et al. utilized cellulose from EFB to produce cellulose/PVA/alginate composites, reinforcing the filament through spinning in a $CaCl_2$ solution. Electron micrographs demonstrated the presence of cellulose and improved mechanical properties of the composite, attributed to the formation of a network between cellulose, PVA, and alginate through strong hydrogen bonds. They revealed that increasing the $CaCl_2$ concentration enhanced the thermal and crystalline properties of the biocomposite but decreased mechanical properties due to calcium saturation (Sailah et al., 2022).

A thicker layer of TOCN is evident in freezing and directional freezing. Micrographs reveal that the surface of biocomposites reinforced by directional freezing tends to be more homogeneous than those obtained by non-directional freezing. In the case of F-EFB-Fe, the surface is notably rough compared to DF-EFB-Fe. This homogeneity is attributed to the higher degree of ordering of the TOCN obtained through directional freezing (Y. Chen et al., 2019). The freezing reinforcement method offers two variations, fast freezing, referred to as non-directional freezing, where impurities are trapped in ice crystals, and slow cooling, known as directional freezing. In the case of directional freezing, the gradual cooling allows water molecules to align more orderly through hydrogen bonding (Shafique et al., 2016).

This freeze-induced crosslinking has been applied to nanocellulose containing aldehyde and carboxylate groups. For instance, Erlandsson et al. synthesized cellulose aerogels oxidized with sodium periodate, involving freezing, solvent exchange with acetone, and drying. Aldehydes derived from periodate oxidation facilitate the formation of hemiacetal bonds between nanocellulose during freezing, resulting in a three-dimensional cross-linked nanocellulose structure that can be dried under ambient conditions through solvent exchange, such as acetone-water. Moreover, the pore size and uniformity of the aerogel are proportional to the number of aldehyde groups present (Erlandsson et al., 2018). Similarly, Chen et al. reported aerogels containing 5% w/w TOCN and compared non-directional freezing (F) with directional freezing using ethanol (DF). The primary distinction between the materials lies in their morphology, with the directional-frozen aerogel exhibiting a more uniform morphology and homogeneous pore size compared to the non-directional-frozen aerogel (Y. Chen et al., 2019).

While the primary goal of reinforcement is typically to enhance mechanical properties, the focus in this study is on leveraging hydrogen bonding interactions and electrostatic forces between the hydroxyl, aldehyde, and carboxylate groups of EFB and TOCN, along with the magnetite present (Scheme 2). This unique strategy aims to form three-dimensional networks of TOCN on the surface, preventing the leaching of magnetite and enhancing material durability. This, in turn, increases the number of reuse cycles in POME treatment. Nanocellulose, including TOCN, is a versatile and effective reinforcement material. Previous studies have demonstrated its capability to establish rigid networks interconnected by hydrogen bonds between the hydroxyl groups of nanocellulose and the

OH- groups of the fiber (Dai et al., 2013; Jabbar et al., 2020; Juntaro et al., 2007; Kargarzadeh et al., 2017).

Figure 21. Optical and SEM images of various EFB biocomposites. The cartoon illustrates the reinforcement process

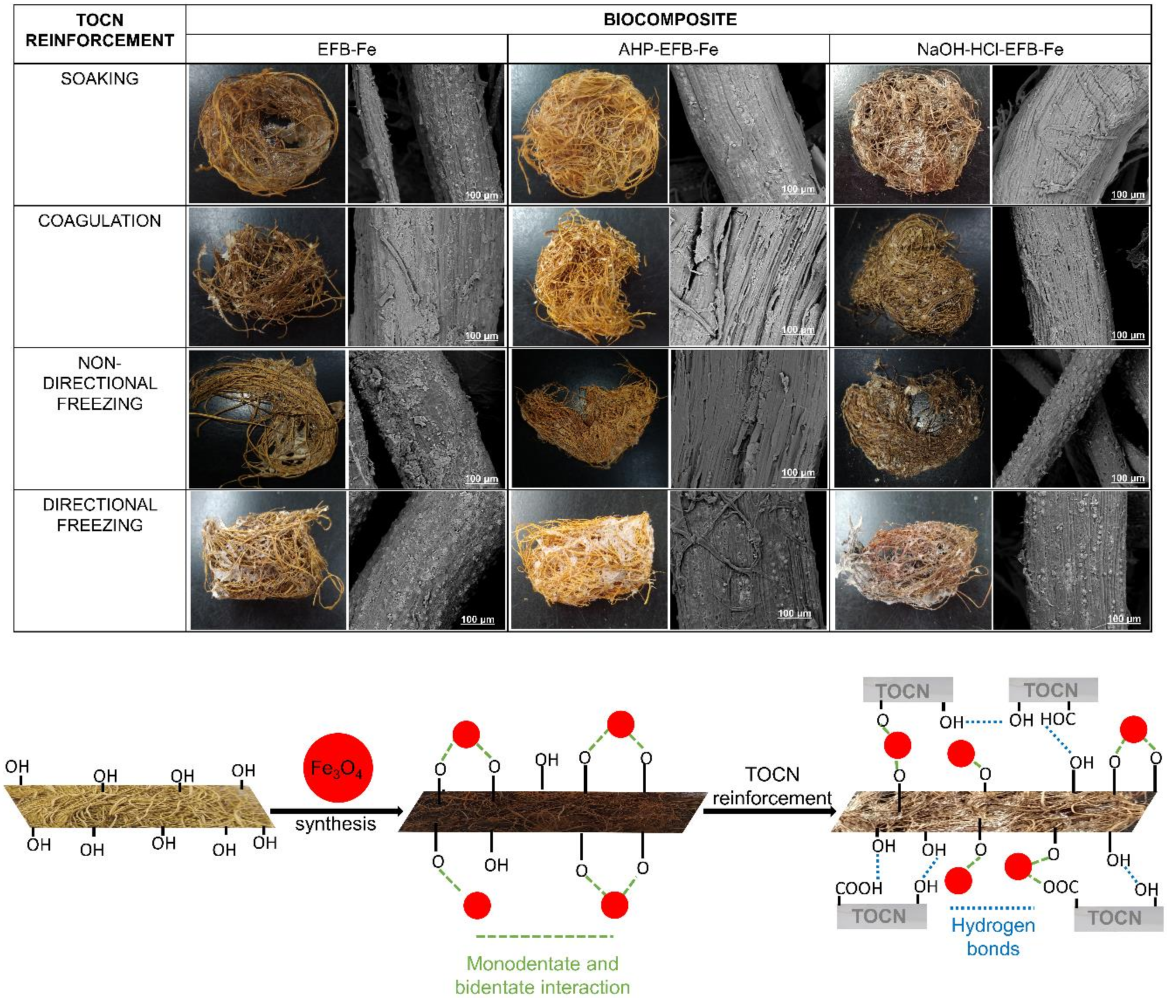

3.4.3. POME treatment with EFB-Fe3O4 biocomposites.

In palm oil production, treating POME is essential for mitigating environmental pollution, ensuring regulatory compliance, promoting resource recovery, supporting sustainable practices, and safeguarding public health and community livelihoods. The traditional ponding system includes an anaerobic pond, a facultative pond, and an aerobic pond, where different types of bacteria break down the organic matter in the POME. Despite its effectiveness in reducing COD, these systems have limitations, such as the need for long retention times and large implementation areas (Althausen, 2016; Yashni et al., 2020). Table 12 compares POME color, COD, and total suspended solids (TSS) for as received, acidified, and acidified/flocculated samples. Raw POME samples, as received from the mill ponding system, are basic, strongly colored, and contain high amounts of suspended solids and organic matter. Upon acidification with H_2SO_4 to pH 3, the pH required to carry out the heterogeneous Fenton reaction with the EFB-Fe_3O_4 biocomposites, only the TSS changes significantly (with a slight color reduction) because of tannins and dissolved lignin precipitation as has been previously reported (Ismail et al., 2020). POME flocculation significantly reduces all water quality parameters: color by 11.3, COD by 48.3, and TSS by 98%, respectively. Flocculation is a widely recognized and cost-effective method for eliminating suspended solids from wastewater. However, primary, and secondary water treatment processes are inefficient in removing dissolved pollutants. Therefore, tertiary treatments like advanced oxidation processes are necessary to degrade pollutants that conventional methods cannot destroy (Bello & Abdul Raman, 2017; Ng et al., 2016). Flocculated POME retains a certain level of color that requires removal to prevent negative impacts on biota and aquatic systems (Sani et al., 2020). POME color is linked to the presence of soluble recalcitrant species, including oxidated fatty acids, humic acids, lipids, tannins, carotenes, and phenolic compounds (Bello et al., 2013; Khongkliang et al., 2023; Sani et al., 2020) Consequently, the implementation of tertiary treatments, such as our biocomposites, becomes imperative for effectively reducing watercolor.

Table 12. POME characterization

Parameter		**POME sample**		
		pH 8* 	pH 3** 	Flocculated/pH 3** 
Color [m^{-1}]	436 nm	621.2 ± 2.3	558.6 ± 2.8	78.3 ± 1.2
	525 nm	370.0 ± 1.8	346.4 ± 2.5	29.0 ± 1.4
	620 nm	248.1 ± 2.2	237.2 ± 2.6	13.4 ± 1.0
COD [mg/L]		>1400	>1400	827.0 ± 4.5
Total suspended solids [mg/L]		5550.0 ± 15.8	3558.3 ± 10.3	92.0 ± 3.8

* As received from the mill ponding system.
** Acidified with a H_2SO_4 solution.
*** Flocculated and acidified.

As reported in the experimental section, to test the performance of the EFB-Fe_3O_4 biocomposites (EFB-Fe, AHP-EFB-Fe, and NaOH-HCl-EFB-Fe without nanocellulose reinforcement) for flocculated POME color removal, we used a 2^3-factorial design with biocomposite and H_2O_2 amounts, and pretreated POME pH as the experimental variables, and color as the response variable. The EFB-Fe_3O_4 biocomposites remove color from POME through a heterogeneous Fenton reaction where iron ions and H_2O_2 produce hydroxyl radicals able to oxidize organic contaminants under acidic conditions as seen in Figure 22 (Saeed et al., 2015; Lim et al., 2017; Gamaralalage et al., 2019; Sani et al., 2020; Mohammad et al., 2021). After conducting tests on a 20 mL flocculated POME sample, we found that the optimal reaction conditions for maximum color removal were at pH 3, with 0.01 mL of 30% H_2O_2 using 0.2 g of biocomposite at

50 °C for 2 hours. The statistical analysis presented in Figures S5-S7 demonstrates that pH, H_2O_2, and the amount of biocomposite used significantly affect the removal of color. The Pareto chart for the three biocomposites revealed that pH and the amount of H_2O_2 are the most influential variables for color removal. Lower pH levels and higher amounts of H_2O_2 increase color removal. Additionally, lower amounts of biocomposite significantly improve color removal, particularly for EFB-Fe and AHP-EFB-Fe.

The UV-vis absorbance behavior of a flocculated/acidified POME sample was analyzed before and after treatment with the EFB-Fe, AHP-EFB-Fe, and NaOH-HCl-EFB-Fe biocomposites, as shown in Figure 22. The POME absorbance in the visible range of 400 to 700 nm significantly decreases after treatment. The color measurement, according to the ISO 7887:2011 method B, at wavelengths of 436, 525, and 620 nm, and the spectral absorption coefficient was determined (International Organization for Standardization ISO, 2011). Therefore, the color removal data at 436 nm were chosen to analyze the data effectively.

The data in Table 13 shows the water quality parameters, including color, COD, total phenols, TSS, and elemental composition, for flocculated POME before and after treatment with the biocomposites. For the flocculated POME, EFB-Fe, AHP-EFB-Fe, and NaOH-HCl-EFB-Fe resulted in color removal percentages of 71.3%, 79.6%, and 65.7%, respectively. The biocomposites effectively removed 94.4% of total phenols in flocculated POME. Although the use of EFB-Fe and AHP-EFB-Fe resulted in a decrease of TSS by 28.3% and 57.4%, respectively, the parameter increased when NaOH-HCl-EFB-Fe was used. Simultaneously, COD levels remained constant before and after the treatment. Increased TSS and constant COD are likely due to the leaching of iron and possible decomposition of structural carbohydrates (cellulose) in the EFB matrix under the oxidant condition of the Fenton process. In fact, the iron content increased by

5.1%, 3.1%, and 8.9% for EFB-Fe, AHP-EFB-Fe, and NaOH-HCl-EFB-Fe treated samples, respectively. Likely, the Fe_3O_4 nanostructures present in AHP-EFB-Fe biocomposite are strongly attached to the fiber's surface through electrostatic interactions and coordinative bonds. This characteristic is perhaps the reason for AHP-EFB-Fe's exceptional performance in removing color and reducing TSS compared to other biocomposites. Although NaOH-HCl-EFB-Fe has a higher iron content, its catalytic activity is hindered due to the possible aggregation of Fe_3O_4 nanostructures, which also increases the leaching of the active oxide.

Figure 22. Heterogeneous Fenton Reaction Scheme and UV-Vis Absorption Profiles of POME Before and After Treatment with EFB-Fe, AHP-EFB-Fe, and NaOH-HCl-EFB-Fe Biocomposites

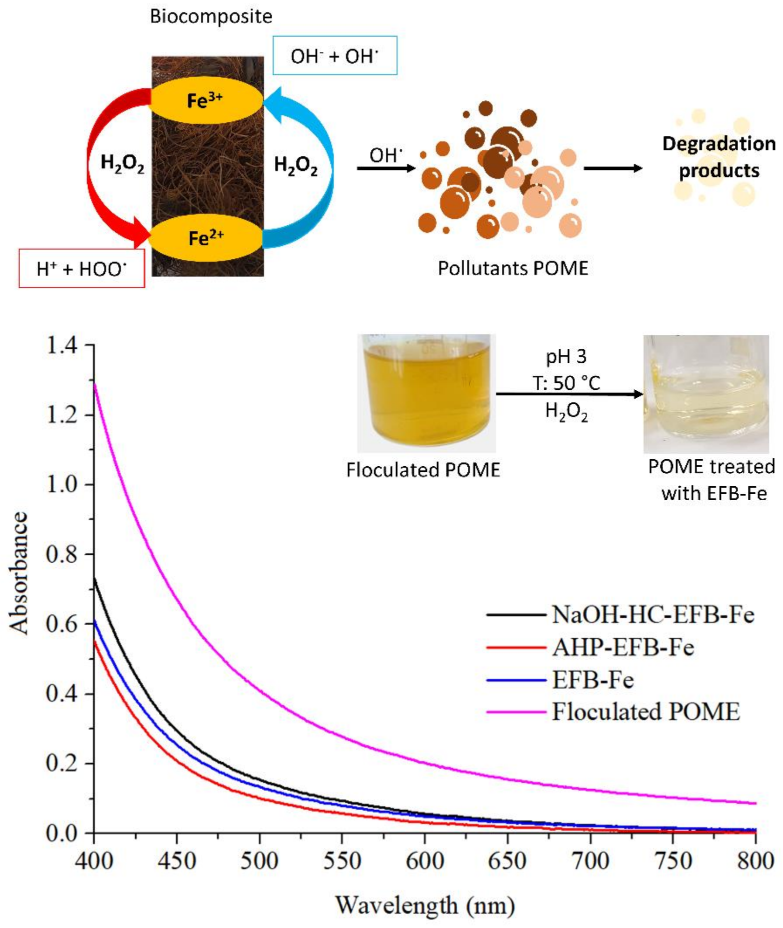

Table 13. Quality parameters for POME before and after treatment with the EFB-Fe_3O_4 biocomposites

Parameter		**Flocculated POME treated with**		
	Flocculated POME	EFB-Fe	AHP-EFB-Fe	NaOH-HCl-EFB-Fe
			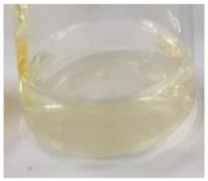	
Color at 436 nm [m^{-1}]	78.3 ± 1.2	22.4 ± 0.2	16.0 ± 0.1	26.9 ± 0.1
COD [mg/L]	827 ± 4.5	830 ± 2.1	826 ± 1.9	828 ± 2.3
Total phenols [mg/L]	1.09 ± 0.05	0.06 ± 0.01	0.07 ± 0.00	0.05 ± 0.01
Total suspended solids [mg/L]	92.0 ± 3.8	66.0 ± 2.1	39.2 ± 1.9	143.8 ± 3.5
Fe [mg/L]*	0.288	6.660	5.774	18.919

Blank samples

	Flocculated POME without biocomposite**	Flocculated POME without H_2O_2***	Flocculated POME without Fe_3O_4****
Color at 436 nm [m^{-1}]	72.1 ± 1.9	89.5 ± 2.2	89.8 ± 1.5

*ICP-OES
** Flocculated POME at pH 3, H_2O_2, 50°C without biocomposite
*** Flocculated POME at pH 3, 50°C with biocomposite
**** Flocculated POME at pH 3, H_2O_2, 50°C with EFB fibers

In Fenton catalysis, hydroxyl radicals can be formed either at the surface of a solid active material (heterogeneous process) or in the solution (homogeneous process) (Shokri & Sanavi Fard, 2023). However, in the case of heterogeneous processes, the presence of an excess of ferrous ions in solution, which may come from leached iron nanoparticles, can hinder the catalytic cycle by reacting with hydroxyl radicals. This reaction can result in a reduction of the pollutant removal efficiency (Ramirez et al., 2005; Xavier et al., 2015). We believe that this phenomenon may have occurred with NaOH-HCl-EFB-Fe, where the excessive iron present in the solution, resulting from leaching, led to a decrease in color removal from POME. Describing how organic contaminants in POME undergo oxidation is difficult because of the effluent compositional complexity. However, hydroxyl radicals from the Fenton reaction can oxidize organic matter through three main mechanisms: hydrogen abstraction from aliphatic carbons, hydrogen addition, and electron transfer. These reactions produce oxidized products through radical intermediates (C. P. Huang et al., 1993; Machulek et al., 2012). It is important to note that each organic component in POME may follow a specific oxidation pathway.

Both homogeneous and heterogeneous Fenton reactions have been studied for the oxidation of organic pollutants in POME. Homogeneous processes require control of various reaction parameters including pH, iron salt concentration, temperature, reaction time, stirring rate, pressure, and POME pre-treatment. For example, Saeed et al. achieved 92% color and 85% COD removal from POME by using 4.57 g/L H_2O_2, 1.88 g/L Fe^{2+} ions, pH 2.9, and a 30-minute reaction at 120 rpm (Saeed et al., 2015). Gamaralalage et al. reported the removal of 91% of total organic carbon (TOC) with a TOC:H_2O_2:Fe^{2+} molar ratio of 1:3.7:0.6 at pH 3 (Gamaralalage et al., 2019). Though homogeneous Fenton processes exhibit high removal percentages of the organic load from wastewater, they generate sludge that requires additional treatment. Also, the catalyst is not recyclable, which adds to the overall cost of the process. This led to the development of heterogeneous Fenton processes. For instance, Chairunnisak et al. (2018) used electro-Fenton with iron electrodes for POME treatment, achieving 99% COD removal (Chairunnisak et al., 2018). Nano zero-valent iron (nZVI) has also been utilized in POME treatment, achieving a 75% COD removal rate with the following parameters, 3.91 g/L of nZVI dosage, 1.84 g/L of H_2O_2 dosage, 23.84 L/h of aeration rate, and a reaction time of 240 minutes (Taha & Ibrahim, 2014).

Another POME treatment involved combining 0.06 g of nZVI with 0.4 mL of H_2O_2 at pH 2 and subjecting the mixture to 2 hours of sonication, resulting in an 80% reduction in COD (Taha et al., 2014). Some of these treatments required significant amounts of H_2O_2, iron salts, and energy, leading to increased costs and decreased treatment sustainability. In contrast, 10 g of our biocomposites incorporating residual biomass from palm oil extraction can treat 1 liter of flocculated POME upon addition of 5 mL of H_2O_2 (30%).

3.4.4. Influence of TOCN reinforcements on biocomposite performance

The number of reuse cycles and color removal efficiency of each biocomposites were determined, maintaining the same reaction conditions (50°C, 2 h of reaction). Figure 23 shows the impact of different reinforcement techniques, soaking (S), coagulation (C), non-directional freezing (F), and directional freezing (DF), on each biocomposite during the treatment of flocculated POME. EFB-Fe, AHP-EFB-Fe, and NaOH-HCl-EFB-Fe exhibited 10, 9, and 8 reuse cycles, respectively, along with varying color removal efficiencies. The evaluation focused on both the material's durability and color removal efficiency. Changes in lignin, moisture and SiO_2 affected the mechanical resistance of the fibers, impacting material durability. AHP-EFB and EFB-NaOH-HCl matrices, with higher moisture and lower lignin and SiO_2 content than EFB, exhibited these effects. Additionally, AHP-EFB contained more SiO_2 and less lignin than EFB-NaOH-HCl, suggesting the influence of SiO_2 on the strength of EFB fibers. The presence of SiO_2 in the matrix facilitated a better distribution of Fe_3O_4 and reduced aggregate formation, improving the catalytic activity of the biocomposites (EFB-Fe and AHP-EFB-Fe). All reinforcements applied to the three biocomposites increased the number of reuse cycles by 1 to 2. Furthermore, they contributed to a reduction in iron leaching, with soaking, coagulation, directional freezing, and freezing reducing iron leaching by an average of 49%, 64%, 45%, and 44% respectively for each biocomposite. As a result, iron concentrations in the treated flocculated POME were below 5 ppm for EFB-Fe and AHP-EFB-Fe, and below 10 ppm for NaOH-HCl- EFB-Fe (Table 14).

Figure 23. Reuse Cycles of biocomposites with Soaking, Freezing, Coagulation and Directional freezing reinforcements a) EFB-Fe, b) AHP-EFB-Fe, and c) NaOH-HCl-EFB-Fe

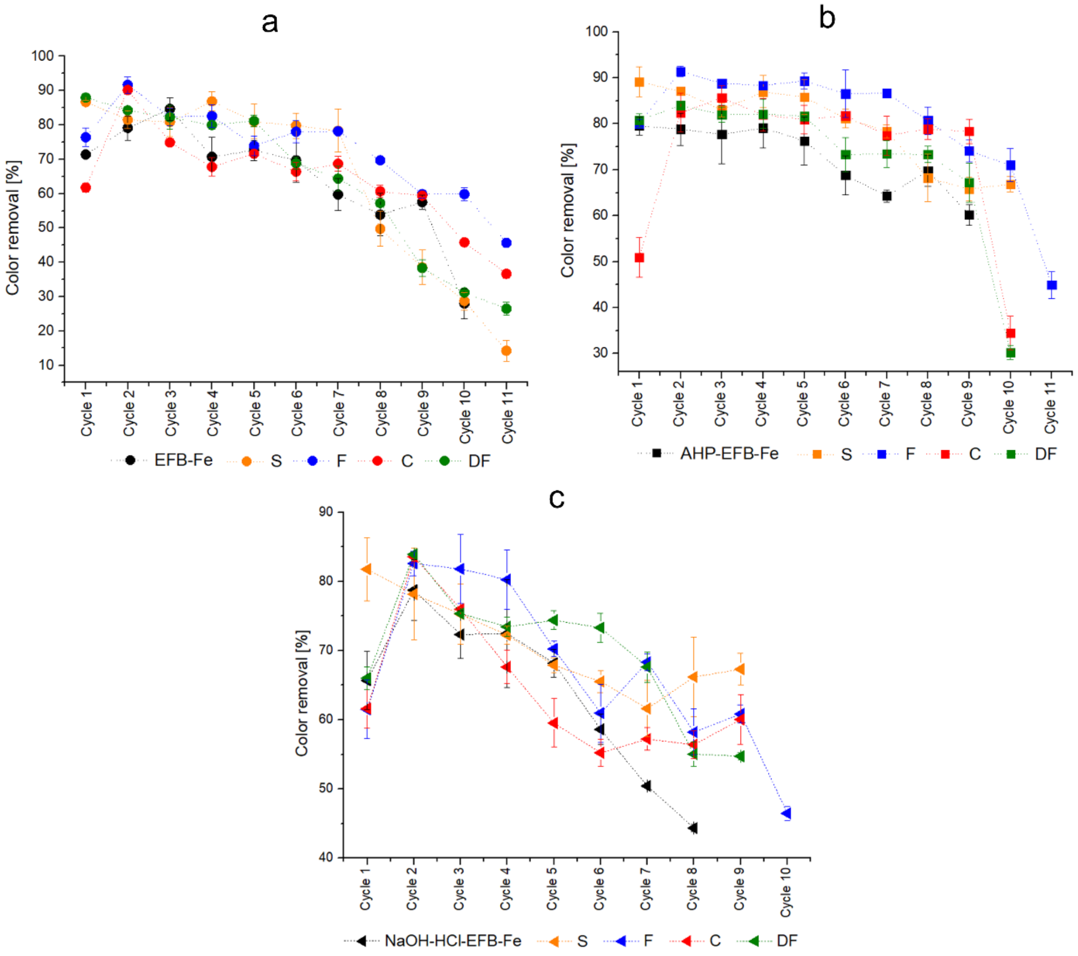

Table 14. Total iron of POME

treated with reinforced biocomposite.

Flocculated POME treated with	**Total Iron Colorimetry, 1,10-Phenanthroline [ppm]**
Flocculated POME	0.29 ± 0.09
EFB-Fe	7.17 ± 0.22
AHP-EFB-Fe	6.47 ± 0.13
NaOH-HCl-EFB-Fe	19.49 ± 0.47
S-EFB-Fe	4.52 ± 0.35
S-AHP- EFB -Fe	3.27 ± 0.48
S-NaOH-HCl-EFB -Fe	7.60 ± 0.36
C-EFB-Fe	3.24 ± 0.41
C-AHP-EFB-Fe	2.01 ± 0.47
C-NaOH-HCl-EFB-Fe	5.88 ± 0.56
F-EFB-Fe	4.57 ± 0.29
F-AHP-EFB-Fe	3.35 ± 0.42
F-NaOH-HCl-EFB-Fe	9.88 ± 0.33
F-EFB-Fe	4.22 ± 0.52
F-AHP-EFB-Fe	3.86 ± 0.43
F-NaOH-HCl-EFB -Fe	9.06 ± 0.51

The EFB-Fe biocomposite and its reinforcements demonstrate that throughout the 11 reuse cycles, the F-reinforced sample removed more color than EFB-Fe, suggesting a positive reinforcement effect (Figura 23a). Overall, methods S, F, and DF demonstrated a greater ability to remove color during the first 8 cycles compared to EFB-Fe. However, in cycle 9, a decrease in color removal efficiency was observed for DF and S methods, with a 20% reduction in the amount of color removed, while methods C and F maintained high efficiency, removing close to 60% of the color. In cycle 10, the EFB-Fe biocomposite experienced disintegration, resulting in a significant decrease in color removal efficiency. In cycle 11, F was the most effective biocomposite in color removal, followed by C, DF, and lastly, S. The F reinforcement was more efficient than DF for EFB-Fe, particularly from cycle 9 onwards, where DF removed less than 40% of the color. This could be attributed to DF having a more ordered structure, which may limit the reaction, as chemical reactivity typically occurs in amorphous areas. Additionally, an unusual behavior was observed in C, which showed low efficiency in the first cycle but then increased significantly in subsequent cycles, reaching up to 90% color removal. Coagulation reinforcement, initially decreased color removal efficiency in the first cycle, possibly due to TOCN obstruction on magnetite's active sites (L. Wang et al., 2019) or superficial calcium saturation (Sailah et al., 2022). In summary, reinforcement F was the most effective in the EFB-Fe matrix, removing over 45% of color over 11 cycles of reuse.

AHP-EFB-Fe demonstrated a remarkable color removal efficiency of over 60% throughout all 11 reuse cycles. AHP-EFB-Fe reinforcements contributed to improved fiber durability and maintained higher color removal efficiency. All reinforcements (S, F, C, DF) applied to AHP-EFB-Fe resulted in a 10-20% greater color removal compared to AHP-EFB-Fe without reinforcement during the 9 cycles of reuse (Figura 23b). In cycle 10, reinforcements C and DF showed a color removal efficiency of less than 40%, whereas S and F achieved 65% and 70% color removal, respectively. Finally, in cycle 11, F, the only biocomposite that reached this cycle, disintegrated and removed less than 50% of the color. For this matrix, a notable difference of 10 to 20% in color removal is observed between reinforcements F and DF, suggesting that F is a more effective reinforcement than DF, similar to what was obtained with EFB-Fe. In AHP-EFB-Fe, the coagulation reinforcement also exhibited lower efficiency in the first cycle, but it increased color removal by 33% from cycle 1 to cycle 2. In contrast to the observed behavior of reinforcements on EFB-Fe, AHP-EFB-Fe matrix exhibits an active surface conducive to OH- group availability, facilitating improved Fe_3O_4 deposition and interaction with TOCN via hydrogen bonding and ion-dipole interactions. Like EFB-Fe, reinforcement F for AHP-EFB-Fe proved to be the most optimal, removing over 71% of color during 10 cycles of reuse.

For NaOH-HCl-EFB-Fe, which initially exhibited over 65% color removal in the first 5 cycles, the efficiency declined thereafter, reaching 44% color removal by cycle 8. During 8 cycles of reuse, all reinforcements increased the material's reuse cycle and improved color removal efficiency (Figure 23c). In cycle 9, S, F, C, and DF removed 67%, 61%, 60%, and 55% of the color respectively before disintegrating. In cycle 10, only F removed 47% of the color. Interestingly, C, F, and DF exhibited lower efficiency in the first cycle, likely due to an obstruction of active sites and a decrease in iron in solution, inhibiting the Homogenous Fenton reaction. However, in the second cycle, the removal increased by 20% for these reinforcements, suggesting a different chemical surface associated with the different pretreatments. While the NaOH-HCl treatment was effective in depositing Fe_3O_4, an excess of magnetite limited the efficiency of the biocomposite. For NaOH-HCl-EFB-Fe, reinforcements F and DF exhibited dynamic behavior, with no consistent trend observed across the cycles. While all reinforcements showed variability over the cycles, reinforcement S achieved over 65% color removal by the end of cycle 9. However, its removal rate dropped below 70% from cycle 5 onwards.

Indeed, all reinforcements resulted in the formation of three-dimensional TOCN networks on the biocomposites, enhancing their resistance and mitigating magnetite leaching. While some reinforcements initially obstructed the active sites of Fe_3O_4, limiting catalytic activity in the first cycle. The overall interactions governing the anchoring between fiber- Fe_3O_4 and TOCN primarily involved Van der Waals forces, hydrogen bonds, and electrostatic forces. The absence of impurities and the presence of SiO_2 created a stable surface chemical environment conducive to the anchoring of both Fe_3O_4 and TOCN. Overall, the AHP-EFB-Fe matrix demonstrated superior durability and color removal efficiency, enduring 9 reuse cycles and removing over 60% of the color. Additionally, reinforcement with non-directional freezing (F) extended the reuse cycle by

1, achieving over 71% color removal across 11 reuse cycles. It is noteworthy that the natural SiO_2 in EFB fibers significantly contributed to the stability and functionality of the biocomposite. Importantly, these biocomposites hold potential for treating pigment-containing effluents from industries such as textiles. However, this research primarily aimed to contribute to the circular economy within the palm oil industry.

3.5. Conclusions

The AHP and NaOH/HCl treatments effectively removed surface impurities, reducing ash and ethanol-toluene matter content by 43.7% and 71.5% respectively compared to untreated material. AHP removed 47.9% of lignin, while NaOH/HCl removed 23.0%. This led to a significant 110% increase in moisture content in treated fibers, attributed to enhanced availability of hydroxyl groups for hydrogen bonding with ambient water. While EFB naturally contains SiO_2, pretreatments with AHP and NaOH/HCl partially removed it. AHP treatment revealed some superficial SiO_2, while NaOH/HCl treatment indicated a surface free of SiO_2, although it persisted in internal cavities. TGA confirmed the pyrolysis stages of natural fibers, with AHP exhibiting a single peak in the DTG curve, indicating the absence of lignin.

Characterizing the biocomposites with magnetite revealed varying iron content: NaOH-HCl-EFB-Fe had 3.0% iron, AHP-EFB-Fe had 2.5%, and EFB-Fe had 1.8%. This indicates that surface cleaning increased the availability of OH- groups, enhancing the interaction between fibers and Fe_3O_4. NaOH/HCl treatment was the most effective in this regard, followed by AHP. Overall, the matrices interacted with Fe_3O_4 through interactions involving hydrogen bonds and ion-dipole. Importantly, the presence of magnetite did not compromise the material's thermal stability, as evidenced by characteristic pyrolysis phases of fibers without Fe_3O_4.

The three biocomposites proved effective in color removal from POME. EFB-Fe endured 10 cycles, removing over 28% of color; AHP-EFB-Fe lasted 9 cycles, removing over 60% of color; and NaOH-HCl-EFB-Fe lasted 8 cycles, removing over 44% of color. Additionally, they achieved over 90% removal of phenolic compounds. Despite EFB-Fe lasting one cycle longer than AHP-EFB-Fe, the latter showed slightly higher removal efficiency, making it a promising option for POME treatment. These materials serve as valuable complementary tertiary treatments to conventional POME treatment methods.

The reinforcing processes with TOCN, including soaking, freezing, coagulation, and directional freezing, increased the durability of biocomposites (EFB-Fe, AHP-EFB-Fe, and NaOH-HCl-EFB-Fe), improved color removal efficiency, and reduced iron leaching by at least 44%. Interactions between TOCN, Fe_3O_4, and the matrix fibers occur through mono- and bidentate interactions, hydrogen bonding, and ion-dipole interactions. The most effective reinforced biocomposite was F-AHP-EFB-Fe, which removed more than 71% of color during 10 reuse cycles.

4. Kinetics and Thermodynamics of Color Removal from POME using EFB/Magnetite Biocomposites

4.1. Abstract

The expanding palm oil industry has generated a surge in lignocellulosic residues, notably empty fruit bunches (EFB) and palm oil mill effluent (POME), posing a growing environmental challenge. While conventional treatments, such as traditional ponds, offer cost-effectiveness, they fall short in addressing the persistent brown coloration in treated POME. In this context, we investigate the application of the advanced oxidation process, specifically the heterogeneous Fenton reaction with EFB/magnetite catalysts. This study delves into the kinetic and thermodynamic intricacies of the reaction, focusing on temperature variations. Chemical kinetics elucidates the mathematical foundations of the reaction, emphasizing rate constants (k_1), and reaction order. The color oxidation of POME was modeled as a first-order reaction rate with a k_1 of 1.6×10^{-2} at 323 K. Furthermore, thermodynamic parameters, including activation energy, entropy, and free energy, were quantified through Eyring and Polanyi theories, indicating an endothermic and non-spontaneous reaction. Aditionally, the elevated activation energy (>70 kJ/mol) suggests chemisorption processes. This research transcends simulated effluents to scrutinize the kinetic and thermodynamic facets of treated POME color removal. The investigation underscores the role of temperature and builds upon an established experimental design, laying the groundwork for optimized reaction conditions.

4.2. Introduction

Palm oil production has witnessed a surge in response to population growth and increased demand, resulting in the generation of lignocellulosic residues like empty fruit bunches (EFB) and palm oil mill effluent (POME) (Aliyu-Yaro et al., 2022). The brown color of POME is attributed to carotenes, tannins, phenolic compounds, and lignin. Traditional treatments for POME, involving serial anaerobic, facultative, and aerobic open ponds, are cost-effective but lack efficiency (Mahmod et al., 2023). The persistent brownish color in treated POME poses environmental concerns upon discharge into water sources, emphasizing the need for supplementary treatments (K. A. Tan et al., 2022). An innovative approach involves the application of the advanced oxidation process (AOP), specifically the Fenton reaction. This process utilizes iron ions and hydrogen peroxide to generate hydroxyl radicals, facilitating the oxidation of contaminants (M. hui Zhang et al., 2019). The mechanism involves the oxidation of iron producing hydroxyl radicals (Equation 7) and the reduction of iron regenerating ferrous ions (Equation 8) in the decomposition of hydrogen peroxide catalyzed by iron oxides in homogeneous Fenton (Zhu et al., 2019).

$$Fe^{2+} + H_2O_2 \rightarrow Fe^{3+} + OH^{\bullet} + OH^{-} \quad k = 40\text{-}80\ M^{-1}s^{-1} \ (7)$$

$$Fe^{3+} + H_2O_2 \rightarrow Fe^{2+} + HO_2^{\bullet} + H \ k = 0.001 - 0.01\ M^{-1}s^{-1} \ (8)$$

The drawbacks associated with homogeneous Fenton reactions, including the generation of iron-rich sludge and high costs, have driven research toward heterogeneous Fenton processes utilizing solid catalysts. Typically, matrices with supported iron oxides are employed, where the catalyst primarily comprises ferric and ferrous ions. Maintaining the redox cycle (Equations 7 and 8) is crucial for sustaining the continuity of the Fenton reaction. Equations 9 and 10 show the mechanism of heterogeneous Fenton, with the reduction of iron serving as the rate-limiting step due to the small value of the rate constant ($0.01 M^{-1}s^{-1}$). Despite the formation of the hydroperoxyl radical during the process, its lower oxidation potential (1.5 V) compared to the hydroxyl radical (2.8 V) is noteworthy (Thomas et al., 2021; Zhu et al., 2019). The mechanism of heterogeneous catalysis may involve leached iron from homogeneous Fenton, heterogeneous catalysis, or a combination of both methods (Shokri & Sanavi Fard, 2023). Heterogeneous Fenton processes have demonstrated efficacy in removing organic contaminants from POME, with reported removal rates exceeding 75% of the organic load and color (Taha et al., 2014; Taha & Ibrahim, 2014).

$$\text{-Fe}^{III} + H_2O_2 \rightarrow \text{-Fe}^{II} + HO_2^{\bullet} + H^{+} \quad (9)$$

$$\text{-Fe}^{II} + H_2O_2 \rightarrow \text{-Fe}^{III} + OH^{\bullet} + OH^{-} \quad (10)$$

Understanding the complex mechanisms governing the heterogeneous Fenton reaction for organic contaminant removal from POME is a challenging task. However, employing principles of chemical kinetics enables a mathematical explanation of these reactions and the determination of crucial parameters, such as reaction rate and rate constant, through transition state theory (TST) (Arnaut, 2021; Ptáček et al., 2018). TST, also known as the theory of absolute reaction rates or the theory of the activated state, fundamentally considers molecules as rigid spheres colliding to form a product by traversing an activated complex. This theory posits that the reaction rate occurs in equilibrium between the reactants and their transition complex, which subsequently decomposes to form products (Ptáček et al., 2018). The reaction rate correlates with the rate of oxidation of pollutants and undergoes fluctuations over the course of the reaction. Moreover, the order of a reaction can be determined based on the rate constant at a given temperature. If the rate remains unaffected by the concentration of reactants or products, it is categorized as a zero-order reaction. Conversely, if it depends on the concentration of reactants or products, it is classified as a first-order reaction. Second-order reactions entail a rate proportional to the square of the concentration of the reactant or product (Ordaz & Arrizabalaga Sáez, 2020; Tamás & Tomlin, 2014).

The oxidation processes of dyes by heterogeneous Fenton are modeled using first, pseudo-first, and second-order kinetics, which depend on the catalyst type, reactant concentrations, reaction conditions, and pollutants involved (Farshchi et al., 2018; Wang et al., 2021; Karim et al., 2022). Additionally, for a reaction to occur, reactant molecules must collide. Temperature increases the number of molecular collisions, thus influencing the reaction rate. Arrhenius' law describes the relationship between the rate and temperature constants, allowing to determine the activation energy (Ea), the minimum energy required for a reaction (Foutch & Johannes, 2003; Gajrani & Sankar, 2020). This modeling quantifies the activation enthalpy, entropy, and free energy through the theory of Eyring and Polanyi, allowing the relationship between kinetics and thermodynamics (Ptáček et al., 2018). Typically, the thermodynamics of heterogeneous Fenton processes exhibit positive enthalpies and negative entropies, indicating endothermic and non-spontaneous reactions (Mehdaoui et al., 2023; Suraj et al., 2019).

In the heterogeneous Fenton processes, magnetite stands out as a widely employed catalyst, prized for its stability, recyclability, cost-effectiveness, and non-toxic nature (X. Liang et al., 2013). The reported Ea for pollutant removal using magnetite in heterogeneous Fenton processes varies across studies: 56.68 KJ/mol (303 to 323 K) for reactive black 5, 47.6 KJ/mol (298 to 348 K) for rhodamine B, and 32.07 KJ/mol (373-453 K) for nitric oxide (F. Chen et al., 2017; Nasuha et al., 2016; S. Yang et al., 2018). Activation energies below 40 KJ/mol suggest physisorption, while values exceeding 40 KJ/mol indicate chemisorption, an irreversible process with high chemical specificity (Hameed et al., 2007). Notably, most activation energies obtained for heterogeneous Fenton processes surpass 40 KJ/mol, signifying chemisorption. In chemisorption, a chemical reaction occurs on the catalyst's surface, leading to the formation of a surface compound (Králik, 2014). Furthermore, thermodynamic parameters reveal the endothermic or exothermic nature of processes and whether reactions are spontaneous. The thermodynamics of heterogeneous Fenton reactions indicate that these reactions are endothermic. The spontaneity of these reactions generally hinges on specific reaction conditions. For instance, The removal of chlorophenol by the Fe_2O_3/SiO_2 heterogeneous Fenton catalyst is characterized as a spontaneous and endothermic reaction, attributed to its positive entropy and enthalpy values (Shokri & Sanavi Fard, 2023). However, there is limited research on the thermodynamic parameters of magnetite in heterogeneous Fenton processes.

Most kinetic and thermodynamic studies involving magnetite as a catalyst have primarily centered around simulated effluents. In light of this, our research shifts the focus to the kinetic and thermodynamic examination of the heterogeneous Fenton reaction for treated POME color removal utilizing EFB/magnetite. Temperature variations are emphasized in this study, building on a prior experimental design aimed at determining optimal reaction conditions.

4.3. Experimental

4.3.1. Materials

Hydrogen peroxide (H_2O_2), Aluminum sulphate 18-hydrate ($Al_2(SO_4)_3.18H_2O$) was purchased from Panreac (E.U.). Sulphuric acid (H_2SO_4 95-97 %) were purchased from Merck (Darmstadt, Germany). The POME used in this study was collected in the last pool of the industrial wastewater treatment system and it was supplied by Extractora Agroince, Aguachica, Cesar, Colombia. The POME was flocculated, centrifuged, and acidified for use. EFB was supplied by Extractora Central, Puerto Wilches, Santander, Colombia. The biocomposites EFB-Fe, AHP-EFB-Fe and NaOH-HCl-EFB-Fe were used in this study, each undergoing different pretreatment processes prior to in situ magnetite deposition. EFB represents untreated, clean fibers, while AHP represents fibers that have undergone delignification by alkaline hydrogen peroxide treatment. In addition, EFB-NaOH-HCl refers to fibers treated with both alkaline and acid solutions (the synthesis of these biocomposites is described in the previous article). The biocomposites EFB-Fe, AHP-EFB-Fe and NaOH-HCl-EFB-Fe contain 1.80, 2.54 and 3.00% of iron oxides.

4.3.2. Reaction kinetics at different temperatures

The reaction conditions for the oxidation of POME pigments were previously established. For the treatment of 20 mL of POME, 0.2 g of each biocomposite, 0.1 mL of 30% H_2O_2, pH 3, 323 K, and a 2-hour reaction time were employed. Subsequent assessments of the kinetics and thermodynamics of oxidation involved conducting color removal tests at temperatures of 308, 323, and 338 K, while maintaining the optimized reaction parameters. Samples were collected at regular intervals over a 120-minute period. Color analysis was performed at three wavelengths (436, 525, and 620 nm) in accordance with ISO 7887:2011 Method B, and measurements were conducted in triplicate. To facilitate the data analysis, the color values obtained at 436 nm were utilized.

The rate constant was determined graphically. The zero order (11) was plotted as color vs. time, the first order (12) was plotted as the natural logarithm of color vs. time, and the second order (13) was plotted as 1/color vs. time. The order was chosen based on the correlation coefficient R^2 (highest value) (Upadhyay, 2006).

$$[C] = -k_0 t + [C_0] \quad (1)$$

$$Ln[C] = -k_1 t + Ln[C_0] \quad (12)$$

$$\frac{1}{[C]} = k_2 t + \frac{1}{[C_0]} \quad (13)$$

Where [C] is the color (m^{-1}) at 436 nm, C_0 is the initial color and k (0, 1 and 2) is the rate constant, and *t* is time (min).

The activation energy (Ea) was determined using the Arrhenius equation (14) (Van Santend & Niemantsverdriet, 1995). Ln[k] was plotted against 1/T and the slope of the graph was solved to obtain Ea. Slope = -Ea/(RT).

$$k = Ae^{\frac{-Ea}{RT}} \rightarrow Ln[K] = Ln\, A - \frac{-Ea}{RT} \quad (14)$$

Where k is the rate constant, Ea activation energy, R is universal gas constant (8.314 J/mol.K)

The thermodynamics studies or transition state theory, modelled by the linearized Erying-Polanyi equation (15), is linked to the Arrhenius equation, from which the activation enthalpy ($\Delta H^{\ddagger}$) and activation entropy ($\Delta S^{\ddagger}$) can be determined (Ptáček et al., 2018). With $\Delta H^{\ddagger}$ and $\Delta S^{\ddagger}$ it is possible to determine the free energy of activation $\Delta G^{\ddagger}$ (16). Slope = - $\Delta H^{\ddagger}/R$ and intercept= $Ln\left[\frac{k_B}{h}\right] + \frac{\Delta S^{\ddagger}}{R}$

$$Ln\frac{k}{T} = \frac{-\Delta H^{\ddagger}}{R} * \frac{1}{T} + Ln\left[\frac{k_B}{h}\right] + \frac{\Delta S^{\ddagger}}{R} \quad (15)$$

$$\Delta G^{\ddagger} = \Delta H^{\ddagger} - T\Delta S^{\ddagger} \quad (16)$$

Where K_B is Boltzmann's constant ($1.38x10^{-23}$ J/K) and h Planck's constant ($6.63x10^{-34}$ J.s).

4.4. Results and Discussion

Figure 24 shows the reaction kinetics of the color obtained after treating the POME with the biocomposites as a function of time, at 3 temperatures (303, 323 and 338 K). In general, the three biocomposites show a similar behaviour when the reaction temperature is varied. The floculated POME treated with EFB-Fe at 303 K decreased in color by 18 % after 120 minutes of reaction. At 323 K, during the initial 40 minutes of the reaction, the color of the POME remained stable with only a 2% decrease. Between 40 and 120 minutes, the color decreased by 71%. Finally, at 338 K, we observed a 65 % reduction in color during the first 35 minutes of reaction, then no more color removal. Certainly, for POME treated with AHP-EFB-Fe at 308 K, a 26% reduction in color was observed over the 120-minute reaction period. Upon elevating the temperature to 323 K, color stability was noted in the initial 30 minutes, followed by a substantial 76% decrease in color over the remaining 90 minutes of the reaction. Furthermore, with an increase in the reaction temperature to 338 K, a rapid 76% reduction in color was observed within the initial 40 minutes of the reaction. From 40 to 120 minutes of reaction, there is no variation in color. Finally, for the NaOH-HCl-EFB-Fe biocomposite at 308 K, the color decrease was 24% in 120 minutes of reaction. At 323 K the color started to decrease after 50 minutes of reaction, between 50 and 120 minutes of reaction the color decreased by 65%. At 338 K the color decreased by 67 % in the first 45 minutes of reaction. As the temperature increased, the reaction time decreased. In summary, each biocomposite exhibited a color removal efficacy surpassing 65% at both 323 K and 338 K, indicative of the endothermic nature of the reaction. Given the energy requirement for the reaction to proceed, none of the biocomposites achieved a color removal exceeding 26%.

Temperature had a critical effect on the rate of color removal, with different behaviors at different temperatures. At 308 K, a sluggish color removal process was evident across all three materials. Upon elevating the temperature by 15 K, a transition to mixed kinetics or two distinct kinetic regimes was observed, consistent with prior studies (Bayat et al., 2012; Brillas, 2022; Quici et al., 2005; Segura et al., 2008). Specifically, at 323 K, an initial phase characterized by slow oxidation spanned the first 35 to 40 minutes, succeeded by a more rapid oxidation thereafter. The kinetics were linked to the type of biocomposite employed. While the behavior of the three biocomposites was similar, the time and percentage response exhibited slight variations. Conversely, at 338 K, a rapid oxidation phase dominated the initial 40 minutes, followed by a plateau with no further color removal. This behavior is attributed to the heightened temperature enhancing the rate of hydroxyl radical production, consequently increasing color removal (Segura et al., 2008). Intriguingly, both the EFB-Fe and AHP-EFB-Fe biocomposites exhibited a reduction in color removal efficiency at 338 K compared to 323 K, suggesting an optimal reaction temperature around 323 K. Conversely, the NaOH-HCl-EFB-Fe biocomposite exhibited a 3% increase in removal efficiency at 338 K. The temperature-induced changes in oxidation rate can be explained by collision theory, where higher temperatures result in more effective collisions between reactants, thereby increasing the likelihood of product formation (Upadhyay, 2006). Consequently, the increase in temperature correlates with a decrease in reaction time.

Figure 24. Color kinetics of pome using the biocomposites a) EFB-Fe, b) AHP-EFB-Fe and c) NaOH-HCl-EFB-Fe

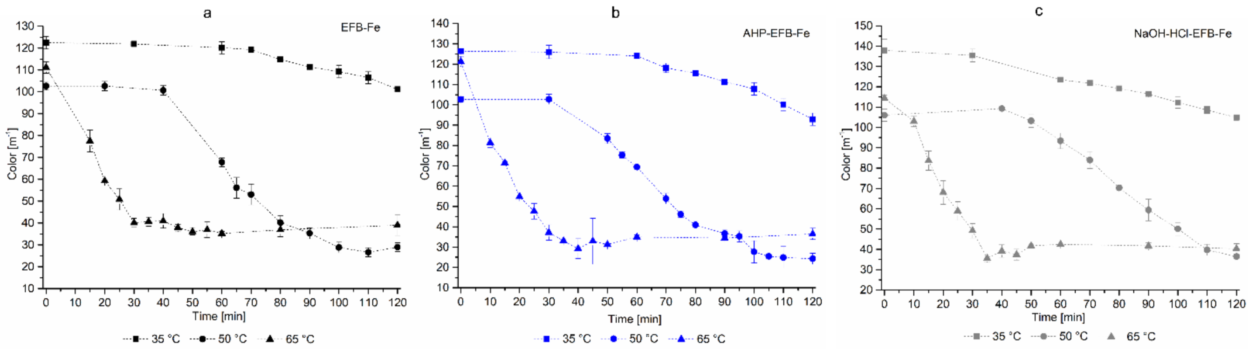

In catalytic processes, such as Fenton dye removal, raising the temperature amplifies the reaction rate and facilitates the removal of contaminants. This is attributed to the increased production of hydroxyl radicals. This observation implies that the reactions involved in dye removal exhibit an endothermic nature (Santana et al., 2019). However, it's crucial to note that there exists an optimal temperature range for Fenton processes. Extremely low or high temperatures can adversely impact the efficiency of the reactions. Low temperatures result in decreased kinetic energies, leading to prolonged reaction times. Conversely, high temperatures can induce the thermal decomposition of hydrogen peroxide, hindering effective color removal (Nidheesh et al., 2013; Santana et al., 2019). The ideal oxidation temperature is contingent upon various factors, including the material, catalyst, reaction conditions, and the specific dye or pollutant involved. Studies have reported 99% removal of acid red 14 at 333 K in heterogeneous Fenton (Idel-aouad et al., 2011) and 98.4% removal of Reactive brilliant orange X-GN at 313 K in heterogeneous photo-Fenton (Q. Chen et al., 2009). Homogeneous Fenton processes for phenol and total organic carbon removal, conducted by Zazo et al., demonstrated improved oxidation rates and mineralization with increasing temperature within the range of 298 to 403 K. Higher temperatures also offer the potential to enhance Fenton processes by reducing the required amounts of iron ions and hydrogen peroxide in the reaction (Zazo et al., 2011). Despite these findings, a majority of studies on POME color removal via Fenton processes are conducted at room temperature, with variations in other reaction conditions such as pH, iron salt quantity, and hydrogen peroxide concentration (Sani et al., 2020). In summary, our work highlights that temperature elevation correlates with increased oxidation rates in POME color removal, with the optimal reaction temperature identified as 323 K.

Identifying the oxidation pathway of dyes in POME is challenging due to its complex composition. However, the presence of pigmented compounds like lignin, phenols, pectins, and carotenoids provides clues to potential oxidation routes (Bello et al., 2013). Studies have shown the bleaching of carotenoids when reacting with hydroxyl radicals via Fenton chemistry. Additionally, three main oxidation pathways for β-carotenoids have been suggested (scheme 3), hydrogen atom transfer (a), radical adduct formation (b), and electron transfer (c) (C. H. Chen et al., 2011; Edge & Truscott, 2018; Sy et al., 2013; Woodall et al., 1997). Gibbs free energies (ΔG) indicate that hydrogen atom transfer reactions are thermodynamically more favorable, followed by radical adduct formation and electron transfer. However, this applies specifically to β-carotenoids (C. H. Chen et al., 2011).

Scheme 3. Possibles pathways for the oxidation of β-carotene a, hydrogen atom transfer, b) radical adduct formation, c) electron transfer (C. H. Chen et al., 2011)

$$\beta\text{-C} + {}^{\bullet}\text{OH} \longrightarrow \beta\text{-C(-H)}^{\bullet} + \text{H}_2\text{O} \quad \Delta G = -214 \text{ kJ/mol} \quad \text{(a)}$$

$$\beta\text{-C} + {}^{\bullet}\text{OH} \longrightarrow \beta\text{-C-OH}^{\bullet} \quad \Delta G = -142 \text{ kJ/mol} \quad \text{(b)}$$

$$\beta\text{-C} + {}^{\bullet}\text{OH} \longrightarrow \beta\text{-C}^{\bullet +} + \text{OH}^{-} \quad \Delta G = -71 \text{ kJ/mol} \quad \text{(c)}$$

Reduced POME color was reported when phenolic compounds were removed (C. H. Chen et al., 2011; Kongnoo et al., 2012). The oxidation mechanism of phenol, a predominant phenolic compound, through the Fenton reaction with the hydroxyl radical has been reported. The process commences with the hydroxyl radical's addition to one of the carbons in the ortho, meta, and para positions of the phenolic ring, leading to the formation of three distinct intermediates. Subsequently, a hydrogen atom is abstracted from the same carbon where the hydroxyl radical was introduced, giving rise to water and yielding three different compounds depending on the position of the hydroxyl radical addition: hydroquinone (*para*), resorcinol (*metha*), and catechol (*Ortho*) (Scheme 4) (Kang et al., 2002; Valdés et al., 2015). This oxidation pathway is likely to occur in the phenolic compounds found in the POME.

Scheme 4. The Fenton oxidation pathway of phenol in the a) para, b) meta, and c) ortho positions adapted from (Valdés et al., 2015)

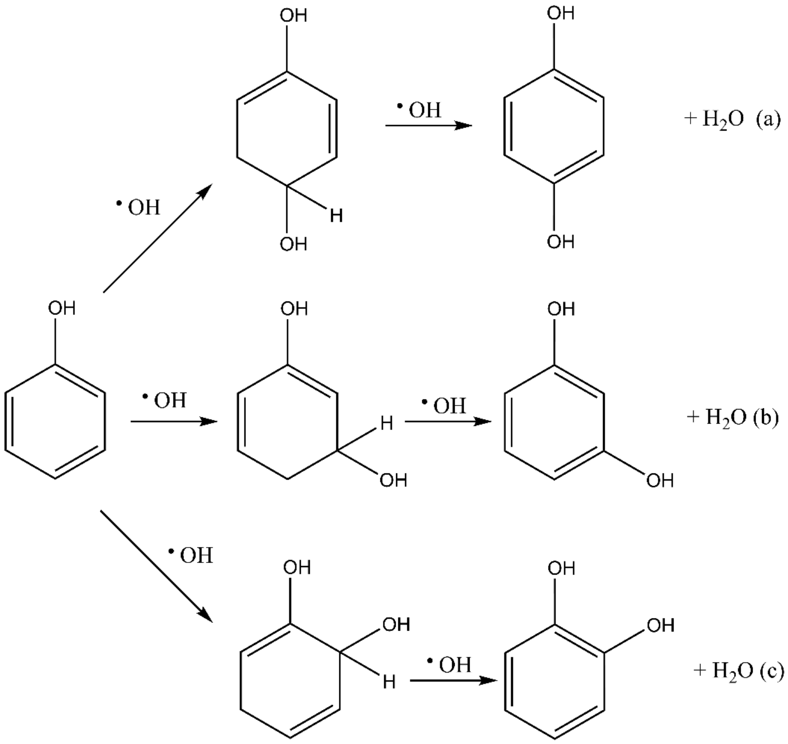

Rate constants were determined through kinetic modeling of the reaction rate, with the response variable being color at 436 nm in treated POME. Table 15 presents the rate constants and correlation coefficients (R^2) for the mathematical models of rate orders 0, 1, and 2 in the advanced oxidation processes of POME colored pigments. Considering the existence of two kinetic regimes at temperatures of 323 and 338 K, the mathematical modeling was conducted in the fast regime. As anticipated, with the increase in reaction temperature for each material, the rate constant exhibited an increase, attributed to the heightened kinetic energy of molecules, facilitating more effective interactions among them. The first-order reaction rate model demonstrated the best fit based on a higher R^2 value (Figure 25). The kinetics of each material exhibited variations contingent on the surface treatment of each biocomposite, with AHP-EFB-Fe showed higher rate constants (k_1) than the other materials at all temperatures. Additionally, NaOH-HCl-EFB-Fe exhibited a slower reaction rate compared to EFB-Fe and AHP-EFB-Fe. While the rate constants differed for each material, they displayed similar trends. Specifically, k_1 exhibited a more significant increase when transitioning from 308 to 323 K than when moving from 323 to 338 K. For the initial 15 K temperature increase, k_1 increased by 10, 8, and 7 times for EFB-Fe, AHP-EFB-Fe, and NaOH-HCl-EFB-Fe, respectively. Subsequently, when transitioning from 323 to 338 K, k_1 increased approximately 2 times for each biocomposite.

Table 15. Kinetic rate constants of the zero (K_0), first (k_1), and second (k_2) order, in the removal of color from POME

Material	**Temp. [K]**	**% Color removal**	**Zero order**		**Fist order**		**Second order**	
			k_0 [m^{-1}/min]	R^2	k_1 [min^{-1}]	R^2	k_2 [m^1/min]	R^2
EFB-Fe	308	17.4	$1.8x10^{-1}$	0.81	$1.5x10^{-3}$	0.81	$1.4x10^{-5}$	0.79
	323	71.2	$8.7x10^{-1}$	0.91	$1.6x10^{-2}$	0.94	$3.2x10^{-4}$	0.92
	338	63.9	2.2	0.96	$3.1x10^{-2}$	0.97	$4.9x10^{-4}$	0.93
AHP-EFB-Fe	308	26.5	$2.7x10^{-1}$	0.80	$2.4x10^{-3}$	0.79	$2.2x10^{-5}$	0.75
	323	76.4	$9.4x10^{-1}$	0.93	$1.8x10^{-2}$	0.97	$4.2x10^{-4}$	0.95
	338	75.9	2.2	0.93	$3.6x10^{-2}$	0.99	$6.7x10^{-4}$	0.97
NaOH-HCl-EFB-Fe	308	23.9	$2.8x10^{-1}$	0.97	$2.3x10^{-3}$	0.97	$1.9x10^{-5}$	0.95
	323	64.7	1.0	0.98	$1.6x10^{-2}$	0.99	$2.6x10^{-4}$	0.95
	338	67.3	1.9	0.93	$2.9x10^{-2}$	0.94	$4.8x10^{-4}$	0.91

Figure 25 . First-order kinetic modelling pome using the biocomposites a) EFB-Fe, b) AHP-EFB-Fe and c) NaOH-HCl-EFB-Fe

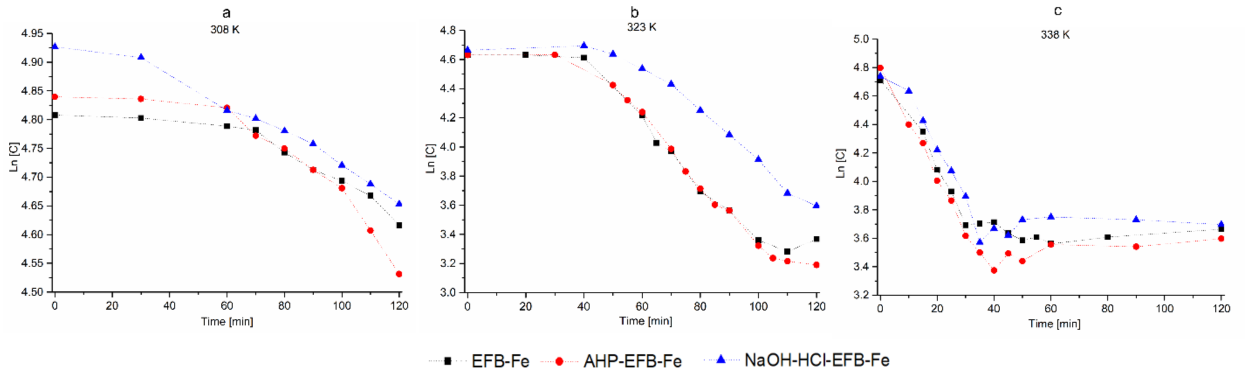

Heterogeneous catalysts feature distinct chemically active sites where reactions occur, and these sites are heterogeneously distributed on the catalyst surface. However, they can be inhibited or poisoned during reactions. The crystalline structure of the solid catalyst, particularly in the case of magnetite, plays a crucial role. In a face-centered cubic system, Fe^{3+} ions occupy the tetrahedral positions, while both Fe^{2+} and Fe^{3+} ions are present in the octahedral positions. This heterogeneity by the crystal structure, impacting the interaction with molecules during reactions (Védrine, 2014). Magnetite's crystalline structure gives rise to two interfacial mechanisms in heterogeneous Fenton reactions. The first mechanism involves an induced homogeneous Fenton process, initiated by the leaching of iron supported in the matrix, typically generated under specific reaction conditions like acidic pH. Homogeneous Fenton systems are characterized by rapid reactions with rate constants in the range of 10^9 to 10^{10} L/mol*s. The second mechanism is associated with heterogeneous catalysis, encompassing processes such as reaction adsorption, surface reaction, and product desorption. This mechanism tends to be slower than homogeneous Fenton. In some cases, both mechanisms may coexist within the same reaction (He et al., 2016). However, an increase in catalyst concentration can lead to a decrease in color removal efficiency due to the oxidation of ferrous ions by the hydroxyl radical (equation 17) (Ramirez et al., 2005; Xavier et al., 2015). The removal efficiency is significantly influenced by the quantity of leached iron. It is important to highlight that in prior investigations, all three biocomposites underwent iron leaching, with NaOH-HCl-EFB-Fe exhibiting the highest leaching, succeeded by EFB-Fe, and finally, AHP-EFB-Fe. Consequently, AHP-EFB-Fe displayed superior removal efficiency, followed by EFB-Fe, and ultimately, NaOH-HCl-EFB-Fe . This finding emphasizes the significant impact of leached iron on determining the efficacy of the biocomposites in removing color from POME.

$$Fe^{2+} + OH^{\bullet} \rightarrow Fe^{3+} + OH^{-} \quad (17)$$

Kongnoo et al. reported homogeneous Fenton-based color removal from POME using 50 mM H_2O_2 and 1 mM Fe^{2+} at pH 3, with a rate constant of 6.2×10^{-2} min-1 (pseudo-first-order reaction) (Kongnoo et al., 2012). The k_1 obtained for our three biocomposites at various temperatures is comparatively lower, as our oxidation reactions utilized 1.79 mM Fe^{2+} and 6.35 mM H_2O_2. Higher concentrations of H_2O_2 in homogeneous Fenton reactions generally lead to increased removal efficiency and a higher rate constant (Gamaralalage et al., 2020; Kongnoo et al., 2012). Homogeneous Fenton processes are typically faster than heterogeneous ones (He et al., 2016). Moreover, the rate constant tends to increase with temperature. For instance, the decolorization of phenol red in homogeneous Fenton at different temperatures followed a first-order model, with rate constants of $1.8\text{x}10^{-2}$, $4.7\text{x}10^{-2}$, $6.6\text{x}10^{-2}$ and $2.3\text{x}10^{-1}$ min^{-}at 293, 303, 313, and 323 K, respectively (Santana et al., 2019). In our biocomposites, a slight increase in the rate constant was observed when elevating the temperature from 323 to 338 K, yet in AHP-EFB-Fe and EFB-Fe, the removal efficiency decreased. Therefore, 323 K stands out as the optimal reaction temperature, as previously indicated.

The Ea for each biocomposite EFB-Fe, AHP-EFB-Fe, and NaOH-HCl-EFB-Fe was determined using the Arrhenius equation based on the rate constants and temperature (Figure 26). The obtained activation energies were 87.6, 78.7, and 73.3 KJ/mol, for EFB-Fe, AHP-EFB-Fe, and NaOH-HCl-EFB-Fe respectively. Ea represents the minimum energy required for a reaction to occur (Gajrani & Sankar, 2020). The magnitude of Ea indicates the type of adsorption involved, with energies between 5 and 40 KJ/mol characteristic of physisorption and energies above 40 KJ/mol indicative of chemisorption (Covinich et al., 2018; Hameed et al., 2007; Nollet et al., 2003). In this context, chemisorption governs the advanced oxidation of POME pigments by biocomposites. However, the activation energies in the Fenton reactions are different for each type of catalyst and each type of contaminant. The kinetic modeling of the oxidation of the azo dye Orange II, employing a carbon-Fe catalyst, was conducted using a first-order reaction. This analysis revealed an Ea of 56.1 KJ/mol for dye removal under specific conditions: 0.2 g/L catalyst, 6 mM H_2O_2, pH 3, and a reaction duration of 4 hours (Ramirez et al., 2007).

Likewise, the decolorization of rhodamine B using magnetite and bismuth ferrite heterogeneous catalysts was conducted with 0.5 g/L catalyst, 10.0 mM H_2O_2, pH 5, and a 2-hour reaction time, modeled with a first-order reaction rate. For magnetite, the rate constants (k_1) and Ea were determined to be 1.47×10^{-3} min^{-1} and 45.6 kJ/mol, respectively, while for bismuth ferrite, the corresponding values were 2.89×10^{-2} min^{-1} and 20.7 KJ/mol (W. Luo et al., 2010). In a similar vein, Han et al. utilized attapulgite-Fe_3O_4 magnetic nanocomposites for the degradation of ethidium bromide. The kinetic studies indicated a pseudo-first order rate constant (k_1) of 2.4 min^{-}

^{1} at T = 323 K, pH 2.0, with H_2O_2 at 30 mM and 1.5 g/L catalyst, and an Ea of 78.39 kJ/mol obtained between 293 and 323 K (S. Han et al., 2017). These studies underscore the applicability of iron catalysts, particularly magnetite, in removing various organic contaminants, following first-order kinetics. The endothermic nature of this oxidation process is influenced by temperature, with the rate constant increasing as temperature rises (Araña et al., 2012). However, there exists an optimum temperature for each set of reaction conditions, as high temperatures can lead to the decomposition of hydrogen peroxide, impacting process efficiency (Ramirez et al., 2007). Examining the activation energy, it becomes evident that it is a function of the catalyst, reagents, temperature, and the pollutant to be oxidized. The Ea values obtained for our biocomposites are higher compared to those reported, indicative of a slower reaction rate. This is attributed to the complexity of treating multiple pigments in POME, requiring an extended reaction time for their oxidation

Figure 26. Plots of (a) lnk versus 1/T and (b) ln (k/T) versus 1/T for the color removal POME

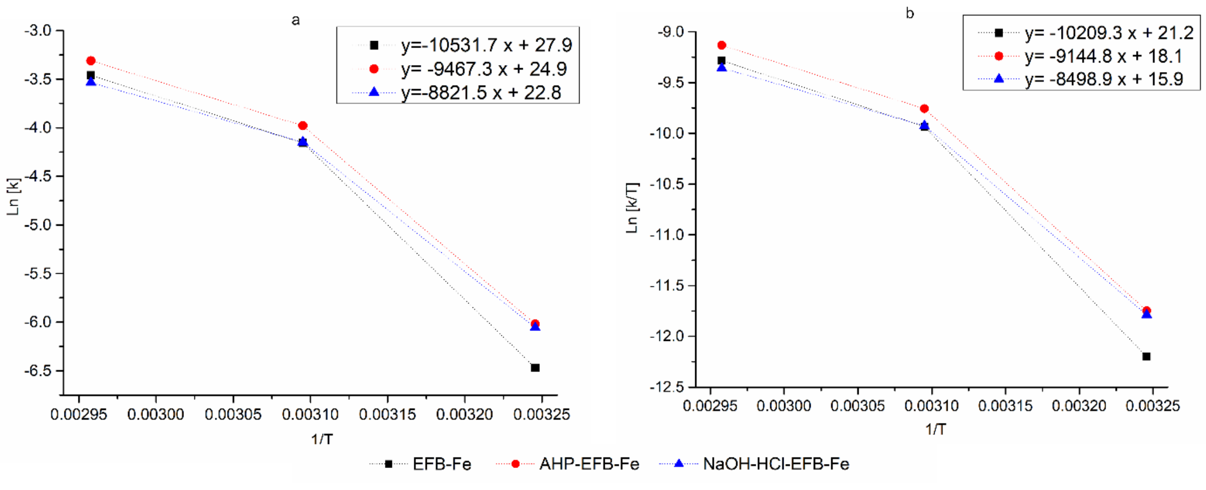

From the plot of Ln(k/T) as a function of 1/T (Figure 26b), the activation enthalpy $\Delta H^{\ddagger}$ and entropy $\Delta S^{\ddagger}$ were determined using the Eyring-Polanyi equation. The free activation energy $\Delta G^{\ddagger}$ was calculated with $\Delta H^{\ddagger}$ and $\Delta S^{\ddagger}$ at 323K (Table 16). The positive value of the enthalpy indicates that the reaction is endothermic, as mentioned above. This is because the system requires energy for oxidation to take place. The negative value of the entropy indicates a higher order of the reactants in the transition state than in the initial state. Finally, a positive value of the free energy of activation indicates that the reaction is not spontaneous. While there have been numerous thermodynamic studies for textile dyes oxidized by Fenton reaction, no such studies have been reported for color removal in POME. However, some thermodynamic studies have reported positive enthalpies and free energies and negative entropies in the oxidation of their contaminants (Alattar et al., 2020; Giwa et al., 2020; Kumar et al., 2020). This study is noteworthy for utilizing authentic samples, facilitating a comprehensive comprehension of the kinetic and thermodynamic behavior of EFB/magnetite biocomposites in the degradation of flocculated POME. This information is crucial for understanding reaction conditions and enables the effective adjustment, optimization, and scaling of processes to an industrial scale.

Table 16. Thermodynamic parameters from the Eyring-Polanyi equation

Biocomposite	**$\Delta H^{\ddagger}$ [KJ/mol]**	**$\Delta S^{\ddagger}$ [J/K*mol]**	**$\Delta G^{\ddagger}$[KJ/mol]**
EFB-Fe	84.9	-21.4	91.8
AHP-EFB-Fe	76.0	-46.7	91.1
NaOH-HCl-EFB-Fe	70.7	-64.5	91.5

4.5. Conclusions

The color oxidation kinetics of POME were described by a first-order reaction model. Furthermore, magnetite leaching was found to be a key factor influencing the reaction kinetics. Excessive presence of magnetite caused system poisoning and resulted in a decreased reaction rate.

The temperature increases from 323 to 338 K revealed two distinct kinetic regimes. At 323 K, the oxidation reaction exhibits a slow pace for the initial 35 minutes, followed by an acceleration. Contrastingly, at 338 K, oxidation reaction is rapid during the first 35 minutes of reaction. Oxidation then stops. This kinetic behavior correlates with the rate of hydroxyl radical production, a process that benefits from elevated temperatures. However, the temperature increase led to a decrease in color removal efficiency for the EFB-Fe and AHP-EFB-Fe biocomposites, and there was a slight improvement for the NaOH-HCl-EFB-Fe biocomposite under the same conditions.

The EFB/magnetite biocomposites exhibited a color removal process in POME, characterized by an activation energy exceeding 70.7 kJ/mol, indicative of complex chemisorption mechanisms. Thermodynamic analysis conclusively identified the reaction as endothermic, with a positive free energy of activation, signifying its non-spontaneous nature. These findings provide crucial insights for potential industrial-scale applications.

Conclusions

In Chapter I, physicochemical characterization was conducted on two cultivars, E.G and the O×G hybrid, considering bunch parts (stalks and spikelets) and bunch conditions (fresh and sterilized). No significant differences were observed between the cultivars, bunch parts, or bunch conditions in terms of morphology, thermal stability, crystallography, and lignocellulosic content. On average, fibers from both cultivars contained approximately 7.0% ash, 4.8% ethanol-toluene extractives, 47.5% cellulose, 19.8% lignin, and 20.6% hemicellulose. However, differences were noted in the elemental composition, with the O×G hybrid showing higher silicon and potassium content compared to the E.G cultivar, while the E.G cultivar had more chlorine. Sterilization was found to increase the sugar content. Additionally, statistically significant variations in compositional content were observed between the stalks and spikelets.

In Chapter II, nanocellulose was successfully isolated via TEMPO oxidation with yields reaching 60%. The TEMPO-oxidation process of EFB revealed that variations in reaction time, the amount of primary oxidant (NaClO), and matrix pretreatment influenced the surface chemistry, particle size, and reaction yield of TOCN isolated from EFB. Particularly, the amount of NaClO had the most significant impact on the degree of oxidation (amount of COO^-) of the final material. Delignification of EFB resulted in increased oxidation and reaction yield (50%) compared to untreated EFB. Remarkably, only the reaction time showed a significant effect on the hydrodynamic radii of TOCN, indicating that a reaction time exceeding 120 minutes was necessary to achieve nanocellulose particles smaller than 100 nm.

In Chapter III, EFB/magnetite biocomposites were synthesized and characterized, confirming the presence of iron. The NaOH-HCl-EFB-Fe biocomposite exhibited a higher iron content (3.00% iron) compared to AHP-EFB-Fe (2.54% iron) and EFB-Fe (1.80% iron). All biocomposites successfully removed 65% of the color and 90% of phenols present in the POME. The best-performing biocomposite was AHP-EFB-Fe, achieving over 60% color removal from the POME during 9 cycles of reuse. Additionally, reinforcements with TOCN enhanced color removal efficiency, reduced iron leaching by 44%, and extended the reuse cycle between 1 and 2 cycles. AHP-EFB-Fe reinforced with TOCN removed more than 71% of the color during 10 cycles of reuse. It is noteworthy that the untreated EFB effectively removed over 70% of the color during the initial 5 reuse cycles while maintaining its stability. In contrast, pretreatments enhanced surface reactivity, which was evidenced by an increased iron content.

In the last chapter, the reaction order for color removal from POME was first-order for all biocomposites (EFB-Fe, AHP-EFB-Fe, and NaOH-HCl-EFB-Fe), indicating an endothermic reaction. The color removal process using EFB/magnetite biocomposites requires an activation energy exceeding 73.5 kJ/mol, suggesting chemisorption processes. Thermodynamic analysis based on the transition state further confirmed the endothermic nature of the reaction.

Future Work

Explore new surface modification treatments to generate stronger interactions between the EFB matrix and metal oxides. Additionally, conduct an in-depth investigation of surface interactions between materials using techniques such as XPS, TEM, and SEM. In terms of reinforcements, analyze different ionic environments considering the surface properties of each compound. Utilize the residues from the biocomposites (when they reach the maximum reuse cycles) as matrices for hydrogel synthesis. Finally, evaluate the performance of the biocomposites in other industrial effluents.

Participation in conferences and articles

During the development of this doctoral thesis project, the following publications in journals and participation in academic events were carried out.

Scientific Production

1. Combariza, M. Y., Martínez-Ramírez, A. P., & Blanco-Tirado, C. (2021). Perspectives in Nanocellulose for Crude Oil Recovery: A Minireview. In *Energy and Fuels* (Vol. 35, Issue 19, pp. 15381–15397). American Chemical Society. https://doi.org/10.1021/acs.energyfuels.1c02230
2. Martínez-Ramírez, A. P., Rincón-Ortiz, S. A., Baldovino-Medrano, G., Blanco-Tirado, C., & Combariza, M. Y. (2023). Influence of reaction variables on the surface chemistry of cellulose nanofibers derived from palm oil empty fruit bunches. *RSC Advances*, *13*, 36117–36129. https://doi.org/10.1039/d3ra06933h.

Academic Events

- Martínez-Ramírez, A. P., Blanco-Tirado, C., & Combariza, M. Y. Exploring experimental variables affecting the degree of oxidation of nanocellulose extracted from oil palm empty fruit bunches. Poster presenter (online). ACS SPRING 2022.
- Martínez-Ramírez, A. P., Blanco-Tirado, C., & Combariza, M. Y. Empty fruit bunch/fexoy composites for palm oil mill effluents treatment. Poster presenter. 35° Congresso latinoamericano de química e 61° congresso brasileiro de química, 2022.
- Martínez-Ramírez, A. P., Blanco-Tirado, C., & Combariza, M. Y. Physicochemical properties of palm oil empty fruit bunches from E. guineensis and E. oleifera x E. guineensis cultivars grown in Colombia. Oral presenter (online). ACS SPRING 2023

.

Appendix

Appendix A. Cross-sectional images of samples

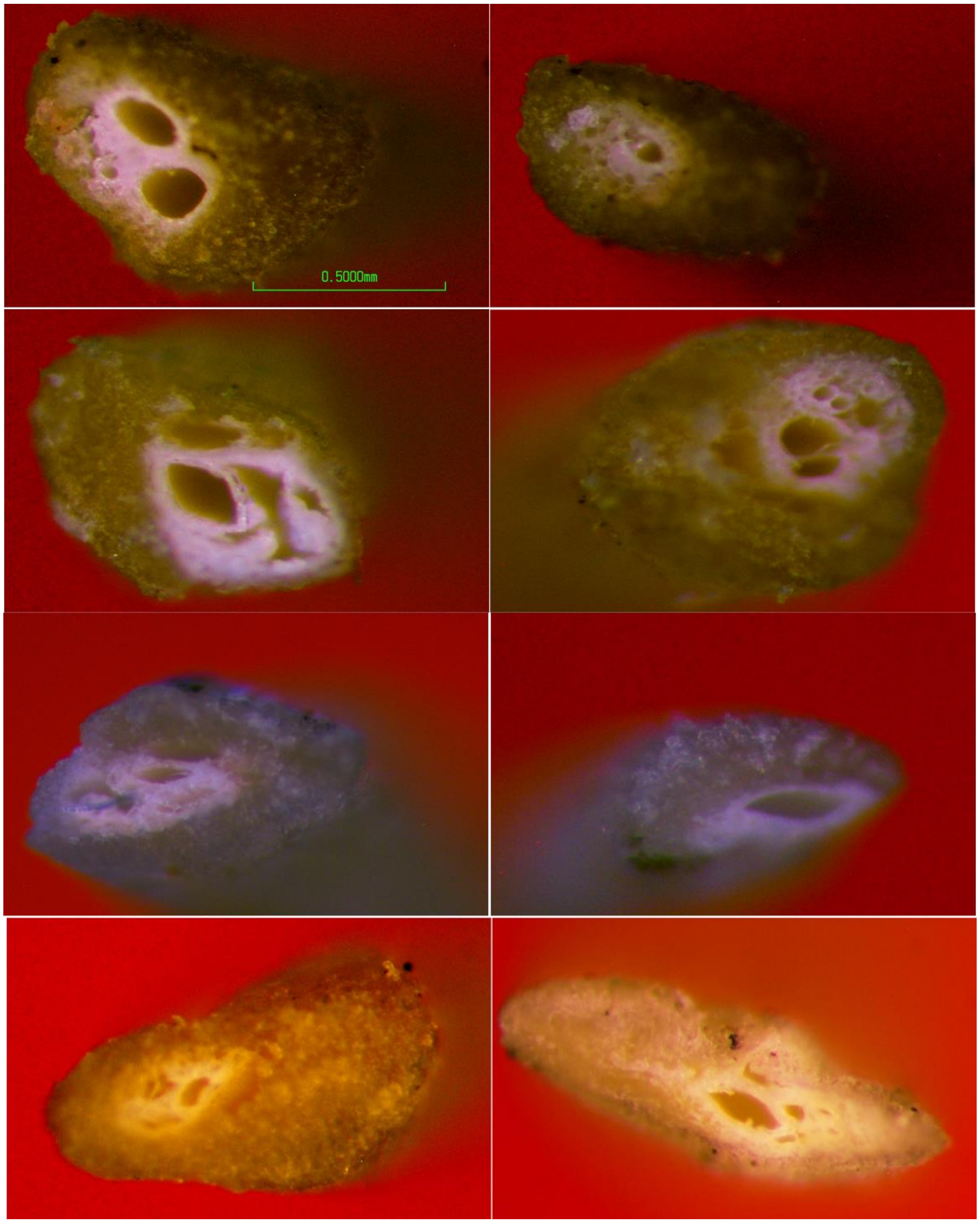

Appendix B. Comparison of the lignocellulose composition obtained by the NREL method and the gravimetric standards (TAPPI 222, Kurscher-Hoffer and Jayme-Wise methods)

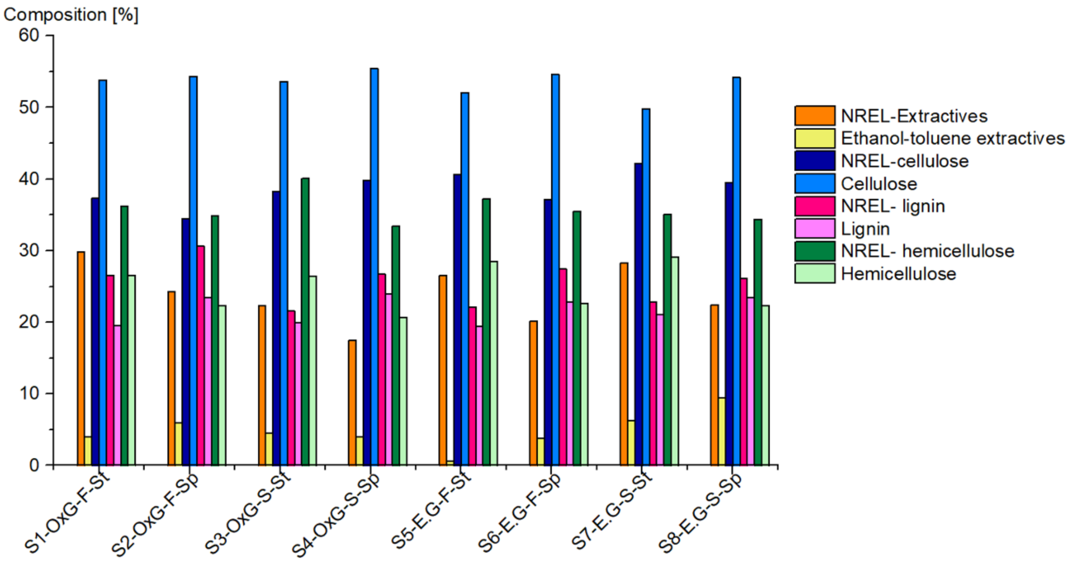

Appendix C. Diffractograms of samples a) S3-S4, b) S5-S6, c) S7-S8 and diffraction patterns d) S1, and e) S2

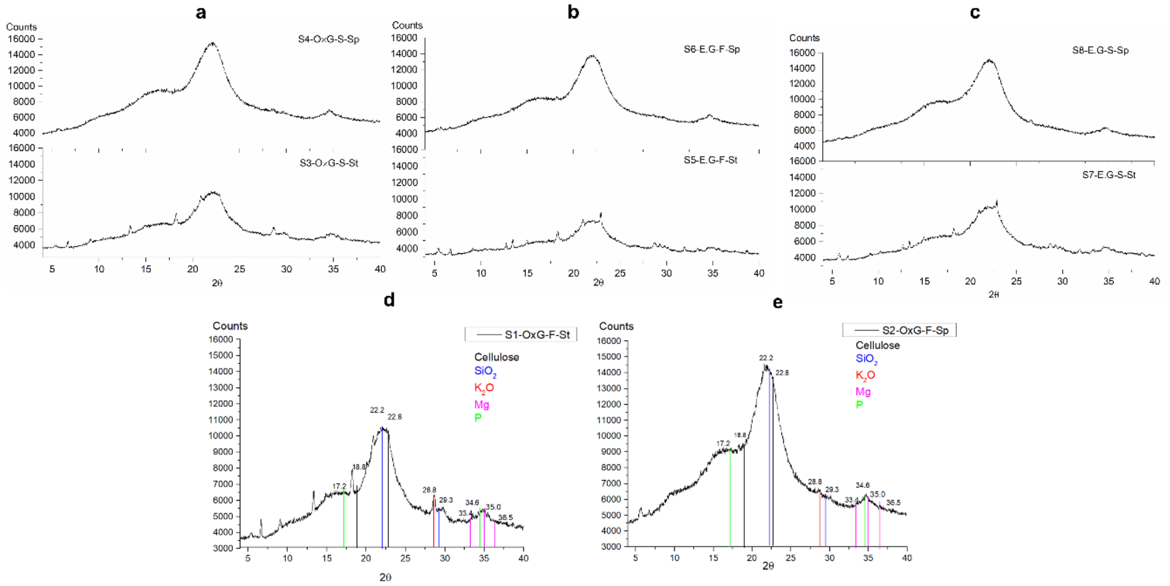

Appendix D Thermogravimetric analysis Samples S1-S4 a) TGA and b) DTG, and samples S5-S8 c) TGA and d) DTG

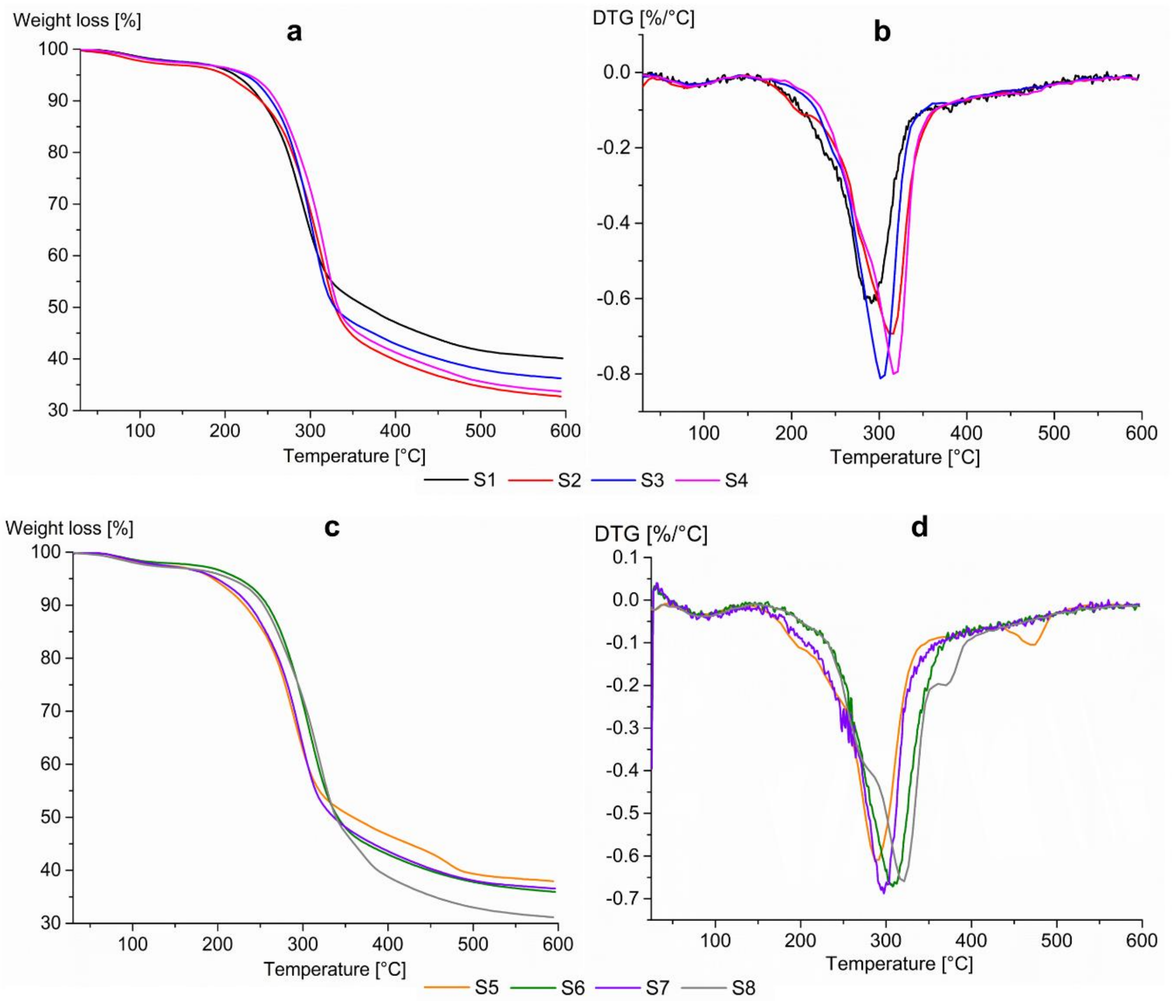

Appendix E Multilevel Factorial Design 2^4

No. Experiments	Identification samples	Experimental parameters	
		Reaction time [min]	**Cellulose:NaClO molar ratio**
1	TOCN 30-1:1	30	1:1
2	TOCN 30-1:5	30	1:5
3	TOCN 30-1:8	30	1:8
4	TOCN 30-1:10	30	1:10
5	TOCN 60-1:1	60	1:1
6	TOCN 60-1:5	60	1:5
7	TOCN 60-1:8	60	1:8
8	TOCN 60-1:10	60	1:10
9	TOCN 90-1:1	90	1:1
10	TOCN 90-1:5	90	1:5
11	TOCN 90-1:8	90	1:8
12	TOCN 90-1:10	90	1:10
13	TOCN 120-1:1	120	1:1
14	TOCN 120-1:5	120	1:5
15	TOCN 120-1:8	120	1:8
16	TOCN 120-1:10	120	1:10

Appendix F. FTIR-ATR spectra of TOCN isolated from Palm Oil Empty Fruit Bunches (EFB). a) Effect of changes in cellulose:NaClO ratios for a reaction time of 120 min for AHP-EFB-TOCN, and b) Effect of changes in reaction time for AHP-EFB-TOCN

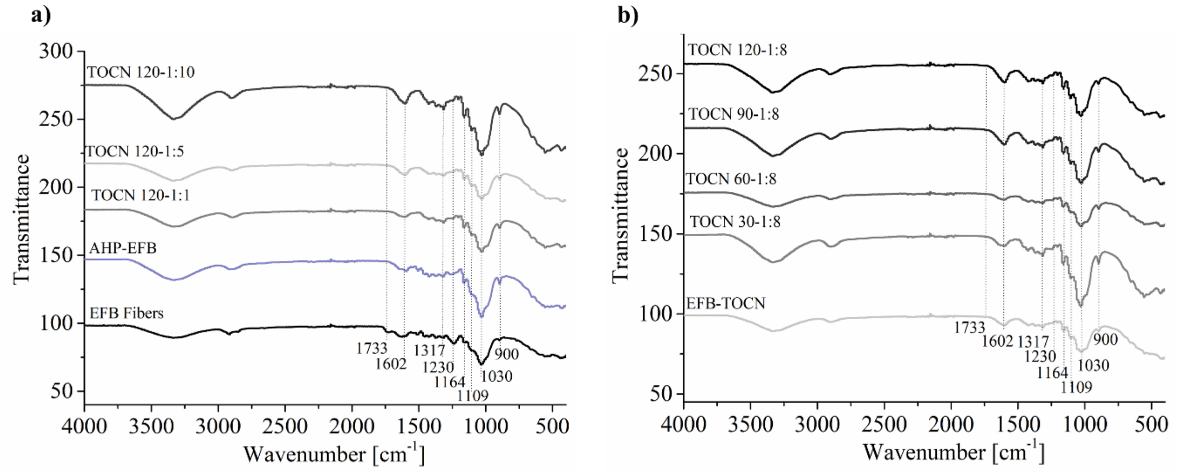

Appendix G. Signal assignment infrared spectroscopy

Wave number [cm^{-1}]	Functional group	Reference
1733	C=O stretch of acetyl and hemicellulose	Kaffashsaie et al., 2021
1602	Stretching C=O in carboxylic acids with sodium	(Chuensangjun et al., 2019; C. F. Huang et al., 2015)
1317	Stretch flexion CH_2 in cellulose	(Traoré et al., 2018)
1230	Asymmetric axial deformation =C-O- in the ether, ester, and phenol group of lignin	
1164	Asymmetrical C-O-C stretch of the pyranose ring	(Fahma et al., 2020)
1109	C-O-C stretch of cellulose	(Traoré et al., 2018)
1030	Cellulose C-O and C-H stretching vibrations	(Fahma et al., 2010)
900	specific C-H anomeric vibration for β-glycosides	

Appendix H. Conductimetric titration graphs of oxidized cellulose suspensions

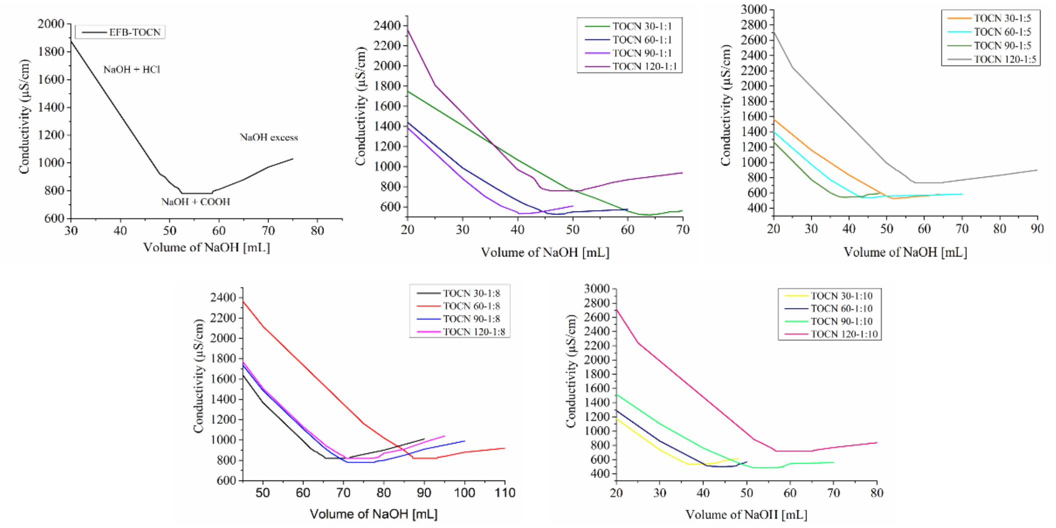

Appendix I. Statistical analysis Pareto chart, Main effects plot, Estimated response surface, and Interaction plot of 1) Charge density, 2) Reaction yield, 3) size distribution and 4) Z-potential

1

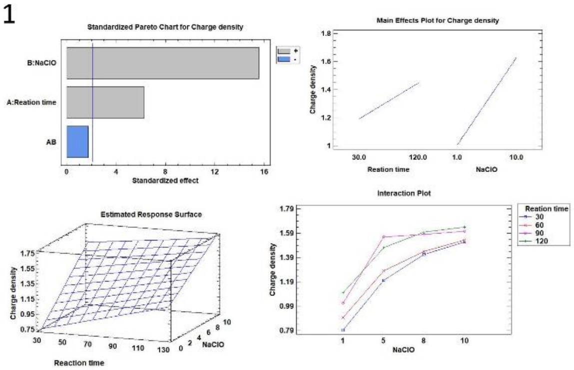

2

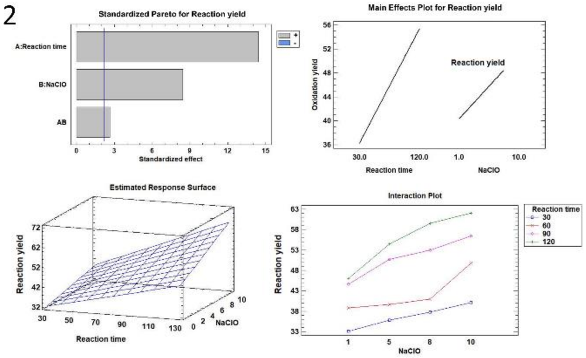

3

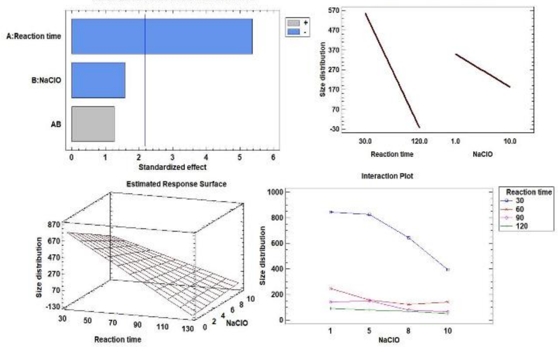

4

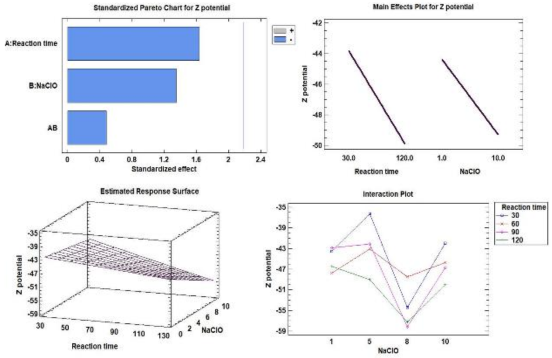

Appendix J Positions and values of FWHM

Atom		**XPS data**	**EFB**	**EFB-AHP**	**EFB-TOCN**	**TOCN 30-1:8**	**TOCN 60-1:8**	**TOCN 90-1:8**	**TOCN 120-1:8**	**TOCN 120-1:1**	**TOCN 120-1:5**	**TOCN 120-1:10**
C	C-H	Position [eV]	284.8	284.8	284.8	284.8	284.8	284.8	284.8	284.8	284.8	284.8
		FWHM	2.37	1.91	1.28	1.30	1.35	1.26	1.20	1.30	1.14	1.21
	C-C-O	Position [eV]	-	286.8	286.5	286.5	286.5	286.5	286.4	286.5	286.5	286.4
		FWHM	-	1.91	1.28	1.30	1.35	1.26	1.20	1.30	1.14	1.21
	O-C-O	Position [eV]	287.9	288.6	288.2	287.9	288.1	288.0	288.3	287.9	287.9	287.7
		FWHM	2.37	1.55	1.28	1.30	1.35	1.26	1.20	1.30	1.14	1.21
	C-COO-	Position [eV]	-	-	289.5	288.8	289.4	289.3	289.5	289.0	288.7	288.6
		FWHM	-	-	1.28	1.30	1.35	1.26	1.20	1.30	1.14	1.21
O		Position [eV]	532.5	532.6	532.3	532.9	532.7	532.8	531.9	533.0	532.9	532.8
		FWHM	2.90	2.52	2.43	1.99	2.4	2.17	2.15	1.88	1.81	1.90
Ca	3/2	Position [eV]	347.5	347.2	347.3	347.5	347.3	347.3	347.3	347.4	347.39	347.3
		FWHM	2.32	1.94	1.48	1.48	1.57	1.54	1.44	1.5	1.46	1.77
	1/2	Position [eV]	351.1	350.9	350.9	351.1	350.9	350.9	350.9	351.0	351.0	350.9
		FWHM	2.20	1.95	1.56	1.59	1.56	1.55	1.52	1.50	1.50	1.83
Si		Position [eV]	101.9	-	-	101.9	101.9	-	101.9	-	-	-
		FWHM	1.94	-	-	1.36	1.42	-	0.98	-	-	-
Na		Position [eV]	-	-	1073.9	1072.9	1073.8	1073.7	1072.2	1074.3	1072.6	1072.1
		FWHM	-	-	1.83	2.18	2.74	2.39	2.25	1.63	1.68	2.22
Cl	3/2	Position [eV]	-	-	198.4	-	-	198.8	-	197.8	198.2	198.2
		FWHM	-	-	1.87	-	-	2.49	-	1.56	2.31	2.12
	1/2	Position [eV]	-	-	200.02	-	-	200.4	-	199.4	199.8	199.8
		FWHM	-	-	1.28	-	-	1.84	-	1.43	2.09	0.98
N		Position [eV]	-	-	398.7	399.9	-	398.7	398.3	400.0	399.8	399.9
		FWHM	-	-	0.78	1.50	-	0.50	0.1	2.34	2.50	1.83

Appendix K. Experimental design color removal of POME

Factor levels			**Samples**	**pH**	**H_2O_2 30%**	**Biocomposite**
Parameter	Low (-)	High (+)	1	-	-	-
pH	3.0	4.0	2	-	-	+
			3	-	+	-
H_2O_2 30 % [mL]	0.05	0.1	4	-	+	+
			5	+	-	-
			6	+	-	+
Biocomposite [g]	0.2	0.4	7	+	+	-
			8	+	+	+

Appendix L. TOCN surface characterization by XPS

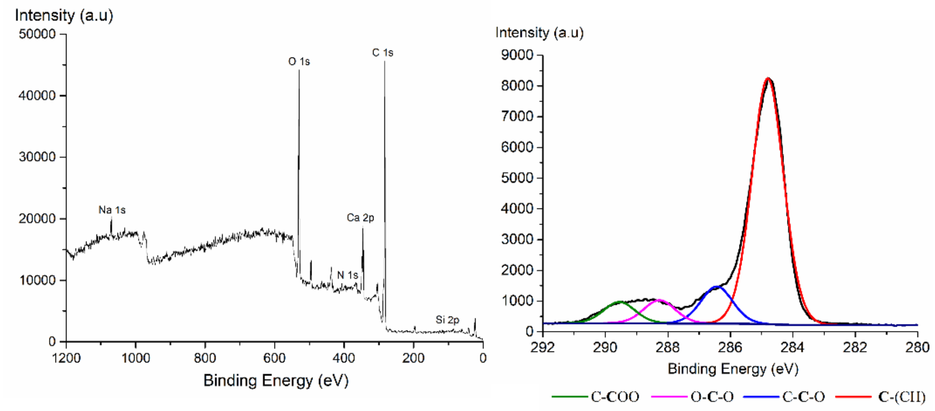

Name		**% Area**
C 1s		71.0
C-C	54.1	
C-O	7.6	
O-C-O/C=O	4.8	
O-C=O	4.5	
O 1s		21.0
Cl 1s		1.0
Na 1s		0.4
Ca 2p		5.7
Si 2p		<0.5
N 1s		<0.5

References

Abdullah, C. I., Azzahari, A. D., Rahman, N. M. M. A., Hassan, A., & Yahya, R. (2019). Optimizing Treatment of Oil Palm-Empty Fruit Bunch (OP-EFB) Fiber: Chemical, Thermal and Physical Properties of Alkalized Fibers. *Fibers and Polymers*, *20*(3), 527–537. https://doi.org/10.1007/s12221-019-8492-0

Ahmad Kuthi, F. A., Haji Badri, K., & Mohmad Azman, A. (2015). X-Ray Diffraction Patterns of Oil Palm Empty Fruit Bunch Fibers with Varying Crystallinity. *Advanced Materials Research*, *1087*, 321–328. https://doi.org/10.4028/www.scientific.net/amr.1087.321

Ahmadzadeh, A., & Zakaria, S. (2009). Preparation of novolak resin by liquefaction of oil palm empty fruit bunches (EFB) and characterization of EFB residue. *Polymer - Plastics Technology and Engineering*, *48*(1), 10–16. https://doi.org/10.1080/03602550802497776

Akhtar, K., Ali, F., Sohni, S., Kamal, T., Asiri, A. M., Bakhsh, E. M., & Khan, S. B. (2020). Lignocellulosic biomass supported metal nanoparticles for the catalytic reduction of organic pollutants. *Environmental Science and Pollution Research*, *27*(1), 823–836. https://doi.org/10.1007/s11356-019-06908-y

Alattar, R. A., Saleh, H. M., AL-Hilfi, J. A., & Ahmed, L. M. (2020). Influence the addition of Fe2+ and H2o2 on removal and decolorization of textile dye (dispersive yellow 42 dye). *Egyptian Journal of Chemistry*, *63*(9), 3453–3463. https://doi.org/10.21608/ejchem.2020.23542.2400

Aliyu-Yaro, N. S., Sutanto, M. H., Habib, N. Z., Napiah, M., Usman, A., Jagaba, A. H., & Al-Sabaeei, A. M. (2022). Application and circular economy prospects of palm oil waste for eco-friendly asphalt pavement industry: A review. *Journal of Road Engineering*, *2*(4), 309–331. https://doi.org/10.1016/j.jreng.2022.10.001

Alle, M., Bandi, R., Sharma, G., Lee, S. H., & Kim, J. C. (2021). Shape recoverable, Au nanoparticles loaded nanocellulose foams as a recyclable catalyst for the dynamic and batch discoloration of dyes. *Carbohydrate Polymers*, *258*. https://doi.org/10.1016/j.carbpol.2021.117693

Al-Maari, M. A., Ahmad, M. A., Din, A. T. M., Hassan, H., & Alsobaai, A. M. (2021). Co-pyrolysis of oil palm empty fruit bunch and oil palm frond with low-density polyethylene and polypropylene for bio-oil production. *Arabian Journal of Chemistry*, *14*(8). https://doi.org/10.1016/j.arabjc.2021.103282

Althausen, M. (2016). Palm Oil Mill Effluent Treatment-Converting a Residue into a Resource. *Revista Palmas*, *37*, 31–37.

Alvarez, V., Rodriguez, E., & Vásquez, A. (2006). Thermal degradation and decomposition of jutevinylester composites. *Journal of Thermal Analysis and Calorimetry*, *85*, 383–389.

Alvarez-Vasco, C., & Zhang, X. (2017). Alkaline hydrogen peroxide (AHP) pretreatment of softwood: Enhanced enzymatic hydrolysability at low peroxide loadings. *Biomass and Bioenergy*, *96*, 96–102. https://doi.org/10.1016/j.biombioe.2016.11.005

Amran, U. A., Zakaria, S., Chia, C. H., Fang, Z., & Masli, M. Z. (2017). Production of Liquefied Oil Palm Empty Fruit Bunch Based Polyols via Microwave Heating. *Energy and Fuels*, *31*(10), 10975–10982. https://doi.org/10.1021/acs.energyfuels.7b02098

Anand, A., Gautam, S., & Chand Ram, L. (2023). A characteristic-based decision tree approach for sustainable energy applications of biomass residues from two major classes. *Fuel*, *339*. https://doi.org/10.1016/j.fuel.2023.127483

Anushree, C., & Philip, J. (2019). Efficient removal of methylene blue dye using cellulose capped Fe 3 O 4 nanofluids prepared using oxidation-precipitation method. *Colloids and Surfaces A: Physicochemical and Engineering Aspects*, *567*, 193–204. https://doi.org/10.1016/j.colsurfa.2019.01.057

Araña, J., Ortega Méndez, J. A., Herrera Melián, J. A., Doña Rodríguez, J. M., González Díaz, O., & Pérez Peña, J. (2012). Thermal effect of carboxylic acids in the degradation by photo-Fenton of high concentrations of ethylene glycol. *Applied Catalysis B: Environmental*, *113–114*, 107–115. https://doi.org/10.1016/j.apcatb.2011.11.025

Araya-Chavarría, K., Rojas, R., Ramírez-Amador, K., Sulbarán-Rangel, B., Rojas, O., & Esquivel-Alfaro, M. (2022). Cellulose Nanofibers as Functional Biomaterial from Pineapple Stubbles via TEMPO Oxidation and Mechanical Process. *Waste and Biomass Valorization*, *13*(3), 1749–1758. https://doi.org/10.1007/s12649-021-01619-3

Arnaut, L. (2021). *Chemical Kinetics From Molecular Structure to Chemical Reactivity: Vol. Second Edition*.

Arunachalam, V. (2012). Oil Palm. In *Genomics of Cultivated Palms* (pp. 29–48). Elsevier. https://doi.org/10.1016/B978-0-12-387736-9.00003-0

Arutanti, O., Sari, A. A., Berkah, A., Nurdin, M., Fitriady, M. A., Parmawati, Y., Rinaldi, N., Yuniarto, A., & Hadibarata, T. (2020). Advanced Degradation of Lignin from Palm Oil Mill Effluent (POME) by a Combination of Photocatalytic-Fenton Treatment and TiO2 Nanoparticle as the Catalyst. *Water, Air, and Soil Pollution*, *231*(6). https://doi.org/10.1007/s11270-020-04617-8

Asadpour, R., Yavari, S., Kamyab, H., Ashokkumar, V., Chelliapan, S., & Yuzir, A. (2021). Study of oil sorption behaviour of esterified oil palm empty fruit bunch (OPEFB) fibre and its kinetics and isotherm studies. *Environmental Technology and Innovation*, *22*. https://doi.org/10.1016/j.eti.2021.101397

Asgarpour Khansary, M., Pouresmaeel-Selakjani, P., Ali Aroon, M., Hallahisani, A., Cookman, J., & Shirazian, Saeed. (2020). A molecular scale analysis of TEMPO-oxidation of native cellulose molecules. *Heliyon*, *6*.

Asim, M., Paridah, M. T., Chandrasekar, M., Shahroze, R. M., Jawaid, M., Nasir, M., & Siakeng, R. (2020a). Thermal stability of natural fibers and their polymer composites. In *Iranian Polymer Journal (English Edition)* (Vol. 29, Issue 7, pp. 625–648). Springer. https://doi.org/10.1007/s13726-020-00824-6

Asim, M., Paridah, M. T., Chandrasekar, M., Shahroze, R. M., Jawaid, M., Nasir, M., & Siakeng, R. (2020b). Thermal stability of natural fibers and their polymer composites. In *Iranian*

Polymer Journal (English Edition) (Vol. 29, Issue 7, pp. 625–648). Springer. https://doi.org/10.1007/s13726-020-00824-6

ASTM International. (2013). *Standard Test Method for Ethanol-Toluene Solubility of Wood*. https://doi.org/10.1520/D1107-96R13

Azizi, A. (2020). Green Synthesis of Fe3O4 Nanoparticles and Its Application in Preparation of Fe3O4/Cellulose Magnetic Nanocomposite: A Suitable Proposal for Drug Delivery Systems. *Journal of Inorganic and Organometallic Polymers and Materials*, *30*(9), 3552–3561. https://doi.org/10.1007/s10904-020-01500-1

Azri Sukiran, M., Palm Oil Board, M., Institusi, P., Baru Bangi, B., Mee Chin, C., & Kartini Abu Bakar, N. (2009). Bio-oils from Pyrolysis of Oil Palm Empty Fruit Bunches Malaysian Palm Oil Board, No. *American Journal of Applied Sciences*, *6*(5), 869–875.

Bajpai, P. (2013). Products from Hemicelluloses. In *Biorefinery in the Pulp and Paper Industry* (pp. 65–98). Elsevier. https://doi.org/10.1016/b978-0-12-409508-3.00004-3

Bajwa, D. S., Pourhashem, G., Ullah, A. H., & Bajwa, S. G. (2019). A concise review of current lignin production, applications, products and their environment impact. *Industrial Crops and Products*, *139*. https://doi.org/10.1016/j.indcrop.2019.111526

Balea, A., Merayo, N., De La Fuente, E., Negro, C., & Blanco, Á. (2017). Assessing the influence of refining, bleaching and TEMPO-mediated oxidation on the production of more sustainable cellulose nanofibers and their application as paper additives. *Industrial Crops and Products*, *97*, 374–387. https://doi.org/10.1016/j.indcrop.2016.12.050

Barazzouk, S., & Daneault, C. (2012). Tryptophan-based peptides grafted onto oxidized nanocellulose. *Cellulose*, *19*(2), 481–493. https://doi.org/10.1007/s10570-011-9633-9

Bastidas, S. (2013). Híbrido OxG Corpoica Elmira de palma de aceite1Avances en el desarrollo de materiales genéticos resistentes a la PC. *Revista Palmas, Bogotá*, *34*, 135–141.

Basu, P. (2018). Biomass characteristics. In *Biomass Gasification, Pyrolysis and Torrefaction: Practical Design and Theory* (pp. 49–91). Elsevier. https://doi.org/10.1016/B978-0-12-812992-0.00003-0

Batista, A. H., Melo, V. F., Gilkes, R., & Roberts, M. (2018). Identification of heavy metals in crystals of sand and silt fractions of soils by scanning electron microscopy (SEM EDS/WD-EPMA). *Revista Brasileira de Ciencia Do Solo*, *42*. https://doi.org/10.1590/18069657rbcs20170174

Bayat, M., Sohrabi, M., & Royaee, S. J. (2012). Degradation of phenol by heterogeneous Fenton reaction using Fe/clinoptilolite. *Journal of Industrial and Engineering Chemistry*, *18*(3), 957–962. https://doi.org/10.1016/j.jiec.2011.09.004

Bello, M. M., & Abdul Raman, A. A. (2017). Trend and current practices of palm oil mill effluent polishing: Application of advanced oxidation processes and their future perspectives. In *Journal of Environmental Management* (Vol. 198, pp. 170–182). Academic Press. https://doi.org/10.1016/j.jenvman.2017.04.050

Bello, M. M., Nourouzi, M. M., Abdullah, L. C., Choong, T. S. Y., Koay, Y. S., & Keshani, S. (2013a). POME is treated for removal of color from biologically treated POME in fixed bed column: Applying wavelet neural network (WNN). *Journal of Hazardous Materials*, *262*, 106–113. https://doi.org/10.1016/j.jhazmat.2013.06.053

Bello, M. M., Nourouzi, M. M., Abdullah, L. C., Choong, T. S. Y., Koay, Y. S., & Keshani, S. (2013b). POME is treated for removal of color from biologically treated POME in fixed bed column: Applying wavelet neural network (WNN). *Journal of Hazardous Materials*, *262*, 106–113. https://doi.org/10.1016/j.jhazmat.2013.06.053

Benhamou, K., Dufresne, A., Magnin, A., Mortha, G., & Kaddami, H. (2014). Control of size and viscoelastic properties of nanofibrillated cellulose from palm tree by varying the TEMPO-mediated oxidation time. *Carbohydrate Polymers*, *99*, 74–83. https://doi.org/10.1016/j.carbpol.2013.08.032

Benkaddour, A., Journoux-Lapp, C., Jradi, K., Robert, S., & Daneault, C. (2014). Study of the hydrophobization of TEMPO-oxidized cellulose gel through two routes: Amidation and esterification process. *Journal of Materials Science*, *49*(7), 2832–2843. https://doi.org/10.1007/s10853-013-7989-y

Bhatnagar, A., & Sain, M. (2005). Processing of cellulose nanofiber-reinforced composites. *Journal of Reinforced Plastics and Composites*, *24*(12), 1259–1268. https://doi.org/10.1177/0731684405049864

Bigham, J. M., & Schulze, D. G. (2002). *Iron Oxides*.

Bolker, H. I., W Rhodes, H. E., & Sing Lee, K. (1965). Procedures for the Analysis of Wood and Wood Products. *Bull. Ecol. Res. Commun. (Stockholm)*, *7*(2), 453–454. https://pubs.acs.org/sharingguidelines

Boonsawang, P., & Youravong, W. (2017). Sustainability Issues, Challenges and Controversies Surrounding the Palm Oil Industry. In *Sustainability Challenges in the Agrofood Sector*.

Brillas, E. (2022). Fenton, photo-Fenton, electro-Fenton, and their combined treatments for the removal of insecticides from waters and soils. A review. In *Separation and Purification Technology* (Vol. 284). Elsevier B.V. https://doi.org/10.1016/j.seppur.2021.120290

Carlson, J. J., & Kawatra, S. K. (2013). Factors affecting zeta potential of iron oxides. *Mineral Processing and Extractive Metallurgy Review*, *34*(5), 269–303. https://doi.org/10.1080/08827508.2011.604697

Chacón-Patiño, M., Blanco-Tirado, C., Hinestroza, J. P., & Combariza, M. Y. (2013). Biocomposite of nanostructured MnO 2 and Fique fibers for efficient dye degradation. *Green Chemistry*, *10*. https://doi.org/10.1039/c0xx00000x

Chairunnisak, A., Arifin, B., Sofyan, H., Lubis, M. R., & Darmadi. (2018). Comparative study on the removal of COD from POME by electrocoagulation and electro-Fenton methods: Process optimization. *IOP Conference Series: Materials Science and Engineering*, *334*(1). https://doi.org/10.1088/1757-899X/334/1/012026

Chang, S. H. (2014a). An overview of empty fruit bunch from oil palm as feedstock for bio-oil production. In *Biomass and Bioenergy* (Vol. 62, pp. 174–181). https://doi.org/10.1016/j.biombioe.2014.01.002

Chang, S. H. (2014b). An overview of empty fruit bunch from oil palm as feedstock for bio-oil production. *Biomass and Bioenergy*, *62*, 174–181. https://doi.org/10.1016/j.biombioe.2014.01.002

Chee Ching, Y., & Sean Ng, T. (2014). Effect of Preparation Conditions on Cellulose from Oil Palm Empty Fruit Bunch Fiber. *BioResources*, *9(4),* 6373–6385.

Chen, C. H., Han, R. M., Liang, R., Fu, L. M., Wang, P., Ai, X. C., Zhang, J. P., & Skibsted, L. H. (2011). Direct observation of the β-carotene reaction with hydroxyl radical. *Journal of Physical Chemistry B*, *115*(9), 2082–2089. https://doi.org/10.1021/jp1100889

Chen, F., Xie, S., Huang, X., & Qiu, X. (2017). Ionothermal synthesis of Fe 3 O 4 magnetic nanoparticles as efficient heterogeneous Fenton-like catalysts for degradation of organic pollutants with H 2 O 2. *Journal of Hazardous Materials*, *322*, 152–162. https://doi.org/10.1016/j.jhazmat.2016.02.073

Chen, Q., Wu, P., Li, Y., Zhu, N., & Dang, Z. (2009). Heterogeneous photo-Fenton photodegradation of reactive brilliant orange X-GN over iron-pillared montmorillonite under visible irradiation. *Journal of Hazardous Materials*, *168*(2–3), 901–908. https://doi.org/10.1016/j.jhazmat.2009.02.107

Chen, S. F., Mowery, R. A., Scarlata, C. J., & Chambliss, C. K. (2007). Compositional analysis of water-soluble materials in corn stover. *Journal of Agricultural and Food Chemistry*, *55*(15), 5912–5918. https://doi.org/10.1021/jf0700327

Chen, Y. W., Lee, H. V., & Abd Hamid, S. B. (2017). Facile production of nanostructured cellulose from Elaeis guineensis empty fruit bunch via one pot oxidative-hydrolysis isolation approach. *Carbohydrate Polymers*, *157*, 1511–1524. https://doi.org/10.1016/j.carbpol.2016.11.030

Chen, Y., Zhou, L., Chen, L., Duan, G., Mei, C., Huang, C., Han, J., & Jiang, S. (2019). Anisotropic nanocellulose aerogels with ordered structures fabricated by directional freeze-drying for fast liquid transport. *Cellulose*, *26*(11), 6653–6667. https://doi.org/10.1007/s10570-019-02557-z

Chen, Z. C., Peng, W. T., Li, J., & Liao, H. (2018). Functional dissection and transport mechanism of magnesium in plants. In *Seminars in Cell and Developmental Biology* (Vol. 74, pp. 142–152). Elsevier Ltd. https://doi.org/10.1016/j.semcdb.2017.08.005

Cheng, F., Liu, C., Wei, X., Yan, T., Li, H., He, J., & Huang, Y. (2017). Preparation and Characterization of 2,2,6,6-Tetramethylpiperidine-1-oxyl (TEMPO)-Oxidized Cellulose Nanocrystal/Alginate Biodegradable Composite Dressing for Hemostasis Applications. *ACS Sustainable Chemistry and Engineering*, *5*(5), 3819–3828. https://doi.org/10.1021/acssuschemeng.6b02849

Cheng, Y. W., Chong, C. C., Lam, M. K., Ayoub, M., Cheng, C. K., Lim, J. W., Yusup, S., Tang, Y., & Bai, J. (2021). Holistic process evaluation of non-conventional palm oil mill effluent (POME) treatment technologies: A conceptual and comparative review. *Journal of*

Hazardous Materials, *409*(October 2020), 124964. https://doi.org/10.1016/j.jhazmat.2020.124964

Chew, S. A., Hinojosa, V. A., & Arriaga, M. A. (2017). Bioresorbable polymer microparticles in the medical and pharmaceutical fields. In *Bioresorbable Polymers for Biomedical Applications: From Fundamentals to Translational Medicine* (pp. 229–264). Elsevier. https://doi.org/10.1016/B978-0-08-100262-9.00011-2

Chiesa, S., & Gnansounou, E. (2014). Use of empty fruit bunches from the oil palm for bioethanol production: A thorough comparison between dilute acid and dilute alkali pretreatment. *Bioresource Technology*, *159*, 355–364. https://doi.org/10.1016/j.biortech.2014.02.122

Chiew, Y. L., & Shimada, S. (2013). Current state and environmental impact assessment for utilizing oil palm empty fruit bunches for fuel, fiber and fertilizer - A case study of Malaysia. *Biomass and Bioenergy*, *51*, 109–124. https://doi.org/10.1016/j.biombioe.2013.01.012

Choi, W.-I., Park, J.-Y., Lee, J.-P., Oh, Y.-K., Chul Park, Y., Seok Kim, J., Min Park, J., Ho Kim, C., & Lee, J.-S. (2013). *Optimization of NaOH-catalyzed steam pretreatment of empty fruit bunch*. http://www.biotechnologyforbiofuels.com/content/6/1/170

Chong, Y. Y., Thangalazhy-Gopakumar, S., Gan, S., Ng, H. K., Lee, L. Y., & Adhikari, S. (2017). Kinetics and Mechanisms for Copyrolysis of Palm Empty Fruit Bunch Fiber (EFBF) with Palm Oil Mill Effluent (POME) Sludge. *Energy and Fuels*, *31*(8), 8217–8227. https://doi.org/10.1021/acs.energyfuels.7b00877

Choo, Y. M., Ma, A. N., & Yap, S. C. (1998). Carotenes, vitamin E and sterols in oils from Elaeis guineensis, Elaeis oleifera and their hybrids. *Palmas*, *19*(2).

Chuensangjun, C., Kanomata, K., Kitaoka, T., Chisti, Y., & Sirisansaneeyakul, S. (2019). Surface-Modified Cellulose Nanofibers-graft-poly(lactic acid)s Made by Ring-Opening Polymerization of l-Lactide. *Journal of Polymers and the Environment*, *27*(4), 847–861. https://doi.org/10.1007/s10924-019-01398-y

Coral Medina, J. D., Woiciechowski, A., Zandona Filho, A., Noseda, M. D., Kaur, B. S., & Soccol, C. R. (2015). Lignin preparation from oil palm empty fruit bunches by sequential acid/alkaline treatment - A biorefinery approach. *Bioresource Technology*, *194*, 172–178. https://doi.org/10.1016/j.biortech.2015.07.018

Covinich, L., Felissia, F., Massa, P., Fenoglio, R., & Area, M. C. (2018). Kinetic modeling of a heterogeneous Fenton-type oxidative treatment of complex industrial effluent. *International Journal of Industrial Chemistry*, *9*(3), 215–229. https://doi.org/10.1007/s40090-018-0151-6

Cui, X., Zhao, X., Zeng, J., Loh, S. K., Choo, Y. M., & Liu, D. (2014). Robust enzymatic hydrolysis of Formiline-pretreated oil palm empty fruit bunches (EFB) for efficient conversion of polysaccharide to sugars and ethanol. *Bioresource Technology*, *166*, 584–591. https://doi.org/10.1016/j.biortech.2014.05.102

Dai, D., Fan, M., & Collins, P. (2013). Fabrication of nanocelluloses from hemp fibers and their application for the reinforcement of hemp fibers. *Industrial Crops and Products*, *44*, 192–199. https://doi.org/10.1016/j.indcrop.2012.11.010

Daniel C.Harris. (2003). *Análisis químico cuantitativo*. Reverté. https://www.google.com.co/books/edition/An%C3%A1lisis_qu%C3%ADmico_cuantitativo/H-_8vZYdL70C?hl=en&gbpv=0

Dassanayake, R. S., Dissanayake, N., Fierro, J. S., Abidi, N., Quitevis, E. L., Boggavarappu, K., & Thalangamaarachchige, V. D. (2023). Characterization of cellulose nanocrystals by current spectroscopic techniques. In *Applied Spectroscopy Reviews* (Vol. 58, Issue 3, pp. 180–205). Taylor and Francis Ltd. https://doi.org/10.1080/05704928.2021.1951283

Daud, Z. A. M., Kaur, D., & Khosla, P. (2012). Health and Nutritional Properties of Palm Oil and Its Components. In *Palm Oil: Production, Processing, Characterization, and Uses* (pp. 545–560). Elsevier Inc. https://doi.org/10.1016/B978-0-9818936-9-3.50021-6

Dutta, S. K., & Chakraborty, S. (2019). Multiscale Dynamics of Hemicellulose Hydrolysis for Biofuel Production. *Industrial and Engineering Chemistry Research*, *58*(21), 8963–8978. https://doi.org/10.1021/acs.iecr.9b01276

Ebringerová, A., Hromádková, Z., & Heinze, T. (2005). Hemicellulose. *Advances in Polymer Science*, *186*, 1–67. https://doi.org/10.1007/B136816/COVER

Edge, R., & Truscott, T. G. (2018). Singlet oxygen and free radical reactions of retinoids and carotenoids—A review. In *Antioxidants* (Vol. 7, Issue 1). MDPI. https://doi.org/10.3390/antiox7010005

Enström et al. (2019). Introducing a new GHG emission calculation approach for alternative methane reduction measures in the wastewater treatment of a palm oil mill. *Environment,* *Development and Sustainability*, *21*(6), 3065–3076. https://doi.org/10.1007/s10668-018-0181-4

Erlandsson, J., Pettersson, T., Ingverud, T., Granberg, H., Larsson, P. A., Malkoch, M., & Wågberg, L. (2018). On the mechanism behind freezing-induced chemical crosslinking in ice-templated cellulose nanofibril aerogels. *Journal of Materials Chemistry A*, *6*(40), 19371–19380. https://doi.org/10.1039/c8ta06319b

Espino-Pérez, E., Domenek, S., Belgacem, N., Sillard, C., & Bras, J. (2014). Green process for chemical functionalization of nanocellulose with carboxylic acids. *Biomacromolecules*, *15*(12), 4551–4560. https://doi.org/10.1021/bm5013458

Esteves, B., Sen, U., & Pereira, H. (2023). Influence of Chemical Composition on Heating Value of Biomass: A Review and Bibliometric Analysis. In *Energies* (Vol. 16, Issue 10). MDPI. https://doi.org/10.3390/en16104226

Fahma, F., Iwamoto, S., Hori, N., Iwata, T., & Takemura, A. (2010). Isolation, preparation, and characterization of nanofibers from oil palm empty-fruit-bunch (OPEFB). *Cellulose*, *17*(5), 977–985. https://doi.org/10.1007/s10570-010-9436-4

Fahma, F., Lisdayana, N., Abidin, Z., Noviana, D., Sari, Y. W., Mukti, R. R., Yunus, M., Kusumaatmaja, A., & Kadja, G. T. M. (2020). Nanocellulose-based fibres derived from palm oil by-products and their in vitro biocompatibility analysis. *Journal of the Textile Institute*, *111*(9), 1354–1363. https://doi.org/10.1080/00405000.2019.1694353

Faiyas, A. P. A., Vinod, E. M., Joseph, J., Ganesan, R., & Pandey, R. K. (2010). Dependence of pH and surfactant effect in the synthesis of magnetite (Fe3O4) nanoparticles and its properties. *Journal of Magnetism and Magnetic Materials*, *322*(4), 400–404. https://doi.org/10.1016/j.jmmm.2009.09.064

Fan, H., Ma, X., Zhou, S., Huang, J., Liu, Y., & Liu, Y. (2019). Highly efficient removal of heavy metal ions by carboxymethyl cellulose-immobilized Fe 3 O 4 nanoparticles prepared via high-gravity technology. *Carbohydrate Polymers*, *213*, 39–49. https://doi.org/10.1016/j.carbpol.2019.02.067

Farhan Hanafi, M., & Sapawe, N. (2020). A review on the water problem associate with organic pollutants derived from phenol, methyl orange, and remazol brilliant blue dyes. *Materials Today: Proceedings*, *31*, A141–A150. https://doi.org/10.1016/j.matpr.2021.01.258

Farooq, A., Patoary, M. K., Zhang, M., Mussana, H., Li, M., Naeem, M. A., Mushtaq, M., Farooq, A., & Liu, L. (2020). Cellulose from sources to nanocellulose and an overview of synthesis and properties of nanocellulose/zinc oxide nanocomposite materials. *International Journal of Biological Macromolecules*, *154*, 1050–1073. https://doi.org/10.1016/j.ijbiomac.2020.03.163

Farshchi, M. E., Aghdasinia, H., & Khataee, A. (2018). Modeling of heterogeneous Fenton process for dye degradation in a fluidized-bed reactor: Kinetics and mass transfer. *Journal of Cleaner Production*, *182*, 644–653. https://doi.org/10.1016/j.jclepro.2018.01.225

Fatah, I. Y. A., Abdul Khalil, H. P. S., Hossain, M. S., Aziz, A. A., Davoudpour, Y., Dungani, R., & Bhat, A. (2014). Exploration of a chemo-mechanical technique for the isolation of nanofibrillated cellulosic fiber from oil palm empty fruit bunch as a reinforcing agent in composites materials. *Polymers*, *6*(10), 2611–2624. https://doi.org/10.3390/polym6102611

Fedepalma. (2021). *La palma de aceite en Colombia | Fedepalma*. https://web.fedepalma.org/la-palma-de-aceite-en-colombia-departamentos

Feng Ma, J. (2003). Functions of Silicon in Higher Plants. In *Progress in Molecular and Subcellular Biology* (Springer, Vol. 33).

Foutch, G. L., & Johannes, A. H. (2003). Reactors in Process Engineering. *Encyclopedia of Physical Science and Technology*, 23–43. https://doi.org/10.1016/B0-12-227410-5/00654-2

Fras, L., Johansson, L. S., Stenius, P., Laine, J., Stana-Kleinschek, K., & Ribitsch, V. (2005). Analysis of the oxidation of cellulose fibres by titration and XPS. *Colloids and Surfaces A: Physicochemical and Engineering Aspects*, *260*(1–3), 101–108. https://doi.org/10.1016/j.colsurfa.2005.01.035

French, A. D. (2014). Idealized powder diffraction patterns for cellulose polymorphs. *Cellulose*, *21*(2), 885–896. https://doi.org/10.1007/s10570-013-0030-4

Fuentes-García, J. A., Diaz-Cano, A. I., Guillen-Cervantes, A., & Santoyo-Salazar, J. (2018). Magnetic domain interactions of Fe3O4 nanoparticles embedded in a SiO2 matrix. *Scientific Reports*, *8*(1). https://doi.org/10.1038/s41598-018-23460-w

Fujisawa, S., Okita, Y., Fukuzumi, H., Saito, T., & Isogai, A. (2011). Preparation and characterization of TEMPO-oxidized cellulose nanofibril films with free carboxyl groups. *Carbohydrate Polymers*, *84*(1), 579–583. https://doi.org/10.1016/j.carbpol.2010.12.029

Gajrani, K. K., & Sankar, M. R. (2020). Sustainable Cutting Fluids: Thermal, Rheological, Biodegradation, Anti-Corrosion, Storage Stability Studies and its Machining Performance. In *Encyclopedia of Renewable and Sustainable Materials: Volume 1-5* (Vols. 1–5, pp. 839–852). Elsevier. https://doi.org/10.1016/B978-0-12-803581-8.11152-X

Gallego, L. J., Cardona, S., Martínez, E., & Rios, L. A. (2020). Valorization of Palm-Oil Residues: Integrated Production of a Good Quality Bio-coal and Electricity via Torrefaction. *Waste and Biomass Valorization*, *11*(5), 2273–2284. https://doi.org/10.1007/s12649-018-0459-7

Gamaralalage, D., Sawai, O., & Nunoura, T. (2019). Degradation behavior of palm oil mill effluent in Fenton oxidation. *Journal of Hazardous Materials*, *364*, 791–799. https://doi.org/10.1016/j.jhazmat.2018.07.023

Gamaralalage, D., Sawai, O., & Nunoura, T. (2020). Effect of reagents addition method in Fenton oxidation on the destruction of organics in palm oil mill effluent. *Journal of Environmental Chemical Engineering*, *8*(4). https://doi.org/10.1016/j.jece.2020.103974

Gan, S., Chen, R. S., Mohammad Padzil, F. N., Moosavi, S., Tarawneh, M. A., Loh, S. K., & Idris, Z. (2023). Potential valorization of oil palm fiber in versatile applications towards sustainability: A review. *Industrial Crops and Products*, *199*, 116763. https://doi.org/10.1016/j.indcrop.2023.116763

García-Núñez, J. A., García-Pérez, M., & Das, K. C. (2008). DETERMINATION OF KINETIC PARAMETERS OF THERMAL DEGRADATION OF PALM OIL MILL BY-PRODUCTS USING THERMOGRAVIMETRIC ANALYSIS AND DIFFERENTIAL SCANNING

CALORIMETRY. *American Society of Agricultural and Biological Engineers*, *51*(2), 547–557.

Garcia-Nunez, J. A., Ramirez-Contreras, N. E., Rodriguez, D. T., Silva-Lora, E., Frear, C. S., Stockle, C., & Garcia-Perez, M. (2016). Evolution of palm oil mills into bio-refineries: Literature review on current and potential uses of residual biomass and effluents. In *Resources, Conservation and Recycling* (Vol. 110, pp. 99–114). Elsevier B.V. https://doi.org/10.1016/j.resconrec.2016.03.022

Genet, M., Dupont-Gillain, C., & Rouxhet, P. (2008). XPS Analysis of Biosystems and Biomaterials. In *Medical Applications of Colloids* (pp. 177–291). Springer New York. https://doi.org/10.1007/978-0-387-76921-9

Geng, L., Mittal, N., Zhan, C., Ansari, F., Sharma, P. R., Peng, X., Hsiao, B. S., & Söderberg, L. D. (2018). Understanding the Mechanistic Behavior of Highly Charged Cellulose Nanofibers in Aqueous Systems. *Macromolecules*, *51*(4), 1498–1506. https://doi.org/10.1021/acs.macromol.7b02642

Ghasemi, S., Tajvidi, M., Bousfield, D. W., & Gardner, D. J. (2018). Reinforcement of natural fiber yarns by cellulose nanomaterials: A multi-scale study. *Industrial Crops and Products*, *111*, 471–481. https://doi.org/10.1016/j.indcrop.2017.11.016

Ghimire, A., Trably, E., Frunzo, L., Pirozzi, F., Lens, P. N. L., Esposito, G., Cazier, E. A., & Escudié, R. (2018). Effect of total solids content on biohydrogen production and lactic acid accumulation during dark fermentation of organic waste biomass. *Bioresource Technology*, *248*, 180–186. https://doi.org/10.1016/j.biortech.2017.07.062

Ghods, P., Isgor, O. B., Brown, J. R., Bensebaa, F., & Kingston, D. (2011). XPS depth profiling study on the passive oxide film of carbon steel in saturated calcium hydroxide solution and the effect of chloride on the film properties. *Applied Surface Science*, *257*(10), 4669–4677. https://doi.org/10.1016/j.apsusc.2010.12.120

Giwa, A. R. A., Bello, I. A., Olabintan, A. B., Bello, O. S., & Saleh, T. A. (2020). Kinetic and thermodynamic studies of fenton oxidative decolorization of methylene blue. *Heliyon*, *6*(8). https://doi.org/10.1016/j.heliyon.2020.e04454

Gong, S. H., Im, H. S., Um, M., Lee, H. W., & Lee, J. W. (2019). Enhancement of waste biomass fuel properties by sequential leaching and wet torrefaction. *Fuel*, *239*, 693–700. https://doi.org/10.1016/j.fuel.2018.11.069

Gray, D. G., Weller, M., Ulkem, N., & Lejeune, A. (2010). Composition of lignocellulosic surfaces: Comments on the interpretation of XPS spectra. *Cellulose*, *17*(1), 117–124. https://doi.org/10.1007/s10570-009-9359-0

Gupta, A. K., & Gupta, M. (2005). Synthesis and surface engineering of iron oxide nanoparticles for biomedical applications. In *Biomaterials* (Vol. 26, Issue 18, pp. 3995–4021). https://doi.org/10.1016/j.biomaterials.2004.10.012

Gupta, G. K., & Mondal, M. K. (2019). Bioenergy generation from agricultural wastes and enrichment of end products. In *Refining Biomass Residues for Sustainable Energy and Bioproducts: Technology, Advances, Life Cycle Assessment, and Economics* (pp. 337–356). Elsevier. https://doi.org/10.1016/B978-0-12-818996-2.00015-6

Gupta, P. K., Uniyal, V., & Naithani, S. (2013). Polymorphic transformation of cellulose i to cellulose II by alkali pretreatment and urea as an additive. *Carbohydrate Polymers*, *94*(2), 843–849. https://doi.org/10.1016/j.carbpol.2013.02.012

Habibi, Y., Chanzy, H., & Vignon, M. R. (2006). TEMPO-mediated surface oxidation of cellulose whiskers. *Cellulose*, *13*(6), 679–687. https://doi.org/10.1007/s10570-006-9075-y

Hafid, H. S., Baharuddin, A. S., Mokhtar, M. N., Omar, F. N., Mohammed, M. A. P., & Wakisaka, M. (2021). Enhanced laccase production for oil palm biomass delignification using biological pretreatment and its estimation at biorefinary scale. *Biomass and Bioenergy*, *144*. https://doi.org/10.1016/j.biombioe.2020.105904

Hameed, B. H., Ahmad, A. A., & Aziz, N. (2007). Isotherms, kinetics and thermodynamics of acid dye adsorption on activated palm ash. *Chemical Engineering Journal*, *133*(1–3), 195–203. https://doi.org/10.1016/j.cej.2007.01.032

Han, J., & Kim, J. (2018). Process Simulation and Optimization of 10-MW EFB Power Plant. In *Computer Aided Chemical Engineering* (Vol. 43, pp. 723–729). Elsevier B.V. https://doi.org/10.1016/B978-0-444-64235-6.50128-5

Han, S., Yu, H., Yang, T., Wang, S., & Wang, X. (2017). Magnetic Activated-ATP@Fe3O4 Nanocomposite as an Efficient Fenton-Like Heterogeneous Catalyst for Degradation of Ethidium Bromide. *Scientific Reports*, *7*(1). https://doi.org/10.1038/s41598-017-06398-3

Hänsch, R., & Mendel, R. R. (2009). Physiological functions of mineral micronutrients (Cu, Zn, Mn, Fe, Ni, Mo, B, Cl). In *Current Opinion in Plant Biology* (Vol. 12, Issue 3, pp. 259–266). https://doi.org/10.1016/j.pbi.2009.05.006

Hassan, N. S., & Badri, K. H. (2016). THERMAL BEHAVIORS OF OIL PALM EMPTY FRUIT BUNCH FIBER UPON EXPOSURE TO ACID-BASE AQUEOUS SOLUTIONS. *Malaysian Journal of Analytical Sciences*, *20*(5), 1095–1103. https://doi.org/10.17576/mjas-2016-2005-15

Hastuti, N., Kanomata, K., & Kitaoka, T. (2019). Characteristics of TEMPO-Oxidized Cellulose Nanofibers from Oil Palm Empty Fruit Bunches Produced by Different Amounts of Oxidant. *IOP Conference Series: Earth and Environmental Science*, *359*(1). https://doi.org/10.1088/1755-1315/359/1/012008

Hayawin, N., Hakimi Ibrahim, M., S Abdul Khalil, H. P., & Ibrahim, Z. (2012). VERMICOMPOSTING OF EMPTY FRUIT BUNCH WITH ADDITION OF PALM OIL MILL EFFLUENT SOLID. *Journal of Oil Palm Research*, *24*, 1542–1549.

Hayawin, Z. N., Astimar, A. A., Ibrahim, M. H., Abdul Khalil, H. P. S., Syirat, Z. B., & Menon, N. R. (2014). The growth and reproduction of Eisenia fetida and Eudrilus eugeniae in mixtures of empty fruit bunch and palm oil mill effluent. *Compost Science and Utilization*, *22*(1), 40–46. https://doi.org/10.1080/1065657X.2014.882247

He, J., Yang, X., Men, B., & Wang, D. (2016). Interfacial mechanisms of heterogeneous Fenton reactions catalyzed by iron-based materials: A review. *Journal of Environmental Sciences (China)*, *39*, 97–109. https://doi.org/10.1016/j.jes.2015.12.003

Hernández-Maya, M. S., Espinosa-Lobo, C. B., Cabanzo-Hernández, R., Mejía-Ospino, E., & Baldovino-Medrano, V. G. (2022). Effects of pH and vanadium concentration during the impregnation of Na-SiO2 supported catalysts for the oxidation of propane. *Molecular Catalysis*, *520*. https://doi.org/10.1016/j.mcat.2022.112158

Hessler, L. E., & Merola, G. V. (1949). Determination of Cellulose in Cotton and Cordage Fiber. In *Analytical chemistry* (Vol. 21, Issue 6).

Ho, M. C., Ong, V. Z., & Wu, T. Y. (2019). Potential use of alkaline hydrogen peroxide in lignocellulosic biomass pretreatment and valorization – A review. *Renewable and Sustainable Energy Reviews*, *112*, 75–86. https://doi.org/10.1016/j.rser.2019.04.082

Hsieh, Y. S. Y., & Harris, P. J. (2009). Xyloglucans of monocotyledons have diverse structures. *Molecular Plant*, *2*(5), 943–965. https://doi.org/10.1093/mp/ssp061

Hu, M., Ye, Z., Zhang, H., Chen, B., Pan, Z., & Wang, J. (2021). Thermochemical conversion of sewage sludge for energy and resource recovery: technical challenges and prospects. In *Environmental Pollutants and Bioavailability* (Vol. 33, Issue 1, pp. 145–163). Taylor and Francis Ltd. https://doi.org/10.1080/26395940.2021.1947159

Huang, C. F., Chen, J. K., Tsai, T. Y., Hsieh, Y. A., & Andrew Lin, K. Y. (2015). Dual-functionalized cellulose nanofibrils prepared through TEMPO-mediated oxidation and surface-initiated ATRP. *Polymer*, *72*, 395–405. https://doi.org/10.1016/j.polymer.2015.02.056

Huang, C. F., Tu, C. W., Lee, R. H., Yang, C. H., Hung, W. C., & Andrew Lin, K. Y. (2019). Study of various diameter and functionality of TEMPO-oxidized cellulose nanofibers on paraquat adsorptions. *Polymer Degradation and Stability*, *161*, 206–212. https://doi.org/10.1016/j.polymdegradstab.2019.01.023

Huang, C. P., Dong, C., & Tang, Z. (1993). ADVANCED CHEMICAL OXIDATION: ITS PRESENT ROLE AND POTENTIAL FUTURE IN HAZARDOUS WASTE TREATMENT. In *WASTE MANAGEMENT* (Vol. 13).

Huang, H., Qiao, Y., Yuan, Y., & Zhang, J. (2023). Surface functionalization for heterogeneous catalysis. *Reference Module in Materials Science and Materials Engineering*, 407–419. https://doi.org/10.1016/B978-0-12-822425-0.00073-7

Huang, W. (2018). Cellulose Nanopapers. In *Nanopapers: From Nanochemistry and Nanomanufacturing to Advanced Applications* (pp. 121–173). Elsevier. https://doi.org/10.1016/B978-0-323-48019-2.00005-0

Huber, D. M., & Jones, J. B. (2013). The role of magnesium in plant disease. *Plant and Soil*, *368*(1–2), 73–85. https://doi.org/10.1007/s11104-012-1476-0

Idel-aouad, R., Valiente, M., Yaacoubi, A., Tanouti, B., & López-Mesas, M. (2011). Rapid decolourization and mineralization of the azo dye C.I. Acid Red 14 by heterogeneous Fenton reaction. *Journal of Hazardous Materials*, *186*(1), 745–750. https://doi.org/10.1016/j.jhazmat.2010.11.056

Insam, H., & Knapp, B. A. (2011). *Recycling of Biomass Ashes*.

International Organization for Standardization ISO. (2011). *Water quality-Examination and determination of colour*.

IPAD International Production Assessment Division. (2022). *Palm Oil Explorer*. Palm Oil Explorer. https://ipad.fas.usda.gov/

Ishii, T. (1991). ACETYLATION AT O-2 OF ARABINOFURANOSE RESIDUES IN FERULOYLATED ARABINOXYLAN FROM BAMBOO SHOOT CELL-WALLS. In *Phytochemistry* (Vol. 30, Issue 7).

Iskandar, W. M. E., Ong, H. R., Rahman Khan, M. M., & Ramli, R. (2022). Effect of ultrasonication on alkaline treatment of empty fruit bunch fibre: Fourier Transform Infrared Spectroscopy (FTIR) and morphology study. *Materials Today: Proceedings*, *66*, 2840–2843. https://doi.org/10.1016/j.matpr.2022.06.526

Ismail, H. S., Ibrahim, A. H., Abidin, C. Z. A., & Ridwan, F. M. (2020). Recovery of nano-lignin from anaerobic treated palm oil mill effluent (AT-POME). *IOP Conference Series: Earth and Environmental Science*, *476*(1). https://doi.org/10.1088/1755-1315/476/1/012093

Isogai, A. (2016). Chapter 18. Cellulose Nanofibers as New Bio-Based Nanomaterials. In *High-Performance and Specialty Fibers Concepts, Technology and Modern Applications of Man-Made Fibers for the Future* (pp. 297–311).

Isogai, A., & Bergström, L. (2018). Preparation of cellulose nanofibers using green and sustainable chemistry. In *Current Opinion in Green and Sustainable Chemistry* (Vol. 12, pp. 15–21). Elsevier B.V. https://doi.org/10.1016/j.cogsc.2018.04.008

Isogai, A., Saito, T., & Fukuzumi, H. (2011). TEMPO-oxidized cellulose nanofibers. *Nanoscale*, *3*(1), 71–85. https://doi.org/10.1039/C0NR00583E

Isroi, Ishola, M. M., Millati, R., Syamsiah, S., Cahyanto, M. N., Niklasson, C., & Taherzadeh, M. J. (2012). Structural changes of oil palm empty fruit bunch (OPEFB) after fungal and phosphoric acid pretreatment. *Molecules*, *17*(12), 14995–15012. https://doi.org/10.3390/molecules171214995

Jabbar, A., Hussain, J., Basit, A., Naeem, M. S., Javaid, M. U., Karahan, M., & Nazir, A. (2020). Influence of Chemical Treatments and Nanocellulose Spray Coating on the Mechanical, Low Velocity Impact and Compression after Impact Performance of Nonwoven Jute Composites. *Journal of Natural Fibers*, *17*(12), 1785–1797. https://doi.org/10.1080/15440478.2019.1598918

Jamari, S. S., & Howse, J. R. (2012). The effect of the hydrothermal carbonization process on palm oil empty fruit bunch. *Biomass and Bioenergy*, *47*, 82–90. https://doi.org/10.1016/j.biombioe.2012.09.061

Jasmani, L., & Adnan, S. (2017). Preparation and characterization of nanocrystalline cellulose from Acacia mangium and its reinforcement potential. *Carbohydrate Polymers*, *161*, 166–171. https://doi.org/10.1016/j.carbpol.2016.12.061

Jaušovec, D., Vogrinčič, R., & Kokol, V. (2015). Introduction of aldehyde vs. carboxylic groups to cellulose nanofibers using laccase/TEMPO mediated oxidation. *Carbohydrate Polymers*, *116*, 74–85. https://doi.org/10.1016/j.carbpol.2014.03.014

Jawaid, M., Boufi, S., & Khalil, A. (2017). *Cellulose-Reinforced Nanofibre Composites*. Elservier.

Jiju, A. (2014). A systematic methodology for Design of Experiments 4.1 Introduction. In *Design of Experiments for Engineers and Scientists (Second Edition)* (pp. 33–50).

Johnson, R., Vishwakarma, K., Hossen, M. S., Kumar, V., Shackira, A. M., Puthur, J. T., Abdi, G., Sarraf, M., & Hasanuzzaman, M. (2022). Potassium in plants: Growth regulation, signaling, and environmental stress tolerance. In *Plant Physiology and Biochemistry* (Vol. 172, pp. 56–69). Elsevier Masson s.r.l. https://doi.org/10.1016/j.plaphy.2022.01.001

Jordan, J. H., Easson, M. W., Dien, B., Thompson, S., & Condon, B. D. (2019). Extraction and characterization of nanocellulose crystals from cotton gin motes and cotton gin waste. *Cellulose*, *26*(10), 5959–5979. https://doi.org/10.1007/s10570-019-02533-7

Juntaro, J., Pommet, M., Mantalaris, A., Shaffer, M., & Bismarck, A. (2007). Nanocellulose enhanced interfaces in truly green unidirectional fibre reinforced composites. *Composite Interfaces*, *14*(7–9), 753–762. https://doi.org/10.1163/156855407782106573

Kaco, H., Baharin, K. W., Zakaria, S., Chia, C. H., Jaafar, S. N. S., Gan, S. Y., & Sajab, M. S. (2017). Preparation and characterization of Fe3O4/regenerated cellulose membrane. *Sains Malaysiana*, *46*(4), 623–628. https://doi.org/10.17576/jsm-2017-4604-15

Kaffashsaie, E., Yousefi, H., Nishino, T., Matsumoto, T., Mashkour, M., Madhoushi, M., & Kawaguchi, H. (2021). Direct conversion of raw wood to TEMPO-oxidized cellulose nanofibers. *Carbohydrate Polymers*, *262*. https://doi.org/10.1016/j.carbpol.2021.117938

Kahar, P., Rachmadona, N., Pangestu, R., Palar, R., Triyono Nugroho Adi, D., Betha Juanssilfero, A., Yopi, Manurung, I., Hama, S., & Ogino, C. (2022). An integrated biorefinery strategy for the utilization of palm-oil wastes. In *Bioresource Technology* (Vol. 344). Elsevier Ltd. https://doi.org/10.1016/j.biortech.2021.126266

Kalia, S., Kaith, B. S., & Kaur, I. (2009). Pretreatments of natural fibers and their application as reinforcing material in polymer composites-a review. *Polymer Engineering and Science*, *49*(7), 1253–1272. https://doi.org/10.1002/pen.21328

Kang, N., Lee, D. S., & Yoon, J. (2002). *Kinetic modeling of Fenton oxidation of phenol and monochlorophenols*. www.elsevier.com/locate/chemosphere

Kargarzadeh, H., Mariano, M., Huang, J., Lin, N., Ahmad, I., Dufresne, A., & Thomas, S. (2017). Recent developments on nanocellulose reinforced polymer nanocomposites: A review. In *Polymer* (Vol. 132, pp. 368–393). Elsevier Ltd. https://doi.org/10.1016/j.polymer.2017.09.043

Karim, M. A. H., Aziz, K. H. H., Omer, K. M., Salih, Y. M., Mustafa, F., Rahman, K. O., & Mohammad, Y. (2022). Degradation of aqueous organic dye pollutants by heterogeneous photo-assisted Fenton-like process using natural mineral activator: Parameter optimization and degradation kinetics. *IOP Conference Series: Earth and Environmental Science*, *958*(1). https://doi.org/10.1088/1755-1315/958/1/012011

Karunakaran, V., Abd-Talib, N., & Kelly Yong, T. L. (2020). Lignin from oil palm empty fruit bunches (EFB) under subcritical phenol conditions as a precursor for carbon fiber production. *Materials Today: Proceedings*, *31*, 100–105. https://doi.org/10.1016/j.matpr.2020.01.252

Katte, A. R., Mwero, J., Gibigaye, M., & Koteng, D. O. (2023). Recycling palm oil wastes for the production of a pozzolanic cement replacement material for concrete. *Results in Engineering*, *17*. https://doi.org/10.1016/j.rineng.2023.100903

Khalil, H. P. S. A., Alwani, M. S., Ridzuan, R., Kamarudin, H., & Khairul, A. (2008a). Chemical composition, morphological characteristics, and cell wall structure of Malaysian oil palm fibers. *Polymer - Plastics Technology and Engineering*, *47*(3), 273–280. https://doi.org/10.1080/03602550701866840

Khalil, H. P. S. A., Alwani, M. S., Ridzuan, R., Kamarudin, H., & Khairul, A. (2008b). Chemical composition, morphological characteristics, and cell wall structure of Malaysian oil palm fibers. *Polymer - Plastics Technology and Engineering*, *47*(3), 273–280. https://doi.org/10.1080/03602550701866840

Khalili, P., Tshai, K. Y., & Kong, I. (2018). Comparative Thermal and Physical Investigation of Chemically Treated and Untreated Oil Palm EFB Fiber. In *Materials Today: Proceedings* (Vol. 5). www.sciencedirect.comwww.materialstoday.com/proceedings2214-7853

Khamparia, S., & Jaspal, D. (2018). Technologies for Treatment of Colored Wastewater from Different Industries. In *Handbook of Environmental Materials Management* (pp. 1–14). Springer International Publishing. https://doi.org/10.1007/978-3-319-58538-3_8-1

Khandanlou, R., Ahmad, M. Bin, Shameli, K., & Kalantari, K. (2013). Synthesis and characterization of rice straw/Fe3O4 nanocomposites by a quick precipitation method. *Molecules, 18*(6), 6597–6607. https://doi.org/10.3390/molecules18066597

Khongkliang, P., Khemkhao, M., Mahathanabodee, S., O-Thong, S., Kadier, A., & Phalakornkule, C. (2023). Efficient removal of tannins from anaerobically-treated palm oil mill effluent using protein-tannin complexation in conjunction with electrocoagulation. *Chemosphere*, *321*. https://doi.org/10.1016/j.chemosphere.2023.138086

Kim, H. (2021). Adoption of TiO2-photocatalysis for palm oil mill effluent (POME) treatment: Strengths, weaknesses, opportunities, threats (SWOT) and its practicality against traditional treatment in Malaysia. *Chemosphere*, *270*(129378 Contents), 1–8. https://doi.org/10.1016/j.chemosphere.2020.129378

Kittivech, T., & Fukuda, S. (2019). Effect of bed material on bed agglomeration for palm empty fruit bunch (EFB) gasification in a bubbling fluidised bed system. *Energies*, *12*(22). https://doi.org/10.3390/en12224336

Kolářová, K., Vosmanská, V., Rimpelová, S., & Švorčík, V. (2013). Effect of plasma treatment on cellulose fiber. *Cellulose*, *20*(2), 953–961. https://doi.org/10.1007/s10570-013-9863-0

Komilis, D., Kissas, K., & Symeonidis, A. (2014). Effect of organic matter and moisture on the calorific value of solid wastes: An update of the Tanner diagram. *Waste Management*, *34*(2), 249–255. https://doi.org/10.1016/j.wasman.2013.09.023

Kongnoo, A., Suksaroj, T., Intharapat, P., Promtong, T., & Suksaroj, C. (2012a). Decolorization and organic removal from palm oil mill effluent by fenton’s process. *Environmental Engineering Science*, *29*(9), 855–859. https://doi.org/10.1089/ees.2011.0181

Kongnoo, A., Suksaroj, T., Intharapat, P., Promtong, T., & Suksaroj, C. (2012b). Decolorization and organic removal from palm oil mill effluent by fenton's process. *Environmental Engineering Science*, *29*(9), 855–859. https://doi.org/10.1089/ees.2011.0181

Konsomboon, S., Pipatmanomai, S., Madhiyanon, T., & Tia, S. (2011). Effect of kaolin addition on ash characteristics of palm empty fruit bunch (EFB) upon combustion. *Applied Energy*, *88*(1), 298–305. https://doi.org/10.1016/j.apenergy.2010.07.008

Králik, M. (2014). Adsorption, chemisorption, and catalysis. In *Chemical Papers* (Vol. 68, Issue 12, pp. 1625–1638). De Gruyter Open Ltd. https://doi.org/10.2478/s11696-014-0624-9

Kumar, V., Pandey, N., Dharmadhikari, S., & Ghosh, P. (2020). Degradation of mixed dye via heterogeneous Fenton process: Studies of calcination, toxicity evaluation, and kinetics. *Water Environment Research*, *92*(2), 211–221. https://doi.org/10.1002/wer.1192

Lai, C., Sheng, L., Liao, S., Xi, T., & Zhang, Z. (2013). Surface characterization of TEMPO-oxidized bacterial cellulose. *Surface and Interface Analysis*, *45*(11), 1673–1679. https://doi.org/10.1002/sia.5306

Lai, D. S., Osman, A. F., Adnan, S. A., Ibrahim, I., Alrashdi, A. A., Salimi, M. N. A., & Ul-Hamid, A. (2021). On the use of opefb-derived microcrystalline cellulose and nano-bentonite for development of thermoplastic starch hybrid bio-composites with improved performance. *Polymers*, *13*(6). https://doi.org/10.3390/polym13060897

Lam, M. K., & Lee, K. T. (2011). Renewable and sustainable bioenergies production from palm oil mill effluent (POME): Win-win strategies toward better environmental protection. In

Biotechnology Advances (Vol. 29, Issue 1, pp. 124–141). Elsevier Inc. https://doi.org/10.1016/j.biotechadv.2010.10.001

Lama-Muñoz, A., del Mar Contreras, M., Espínola, F., Moya, M., Romero, I., & Castro, E. (2020). Characterization of the lignocellulosic and sugars composition of different olive leaves cultivars. *Food Chemistry*, *329*. https://doi.org/10.1016/j.foodchem.2020.127153

Lassfolk, R., Pedrón, M., Tejero, T., Merino, P., Wärnå, J., & Leino, R. (2022). Acetyl Group Migration in Xylan and Glucan Model Compounds as Studied by Experimental and Computational Methods. *Journal of Organic Chemistry*, *87*(21), 14544–14554. https://doi.org/10.1021/acs.joc.2c01956

Latip, N. A., Sofian, A. H., Ali, M. F., Ismail, S. N., & Idris, D. M. N. D. (2018). Structural and morphological studies on alkaline pre-treatment of oil palm empty fruit bunch (OPEFB) fiber for composite production. In *Materials Today: Proceedings* (Vol. 00). www.sciencedirect.comwww.materialstoday.com/proceedings2214-7853

Law, K.-N., Rosli, W., Daud, W., & Ghazali, A. (2007). *MORPHOLOGICAL AND CHEMICAL NATURE OF FIBER STRANDS OF OIL PALM EMPTY-FRUIT-BUNCH (OPEFB)*.

Le Gars, M., Delvart, A., Roger, P., Belgacem, M. N., & Bras, J. (2020). Amidation of TEMPO-oxidized cellulose nanocrystals using aromatic aminated molecules. *Colloid and Polymer Science*, *298*(6), 603–617. https://doi.org/10.1007/s00396-020-04640-5

Lee, J., Kim, S., Lee, K. H., Lee, S. K., Chun, Y., Kim, S. W., Park, C., & Yoo, H. Y. (2022). Improvement of bioethanol production from waste chestnut shells via evaluation of mass balance-based pretreatment and glucose recovery process. *Environmental Technology and Innovation*, *28*. https://doi.org/10.1016/j.eti.2022.102955

Levanič, J., Svedström, K., Liljeström, V., Šernek, M., Osojnik Črnivec, I. G., Poklar Ulrih, N., & Haapala, A. (2022). Cellulose fiber and nanofibril characteristics in a continuous sono-assisted process for production of TEMPO-oxidized nanofibrillated cellulose. *Cellulose*, *29*(17), 9121–9142. https://doi.org/10.1007/s10570-022-04845-7

Levantovsky, R., Allen-Blevins, C. R., & Sela, D. A. (2017). Nutritional Requirements of Bifidobacteria. In *The Bifidobacteria and Related Organisms: Biology, Taxonomy, Applications* (pp. 115–129). Elsevier. https://doi.org/10.1016/B978-0-12-805060-6.00006-5

Li, B., Hoy, L., Song, C., Wang, Z., Xue, Q., Li, Y., Qin, J., Cao, N., Jia, C., Zhang, Y., & Shi, W. (2022). Biological function of calcium-sensing receptor (CAS) and its coupling calcium signaling in plants. *Plant Physiology and Biochemistry*, *180*, 74–80.

Li, X., Tabil, L. G., & Panigrahi, S. (2007). Chemical treatments of natural fiber for use in natural fiber-reinforced composites: A review. In *Journal of Polymers and the Environment* (Vol. 15, Issue 1, pp. 25–33). https://doi.org/10.1007/s10924-006-0042-3

Liang, L., Huang, C., Hao, N., & Ragauskas, A. J. (2019). Cross-linked poly(methyl vinyl ether-co-maleic acid)/poly(ethylene glycol)/nanocellulosics foams via directional freezing. *Carbohydrate Polymers*, *213*, 346–351. https://doi.org/10.1016/j.carbpol.2019.02.073

Liang, X., He, Z., Zhong, Y., Tan, W., He, H., Yuan, P., Zhu, J., & Zhang, J. (2013). The effect of transition metal substitution on the catalytic activity of magnetite in heterogeneous Fenton reaction: In interfacial view. *Colloids and Surfaces A: Physicochemical and Engineering Aspects*, *435*, 28–35. https://doi.org/10.1016/j.colsurfa.2012.12.038

Liao, J. J., Latif, N. H. A., Trache, D., Brosse, N., & Hussin, M. H. (2020). Current advancement on the isolation, characterization and application of lignin. In *International Journal of Biological Macromolecules* (Vol. 162, pp. 985–1024). Elsevier B.V. https://doi.org/10.1016/j.ijbiomac.2020.06.168

Lieb, V. M., Kerfers, M. R., Kronmüller, A., Esquivel, P., Alvarado, A., Jiménez, V. M., Schmarr, H. G., Carle, R., Schweiggert, R. M., & Steingass, C. B. (2017). Characterization of Mesocarp and Kernel Lipids from Elaeis guineensis Jacq., Elaeis oleifera [Kunth] Cortés, and Their Interspecific Hybrids. *Journal of Agricultural and Food Chemistry*, *65*(18), 3617–3626. https://doi.org/10.1021/acs.jafc.7b00604

Lim, C. H., Ang, J. J., Lau, S., & Tay, M. G. (2017). Optimization of hydroxyl radical production using electro-Fenton method for chemical oxygen demand reduction in diluted palm oil mill effluent. *Water and Environment Journal*, *31*(4), 578–583. https://doi.org/10.1111/wej.12281

Liu, G., Ji, C., Li, J., & Pan, X. (2022). Facile preparation and properties of superhydrophobic nanocellulose membrane. *Arabian Journal of Chemistry*, *15*(8). https://doi.org/10.1016/j.arabjc.2022.103964

Liu, S., Low, Z. X., Xie, Z., & Wang, H. (2021). TEMPO-Oxidized Cellulose Nanofibers: A Renewable Nanomaterial for Environmental and Energy Applications. In *Advanced Materials Technologies* (Vol. 6, Issue 7). John Wiley and Sons Inc. https://doi.org/10.1002/admt.202001180

Llorente, M. J. F., & García, J. E. C. (2008). Suitability of thermo-chemical corrections for determining gross calorific value in biomass. *Thermochimica Acta*, *468*(1–2), 101–107. https://doi.org/10.1016/j.tca.2007.12.003

Lou, R., Ma, R., Lin, K. T., Ahamed, A., & Zhang, X. (2019). Facile Extraction of Wheat Straw by Deep Eutectic Solvent (DES) to Produce Lignin Nanoparticles. *ACS Sustainable Chemistry and Engineering*, *7*, 10248–10256. https://doi.org/10.1021/acssuschemeng.8b05816

Lou, Z., Han, X., Liu, J., Ma, Q., Yan, H., Yuan, C., Yang, L., Han, H., Weng, F., & Li, Y. (2021). Nano-Fe3O4/bamboo bundles/phenolic resin oriented recombination ternary composite with enhanced multiple functions. *Composites Part B: Engineering*, *226*. https://doi.org/10.1016/j.compositesb.2021.109335

Luo, W., Zhu, L., Wang, N., Tang, H., Cao, M., & She, Y. (2010). Efficient removal of organic pollutants with magnetic nanoscaled BiFeO 3 as a reusable heterogeneous fenton-like catalyst. *Environmental Science and Technology*, *44*(5), 1786–1791. https://doi.org/10.1021/es903390g

Luo, Y., Li, Z., Li, X., Liu, X., Fan, J., Clark, J. H., & Hu, C. (2019). The production of furfural directly from hemicellulose in lignocellulosic biomass: A review. *Catalysis Today*, *319*, 14–24. https://doi.org/10.1016/j.cattod.2018.06.042

Luo, Y., Li, Z., Zuo, Y., Su, Z., & Hu, C. (2017). A Simple Two-Step Method for the Selective Conversion of Hemicellulose in Pubescens to Furfural. *ACS Sustainable Chemistry and Engineering*, *5*(9), 8137–8147. https://doi.org/10.1021/acssuschemeng.7b01766

Ma, J. F., & Yamaji, N. (2008). Functions and transport of silicon in plants. In *Cellular and Molecular Life Sciences* (Vol. 65, Issue 19, pp. 3049–3057). https://doi.org/10.1007/s00018-008-7580-x

Machulek, A., Quina, F. H., Gozzi, F., Silva, V. O., Friedrich, L. C., & Moraes, J. E. F. (2012). Fundamental Mechanistic Studies of the Photo-Fenton Reaction for the Degradation of Organic Pollutants. In T. Puzyn & A. Mostrag-Szlichtyng (Eds.), *Organic Pollutants Ten Years After the Stockholm Convention - Environmental and Analytical Update* (pp. 1–455). www.intechopen.com

Mahmod, S. S., Takriff, M. S., AL-Rajabi, M. M., Abdul, P. M., Gunny, A. A. N., Silvamany, H., & Jahim, J. M. (2023). Water reclamation from palm oil mill effluent (POME): Recent technologies, by-product recovery, and challenges. In *Journal of Water Process Engineering* (Vol. 52). Elsevier Ltd. https://doi.org/10.1016/j.jwpe.2023.103488

Mao, L., Ma, P., Law, K., Daneault, C., & Brouillette, F. (2010). Studies on kinetics and reuse of spent liquor in the TEMPO-mediated selective oxidation of mechanical pulp. *Industrial and Engineering Chemistry Research*, *49*(1), 113–116. https://doi.org/10.1021/ie901039r

Martínez-Ramírez, A. P., Rincón-Ortiz, S. A., Baldovino-Medrano, G., Blanco-Tirado, C., & Combariza, M. Y. (2023a). Influence of reaction variables on the surface chemistry of cellulose nanofibers derived from palm oil empty fruit bunches. *RSC Advances*, *13*, 36117–36129. https://doi.org/10.1039/d3ra06933h

Martínez-Ramírez, A. P., Rincón-Ortiz, S. A., Baldovino-Medrano, V. G., Blanco-Tirado, C., & Combariza, M. Y. (2023b). Influence of reaction variables on the surface chemistry of cellulose nanofibers derived from palm oil empty fruit bunches. *RSC Advances*, *13*(51), 36117–36129. https://doi.org/10.1039/d3ra06933h

Mat Hassan, N. S., Sohrab Hossain, M., Balakrishnan, V., Zuknik, M. H., Mustaner, M., Easa, A. M., Al-Gheethi, A., & Yahaya, A. N. A. (2021). Influence of fresh palm fruit sterilization in the production of carotenoid-rich virgin palm oil. *Foods, 10*(11). https://doi.org/10.3390/foods10112838

Mccann, M. C., Buckeridge, M. S., & Carpita, N. C. (2013). *Plants and BioEnergy*. http://www.springer.com/series/8047

McFarlane, H. E., Döring, A., & Persson, S. (2014). The cell biology of cellulose synthesis. In *Annual Review of Plant Biology* (Vol. 65, pp. 69–94). Annual Reviews Inc. https://doi.org/10.1146/annurev-arplant-050213-040240

Medina, J. D. C., Woiciechowski, A., Filho, A. Z., Nigam, P. S., Ramos, L. P., & Soccol, C. R. (2016). Steam explosion pretreatment of oil palm empty fruit bunches (EFB) using autocatalytic hydrolysis: A biorefinery approach. *Bioresource Technology*, *199*, 173–180. https://doi.org/10.1016/j.biortech.2015.08.126

Medronho, B., & Lindman, B. (2015). Brief overview on cellulose dissolution/regeneration interactions and mechanisms. In *Advances in Colloid and Interface Science* (Vol. 222, pp. 502–508). Elsevier. https://doi.org/10.1016/j.cis.2014.05.004

Mehdaoui, R., Agren, S., El Haskouri, J., Beyou, E., Lahcini, M., & Baouab, M. H. V. (2023). An optimized sono-heterogeneous Fenton degradation of olive-oil mill wastewater organic matter by new magnetic glutarlaldehyde-crosslinked developed cellulose. *Environmental Science and Pollution Research*, *30*(8), 20450–20468. https://doi.org/10.1007/s11356-022-23276-2

Melati, R. B., Shimizu, F. L., Oliveira, G., Pagnocca, F. C., de Souza, W., Sant'Anna, C., & Brienzo, M. (2019). Key Factors Affecting the Recalcitrance and Conversion Process of Biomass. In *Bioenergy Research* (Vol. 12, Issue 1). Springer New York LLC. https://doi.org/10.1007/s12155-018-9941-0

Meng, J., Chroumpi, T., Mäkelä, M. R., & de Vries, R. P. (2022). Xylitol production from plant biomass by Aspergillus niger through metabolic engineering. *Bioresource Technology*, *344*. https://doi.org/10.1016/j.biortech.2021.126199

Mesa Dishington, J., & Azuero Garcia, A. F. (2021). Balance 2020 y perspectivas 2021 de la agroindustria de la palma de aceite. *Fedepalma*, 41.

Milanovic, J., Kostic, M., Milanovic, P., & Skundric, P. (2012). Influence of TEMPO-mediated oxidation on properties of hemp fibers. *Industrial and Engineering Chemistry Research*, *51*(29), 9750–9759. https://doi.org/10.1021/ie300713x

Mishra, S. P., Manent, A. S., Chabot, B., & Daneault, C. (2012). The use of sodium chlorite in post-oxidation of TEMPO-oxidized pulp: Effect on pulp characteristics and nanocellulose yield. *Journal of Wood Chemistry and Technology*, *32*(2), 137–148. https://doi.org/10.1080/02773813.2011.624666

Mo, Z., Zhang, C., Guo, R., Meng, S., & Zhang, J. (2011). Synthesis of Fe3O4 nanoparticles using controlled ammonia vapor diffusion under ultrasonic irradiation. *Industrial and Engineering Chemistry Research*, *50*(6), 3534–3539. https://doi.org/10.1021/ie101683x

Mohammad Padzil, F. N., Lee, S. H., Ainun, Z. M. A. ari, Lee, C. H., & Abdullah, L. C. (2020). Potential of oil palm empty fruit bunch resources in nanocellulose hydrogel production for versatile applications: A review. In *Materials* (Vol. 13, Issue 5). MDPI AG. https://doi.org/10.3390/ma13051245

Mohammad, S., Baidurah, S., Kobayashi, T., Ismail, N., & Leh, C. P. (2021). Palm oil mill effluent treatment processes—A review. In *Processes* (Vol. 9, Issue 5). MDPI AG. https://doi.org/10.3390/pr9050739

Mohammed, M. A. A., Salmiaton, A., Wan Azlina, W. A. K. G., & Mohamad Amran, M. S. (2012). Gasification of oil palm empty fruit bunches: A characterization and kinetic study. *Bioresource Technology*, *110*, 628–636. https://doi.org/10.1016/j.biortech.2012.01.056

Mohd Omar, A. K., Tengku Norsalwani, T. L., Asmah, M. S., Badrulhisham, Z. Y., Easa, A. M., Omar, F. M., Hossain, M. S., Zuknik, M. H., & Nik Norulaini, N. A. (2018). Implementation of the supercritical carbon dioxide technology in oil palm fresh fruits bunch sterilization: A review. In *Journal of CO2 Utilization* (Vol. 25, pp. 205–215). Elsevier Ltd. https://doi.org/10.1016/j.jcou.2018.03.021

Moreno-Chacón, A. L., Camperos-Reyes, J. E., Ávila Diazgranados, R. A., & Romero, H. M. (2013). Biochemical and physiological responses of oil palm to bud rot caused by

Phytophthora palmivora. *Plant Physiology and Biochemistry*, *70*, 246–251. https://doi.org/10.1016/j.plaphy.2013.05.026

Motghare, K. A., Rathod, A. P., Wasewar, K. L., & Labhsetwar, N. K. (2016). Comparative study of different waste biomass for energy application. *Waste Management*, *47*, 40–45. https://doi.org/10.1016/j.wasman.2015.07.032

Motta, I. L., Miranda, N. T., Maciel Filho, R., & Wolf Maciel, M. R. (2018). Biomass gasification in fluidized beds: A review of biomass moisture content and operating pressure effects. In *Renewable and Sustainable Energy Reviews* (Vol. 94, pp. 998–1023). Elsevier Ltd. https://doi.org/10.1016/j.rser.2018.06.042

Mozzon, M., Pacetti, D., Lucci, P., Balzano, M., & Frega, N. G. (2013). Crude palm oil from interspecific hybrid Elaeis oleifera × Elaeis guineensis: Fatty acid regiodistribution and molecular species of glycerides. *Food Chemistry*, *141*(1), 245–252. https://doi.org/10.1016/j.foodchem.2013.03.016

Munawar, M. A., Khoja, A. H., Naqvi, S. R., Mehran, M. T., Hassan, M., Liaquat, R., & Dawood, U. F. (2021). Challenges and opportunities in biomass ash management and its utilization in novel applications. In *Renewable and Sustainable Energy Reviews* (Vol. 150). Elsevier Ltd. https://doi.org/10.1016/j.rser.2021.111451

Naik, G. P., Poonia, A. K., & Chaudhari, P. K. (2022). Role of extractives in biomethane production: characterization and comparison of different cultivars of rice straw. *Clean Technologies and Environmental Policy*, *24*(9), 2899–2909. https://doi.org/10.1007/s10098-022-02375-1

Naji Givi, A., Abdul Rashid, S., Aziz, F. N. A., & Salleh, M. A. M. (2011). The effects of lime solution on the properties of SiO2 nanoparticles binary blended concrete. *Composites Part B: Engineering*, *42*(3), 562–569. https://doi.org/10.1016/j.compositesb.2010.10.002

Nasrollahzadeh, M., Soleimani, F., Bidgoli, N. S. S., Nezafat, Z., Orooji, Y., & Baran, T. (2021). Recent developments in polymer-supported ruthenium nanoparticles/complexes for oxidation reactions. *Journal of Organometallic Chemistry*, *933*, 121658. https://doi.org/10.1016/j.jorganchem.2020.121658

Nasuha, N., Ismail, S., & Hameed, B. H. (2016). Activated electric arc furnace slag as an efficient and reusable heterogeneous Fenton-like catalyst for the degradation of Reactive Black 5. *Journal of the Taiwan Institute of Chemical Engineers*, *67*, 235–243. https://doi.org/10.1016/j.jtice.2016.07.023

Navia, E. A., Ávila, R. A., Daza, E. E., Restrepo, E. F., & Romero, H. M. (2014). Assessment of tolerance to bud rot in oil palm under field conditions. *European Journal of Plant Pathology*, *140*(4), 711–720. https://doi.org/10.1007/s10658-014-0491-9

Negrão, D. R., Grandis, A., Buckeridge, M. S., Rocha, G. J. M., Leal, M. R. L. V., & Driemeier, C. (2021). Inorganics in sugarcane bagasse and straw and their impacts for bioenergy and biorefining: A review. In *Renewable and Sustainable Energy Reviews* (Vol. 148). Elsevier Ltd. https://doi.org/10.1016/j.rser.2021.111268

Ng, K. H., Lee, C. H., Khan, M. R., & Cheng, C. K. (2016). Photocatalytic degradation of recalcitrant POME waste by using silver doped titania: Photokinetics and scavenging studies. *Chemical Engineering Journal*, *286*, 282–290. https://doi.org/10.1016/j.cej.2015.10.072

Nidheesh, P. V., Gandhimathi, R., & Ramesh, S. T. (2013). Degradation of dyes from aqueous solution by Fenton processes: A review. In *Environmental Science and Pollution Research* (Vol. 20, Issue 4, pp. 2099–2132). Springer Verlag. https://doi.org/10.1007/s11356-012-1385-z

Nieves, D. C., Karimi, K., & Horváth, I. S. (2011). Improvement of biogas production from oil palm empty fruit bunches (OPEFB). *Industrial Crops and Products*, *34*(1), 1097–1101. https://doi.org/10.1016/j.indcrop.2011.03.022

Nollet, H., Roels, M., Lutgen, P., Van Der Meeren, P., & Verstraete, W. (2003). Removal of PCBs from wastewater using fly ash. *Chemosphere*, *53*(6), 655–665. https://doi.org/10.1016/S0045-6535(03)00517-4

Norrrahim, M. N. F., Farid, M. A. A., Lawal, A. A., Tengku Yasim-Anuar, T. A., Samsudin, M. H., & Zulkifli, A. A. (2022). Emerging technologies for value-added use of oil palm biomass. In *Environmental Science: Advances* (Vol. 1, Issue 3, pp. 259–275). Royal Society of Chemistry. https://doi.org/10.1039/d2va00029f

Novianti, S., Nurdiawati, A., Zaini, I. N., Prawisudha, P., Sumida, H., & Yoshikawa, K. (2015). Low-potassium Fuel Production from Empty Fruit Bunches by Hydrothermal Treatment Processing and Water Leaching. *Energy Procedia*, *75*, 584–589. https://doi.org/10.1016/j.egypro.2015.07.460

Omar, F. N., Afandi, M., Mohammed, P., & Samsu Baharuddin, A. (2014). Microstructure Modelling of Silica Bodies from Oil Palm Empty Fruit Bunch (OPEFB) Fibres. *BioResources*, *9*, 938–951.

Omar, R., Idris, A., Yunus, R., Khalid, K., & Aida Isma, M. I. (2011). Characterization of empty fruit bunch for microwave-assisted pyrolysis. *Fuel*, *90*(4), 1536–1544. https://doi.org/10.1016/j.fuel.2011.01.023

Ordaz, F. A., & Arrizabalaga Sáez, A. (2020). *Cinética química*.

Ouarhim, W., Zari, N., Bouhfid, R., & Qaiss, A. E. K. (2018). Mechanical performance of natural fibers-based thermosetting composites. In *Mechanical and Physical Testing of Biocomposites, Fibre-Reinforced Composites and Hybrid Composites* (pp. 43–60). Elsevier. https://doi.org/10.1016/B978-0-08-102292-4.00003-5

Ovalle-Serrano, S. A., Gómez, F. N., Blanco-Tirado, C., & Combariza, M. Y. (2018). Isolation and characterization of cellulose nanofibrils from Colombian Fique decortication by-products. *Carbohydrate Polymers*, *189*, 169–177. https://doi.org/10.1016/j.carbpol.2018.02.031

Ovalle-Serrano, S., Blanco-Tirado, C., & Combariza, Y. (2018). Exploring the composition of raw and delignified Colombian fique fibers, tow and pulp. *Cellulose*, *25*, 151–165. https://doi.org/10.1007/s10570

Palamae, S., Dechatiwongse, P., Choorit, W., Chisti, Y., & Prasertsan, P. (2017a). Cellulose and hemicellulose recovery from oil palm empty fruit bunch (EFB) fibers and production of sugars from the fibers. *Carbohydrate Polymers, 155,* 491–497. https://doi.org/10.1016/j.carbpol.2016.09.004

Palamae, S., Dechatiwongse, P., Choorit, W., Chisti, Y., & Prasertsan, P. (2017b). Cellulose and hemicellulose recovery from oil palm empty fruit bunch (EFB) fibers and production of sugars from the fibers. *Carbohydrate Polymers*, *155*, 491–497. https://doi.org/10.1016/j.carbpol.2016.09.004

Palamae, S., Palachum, W., Chisti, Y., & Choorit, W. (2014). Retention of hemicellulose during delignification of oil palm empty fruit bunch (EFB) fiber with peracetic acid and alkaline peroxide. *Biomass and Bioenergy*, *66*, 240–248. https://doi.org/10.1016/j.biombioe.2014.03.045

Pandey Swatiimahiwal, G. K. (2020). *Role offPotassium in Plants*. http://www.springer.com/series/10080

Park, S., Kim, S. J., Oh, K. C., Cho, L. H., Jeon, Y. K., Lee, C., & Kim, D. H. (2022). Thermogravimetric analysis-based proximate analysis of agro-byproducts and prediction of calorific value. *Energy Reports*, *8*, 12038–12044. https://doi.org/10.1016/j.egyr.2022.09.040

Pattanaik, L., Naik, S. N., & Hariprasad, P. (2019). Valorization of waste Indigofera tinctoria L. biomass generated from indigo dye extraction process—potential towards biofuels and compost. *Biomass Conversion and Biorefinery*, *9*(2), 445–457. https://doi.org/10.1007/s13399-018-0354-2

Pattiya, A. (2017). Fast pyrolysis. In *Direct Thermochemical Liquefaction for Energy Applications* (pp. 3–28). Elsevier. https://doi.org/10.1016/B978-0-08-101029-7.00001-1

Peng, N., Huang, D., Gong, C., Wang, Y., Zhou, J., & Chang, C. (2020). Controlled Arrangement of Nanocellulose in Polymeric Matrix: From Reinforcement to Functionality. In *ACS Nano* (Vol. 14, Issue 12, pp. 16169–16179). American Chemical Society. https://doi.org/10.1021/acsnano.0c08906

Pesce, G. R., Alves-Ferreira, J., Hsiao, A., Torrado, I., Martinez, A., Mauromicale, G., & Fernandes, M. C. (2023). Bioethanol Production from Globe Artichoke Residues: from the Field to the Fermenter. *Bioenergy Research*, *16*(3), 1567–1578. https://doi.org/10.1007/s12155-022-10548-5

Petrova, T. M., Fachikov, L., & Hristov, J. (2011). The Magnetite as Adsorbent for Some Hazardous Species from Aqueous Solutions: a Review. In *International Review of Chemical Engineering (I.RE.CH.E.)* (Vol. 3, Issue 2).

Pierre, G., Punta, C., Delattre, C., Melone, L., Dubessay, P., Fiorati, A., Pastori, N., Galante, Y. M., & Michaud, P. (2017). TEMPO-mediated oxidation of polysaccharides: An ongoing story. In *Carbohydrate Polymers* (Vol. 165, pp. 71–85). Elsevier Ltd. https://doi.org/10.1016/j.carbpol.2017.02.028

Pintori, G., & Cattaruzza, E. (2022). XPS/ESCA on glass surfaces: A useful tool for ancient and modern materials. In *Optical Materials: X* (Vol. 13). Elsevier B.V. https://doi.org/10.1016/j.omx.2021.100108

Poletto, M., Ornaghi Júnior, H. L., & Zattera, A. J. (2014). Native cellulose: Structure, characterization and thermal properties. *Materials*, *7*(9), 6105–6119. https://doi.org/10.3390/ma7096105

Pönni, R., Pääkkönen, T., Nuopponen, M., Pere, J., & Vuorinen, T. (2014). Alkali treatment of birch kraft pulp to enhance its TEMPO catalyzed oxidation with hypochlorite. *Cellulose*, *21*(4), 2859–2869. https://doi.org/10.1007/s10570-014-0278-3

Ptáček, P., Šoukal, F., & Opravil, T. (2018). Introduction to the Transition State Theory. In *Introducing the Effective Mass of Activated Complex and the Discussion on the Wave Function of this Instanton*. InTech. https://doi.org/10.5772/intechopen.78705

Pua, F. L., Subari, M. S., Ean, L. W., & Krishnan, S. G. (2020). Characterization of biomass fuel pellets made from Malaysia tea waste and oil palm empty fruit bunch. *Materials Today: Proceedings*, *31*, 187–190. https://doi.org/10.1016/j.matpr.2020.02.218

Puangsin, B., Soeta, H., Saito, T., & Isogai, A. (2017). Characterization of cellulose nanofibrils prepared by direct TEMPO-mediated oxidation of hemp bast. *Cellulose*, *24*(9), 3767–3775. https://doi.org/10.1007/s10570-017-1390-y

Qin, Y., Li, Y., Wu, R., Wang, X., Qin, J., Fu, Y., Qin, M., Wang, Z., Zhang, Y., & Zhang, F. (2022). Bilayer Designed Paper-Based Solar Evaporator for Efficient Seawater Desalination. *Nanomaterials*, *12*(19). https://doi.org/10.3390/nano12193487

Quici, N., Morgada, M. E., Piperata, G., Babay, P., Gettar, R. T., & Litter, M. I. (2005). Oxalic acid destruction at high concentrations by combined heterogeneous photocatalysis and photo-Fenton processes. *Catalysis Today*, *101*(3-4 SPEC. ISS.), 253–260. https://doi.org/10.1016/j.cattod.2005.03.002

Rahman, S. H. A., Choudhury, J. P., & Ahmad, A. L. (2006). Production of xylose from oil palm empty fruit bunch fiber using sulfuric acid. *Biochemical Engineering Journal*, *30*(1), 97–103. https://doi.org/10.1016/j.bej.2006.02.009

Rama Rao, P., & Ramakrishna, G. (2022). Oil palm empty fruit bunch fiber: surface morphology, treatment, and suitability as reinforcement in cement composites- A state of the art review. *Cleaner Materials*, *6*. https://doi.org/10.1016/j.clema.2022.100144

Raman, J. K., & Gnansounou, E. (2014). Ethanol and lignin production from Brazilian empty fruit bunch biomass. *Bioresource Technology*, *172*, 241–248. https://doi.org/10.1016/j.biortech.2014.09.043

Ramirez, J. H., Costa, C. A., & Madeira, L. M. (2005). Experimental design to optimize the degradation of the synthetic dye Orange II using Fenton's reagent. *Catalysis Today*, *107–108*, 68–76. https://doi.org/10.1016/j.cattod.2005.07.060

Ramirez, J. H., Maldonado-Hódar, F. J., Pérez-Cadenas, A. F., Moreno-Castilla, C., Costa, C. A., & Madeira, L. M. (2007). Azo-dye Orange II degradation by heterogeneous Fenton-like reaction using carbon-Fe catalysts. *Applied Catalysis B: Environmental*, *75*(3–4), 312–323. https://doi.org/10.1016/j.apcatb.2007.05.003

Ramirez-Contreras, N. E., Munar-Florez, D. A., Garcia-Nuñez, J. A., Mosquera-Montoya, M., & Faaij, A. P. C. (2020). The GHG emissions and economic performance of the Colombian palm oil sector; current status and long-term perspectives. *Journal of Cleaner Production*, *258*. https://doi.org/10.1016/j.jclepro.2020.120757

Ramírez-Contreras, N., Silva Ramirez, A., Garzon, E., & Yáñez, E. (2011). *Caracterización y manejo de subproductos del beneficio del fruto de palma de aceite*. www.cenipalma.org

Ramlee, N. A., Naveen, J., & Jawaid, M. (2021). Potential of oil palm empty fruit bunch (OPEFB) and sugarcane bagasse fibers for thermal insulation application – A review. In *Construction and Building Materials* (Vol. 271). Elsevier Ltd. https://doi.org/10.1016/j.conbuildmat.2020.121519

Rashid, R., Ejaz, U., & Shail, M. (2021). Biomass to Xylose. In A. Khan (Ed.), *Sustainable Bioconversion of Waste to Value Added Products* (pp. 247–265). http://www.springer.com/series/15883

Rathamat, Z., Choorit, W., Chisti, Y., & Prasertsan, P. (2021). Two-step isolation of hemicellulose from oil palm empty fruit bunch fibers and its use in production of xylooligosaccharide prebiotic. *Industrial Crops and Products*, *160*. https://doi.org/10.1016/j.indcrop.2020.113124

Rattaz, A., Mishra, S. P., Chabot, B., & Daneault, C. (2011). Cellulose nanofibres by sonocatalysed-TEMPO-oxidation. *Cellulose*, *18*(3), 585–593. https://doi.org/10.1007/s10570-011-9529-8

Ravelo-Nieto, E., Ovalle-Serrano, S. A., Gutiérrez-Pineda, E. A., Blanco-Tirado, C., & Combariza, M. Y. (2023). Textile wastewater depuration using a green cellulose based Fe3O4 bionanocomposite. *Journal of Environmental Chemical Engineering*, *11*(2). https://doi.org/10.1016/j.jece.2023.109516

Ravindran, L., Sreekala, M. S., & Thomas, S. (2019). Novel processing parameters for the extraction of cellulose nanofibres (CNF) from environmentally benign pineapple leaf fibres (PALF): Structure-property relationships. *International Journal of Biological Macromolecules, 131*, 858–870. https://doi.org/10.1016/j.ijbiomac.2019.03.134

Redlinger-Pohn, J. D., Petkovšek, M., Gordeyeva, K., Zupanc, M., Gordeeva, A., Zhang, Q., Dular, M., & Söderberg, L. D. (2022). Cavitation Fibrillation of Cellulose Fiber. *Biomacromolecules*, *23*(3), 847–862. https://doi.org/10.1021/acs.biomac.1c01309

Reneta Nafu, Y., Foba-Tendo, J., Njeugna, E., Oliver, G., & Omar Cooke, K. (2015). Extraction and Characterization of Fibres from the Stalk and Spikelets of Empty Fruit Bunch. *Journal of Applied Chemistry, 2015*, 1–10. https://doi.org/10.1155/2015/750818

Ribeiro, J. P., & Nunes, M. I. (2021). Recent trends and developments in Fenton processes for industrial wastewater treatment – A critical review. In *Environmental Research* (Vol. 197). Academic Press Inc. https://doi.org/10.1016/j.envres.2021.110957

Rocha, S., Candia, O., Valdebenito, F., Flavio Espinoza-Monje, J., & Azócar, L. (2020). Biomass quality index: Searching for suitable biomass as an energy source in Chile. *Fuel*, *264*. https://doi.org/10.1016/j.fuel.2019.116820

Rodionova, G., Saito, T., Lenes, M., Eriksen, Ø., Gregersen, Ø., Kuramae, R., & Isogai, A. (2013). TEMPO-Mediated Oxidation of Norway Spruce and Eucalyptus Pulps: Preparation and Characterization of Nanofibers and Nanofiber Dispersions. *Journal of Polymers and the Environment*, *21*(1), 207–214. https://doi.org/10.1007/s10924-012-0483-9

Rodríguez-Zúñiga, U. F., Cannella, D., Giordano, R. D. C., Giordano, R. D. L. C., Jørgensen, H., & Felby, C. (2015). Lignocellulose pretreatment technologies affect the level of enzymatic cellulose oxidation by LPMO. *Green Chemistry*, *17*(5), 2896–2903. https://doi.org/10.1039/c4gc02179g

Rojas, O. (2016). *Cellulose Chemistry and Properties: Fibers, Nanocelluloses and Advanced Materials*. http://www.springer.com/series/12

Rojas, O. J. (2016). Cellulose Chemistry and Properties: Fibers, Nanocelluloses and Advanced Materials. In *Advances in Polymer Science* (Vol. 271).

Rom, V., & Marschner, H. (1991). *Function of Micronutrients in Plants*.

Rouxhet, P. G., & Genet, M. J. (2011). XPS analysis of bio-organic systems. *Surface and Interface Analysis*, *43*(12), 1453–1470. https://doi.org/10.1002/sia.3831

Rui et al. (2019). Facile Extraction of Wheat Straw by Deep Eutectic Solvent (DES) to Produce Lignin Nanoparticles [Research-article]. *ACS Sustainable Chemistry and Engineering*, *7*(12), 10248–10256. https://doi.org/10.1021/acssuschemeng.8b05816

Saeed, M. O., Azizli, K., Isa, M. H., & Bashir, M. J. K. (2015). Application of CCD in RSM to obtain optimize treatment of POME using Fenton oxidation process. *Journal of Water Process Engineering*, *8*, e7–e16. https://doi.org/10.1016/j.jwpe.2014.11.001

Saez Zobiole, L. H., Dantas dos Santos, W., Bonini, E., Ferrase-Filho, O., Kremer, R., Silvério de Oliverira Jr, R., & Constantin, J. (2012). Lignin : properties and applications in biotechnology and bioenergy. In R. J. Paterson (Ed.), *Lignin : properties and applications in biotechnology and bioenergy* (Uk Ed., pp. 419–434). Nova Sicence Publisherts, Inc.

Sailah, I., Fahma, F., & Sihite, R. (2022). The Effects of CaCl2 and Cellulose Concentrations on the Cellulose PVA Alginate Based Filaments Production by Wet Spinning. *Trends in Sciences, 19(18)*(5816), 1–10.

Saito, T., Kimura, S., Nishiyama, Y., & Isogai, A. (2007). Cellulose nanofibers prepared by TEMPO-mediated oxidation of native cellulose. *Biomacromolecules*, *8*(8), 2485–2491. https://doi.org/10.1021/bm0703970

Sajab, M. S., Chia, C. H., Zakaria, S., & Khiew, P. S. (2013). Cationic and anionic modifications of oil palm empty fruit bunch fibers for the removal of dyes from aqueous solutions. *Bioresource Technology*, *128*, 571–577. https://doi.org/10.1016/j.biortech.2012.11.010

Saksena, H. B., Sharma, M., Singh, D., & Laxmi, A. (2020). The versatile role of glucose signalling in regulating growth, development and stress responses in plants. *Journal of Plant Biochemistry and Biotechnology*, *29*(4), 687–699. https://doi.org/10.1007/s13562-020-00614-4

Sander, K., Dütsch, L., Bremer, M., Fischer, S., Vogt, C., & Zuber, J. (2023). Characterization of Soluble and Insoluble Lignin Oligomers by Means of Ultrahigh Resolving Mass Spectrometry. *Energy and Fuels*, *37*(1), 439–449. https://doi.org/10.1021/acs.energyfuels.2c03538

Sani, S., Dashti, A. F., & Adnan, R. (2020a). Applications of Fenton oxidation processes for decontamination of palm oil mill effluent: A review. *Arabian Journal of Chemistry*, *13*(10), 7302–7323. https://doi.org/10.1016/j.arabjc.2020.08.009

Sani, S., Dashti, A. F., & Adnan, R. (2020b). Applications of Fenton oxidation processes for decontamination of palm oil mill effluent: A review. In *Arabian Journal of Chemistry* (Vol. 13, Issue 10, pp. 7302–7323). Elsevier B.V. https://doi.org/10.1016/j.arabjc.2020.08.009

Santana, C. S., Ramos, M. D. N., Velloso, C. C. V., & Aguiar, A. (2019). Kinetic evaluation of dye decolorization by fenton processes in the presence of 3-hydroxyanthranilic acid. *International Journal of Environmental Research and Public Health*, *16*(9). https://doi.org/10.3390/ijerph16091602

Sbiai, A., Maazouz, A., Fleury, E., Sautereau, H., & Kaddami, H. (2012). TEMPO-Mediated Oxidation of Lignocellulosic Fibers from Date Palm Leaves: Effect of the Oxidation on the Processing by RTM Process and Properties of Epoxy Based Composites. In *Composites and Their Applications*. InTech. https://doi.org/10.5772/47763

Seddiqi, H., Oliaei, E., Honarkar, H., Jin, J., Geonzon, L. C., Bacabac, R. G., & Klein-Nulend, J. (2021). Cellulose and its derivatives: towards biomedical applications. In *Cellulose* (Vol. 28, Issue 4, pp. 1893–1931). Springer Science and Business Media B.V. https://doi.org/10.1007/s10570-020-03674-w

Segura, C., Zaror, C., Mansilla, H. D., & Mondaca, M. A. (2008). Imidacloprid oxidation by photo-Fenton reaction. *Journal of Hazardous Materials*, *150*(3), 679–686. https://doi.org/10.1016/j.jhazmat.2007.05.018

Shafique, U., Anwar, J., Ali Munawar, M., Zaman, W. uz, Rehman, R., Dar, A., Salman, M., Saleem, M., Shahid, N., Akram, M., Naseer, A., & Jamil, N. (2016). Chemistry of ice: Migration of ions and gases by directional freezing of water. *Arabian Journal of Chemistry*, *9*, S47–S53. https://doi.org/10.1016/j.arabjc.2011.02.019

Shaiful Sajab, M., Harun, S., Saiful Irwan Zubairi, T., Md Jahim, J., Mohd Tajuddin, A., Irwan Zubairi, S., Markom, M., Tusirin Mohd Nor, M., Amrin Abdullah, M., & Hashim, N. (2019). Influence of Deep Eutectic Solvent (DES) Pretreatment on Various Chemical Composition of Empty Fruit Bunch (EFB). *International Journal of Engineering & Technology*, *8*(1), 266–274. https://doi.org/10.14419/ijet.v8i1.2.24913

Shamsudin, S., Md Shah, U. K., Zainudin, H., Abd-Aziz, S., Mustapa Kamal, S. M., Shirai, Y., & Hassan, M. A. (2012). Effect of steam pretreatment on oil palm empty fruit bunch for the production of sugars. *Biomass and Bioenergy*, *36*, 280–288. https://doi.org/10.1016/j.biombioe.2011.10.040

Shi, F., Wang, Y., Davaritouchaee, M., Yao, Y., & Kang, K. (2020). Directional Structure Modification of Poplar Biomass-Inspired High Efficacy of Enzymatic Hydrolysis by Sequential Dilute Acid-Alkali Treatment. *ACS Omega*, *5*(38), 24780–24789. https://doi.org/10.1021/acsomega.0c03419

Shokri, A., & Sanavi Fard, M. (2023). Using α-Fe2O3/SiO2 as a heterogeneous Fenton catalyst for the removal of chlorophenol in aqueous environment: Thermodynamic and kinetic studies. *International Journal of Environmental Science and Technology*, *20*(1), 383–396. https://doi.org/10.1007/s13762-022-04498-w

Siddiqui, H., Sami, F., & Hayat, S. (2020). Glucose: Sweet or bitter effects in plants-a review on current and future perspective. In *Carbohydrate Research* (Vol. 487). Elsevier Ltd. https://doi.org/10.1016/j.carres.2019.107884

Silva, H. D., Cerqueira, M. Â., & Vicente, A. A. (2012). Nanoemulsions for Food Applications: Development and Characterization. In *Food and Bioprocess Technology* (Vol. 5, Issue 3, pp. 854–867). Springer New York LLC. https://doi.org/10.1007/s11947-011-0683-7

Silva, V. A. J., Andrade, P. L., Silva, M. P. C., Bustamante, A. D., De Los Santos Valladares, L., & Albino Aguiar, J. (2013). Synthesis and characterization of Fe3O4 nanoparticles coated with fucan polysaccharides. *Journal of Magnetism and Magnetic Materials*, *343*, 138–143. https://doi.org/10.1016/j.jmmm.2013.04.062

Simarani, K., Hassa, M. A., Abd-Aziz, S., Wakisaka, M., & Shirai, Y. (2009). Effect of Palm Oil Mill Sterilization Process on the Physicochemical Characteristics and Enzymatic Hydrolysis of Empty Fruit Bunch. *Asian Journal of Biotechnology*, *1(2)*, 57–66.

Singh, P., Duarte, H., Alves, L., Antunes, F., Le Moigne, N., Dormanns, J., Duchemin, B., Staiger, M. P., & Medronho, B. (2015). From Cellulose Dissolution and Regeneration to Added Value Applications — Synergism Between Molecular Understanding and Material Development. In *Cellulose - Fundamental Aspects and Current Trends*. InTech. https://doi.org/10.5772/61402

Sluiter, A., Hames, B., Hyman, D., Payne, C., Ruiz, R., Scarlata, C., Sluiter, J., Templeton, D., & Wolfe, J. (2008). Determination of Total Solids in Biomass and Total Dissolved Solids in

Liquid Process Samples Laboratory Analytical Procedure (LAP) Issue Date: 3/31/2008. In *NREL*. www.nrel.gov

Sluiter, A., Hames, B., Ruiz, R., Scarlata, C., Sluiter, J., Templeton, D., & Crocker, D. (2008). *Determination of Structural Carbohydrates and Lignin in Biomass: Laboratory Analytical Procedure (LAP) (Revised July 2011)*. http://www.nrel.gov/biomass/analytical_procedures.html

Sluiter, J. B., Ruiz, R. O., Scarlata, C. J., Sluiter, A. D., & Templeton, D. W. (2010). Compositional analysis of lignocellulosic feedstocks. 1. Review and description of methods. *Journal of Agricultural and Food Chemistry, 58*(16), 9043–9053. https://doi.org/10.1021/jf1008023

statista. (2020, June 26). *Vegetable oil yields per hectare by type | Statista*. Https://Www.Statista.Com/Statistics/1263201/Vegetable-Oil-Yields-per-Hectare-Worldwide-by-Type-Globally/. https://www.statista.com/statistics/1263201/vegetable-oil-yields-per-hectare-worldwide-by-type-globally/

Sudiyani, Y., Sembiring, K. C., Hendarsyah, H., & Alawiyah, S. (2010). *Alkaline pretreatment and enzymatic saccharification of oil palm empty fruit bunch fiber for ethanol production 1) Pengolahan awal dengan basa NaOH dan sakarifikasi enzimatis serat tandan kosong kelapa sawit (TKKS) untuk produksi etanol* (Vol. 78, Issue 2).

Sukaribin, N., & Khalid, K. (2009). Effectiveness of sterilisation of oil palm bunch using microwave technology. In *Industrial Crops and Products* (Vol. 30, Issue 2, pp. 179–183). https://doi.org/10.1016/j.indcrop.2009.05.001

Suraj, P., Kumar, V., Thakur, C., & Ghosh, P. (2019). Taguchi optimization of COD removal by heterogeneous Fenton process using copper ferro spinel catalyst in a fixed bed reactor - RTD, kinetic and thermodynamic study. *Journal of Environmental Chemical Engineering*, *7*(1). https://doi.org/10.1016/j.jece.2018.102859

Sy, C., Dangles, O., Borel, P., & Caris-Veyrat, C. (2013). Iron-induced oxidation of (all-E)-carotene under model gastric conditions: Kinetics, products, and mechanism. *Free Radical Biology and Medicine*, *63*, 195–206. https://doi.org/10.1016/j.freeradbiomed.2013.05.017

Taha, M. R., & Ibrahim, A. H. (2014a). Characterization of nano zero-valent iron (nZVI) and its application in sono-Fenton process to remove COD in palm oil mill effluent. *Journal of Environmental Chemical Engineering*, *2*(1), 1–8. https://doi.org/10.1016/j.jece.2013.11.021

Taha, M. R., & Ibrahim, A. H. (2014b). COD removal from anaerobically treated palm oil mill effluent (AT-POME) via aerated heterogeneous Fenton process: Optimization study. *Journal of Water Process Engineering*, *1*, 8–16. https://doi.org/10.1016/j.jwpe.2014.02.002

Taha, M. R., Ibrahim, A. H., Amat, R. C., & Azhari, A. W. (2014). Applicability of nano zero valent iron (nZVI) in sono-Fenton process. *Journal of Physics: Conference Series*, *495*(1). https://doi.org/10.1088/1742-6596/495/1/012010

Tajmirriahi, M., Karimi, K., & Kumar, R. (2021). Effects of pinewood extractives on bioconversion of pinewood. *Fuel*, *283*. https://doi.org/10.1016/j.fuel.2020.119302

Tamás, T., & Tomlin, A. S. (2014). *Analysis of Kinetic Reaction Mechanisms*.

Tan, K. A., Wan Maznah, W. O., Morad, N., Lalung, J., Ismail, N., Talebi, A., & Oyekanmi, A. A. (2022). Advances in POME treatment methods: potentials of phycoremediation, with a focus on South East Asia. In *International Journal of Environmental Science and Technology* (Vol. 19, Issue 8, pp. 8113–8130). Springer Science and Business Media Deutschland GmbH. https://doi.org/10.1007/s13762-021-03436-6

Tan, K. T., Lee, K. T., Mohamed, A. R., & Bhatia, S. (2009). Palm oil: Addressing issues and towards sustainable development. *Renewable and Sustainable Energy Reviews*, *13*(2), 420–427. https://doi.org/10.1016/j.rser.2007.10.001

Tan, Z., Liew, C. K., Yee, F. C., Talamona, D., & Goh, K. L. (2017). Oil Palm Empty Fruit Bunch Fibresand Biopolymer Composites: PossibleEffects of Moisture on the Elasticity,Fracture Properties and Reliability. In M. Jawaid, S. M. Sapuan, & O. Y. Alothman (Eds.), *Green Energy and Technology Green Biocomposites Manufacturing and Properties*. http://www.springer.com/series/8059

Tarrés, Q., Delgado-Aguilar, M., Pèlach, M. A., González, I., Boufi, S., & Mutjé, P. (2016). Remarkable increase of paper strength by combining enzymatic cellulose nanofibers in bulk and TEMPO-oxidized nanofibers as coating. *Cellulose*, *23*(6), 3939–3950. https://doi.org/10.1007/s10570-016-1073-0

Teleman, A., Lundqvist, J., Tjerneld, F., Stålbrand, H., & Dahlman, O. (2000). *Characterization of acetylated 4-O-methylglucuronoxylan isolated from aspen employing 1 H and 13 C NMR spectroscopy*. www.elsevier.nl/locate/carres

Thomas, N., Dionysiou, D. D., & Pillai, S. C. (2021). Heterogeneous Fenton catalysts: A review of recent advances. In *Journal of Hazardous Materials* (Vol. 404). Elsevier B.V. https://doi.org/10.1016/j.jhazmat.2020.124082

Traoré, M., Kaal, J., & Martínez Cortizas, A. (2018). Differentiation between pine woods according to species and growing location using FTIR-ATR. *Wood Science and Technology*, *52*(2), 487–504. https://doi.org/10.1007/s00226-017-0967-9

Turner, S., & Kumar, M. (2018). Cellulose synthase complex organization and cellulose microfibril structure. In *Philosophical Transactions of the Royal Society A: Mathematical, Physical and Engineering Sciences* (Vol. 376, Issue 2112). Royal Society Publishing. https://doi.org/10.1098/rsta.2017.0048

Ummartyotin, S., & Manuspiya, H. (2015). A critical review on cellulose: From fundamental to an approach on sensor technology. In *Renewable and Sustainable Energy Reviews* (Vol. 41, pp. 402–412). Elsevier Ltd. https://doi.org/10.1016/j.rser.2014.08.050

Umor, N. A., Abdullah, S., Mohamad, A., Ismail, S. Bin, Ismail, S. I., & Misran, A. (2021). Energy potential of oil palm empty fruit bunch (Efb) fiber from subsequent cultivation of volvariella volvacea (bull.) singer. *Sustainability (Switzerland)*, *13*(23). https://doi.org/10.3390/su132313008

Unidas., N. (n.d.). *Agua | Naciones Unidas*. Retrieved September 8, 2019, from https://www.un.org/es/sections/issues-depth/water/index.html

Upadhyay, S. (2006). *Chemical Kinetics and Reaction Dynamics* (Springer).

U.S. Department of Agriculture. (2023, February). *Palm Oil Explorer*. Https://Ipad.Fas.Usda.Gov/Cropexplorer/Cropview/CommodityView.Aspx?Cropid=4243000. https://ipad.fas.usda.gov/cropexplorer/cropview/commodityView.aspx?cropid=4243000

Valdés, C., Alzate-Morales, J., Osorio, E., Villaseñor, J., & Navarro-Retamal, C. (2015). A characterization of the two-step reaction mechanism of phenol decomposition by a Fenton reaction. *Chemical Physics Letters*, *640*, 16–22. https://doi.org/10.1016/j.cplett.2015.10.005

Vallejos, M. E., Felissia, F. E., Area, M. C., Ehman, N. V., Tarrés, Q., & Mutjé, P. (2016). Nanofibrillated cellulose (CNF) from eucalyptus sawdust as a dry strength agent of unrefined eucalyptus handsheets. *Carbohydrate Polymers*, *139*, 99–105. https://doi.org/10.1016/j.carbpol.2015.12.004

Van Hai, L., Zhai, L., Kim, H. C., Kim, J. W., Choi, E. S., & Kim, J. (2018). Cellulose nanofibers isolated by TEMPO-oxidation and aqueous counter collision methods. *Carbohydrate Polymers*, *191*, 65–70. https://doi.org/10.1016/j.carbpol.2018.03.008

Van Santend, R. A., & Niemantsverdriet, J. W. (1995). *Chemical Kinetics and Catalysis*.

Vanholme, R., Morreel, K., Ralph, J., & Boerjan, W. (2008). Lignin engineering. In *Current Opinion in Plant Biology* (Vol. 11, Issue 3, pp. 278–285). https://doi.org/10.1016/j.pbi.2008.03.005

Védrine, J. C. (2014). Revisiting active sites in heterogeneous catalysis: Their structure and their dynamic behaviour. *Applied Catalysis A: General*, *474*, 40–50. https://doi.org/10.1016/j.apcata.2013.05.029

Veluchamy, C., & Kalamdhad, A. S. (2020). Effect of Total Solid Content of Lignocellulose Pulp and Paper Mill Sludge on Methane Production and Modeling. *Journal of Environmental Engineering*, *146*(3). https://doi.org/10.1061/(asce)ee.1943-7870.0001650

Venkateswar Rao, L., Goli, J. K., Gentela, J., & Koti, S. (2016). Bioconversion of lignocellulosic biomass to xylitol: An overview. In *Bioresource Technology* (Vol. 213, pp. 299–310). Elsevier Ltd. https://doi.org/10.1016/j.biortech.2016.04.092

Verma, A., Parasah, A., Naman Jain, V. K., Singh, S., Mavinkere Rangappa, & Suchart Siengchin. (2020). Surface Modification Techniques for the Preparation of Different Novel Biofibers for Composites. In A. Khan & Mavinkere Sanjay (Eds.), *Biofibers and Biopolymers for Biocomposites,* (pp. 1–34).

Wang, C., Sun, R., Huang, R., & Cao, Y. (2021). A novel strategy for enhancing heterogeneous Fenton degradation of dye wastewater using natural pyrite: Kinetics and mechanism. *Chemosphere*, *272*. https://doi.org/10.1016/j.chemosphere.2021.129883

Wang, L., Lundahl, M. J., Greca, L. G., Papageorgiou, A. C., Borghei, M., & Rojas, O. J. (2019). Effects of non-solvents and electrolytes on the formation and properties of cellulose I filaments. *Scientific Reports*, *9*(1). https://doi.org/10.1038/s41598-019-53215-0

Wang, S., Lu, A., & Zhang, L. (2016). Recent advances in regenerated cellulose materials. In *Progress in Polymer Science* (Vol. 53, pp. 169–206). Elsevier Ltd. https://doi.org/10.1016/j.progpolymsci.2015.07.003

Wang, X., Hu, J., & Zeng, J. (2012). SEP pulping of EFB fiber. In *BioResources* (Vol. 7, Issue 1).

Wang, Z., & Deuss, P. J. (2023). The isolation of lignin with native-like structure. In *Biotechnology Advances* (Vol. 68). Elsevier Inc. https://doi.org/10.1016/j.biotechadv.2023.108230

Westereng, B., Cannella, D., Wittrup Agger, J., Jørgensen, H., Larsen Andersen, M., Eijsink, V. G. H., & Felby, C. (2015). Enzymatic cellulose oxidation is linked to lignin by long-range electron transfer. *Scientific Reports*, *5*. https://doi.org/10.1038/srep18561

White, P. J., & Broadley, M. R. (2003). Calcium in plants. In *Annals of Botany* (Vol. 92, Issue 4, pp. 487–511). https://doi.org/10.1093/aob/mcg164

Wong, W. Y., Lim, S., Pang, Y. L., Shuit, S. H., Chen, W. H., & Lee, K. T. (2020). Synthesis of renewable heterogeneous acid catalyst from oil palm empty fruit bunch for glycerol-free biodiesel production. *Science of the Total Environment*, *727*. https://doi.org/10.1016/j.scitotenv.2020.138534

Woodall, A. A., Wai-Ming Lee, S., Weesie, R. J., Jackson, M. J., & Britton, G. (1997). Oxidation of carotenoids by free radicals: relationship between structure and reactivity. In *Biochimica et Biophysica Acta* (Vol. 1336).

Wu, W.-B., Jing, Y., Gong, M.-R., Zhou, X.-F., & Dai, H.-Q. (2011). Magnetic cellulose composites. In *BioResources* (Vol. 6, Issue 3).

Xavier, S., Gandhimathi, R., Nidheesh, P. V., & Ramesh, S. T. (2015). Comparison of homogeneous and heterogeneous Fenton processes for the removal of reactive dye Magenta MB from aqueous solution. *Desalination and Water Treatment*, *53*(1), 109–118. https://doi.org/10.1080/19443994.2013.844083

Xiang, L. Y., Mohammed, M. A., & Samsu Baharuddin, A. (2016). Characterisation of microcrystalline cellulose from oil palm fibres for food applications. *Carbohydrate Polymers*, *148*, 11–20. https://doi.org/10.1016/j.carbpol.2016.04.055

Xu, H., Huang, L., Xu, M., Qi, M., Yi, T., Mo, Q., Zhao, H., Huang, C., Wang, S., & Liu, Y. (2020). Preparation and Properties of Cellulose-Based Films Regenerated from Waste Corrugated Cardboards Using [Amim]Cl/CaCl2. *ACS Omega*, *5*(37), 23743–23754. https://doi.org/10.1021/acsomega.0c02713

Xu, H., Sanchez-Salvador, J. L., Balea, A., Blanco, A., & Negro, C. (2022). Optimization of reagent consumption in TEMPO-mediated oxidation of Eucalyptus cellulose to obtain cellulose nanofibers. *Cellulose*, *29*(12), 6611–6627. https://doi.org/10.1007/s10570-022-04672-w

Xu, Q., Chen, C., Rosswurm, K., Yao, T., & Janaswamy, S. (2016). A facile route to prepare cellulose-based films. *Carbohydrate Polymers*, *149*, 274–281. https://doi.org/10.1016/j.carbpol.2016.04.114

Yahya, A. K. (Ahmad K., & Talari, M. K. (Mahesh K. (2010). *Progress of physics research in Malaysia : PERFIK2009, Malacca, Malaysia, 7-9 December 2009*. American Institute of Physics.

Yang, H., Yan, R., Chen, H., Lee, D. H., & Zheng, C. (2007). Characteristics of hemicellulose, cellulose and lignin pyrolysis. *Fuel*, *86*(12–13), 1781–1788. https://doi.org/10.1016/j.fuel.2006.12.013

Yang, S. I., Wu, M. S., & Wu, C. Y. (2014). Application of biomass fast pyrolysis part I: Pyrolysis characteristics and products. *Energy*, *66*, 162–171. https://doi.org/10.1016/j.energy.2013.12.063

Yang, S., Xiong, Y., Ge, Y., & Zhang, S. (2018). Heterogeneous Fenton oxidation of nitric oxide by magnetite: Kinetics and mechanism. *Materials Letters, 218,* 257–261. https://doi.org/10.1016/j.matlet.2018.01.171

Yang, W., Tian, H., Liao, J., Wang, Y., Liu, L., Zhang, L., & Lu, A. (2020). Flexible and strong Fe3O4/cellulose composite film as magnetic and UV sensor. *Applied Surface Science*, *507*. https://doi.org/10.1016/j.apsusc.2019.145092

Yao, T. (2012). *Green Energy and Technology*. http://www.springer.com/series/8059

Yashni, G., Al-Gheethi, A., Radin Mohamed, R. M. S., Arifin, S. N. H., & Mohd Salleh, S. N. A. (2020). Conventional and advanced treatment technologies for palm oil mill effluents: a systematic literature review. *Journal of Dispersion Science and Technology*, 1–19. https://doi.org/10.1080/01932691.2020.1788950

Yoo, C. G., Meng, X., Pu, Y., & Ragauskas, A. J. (2020). The critical role of lignin in lignocellulosic biomass conversion and recent pretreatment strategies: A comprehensive review. In *Bioresource Technology* (Vol. 301). Elsevier Ltd. https://doi.org/10.1016/j.biortech.2020.122784

Yoshida, B. Y., & Prudencio, S. H. (2020). Alkaline hydrogen peroxide improves physical, chemical, and techno-functional properties of okara. *Food Chemistry*, *323*. https://doi.org/10.1016/j.foodchem.2020.126776

Yoshizaki, T., Shirai, Y., Hassan, M. A., Baharuddin, A. S., Raja Abdullah, N. M., Sulaiman, A., & Busu, Z. (2013). Improved economic viability of integrated biogas energy and compost production for sustainable palm oil mill management. *Journal of Cleaner Production*, *44*, 1–7. https://doi.org/10.1016/j.jclepro.2012.12.007

Yunus, R., Salleh, S. F., Abdullah, N., & Biak, D. R. A. (2010). Effect of ultrasonic pre-treatment on low temperature acid hydrolysis of oil palm empty fruit bunch. *Bioresource Technology*, *101*(24), 9792–9796. https://doi.org/10.1016/j.biortech.2010.07.074

Zainal, S. H., Mohd, N. H., Suhaili, N., Anuar, F. H., Lazim, A. M., & Othaman, R. (2021). Preparation of cellulose-based hydrogel: A review. In *Journal of Materials Research and Technology* (Vol. 10, pp. 935–952). Elsevier Editora Ltda. https://doi.org/10.1016/j.jmrt.2020.12.012

Zakaria, S., & Poh, L. K. (2007). POLYSTYRENE-BENZOYLATED EFB REINFORCED COMPOSITES. *Polymer-Plastics Technology and Engineering*, *41*(5), 951–962. https://doi.org/10.1081/PPT-120014397

Zawawi, A. Z., Gaik, L. P., Sebran, N. H., Othman, J., & Hussain, A. S. (2018). An optimisation study on biomass delignification process using alkaline wash. *Biomass Conversion and Biorefinery*, *8*(1), 59–68. https://doi.org/10.1007/s13399-017-0246-x

Zazo, J. A., Pliego, G., Blasco, S., Casas, J. A., & Rodriguez, J. J. (2011). Intensification of the Fenton process by increasing the temperature. *Industrial and Engineering Chemistry Research*, *50*(2), 866–870. https://doi.org/10.1021/ie101963k

Zhang, L., Yu, H., Wang, P., Dong, H., & Peng, X. (2013). Conversion of xylan, d-xylose and lignocellulosic biomass into furfural using AlCl3 as catalyst in ionic liquid. *Bioresource Technology*, *130*, 110–116. https://doi.org/10.1016/j.biortech.2012.12.018

Zhang, M. hui, Dong, H., Zhao, L., Wang, D. xi, & Meng, D. (2019). A review on Fenton process for organic wastewater treatment based on optimization perspective. In *Science of the Total Environment* (Vol. 670, pp. 110–121). Elsevier B.V. https://doi.org/10.1016/j.scitotenv.2019.03.180

Zhang, X., He, M., He, P., Li, C., Liu, H., Zhang, X., & Ma, Y. (2018). Ultrafine nano-network structured bacterial cellulose as reductant and bridging ligands to fabricate ultrathin K-birnessite type MnO 2 nanosheets for supercapacitors. *Applied Surface Science*, *433*, 419–427. https://doi.org/10.1016/j.apsusc.2017.10.053

Zhao, X., Dong, L., Chen, L., & Liu, D. (2013). Batch and multi-step fed-batch enzymatic saccharification of Formiline-pretreated sugarcane bagasse at high solid loadings for high sugar and ethanol titers. *Bioresource Technology*, *135*, 350–356. https://doi.org/10.1016/j.biortech.2012.09.074

Zhao, X., Zhou, H., Sikarwar, V. S., Zhao, M., Park, A. H. A., Fennell, P. S., Shen, L., & Fan, L. S. (2017). Biomass-based chemical looping technologies: The good, the bad and the future.

In *Energy and Environmental Science* (Vol. 10, Issue 9, pp. 1885–1910). Royal Society of Chemistry. https://doi.org/10.1039/c6ee03718f

Zhao, Y., Jiang, C., Xiong, Y., Ma, Y., Zhang, T., Zhang, X., Qin, J., Shi, X., & Zhang, G. (2023). Flexible and robust TEMPO-oxidized cellulose nanofibrils/mica composite as paper dielectrics with enhanced dielectric property. *Journal of Materials Science: Materials in Electronics*, *34*(4). https://doi.org/10.1007/s10854-022-09761-x

Zhu, Y., Zhu, R., Xi, Y., Zhu, J., Zhu, G., & He, H. (2019). Strategies for enhancing the heterogeneous fenton catalytic reactivity: A review. In *Applied Catalysis B: Environmental* (Vol. 255). Elsevier B.V. https://doi.org/10.1016/j.apcatb.2019.05.041